

The Pennsylvania State University

The Graduate School

**CONFORMATIONAL AND COLLOIDAL STABILITY OF
MACROMOLECULES IN AQUEOUS SALT SOLUTIONS**

A Dissertation in

Chemistry

by

Bradley A. Rogers

© 2019 Bradley A. Rogers

Submitted in Partial Fulfillment

of the Requirements

for the Degree of

Doctor of Philosophy

December 2019

The dissertation of Bradley A. Rogers was reviewed and approved* by the following:

Paul S. Cremer
J. Lloyd Huck Chair in Natural Sciences
Professor of Chemistry
Professor of Biochemistry and Molecular Biology
Dissertation Advisor
Chair of Committee

Mark Maroncelli
Distinguished Professor of Chemistry

Scott A. Showalter
Professor of Chemistry
Professor of Biochemistry and Molecular Biology

Michael A. Hickner
Professor of Materials Science and Engineering

Phil Bevilacqua
Distinguished Professor of Chemistry
Distinguished Professor of Biochemistry and Molecular Biology
Head of the Department of Chemistry

*Signatures are on file in the Graduate School

ABSTRACT

The conformational and colloidal stability of proteins in aqueous solutions are critical to the function of biological cells and the shelf-life of biopharmaceutical drug products. These properties of protein macromolecules are strongly influenced by cosolutes in the solution, including inorganic salt ions and non-ionic crowding agents. The intrinsic and cosolute-modulated properties of proteins are governed by specific interactions between proteins, water, and cosolutes. Herein, the non-covalent interactions that drive two phenomena are explored, including anion-induced denaturation of proteins and the liquid-liquid phase separation of therapeutic antibody solutions. In the first aim, protein folding is mimicked by thermoresponsive polymers model systems that undergo hydrophobic collapse upon heating. A combination of light scattering measurements as well as vibrational and nuclear magnetic resonance spectroscopies on these thermoresponsive polymers reveal that the structure of water-water hydrogen bonding at hydrophobic surfaces can modulate the binding affinity of weakly hydrated anions over several orders of magnitude. In the second aim, the colloidal phase separation of concentrated antibody formulations is imaged by dark-field microscopy on a temperature gradient microfluidics platform. This platform facilitates high-throughput measurements of phase separation across a range of temperatures and solution conditions, simultaneously. Analysis of the dark-field images over time reveals that the phase separation is a multistep reaction. Collectively, this work provides novel insights into the conformational and colloidal stability of proteins, which advance the current understanding of protein behavior in biological and biotechnological solutions.

TABLE OF CONTENTS

LIST OF FIGURES	vi
LIST OF TABLES	xx
ACKNOWLEDGEMENTS	xxi
Chapter 1 The Role of Non-Covalent Interactions in Protein Stability and Ion-Specific Effects in Aqueous Solutions	1
Conformational and Colloidal Behavior of Proteins in Aqueous Solutions	2
Ion-Specific Effects on Proteins and Macromolecules	5
Light Scattering Measurements of Phase Separation in Polymer and Protein Solutions	6
Spectroscopic Tools for Ion-Protein Interactions and Water Structure	12
Project Overview and Key Findings	15
Chapter 2 Ion-Specific Effects on the Hydrophobic Collapse of Thermoresponsive Polymers.....	17
Hydrophobic Collapse of Thermoresponsive Polymers.....	17
Thermodynamic Investigations of Hofmeister Anion Interactions with PEO	20
Spectroscopic Investigations of Hofmeister Anion Interactions with PEO	25
The Role of Cations in the Adsorption of Weakly Hydrated Anions to PEO.....	34
Driving Forces for the Adsorption of Weakly Hydrated Anions to Polymer Chains	37
Chapter 3 Surface Curvature and the Adsorption of Weakly Hydrated Anions to Hydrophobic Interfaces.....	40
Discrepancies in the Literature on the Adsorption of Weakly Hydrated Anions to Hydrophobic Surfaces	41
¹ H NMR Peak Assignments for Polyethers of Varying Chain Length	48
¹ H NMR Measurements of SCN ⁻ Interactions with Polyethers of Varying Chain Length.....	57
Consolidating the Heterogeneous Adsorption by Curvature of the Aliphatic Binding Site	66
Measuring Water Structure by Vibrational Spectroscopy.....	69
Hydration Shell Water Structure for Polyethers of Varying Chain Length	76
Surface Curvature Connects Hydrophobicity and Hofmeister Chemistry	82
Chapter 4 Crowder-Induced Phase Separation of Therapeutic Antibody Solutions.....	87
Challenges and Current Strategies for Formulating High Concentration Liquids ...	89
Phase Separation Temperature Measurements on a Temperature Gradient	94

Aqueous Two-Phase System Formation Measurements on a Temperature Gradient	107
Discussion of LLPS Assays to Monitor Colloidal Stability in Concentrated Protein Solutions	111
Chapter 5 A Stepwise Mechanism for Aqueous Two-Phase System Formation in Concentrated Antibody Solutions	113
Phase Separation and the Colloidal Stability of Therapeutic Protein Solutions	114
Measuring Aqueous Two-Phase System Formation on a Temperature Gradient....	117
Modeling the Kinetics of Aqueous Two-Phase System Formation	126
A Stepwise Mechanism to Explain the Non-Arrhenius Kinetics of ATPS Formation	143
Conclusion and Implications	155
References	157
Appendix A Supporting Information for Chapters 2-3	188
Appendix B Supporting Information for Chapters 4-5	208

LIST OF FIGURES

- Figure 1-1: (A) Bond-line structure of a protein, where the side chains are indicated by R. (B) Schematic illustration of a protein chain in an extended denatured state and a compact native structure. The hydrophobic and hydrophilic side chains are indicated by filled and open circles, respectively. As illustrated, the hydrophobic side chains self-assemble to form the core of the native state. 3
- Figure 1-2: Schematic illustration of irreversible aggregation due to conformational instability versus phase separation due to colloidal association. The protein macromolecules are drawn as curved lines. Distinct protein chains are colored for clarity of the protein-protein interactions. 4
- Figure 1-3: Schematic illustration of ion-protein interactions. Cartoon model of the structure of lysozyme determined by x-ray crystallography. The insets portray anions and cations of inorganic salts interacting with proteins through ion-pairing with charged side chains or by adsorbing to the amide backbone. 6
- Figure 1-4: Schematic phase diagram for the separation of solutes at low and high temperatures. The dark shaded regions of the diagram indicate conditions where the solution separates into two phases. The open white circles mark the LCST and UCST. Cartoons of the interactions that drive separation are provided on the right-hand side. 7
- Figure 1-5: Hydrophobic collapse of thermoresponsive polymers. (A) The structure of several non-ionic polymers that undergo hydrophobic collapse at high temperature. (B) Images of the light scattering from a poly *N*-isopropylacrylamide solution above and below the phase separation temperature. Cartoon insets are provided to illustrate the extended and soluble at cold temperatures versus the collapsed and aggregated structures that form upon heating. 8
- Figure 1-6: Phase separation of folded proteins. (A) X-ray crystal structures of four proteins that undergo phase separation at cold temperatures. The surface of the protein structures are colored to indicate the electrostatic charge, where red is negative and blue is positive. (B) Images of the light scattering from an antibody solution above and below the phase separation temperature. Schematics are provided to illustrate the homogeneous distribution of proteins at high temperature versus the formation of phase separated droplets at cold temperatures. 9
- Figure 1-7: Schematic illustrations of the temperature gradient microfluidics technology. (A) Cartoon of a capillary containing a protein solution exhibiting UCST behavior on the temperature gradient, where the solution is cloudy on the cold side of the gradient. (B) Schematic of several capillary tubes on the temperature gradient device, which are imaged using a dark-field microscope. 10
- Figure 1-8: Kinetics of aqueous two-phase system (ATPS) formation. (A) Images of ATPS formation over time in a centrifuge tube. Schematics are provided to illustrate

- the structure of the initial protein-rich droplets and equilibrated ATPS. (B) Schematic illustration of the Arrhenius analysis of the temperature kinetics of ATPS formation. The apparent activation energy, $E_{A,app}$, extracted from the slope of the Arrhenius plot in (B) relates to the barrier for converting a droplet suspension into an ATPS formation, as illustrated schematic reaction coordinate diagram in (C)..... 11
- Figure 1-9:** Schematics of ion-solute interactions and the hydration shell. The insets depict ^1H spin of nuclei along the polymer backbone and the OH stretch of water vibrational spectroscopies to study local chemical environments, like ion adsorption and hydrogen bonding architectures. 12
- Figure 1-10:** Schematic illustration of the solute partitioning model. The left-hand side of the schematic illustrates a folded protein, while the right-hand side depicts the protein in a denatured state. Strongly hydrated anions, like SO_4^{2-} , are repelled from the protein surface. As such, they are excluded from the region surrounding the macromolecule. This excluded volume is smaller for the folded state, rather than the extended. In contrast, weakly hydrated anions, like SCN^- , are attracted to the protein surface and are enriched or included in the polymer's hydration shell. These attractive ion-protein interactions shift the folding equilibrium toward the denatured state because this maximizes the binding site exposure to the solution. 14
- Figure 2-1:** Structure and temperature-dependent conformations of proteins and thermoresponsive polymers (A) The bond-line structure of a protein and a schematic of the unfolding and folding of the chain. (B) Bond-line structures of several thermoresponsive polymers. The schematic on the right-hand side illustrates the hydrophobic collapse that occurs upon heating these polymer solutions. 18
- Figure 2-2:** Light scattering measurements of hydrophobic collapse of PEO solutions. (A) Images of a PEO solution below and above the LCST. (B) Raw data from the melting point temperature apparatus for a solution containing 10 mg/mL PEO and 1 M NaCl. The LCST is determined from the onset of light scattering, which is marked by the red arrow and intersection of the two red lines. 20
- Figure 2-3:** LCST phase diagrams for PEO as a function of various sodium salt concentrations. (A) The effects of NaCl on the LCST. A schematic is provided to illustrate the interpretation of the data. (B) Comparison of Na_2SO_4 , NaCl, and NaSCN effects on the LCST of PEO. The circles are the LCST data points and the solid curves are best fits to the data using either Equations 2-1, 2-2, or 2-3 for Na_2SO_4 , NaCl, and NaSCN, respectively. 22
- Figure 2-4:** LCST phase diagram and proposed mechanism of anion-polymer interactions. (A) The data points are LCST values for PEO as a function of NaSCN concentration. The solid red curve is a fit to the data using Equation 2-3. (B) Cartoon illustration of the binding of anions to the polymer chain. The three cartoons are meant to represent increasing salt concentration from left to the right..... 24
- Figure 2-5:** Schematic illustrations of nuclear magnetic resonance spectroscopy. (A) Cartoon of the spin property of nuclei covalent bound to the PEO chain. (B) The

- effect of magnetic fields on the energy of the spin up and spin down states. The diagram is drawn so that the external magnetic field, B_0 , is pointing in the up direction, as indicated by the thick black arrow. (C) A simplified cartoon illustration of the hardware used to perform a nuclear magnetic resonance experiment. (D) Sample geometry and composition used to acquire ^1H NMR spectra. Insets are provided to illustrate the general composition of the sample and reference solutions tested in this work. 26
- Figure 2-6: Spectrum of a PEO proton, where the chemical shift is marked by the vertical brown line. The black data points represent frequencies measured by the spectrometer, while the solid brown curve was obtained by zero-point filling in the Mnova software..... 28
- Figure 2-7: Salt-induced changes in the ^1H NMR spectrum of PEO. (A) Offset spectra acquired at different NaSCN concentrations. (B) The chemical shift of the methylene proton peak plotted as a function of salt concentration. The brown circles are the chemical shift data and the solid brown curve is a fit to the data using Equation 2-5. The error bars represent the standard deviation between 2-3 solutions preparations. (C) Schematic illustration of the physical interpretation of the model. The model describes the NaSCN effect with two contributions, including a dominant linear shielding effect that may involve indirect interactions and a smaller saturable deshielding contribution due direct adsorption of SCN^- anions to the aliphatic methylene units. 29
- Figure 2-8: Comparisons of models for the NaSCN-induced chemical shift data of PEO-20k. (A) Chemical shift of the PEO-20k protons versus NaSCN concentration, where the solid brown curve is a fit to a line. (B) The residual chemical shift of (A) calculated using Equation 2-6. (C) Chemical shift of the PEO protons versus NaSCN concentration, where the solid brown curve is a fit to Equation 2-5. (D) The residual chemical shift of (C) calculated using Equation 2-6..... 31
- Figure 2-9: The temperature dependence of the chemical shift of PEO in D_2O . Two schematics are provided to illustrate the proposed mechanism for the decrease in the chemical shift. 32
- Figure 2-10: Salt-induced chemical shifts of PEO protons. (A) The chemical shift as a function of NaSCN, NaCl, and Na_2SO_4 . The data points are plotted as circles and the solid lines are fits to the data, using Equation 2-5 for NaSCN and Equation 2-7 for NaCl and Na_2SO_4 . (B) The residual chemical shifts for simple linear fits to each of the titration curves. The residual chemical shift data show distinct deviation for NaSCN in comparison the NaCl and Na_2SO_4 33
- Figure 2-11: LCST phase diagrams for PEO in the presence of various alkali iodide salts. The data points are measurements of the LCST, while the solid curves are fits to the data. 35
- Figure 2-11: Salt-induced chemical shifts of PEO protons. (A) The chemical shift as a function of LiI, NaI, and CsI. The data points are plotted as circles and the solid

- lines are fits to the data, using Equation 2-5. (B) The residual chemical shifts for simple linear fits to each of the titration curves. The residual chemical shift data show similar nonlinearity as the NaSCN. 37
- Figure 2-12: Schematic illustration of anion adsorption to a hydrophobic polymer chain. The top cartoons represent the interactions in vacuum, while the lower schematics highlight the importance of interfacial water structure in the process of adsorption. 39
- Figure 3-1: Surface curvature and binding affinity hypothesis. The structures of several molecules are provided along with cartoons to illustrate the general shapes. The binding constants determined for these molecules and others are summarized at the bottom of the figure. The values for the K_D are provided in molar units. 42
- Figure 3-2: Surface curvature and solubility. The structure of several soluble small molecules are provided in contrast with polymers and lipids that self assemble in water. The origins of the difference in solubility can be understood by the structure of water-water hydrogen bonding at the surface of small, curved solutes versus larger solutes, whose surfaces appear locally more flat. 44
- Figure 3-3: Proposed mechanism for the connection of hydrophobicity to ion-specific effects. Surface curvature impacts the order of the hydration shell. Weakly hydrated anions are excluded from the well-ordered hydration shells of small molecules. They readily adsorb to flat interfaces because they displace water molecules that exhibit broken hydrogen bonding. The Small solutes, depicted by the small grey sphere, exhibit positive curvature and have ordered hydration shells. The macroscopic interfaces, depicted by the grey slab, are flatter and contain sites of defective hydrogen bonding. 45
- Figure 3-4: Schematic illustration of the experimental approach to systematically investigate the surface curvature hypothesis. Polymers of PEG and PEO were used as model systems ranging from monomers to 100,000 mers. The specific lengths used in these studies are summarized in the two grey horizontal bars. The key results from the study are summarized in the lower two panels. Namely, SCN^- anions are repelled from monomers and the termini of polymers, but are attracted to the middle of polymer chains, where the surface curvatures is locally more flat. Herein, it is shown that SCN^- is excluded from the termini of chains where the hydration shell is well-ordered (blue arrow). In contrast, SCN^- preferentially adsorbs to the center of polymer chains where the water structure is more disordered (red arrow). 46
- Figure 3-5: 1H NMR spectra of PEO-*n* mers. (A) Bond-line structure of PEO-*n* mers. (B) 1H NMR spectra of PEO-*n* mers, the solute length is labeled on the left-hand side of each spectrum. Two sets of peaks corresponding to the methyl termini and the central methylene are labeled with circles in (A) and dashed vertical lines in (B). 49
- Figure 3-6: 1H NMR spectra of the methylene protons as a function of PEO-*n* mer chain length (A) The spectral region corresponding to the methylene protons from Figure 3-5. The spectrum for each chain length is provided and labeled on the left-hand

- side. (B) Bond-line structures for the various chain lengths. The colored circles in (B) are assignments to specific peaks in the ^1H NMR spectra of (A)..... 52
- Figure 3-7: ^1H NMR spectra of the methylene protons as a function of PEG- n mer chain length (A) The spectral region corresponding to the methylene protons. The spectrum for each chain length is provided and labeled on the left-hand side. (B) Bond-line structures for the various chain lengths. The colored circles in (B) are assignments to specific peaks in the ^1H NMR spectra of (A)..... 54
- Figure 3-8: ^1H NMR spectra of the methylene protons as a function of PEG- n and PEO- n mer chain length (A) The spectral region corresponding to the methylene protons. The spectrum for each chain length is provided and labeled on the left-hand side. (B) Bond-line structures for the various chain lengths. The colored circles in (B) are assignments to specific peaks in the ^1H NMR spectra of (A)..... 56
- Figure 3-9: NaSCN-induced chemical shifts of the most central methylene proton on various polyether chains. The data is grouped into three panels for different solutes, including (A) PEO- n mers, (B) PEG- n mers from $n = 1$ to 35 monomer units, and (C) long chain PEO- n and PEG- n mers. The solid curves are fits to Equation 3-2..... 59
- Figure 3-10: NaSCN-induced chemical shifts for PEG-1 and PEG-2. The solid curves are fits to the data using either Equation 3-3 or 3-4, for PEG-2 and PEG-1, respectively. ... 60
- Figure 3-11: NaSCN-induced chemical shifts for protons located on the methyl termini of PEO- n mers. 61
- Figure 3-12: Estimates of the lower limit of detection for the Langmuir isotherm contribution to the salt-induced chemical shift effects. (A) Four theoretical titration curves simulated using parameters $a = -0.0215 \text{ ppm M}^{-1}$, $\delta_{\text{max}} = 0.003 \text{ ppm}$, and K_D values ranging from 0.01 M to 10 M. (B) The residual chemical shift effects relative to linear fits for the data in (A). (C) The RMSD calculated from residual chemical shifts plotted versus the K_D value used to generate the simulated data set. The dashed red lines in (C) mark the K_D value of 2.4 M that equaled the typical error of the chemical shift data in the experiments of 0.0002 ppm..... 63
- Figure 3-13: Summary of NaSCN-induced effects on the ^1H chemical shifts of the central-most methylene protons of PEO- n and PEG- n solutes obtained from fits to Equation 3-2. The fitted parameters are plotted as a function of chain length, including (A) K_D , (B) δ_{max} , and (C) a . The data sets for PEG- n and PEG- n mers are plotted as black and green data points, respectively. The black curves are empirical fits to Equation 3-6. The crossover lengths obtained from these fits are provided on each panel..... 65
- Figure 3-14: The interaction of SCN^- with polyether chains. (A) The bond line structure of PEO-5 and schematic of heterogeneous SCN^- adsorption. (B) The NaSCN-induced chemical shifts for the central methylene (red data points), penultimate methylene (orange data points), and end methylene (green data points), and terminal methyl (blue data points) protons of PEO-5 measured by ^1H NMR spectroscopy. The

solid lines in (B) are fits to Equation 3-2. The location of each proton is circled in (A). (C) The free energy of adsorption for SCN-polymer interactions as a function of position along the chain. The black curve is a guide to the eye..... 69

Figure 3-15: Basics of vibrational spectroscopy for the OH stretch of water. (A) Schematic illustration of the ground and excited states of the OH stretching vibration. The average bond length, r_{OH} , extends when the molecule is excited. (B) Energy landscape as a function of OH bond length. The Raman experiment is illustrated by the colored vertical arrows, which excite the molecules into a virtual state of vary high energy that instantaneously scatter as a red-shifted photon due to the loss of energy via the vibration. (C) Schematic illustration of the experimental se, where a laser is directed toward a sample and the scattered light is analyzed. (D) Raman spectrum of pure water at 20 °C..... 71

Figure 3-16. Two-state model interpretation for the Raman spectrum of liquid water. (A) Raman spectra of water measured as a function of temperature. The two peaks of the spectrum are labeled with dashed vertical lines. (B) Schematic illustration of the hydrogen bonding structures assigned to the two peaks of the Raman spectrum. The water molecule indicated by the colored arrows are intended to give rise to specific vibrational frequencies. 73

Figure 3-17: Basics of hydration shell spectroscopy by Raman-multivariate curve resolution. (A) Schematic illustration of PEG-1, its hydration shell, and bulk water residing beyond the first layer of water. (B) Raman spectra of pure water and a solution of 0.5 M PEG-1. (C) The solute-correlated spectrum of PEG-1 obtained via Raman-MCR. The black circles are the data points, while the solid black curve is the sum of a fit to multiple gaussian components. The CH stretch gaussians are colored in grey, while the two OH stretching modes are colored in blue or red to mark the 3250 cm^{-1} and 3450 cm^{-1} , respectively..... 75

Figure 3-18: Solute correlated spectrum for (A) PEO-1 and (B) PEO-20k. Each spectrum is normalized to the area under the CH stretch bands. 77

Figure 3-19: Chain length dependence of the OH stretch bands in the hydration shells of polyethers. (A) Solute correlated spectra for several PEG- n and PEO- n mers. The data have been normalized so that the intensity at 3450 cm^{-1} is equal to 1. The open circles are the measured spectra, while the solid curves are fits to Equation 3-8. (B) The ratio of the two OH stretch populations as a function of chain length. The data sets for the PEG- n and PEO- n mers are plotted in black and green, respectively. The solid black curve in (B) is a fit to Equation 3-6. 78

Figure 3-20: Chain length dependence of the OH stretch in the hydration shell of PEO- n mers. (A) Solute-correlated spectra for PEO-1 in blue and PEO-20k in red. The two OH stretch bands are marked with dashed vertical lines and labeled with their structure and frequency. (B) Ratio of the ordered-to-disordered areas of the two populations. The data are shown for PEO-1 to PEO-4 and then combined with the PEG-4 to PEG-227. The longest polymer chains were PEO-2k and PEO-20k. The

- solid black curve in (B) is a fit to the segmentation model described by Equation 3-9..... 79
- Figure 3-21: Fit assessment for the segmentation model describing the length dependence the OH stretch bands in the hydration shells of polyether solutes. (A) Schematic illustration of the segmentation model, where the PEO-5 solute has been segmented into four types of surfaces. The ratio of ordered-to-disordered peak areas is plotted as a function of chain length in (B-D). The black curve is the best fit to the four segment model, shown in (B-D) for comparison. The fits to two segments and three segments models are portrayed in (C). Lastly, in (D) the comparison of various fits to the four segments model using fixed parameters for the central and penultimate groups. The averages of these fits were used in the black curves shown in (B-D)..... 81
- Figure 3-22: Correlation of the adsorption free energies measured via ^1H NMR spectroscopy and the ratio of ordered-to-disordered water structures near the surface of specific segments of polyether solutes. The data are grouped based on the four-segment model and labeled accordingly. 83
- Figure 3-23: Schematic illustration of the mechanism for the surface curvature effect. 84
- Figure 4-1: Literature overview of liquid-liquid phase separation. The center panel provides a cartoon depiction of the formation of protein-rich droplets, where each protein monomer is drawn as a grey sphere. The images that emanate from the central schematic provide examples of LLPS in other systems, including oil-water mixtures, inside of the cytoplasm of living cells, thermoresponsive polymers, and concentrated formulations of biologics. The behavior of macromolecules inside of these droplets, e.g. crystallization, has also become a topic of interest. Adapted from references 15 and 16..... 88
- Figure 4-2: Development and degradation of mAb-based drug products. (A) Schematic cartoon illustrating the structure of a mAb, which is engineered to bind to specific medicinal targets. (B) Drug development timeline, where the funnel at the top of the figure portrays information about the stages of drug candidate selection. (C) Image of a liquid injectable modality for mAb therapeutics. (D) Degradation pathways for protein-based pharmaceutical drug products, including chemical, conformational, and colloidal interactions. 90
- Figure 4-3: Schematic of a sample placed on the temperature gradient device. The primary advantages of this approach are summarized by the conditions on the right-hand side of the Figure..... 93
- Figure 4-4: Images and schematics of temperature quenching. (A) Images and schematics of a protein solution, held at warm temperatures, marked by 1. Upon a temperature quench to colder conditions, labeled as 2 in (B), the solution becomes cloudy due to the formation of protein-rich droplets, which scatter light. (C) Colloid phase diagram exhibiting an upper critical solution temperature (UCST). The red curve delineates conditions where the system prefers to be in one or two phases. The temperature

- quench is depicted on the phase diagram with the black circles and arrows. The numbers on the black circles in (C) correspond to the images in (A) and (B)..... 95
- Figure 4-5: Measurements of T_{ph} on a temperature gradient. (A) Schematic of the temperature gradient device (B) Image of a 90 mg/mL mAb solution containing 20 mg/mL PEG. A line scan from the image is plotted to demonstrate how T_{ph} is quantitatively measured from the data. (C) The temperature gradient experiment probes a vertical slice of the phase diagram, unlike the temperature quenching assays described in Figure 4-4..... 96
- Figure 4-6: PEG-induced LLPS for a mAb solution containing 90 mg/mL mAb at pH 6.8. (A) Schematic illustration of the excluded volume mechanism by which PEG is believed to crowd proteins out of solution. (B) The values of T_{ph} measured as a function of the PEG concentration. The red circles are the T_{ph} measurements, while the red line is fit to Equation 4-1..... 98
- Figure 4-7: Hofmeister anion studies on the T_{ph} of a 90 mg/mL mAb-1 solution in 14 mM bis-tris at pH 6.8 and 7.5 mg/mL PEG..... 99
- Figure 4-8: Hofmeister anion effects on T_{ph} of mAb-1. (A) Cloud point temperatures measured in below the pI in 7.5 mg/mL PEG and 14 mM bis-tris at a solution pH of 6.8. (B) Cloud point temperature measured near the pI in 7.5 mg/mL PEG and 28 mM tris at a solution pH of 7.9. The mAb-1 concentration was held constant at 90 mg/mL for the experiments summarized in both (A) and (B). The solid curves are guides to the eye..... 100
- Figure 4-9: Hofmeister anion and cation effects on T_{ph} of mAb-1 with 7.5 mg/mL PEG and 28 mM tris at a solution pH of 7.9, which is near the pI of 8.2. The data are grouped by (A) sodium salt titrations and (B) chloride salt titrations..... 101
- Figure 4-10: Proposed mechanism for the effects of salt on T_{ph} . The mAb is depicted as a grey sphere with charges representing ionic side chains. The adsorption of anions to positive charge sites first neutralizes the total charge of the protein leading to a “salting-out” effect. At higher salt concentrations additional binding of anions leads to overcharging and a “salting-in” effect. 102
- Figure 4-11: Basics of ATR-FTIR spectroscopy. The IR radiation is illustrated by the solid red arrows, while the evanescent field is depicted by the filled in red wave. 103
- Figure 4-12: Schematic illustration of phase separation experiments on the ATR-FTIR stage. The proteins are depicted as grey spheres..... 103
- Figure 4-13: Amide I and amide II vibrational spectra of a 90 mg/mL mAb-1 sample in bis-tris buffer at pH 7.9. The solution also contained 25 mg/mL PEG and 100 mM Na_2SO_4 104
- Figure 4-14: ATR-FTIR spectra of 90 mg/mL mAb-1 sample in bis-tris buffer at pH 7.9 and 25 mg/mL PEG. The two panels represent these conditions in addition to (A) 100 mM Na_2SO_4 and (B) 100 mM NaSCN 105

Figure 4-15: ATR-FTIR spectra of the ion peaks for solutions containing 90 mg/mL mAb-1 sample in bis-tris buffer at pH 7.9 and 25 mg/mL PEG. The two panels represent these conditions in addition to (A) 100 mM Na ₂ SO ₄ and (B) 100 mM NaSCN.	106
Figure 4-16: Solute-correlated spectra of a 90 mg/mL mAb-1 solution at various pH values.....	107
Figure 4-17: Images and schematics of ATPS formation.	108
Figure 4-18: Schematic illustration of the temperature gradient and kinetics measurements that can be analyzed with the Arrhenius law.....	109
Figure 4-19: Measurements of the kinetics of ATPS formation on a temperature gradient. (A) TGM cartoon, reiterating the imaging of the capillary from a top-down orientation. (B) Dark-field images of a 90 mg/mL mAb-1 sample over time on the TGM device. (C) The rate constant of ATPS formation was measured by extracting the light scattering at specific temperatures. The open circles are the data from the dashed green line in (B) and the solid curve is a fit to the data using the model written in the top right of (C).	110
Figure 4-20: Non-Arrhenius kinetics of ATPS formation of mAb solutions. (A) Arrhenius plot and (B) the proposed reaction coordinate diagram to describe the data measured in (A). This figure is adapted from Reference 94.	111
Figure 4-21: Schematic illustrations of (A) TGM apparatus, (B) parameters of colloid phase separation, (C) hypothesis of a correlation between the rate constant of long-term aggregation (k_{agg}) versus LLPS parameters, and (D) potential driving forces for reversible colloidal protein-protein interactions.	112
Figure 5-1: Schematic phase diagram of a colloidal system with attractive interactions displaying an upper critical solution temperature. The binodal (red), spinodal (green), and gelation (blue) curves delineate the various regions of the diagram. Temperature gradient experiments were performed at concentrations below the critical point (open black circle at the top of the binodal and spinodal curves), as illustrated by the vertical bar at C_0 (red to blue gradient with decreasing temperature). T_{ph} , T_{meta} , and T_{gel} values were extracted from each experiment and are denoted by open colored circles.	116
Figure 5-2: ATPS formation of a mAb solution on the temperature gradient device. (A) Dark-field images at time points ranging from $t = 1$ to $t = 60$ min during the experiment. The two, short upward-pointing black arrows at the bottom of the image denote the temperatures at each of these two points, respectively, while the colored arrows denote the positions of the three transition temperatures. (B) Schematic diagrams of ATPS formation along the temperature gradient device corresponding to the time points in (A). The schematics on the right are drawn from a side-on perspective of the rectangular capillary tube. The droplet cartoons on the far right side depict more detailed structures corresponding, in descending order, to a protein-	

rich droplet, two coalescing droplets, an equilibrated ATPS, and the gel state, respectively. The protein molecules are depicted as grey spheres in each droplet cartoon. (C) Line scans of scattering intensity versus temperature. The line scans plotted in (C) correspond to the dashed horizontal lines on the images in (A), which are color coded accordingly. The dashed vertical lines mark the phase transition temperatures. 119

Figure 5-3: Dark-field images and schematics of phase separation on the temperature gradient device versus images of temperature quenches performed on macroscopic samples. The dark field images of the temperature gradient experiments are provided at five time points (columns A-E) during the separation of a solution containing 90 mg/mL mAb and 20 mg/mL PEG. Specifically, we show (A) an image of a sample exposed to a constant temperature (318 K) versus a linear temperature gradient (278 – 318 K) at (B) 1 min, (C) 5 min, (D) 7 min, and (E) 60 min after sample introduction. The white circles in the schematics represent protein-rich droplets, which scatter light (B-E). The droplets coalesce to form the clear protein-rich phase of an ATPS, as depicted by the large grey droplet (D-E). For comparison, we also recorded images of the phase separation process in centrifuge tubes upon temperature quenches at (Quench 1) 293 K and (Quench 2) 277 K, which reside in the spinodal and gel regions, respectively. We provide (F) an image recorded at 318 K, prior to the temperature quench, versus images captured at (G) 1 min, (H) 15 min, (I) 60 min after the temperature quench. 122

Figure 5-4: Line scans of scattering intensity as a function of temperature at three time points of phase separation for the 90 mg/mL mAb and 20 mg/mL PEG solution. The line scans were obtained from the dark field images shown in Figure 5-3. The line scans are given for (A) $t = 1$ min, (B) $t = 7$ min, and (C) $t = 60$ min. The solid lines are provided as visual aids for the transition temperature determinations of T_{ph} (red lines), T_{meta} (green lines), and T_{gel} (blue lines). 124

Figure 5-5: Colloidal phase diagram measured at 20 mg/mL PEG-3350. T_{ph} (red data points) and T_{gel} (blue data points) were measured at $t = 1$ min and $t = 60$ min, respectively; while T_{meta} (green data points) was measured at the first time point when ATPS formation had come to completion below T_{ph} . The red and green curves are guides to the eye, while the blue curve is a linear fit to the T_{gel} data. 125

Figure 5-6: Phase transition temperatures measured as a function of PEG concentration at a fixed mAb concentration. The slopes of T_{ph} , T_{meta} , and T_{gel} were 0.80, 0.71, and $0.63 \text{ K (mg/mL)}^{-1}$, respectively. 126

Figure 5-7: Kinetic analysis of the light scattering data obtained in Figure 5-2. (A) The scattering intensity is plotted as a function of both time and temperature. The data are shown at 15 s time intervals for clarity. (B) Three isothermal decays of the normalized scattering intensity as a function of time from the three distinct kinetic regions along the temperature gradient. The open circles are data points and the solid lines are fits to the data using Equation 5-1. 127

Figure 5-8: Control experiments on the establishment of a temperature gradient and a demonstration of the procedure for processing the light scattering kinetic data. (A) The line scans of a 10 mg/mL PNIPAM sample containing 0.8 M NaCl over time along a linear temperature gradient (278 – 318 K). The apparent LCST values (blue data points) determined from (A) are plotted in (B) along with a direct measurement of the temperature by a thermocouple (red data points) as a function of time. The shift of the LCST with time is illustrated schematically in (C). Two pictures demonstrate the thermocouple measurement technique (D). (E-G) The sequential processing of raw data is shown for an isotherm at 293.3 K of a 90 mg/mL mAb and 20 mg/mL PEG solution. The light scattering intensity is plotted as a function of time in (E). Note, the vertical red line denotes the time required to reach a steady-state temperature gradient. After discarding the first minute of raw data, the intensity was plotted as a function of shifted time in (F). The normalized data are provided in (G). 129

Figure 5-9: Normalized light scattering isotherms and KWW fits. The data are grouped into three panels corresponding to (red box) 90 mg/mL, (green box) 60 mg/mL, and (blue box) 40 mg/mL mAb concentrations all at 20 mg/mL PEG. The 90 mg/mL data are displayed in six plots with decreasing temperature: (A) 299.7 – 298.8 K, (B) 298.7 – 297.1 K, (C) 297.0 – 295.4 K, (D) 295.2 – 293.7 K, (E) 293.5 – 292.3 K, and (F) 292.2 – 290.1 K. The 60 mg/mL data are displayed in four plots with decreasing temperature: (G) 296.8 – 295.8 K, (H) 295.7 – 294.0 K, (I) 293.8 – 292.2 K, and (J) 292.0 – 288.7 K. The 40 mg/mL data are displayed in two plots with decreasing temperature: (K) 294.0 – 292.1 K and (L) 292.0 – 289.4 K. 133

Figure 5-10: Temperature-dependent KWW parameters for the kinetics of ATPS formation in a solution of 90 mg/mL mAb and 20 mg/mL PEG. (A) The cooperativity exponent, β , is plotted as a function of temperature. The β values are colored to indicate the gel region from 290.4 to 292.8 K (blue data points), the spinodal region from 293.0 - 295.8 K (green data points), and the metastable region from 295.9 - 299.9 K (red data points). (B) The natural log of the rate constants, $\ln(k)$, are presented in an Arrhenius plot. The $\ln(k)$ data points are colored according to the regions defined in (A). The two solid black lines are linear fits to the data on either side of T_{meta} , which were used to determine the apparent activation energies, $E_{A,\text{app}}$, for ATPS formation in the metastable and spinodal regions. 135

Figure 5-11: Summary of (A) the KWW cooperativity exponents and (B) the rate constants as a function of temperature for three mAb concentrations in 20 mg/mL PEG. (C) An Arrhenius plot of $\ln(k)$ vs. $1000/T$ and (D) a VFT plot of $\ln(\tau)$ versus T were prepared from the KWW parameters. The data points in (A-D) are colored according to the mAb concentration of either 40 mg/mL (blue), 60 mg/mL (green), or 90 mg/mL (red). The solid lines in (D) represent fits to the VFT model 137

Figure 5-12: Arrhenius plots for the kinetics of ATPS formation in solutions containing 90 mg/mL (circle data points), 60 mg/mL (square data points), and 40 mg/mL (triangle data points) mAb in the presence of 20 mg/mL PEG. The natural log of the rate constants, $\ln(k)$, for each mAb concentration versus inverse temperature, $1000/T$, is divided into metastable (red data points), spinodal (green data points), and

gel (blue data points) regions. The solid red and blue curves are provided as guides to the eye.	138
Figure 5-13: Time constants for ATPS formation as a function of temperature near T_{gel} for a solution of 90 mg/mL mAb and 20 mg/mL PEG. The natural log values of the time constants, $\ln(\tau)$, in the gel region, where $\beta < 1$, are plotted as blue data points along with the fit to the VFT model, shown as a solid blue curve.....	140
Figure 5-14: Point-by-point activation energy determinations as a function of temperature.....	142
Figure 5-15: Phase separation and gelation temperatures versus PEG concentration at two pH values.....	143
Figure 5-16: Two-step mechanism for ATPS formation. (A) ATPS formation begins with droplet growth (Step 1 in A) involving the sequential, reversible association of protein monomers with protein-rich droplets, characterized by the association, k_1 , and dissociation, k_{-1} . The circles represent folded protein monomers, several of which have been colored in black to highlight the growth mechanism. The number of monomers in the droplets, n , are not drawn to scale. The final stage of ATPS formation is the irreversible coalescence of droplets (Step 2 in A), characterized by the coalescence rate constant, k_2 . (B) The reaction coordinate diagrams for ATPS formation at hot (red curve) and cold (blue curve) temperatures relate the apparent activation energies measured in Figure 5-10 to the two-step mechanism in (A). The activation energies for the elementary steps are not drawn to scale in (B).....	145
Figure 5-17: Analysis of the kinetics data, which was inspired by classical nucleation theory. (A) Binodal phase diagram, reproduced from Figure 5-5. The method for estimating the supersaturation is illustrated with the dashed and solid black lines in (A). The dashed vertical black line on the right hand side of the figure marks the initial protein concentration, C_0 . After a temperature quench to a final temperature, T_{final} . The equilibrium concentration of the protein-poor phase, C_{poor} , should be defined by the dashed vertical black line on the left hand side of (A). (B) The measured rate constants for ATPS formation plotted against the supersaturation. The solid black line in (B) is a linear fit to the data measured in the metastable region, consistent with growth kinetics as opposed to the exponential dependence expected for nucleation.	154
Figure 5-18: Schematic illustration of the effects of non-ionic crowders and salt ions on the association and dissociation of protein monomers to phase separated protein-rich droplets.....	156
Figure A-1: Solute-correlated spectrum for PEG-1. The spectrum is normalized to the area under the CH stretches from 2600 to 3050 cm^{-1}	188
Figure A-2: Solute-correlated spectrum for PEG-2. The spectrum is normalized to the area under the CH stretches from 2600 to 3050 cm^{-1}	189

Figure A-3: Solute-correlated spectrum for PEG-3. The spectrum is normalized to the area under the CH stretches from 2600 to 3050 cm^{-1}	190
Figure A-4: Solute-correlated spectrum for PEG-4. The spectrum is normalized to the area under the CH stretches from 2600 to 3050 cm^{-1}	191
Figure A-5: Solute-correlated spectrum for PEG-5. The spectrum is normalized to the area under the CH stretches from 2600 to 3050 cm^{-1}	192
Figure A-6: Solute-correlated spectrum for PEG-6. The spectrum is normalized to the area under the CH stretches from 2600 to 3050 cm^{-1}	193
Figure A-7: Solute-correlated spectrum for PEG-8. The spectrum is normalized to the area under the CH stretches from 2600 to 3050 cm^{-1}	194
Figure A-8: Solute-correlated spectrum for PEG-35. The spectrum is normalized to the area under the CH stretches from 2600 to 3050 cm^{-1}	195
Figure A-9: Solute-correlated spectrum for PEG-75. The spectrum is normalized to the area under the CH stretches from 2600 to 3050 cm^{-1}	196
Figure A-10: Solute-correlated spectrum for PEG-227. The spectrum is normalized to the area under the CH stretches from 2600 to 3050 cm^{-1}	197
Figure A-11: Solute-correlated spectrum for PEG-2k. The spectrum is normalized to the area under the CH stretches from 2600 to 3050 cm^{-1}	198
Figure A-12: Solute-correlated spectrum for PEG-20k. The spectrum is normalized to the area under the CH stretches from 2600 to 3050 cm^{-1}	199
Figure A-13: Solute-correlated spectrum for PEO-1. The spectrum is normalized to the area under the CH stretches from 2600 to 3050 cm^{-1}	200
Figure A-14: Solute-correlated spectrum for PEO-2. The spectrum is normalized to the area under the CH stretches from 2600 to 3050 cm^{-1}	201
Figure A-15: Solute-correlated spectrum for PEO-3. The spectrum is normalized to the area under the CH stretches from 2600 to 3050 cm^{-1}	202
Figure A-16: Solute-correlated spectrum for PEO-4. The spectrum is normalized to the area under the CH stretches from 2600 to 3050 cm^{-1}	203
Figure A-17: OH stretch parameters obtained from the gaussian deconvolution plotted as a function of solute chain length. (A) Effect of chain length on the amplitude. (B) Effect of chain length on the ratio of the amplitudes.....	204
Figure A-18: OH stretch parameters obtained from the gaussian deconvolution plotted as a function of solute chain length. (A) Effect of chain length on the amplitude. (B) Overlay of the CH stretches of PEG- <i>n</i> solutes.....	204

Figure A-19: Overlay of the CH stretches of PEG- <i>n</i> solutes.....	205
--	-----

LIST OF TABLES

Table 2-1 : Best fit parameters of Equations 2-1 , 2-2 , and 2-3 for the effect of sodium salts on the LCST of PEO-20k.....	25
Table 2-2 : Best fit parameters of Equations 2-5 and 2-7 for the effect of sodium salts on the ^1H NMR chemical shift of PEO-20k.....	34
Table 2-3 : Best fit parameters of Equation 2-3 for the effect of iodide salts on the LCST of PEO-20k.....	36
Table 2-4 : Best fit parameters of Equation 2-5 for the effect of iodide salts on the ^1H NMR chemical shifts of PEO-20k.	37
Table 3-1 : Summary of distinct proton populations observed in the ^1H NMR spectra of polyethylene oxides and polyethylene glycols of various chain length.....	57
Table 3-2 : Equilibrium dissociation constants, K_D , for the adsorption of NaSCN to polyether solutes. The data are organized by chain length and proximity to the termini.	67
Table A-1 : Center frequencies, ν_c , of the Gaussian peaks obtained from fits to the solute-correlated spectra of polyether solutes. The data are arranged as a function of chain length and peak number.	206
Table A-2 : Width parameters, w , for the Gaussian peaks obtained from fits to the solute-correlated spectra of polyether solutes. The data are arranged as a function of chain length and peak number.	206
Table A-3 : Center frequencies for various Gaussian peaks obtained from fits to the solute-correlated spectra of PEO- n solutes. The data are arranged as a function of chain length and peak number.....	206
Table B-1 : Summary of fitted parameters for the effects of mAb concentration on the phase transition temperatures using Equation 5-12	208
Table B-2 : Fitted parameters of the KWW model for the 90, 60, and 40 mg/mL mAb solutions with 20 mg/mL PEG-3350.....	208
Table B-3 : The fitted parameters of the VFT model for various mAb concentrations.....	209

ACKNOWLEDGEMENTS

My journey through graduate school has been supported and enriched by a number of people in my personal and scientific life. Firstly, I want to thank my family. I wouldn't be where I am today without your unconditional support. You have always encouraged me to stay the course and to be optimistic in your own ways. On a day-to-day basis, I have had the blessing of working with intelligent, talented, good-natured and adventurous coworkers. You have been more than coworkers to me and your friendship has been essential to maintaining a healthy work-life balance. I'm also thankful for my advisor, who has provided me with unwavering encouragement and opportunities to develop scientific independence. Your attention to detail and intuitive perspective of science has been inspirational. I am also grateful for the countless mentors that have guided my career. My undergraduate advisor, current lab manager and fellow graduate students have bolstered a thought-provoking and positive scientific environment. Lastly, I want to thank my collaborators for all of their help, insights, and motivation. Your contributions have reinforced and expanded my work beyond what I considered possible. Collectively, you all have been an invaluable source of foundation and motivation. I hope to pay it forward one day.

This material is based upon work supported by the National Science Foundation under Award No. 17097356, as well as AstraZeneca and Sanofi. Any opinions, findings, and conclusions or recommendations expressed in this publication are those of the author(s) and do not necessarily reflect the views of the National Science Foundation, AstraZeneca, and Sanofi.

Chapter 1

The Role of Non-Covalent Interactions in Protein Stability and Ion-Specific Effects in Aqueous Solutions

Aqueous solutions are liquid mixtures of solute molecules homogeneously dissolved in a water solvent. Water is an abundant chemical on earth and can solvate an array of polar, hydrogen bonding, and ionic solutes. Neutral solutes, like inert gases or hydrocarbons, however, do not mix well with water. The solubility of solutes in water is directly linked to the balance of water-water, solute-solute, and solute-water interactions. Protein solutes are polymer chains with remarkable chemical heterogeneity, including a polar amide backbone as well as ionic and hydrophobic side chains. When dissolved in water, proteins can sample various conformations ranging from an extended, denatured state to a compact, native structure. Proteins can also associate with other proteins to assemble into quaternary structures, phase separated droplets, or irreversible aggregates.

The intrinsic behavior of solutes and polymers in neat water is complex, but to understand their behavior in more complex solutions is a remarkable challenge with practical significance. Indeed, biological cells and protein-based drug formulations are aqueous solutions that contain high concentrations of proteins and additional solutes known as cosolutes, like inorganic salt ions. Salt concentration and identity are known to influence protein conformation and protein-protein interactions, yet many details of the molecular-level interactions underlying these effects remain elusive.^{1,2} A simple ground rule that has emerged from the past two decades of research is that ion-specific effects are driven by direct interactions of ions with the surfaces of interest, rather than effects on the bulk structure of water.³⁻⁸

This chapter presents an overview of the non-covalent interactions involved in protein stability and ion-specific effects. Particular emphasis is placed on the denaturation of protein model systems by weakly hydrated anions and the phase separation of concentrated therapeutic antibody formulations. The chapter is concluded by a summary of projects designed to advance fundamental insight into ion-specific chemistry and to develop assays for quantifying the colloidal protein-protein interactions.

Conformational and Colloidal Behavior of Proteins in Aqueous Solutions

Proteins are biological polymers of amino acid subunits, as depicted schematically in Figure **1-1A**. These macromolecules are comprised of a neutral amide backbone and side chains that can be hydrophobic, polar, or ionic. Most proteins fold from an extended, denatured structure into a compact, native conformation that buries hydrophobic side chains from the water solvent, as illustrated in Figure **1-1B**.⁹ Salt bridges and hydrogen bonding interactions also contribute to the stability of the folded state; however, the self-assembly of the hydrophobic core is considered to be a major driving force for protein folding.¹⁰ Conformational stability is important for the function of many biological proteins. In fact, the misfolding or denaturation of proteins due to thermal stress or chemical denaturants can lead to a loss of function because the active site of the protein can no longer recognize the ligand substrate.¹¹

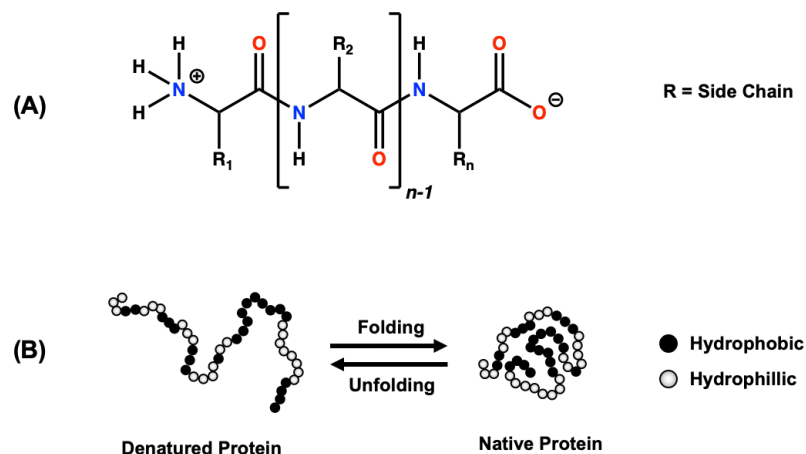


Figure 1-1: (A) Bond-line structure of a protein, where the side chains are indicated by R. (B) Schematic illustration of a protein chain in an extended denatured state and a compact native structure. The hydrophobic and hydrophilic side chains are indicated by filled and open circles, respectively. As illustrated, the hydrophobic side chains self-assemble to form the core of the native state.

Once a native protein unfolds and exposes its hydrophobic patches to the aqueous environment it can irreversibly aggregate with other denatured proteins, as portrayed in **Figure 1-2**. Aggregation has been implicated in various neurodegenerative diseases and reduction of protein-based therapeutics shelf-life.^{12,13} In addition to conformational stability and irreversible aggregation, proteins also associate through colloidal interactions while remaining in their folded states, as depicted in **Figure 1-2**.^{14,15} Unlike the hydrophobic forces that drive protein folding and aggregation, colloidal association is typically dominated by electrostatic interactions. Indeed, the surfaces of proteins are typically decorated with ionic moieties, which impart high solubility in an aqueous environment. The sign and structure of these electrostatic patches can lead to attractive or repulsive interactions. Under certain conditions, colloidal association can lead to the formation of protein-rich droplets by liquid-liquid phase separation (LLPS).^{16,17}

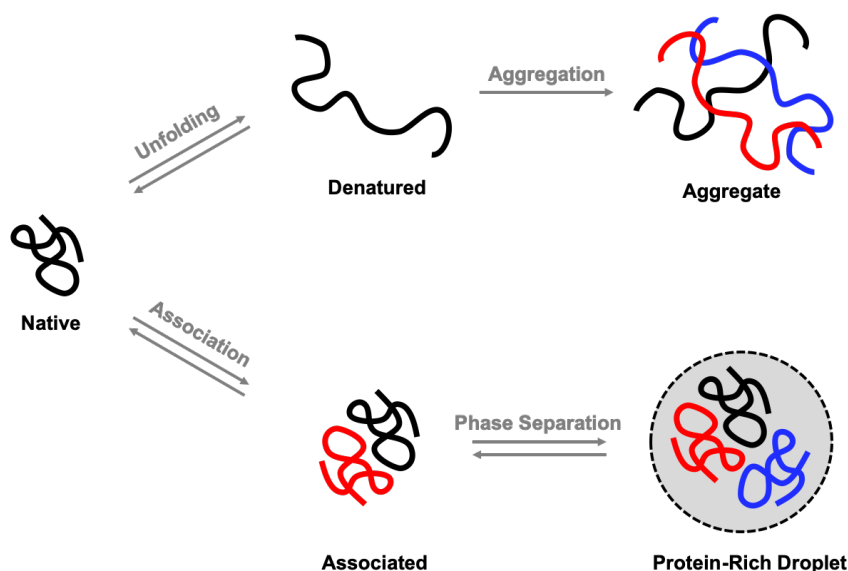
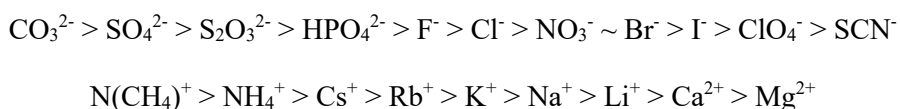


Figure 1-2: Schematic illustration of irreversible aggregation due to conformational instability versus phase separation due to colloidal association. The protein macromolecules are drawn as curved lines. Distinct protein chains are colored for clarity of the protein-protein interactions.

Over the past decade, protein-protein interactions have become a hot topic in molecular biology because of their relevance to the assembly of proteins and ribonucleotides into membranellar compartments insides of living cells.^{18–20} Biological cells use LLPS to concentrate or exclude molecules in localized regions of the cellular milieue.^{21–23} Unfortunately, these protein-rich droplets can accelerate protein aggregation leading to cataracts, neurodegenerative diseases, and sickle-cell anemia.^{14,24–30} Aggregation and phase separation also compromise the stability of therapeutic monoclonal antibody, mAb, formulations that have been engineered to fight cancer, autoimmune and neurodegenerative diseases.^{31–34} The phase space for exploring and modulating the behavior of proteins is extremely large and remains poorly understood due to the complexities of both protein and solution chemistries.^{31,32,34–42}

Ion-Specific Effects on Proteins and Macromolecules

The situation is particularly complex as pH, salts, surfactants, and crowders can influence hydrophobic and electrostatic interactions.^{16,36,43–46} Substantial research efforts have focused on the effects inorganic salt ions on protein behavior.^{1,2,5,47–55} The earliest studies of ion-specific effects on protein solubility were conducted in 1888 by a Czech scientist, Franz Hofmeister.^{56,57} Over the past two decades, however, interest in ion-specific chemistry has undergone a renaissance.^{58,59} Using both experimental and theoretical methods, new and significant molecular level insights have been gleaned on the mechanisms involved in the empirical rank ordering of cations and anions for affecting the physical properties of solutions involving oil, water, and salt.^{8,60} This includes understanding protein activity, protein stability, the formation of micelles, as well as changes in the surface tension at the air/water interface in the presence of specific salt ions.^{1,61–68} The majority of these studies have involved relatively simple ions such as those found in the Hofmeister's original anionic and cationic series:



For these two series, ions on the left help to salt macromolecules out of solution, while the ions on the right help to salt them in. Factors such as ion size, charge, and geometry have been implicated in the ability of a salt to modulate the behavior of macromolecules.^{51,69} Collectively, the literature supports the notion that ion-specific effects are driven by direct interactions of the ions with the macromolecular surface.^{3,4,6,51,70–74} Investigating ion-specific effects on biological proteins is complicated by the heterogeneity of protein surfaces which display a range of charged and neutral patches to the aqueous environment. Indeed, ions can exhibit diverse interactions with

protein surfaces as depicted in Figure 1-3, which includes ion-pairing interactions with charged side chains and ion adsorption to the polar and non-polar portions of the protein backbone.^{44,75,76}

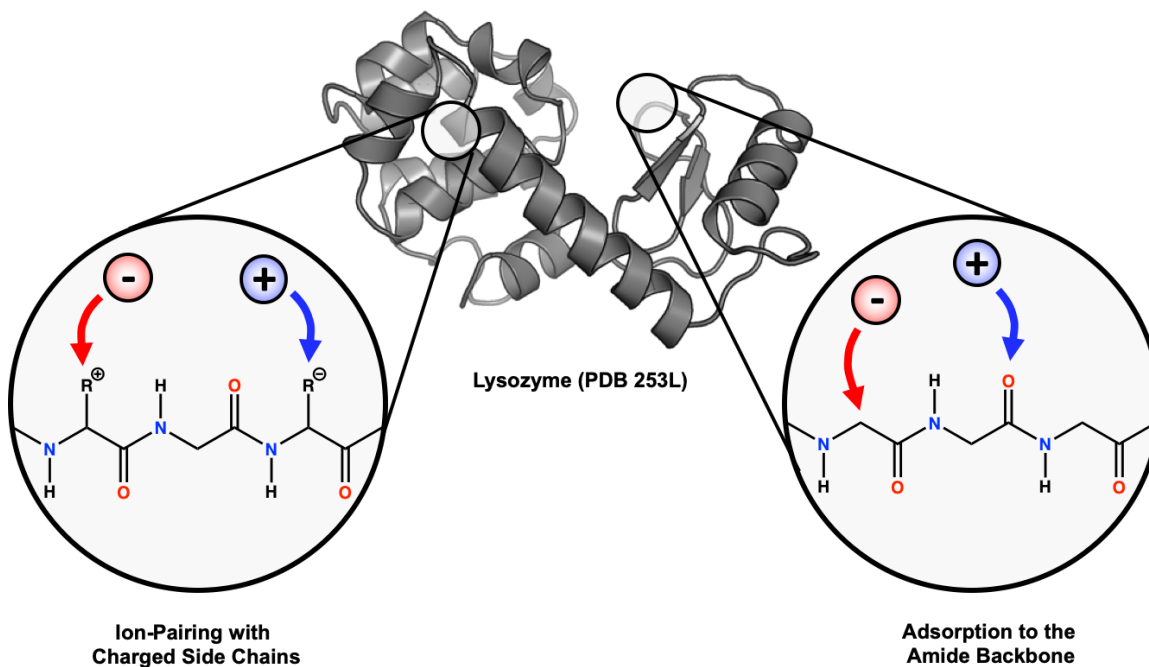


Figure 1-3: Schematic illustration of ion-protein interactions. Cartoon model of the structure of lysozyme determined by x-ray crystallography. The insets portray anions and cations of inorganic salts interacting with proteins through ion-pairing with charged side chains or by adsorbing to the amide backbone.

Light Scattering Measurements of Phase Separation in Polymer and Protein Solutions

Solutes that undergo temperature-induced phase transitions have been vital for exploring the driving forces for distinct hydrophobic versus electrostatic non-covalent interactions. In general, thermoresponsive solutes can exist in a homogeneous state, where solute-solvent interactions are maximized, or a separated state where solute-solute or solvent-solvent interactions are maximized. This behavior can be described by phase diagrams, like the schematic

provided in Figure 1-4. At high temperatures, nonpolar solutes can undergo phase separation, which should be driven by the release of water molecules from hydrophobic hydration shells into the bulk solution. The minimum temperature of the phase separated region is defined by a lower critical solution temperature, LCST. On the other hand, attractive solute-solute interactions, like ion-pairing, should lead to association at cold temperatures. The upper limit for this attractive phase separation is defined by the upper critical solution temperature, UCST. Above the UCST, the thermal energy is sufficient to break up the electrostatic interactions between solutes.

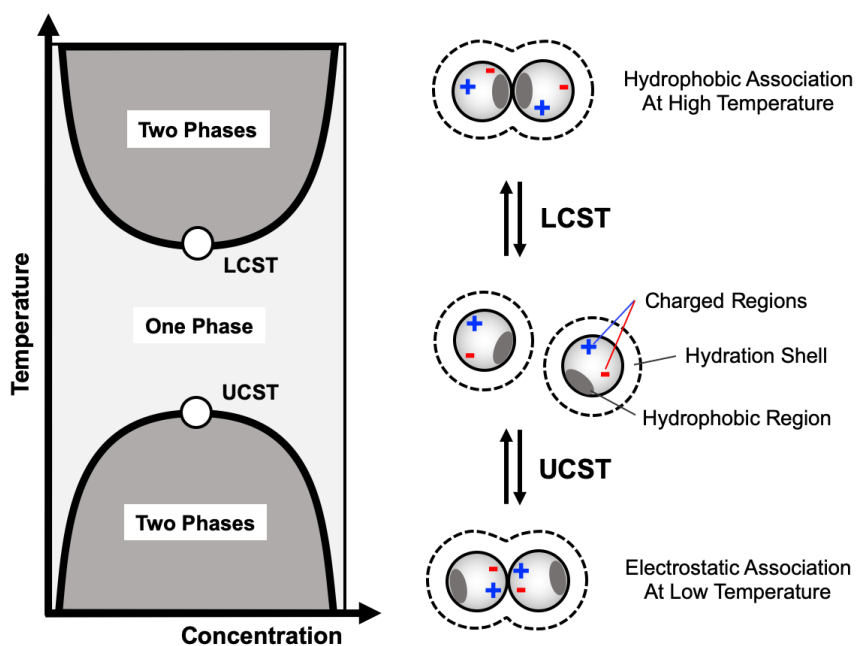


Figure 1-4: Schematic phase diagram for the separation of solutes at low and high temperatures. The dark shaded regions of the diagram indicate conditions where the solution separates into two phases. The open white circles mark the LCST and UCST. Cartoons of the interactions that drive separation are provided on the right-hand side.

Thermoresponsive model systems that mimic the structure of proteins have played an important role in dissecting the ion-protein and protein-protein interactions. For example, thermoresponsive polymers that undergo hydrophobic collapse at high temperatures provide a

chemically simple system for the hydrophobic forces involved in protein folding.⁷⁷ The structures of several non-ionic thermoresponsive polymers are summarized in Figure 1-5A. Solutions of these polymers appeared transparent at cold temperatures, where the chains are soluble and extended. When the temperature is increased above the LCST, however, the solutions became cloudy due to the collapse and aggregation of the polymers. Images and schematics of a thermoresponsive polymer solution below and above the LCST are summarized in Figure 1-5B.

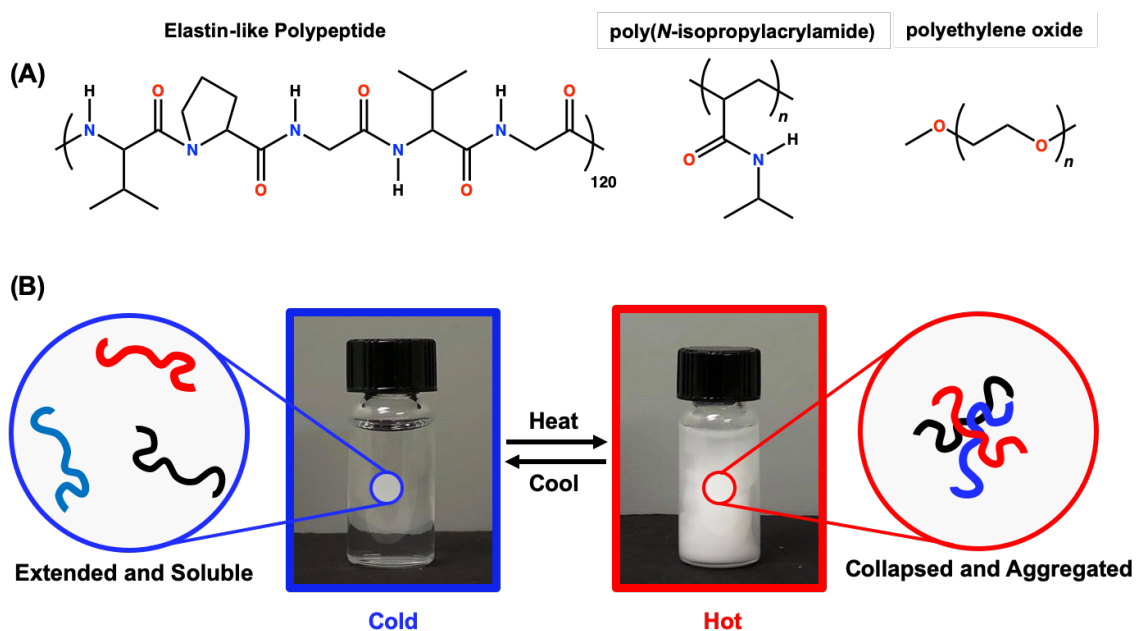


Figure 1-5: Hydrophobic collapse of thermoresponsive polymers. (A) The structure of several non-ionic polymers that undergo hydrophobic collapse at high temperature. (B) Images of the light scattering from a poly *N*-isopropylacrylamide solution above and below the phase separation temperature. Cartoon insets are provided to illustrate the extended and soluble at cold temperatures versus the collapsed and aggregated structures that form upon heating.

Some biological proteins display phase transitions that can easily be monitored by turbidity. For example, lysozyme is particularly well-known for its UCST behavior and has been used as a model system to study protein-protein and ion-protein interactions.^{43,44,78} Unlike hydrophobic polymers, protein surfaces are typically decorated with charged moieties. Figure 1-

6A provides electrostatic maps for the surface of several proteins that are known to undergo phase separation at cold temperatures. The blue and red regions represent positively and negatively charged sites. As can be seen, the surfaces show dramatic charge heterogeneity. Attractive interactions between patches of charge drive the formation of protein-rich droplets in concentrated protein solutions. These attractive protein-protein interactions in hemoglobin or γ -crystallin have been implicated in sickle-cell anemia and cataracts, respectively.^{25,26,79,80} High concentration formulations of antibody-based drugs are also susceptible to phase separation, which compromises their shelf-life during storage at refrigerated conditions.^{36,41,81,82} Images and schematics of a concentrated antibody solution below and above its UCST are provided in Figure 1-6B.

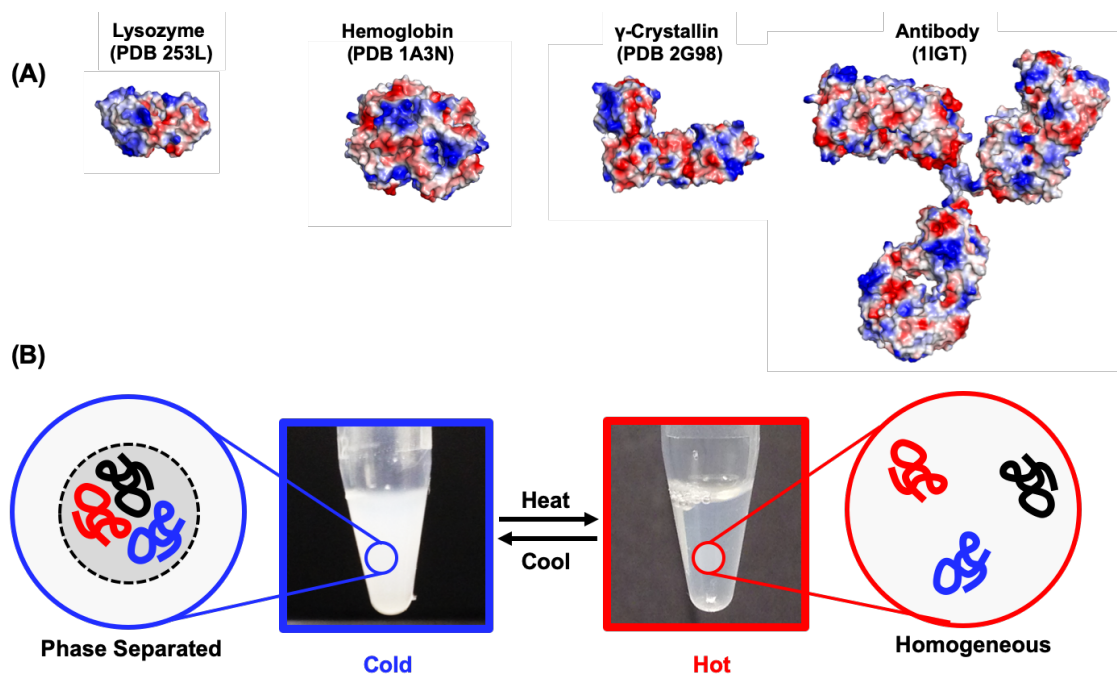


Figure 1-6: Phase separation of folded proteins. (A) X-ray crystal structures of four proteins that undergo phase separation at cold temperatures. The surface of the protein structures are colored to indicate the electrostatic charge, where red is negative and blue is positive. (B) Images of the light scattering from an antibody solution above and below the phase separation temperature. Schematics are provided to illustrate the homogeneous distribution of proteins at high temperature versus the formation of phase separated droplets at cold temperatures.

Phase transition temperatures provide a convenient metric to explore the non-covalent interactions of macromolecules in aqueous solutions in the presence of different salts. Systematic phase transition temperatures measurements have been enabled by high-throughput, small-volume analytical platforms, like temperature gradient microfluidics. This analytical platform was critical to early research into LCST and UCST measurements as a function of Hofmeister anion identity.^{44,51,70,83–92} A schematic illustration of a sample exhibiting UCST behavior on the temperature gradient microfluidics technology is provided in Figure 1-7A. The temperature gradient is formed across a sample by placing it in contact with a heat source on one side and a heat sink on the other. The light scattering emanating from the sample is then imaged by dark-field microscopy, as shown in Figure 1-7B.⁹³ The critical advantage of performing measurements on the temperature gradient is the ability to monitor protein phase behavior over a range of temperatures, simultaneously. Furthermore, LCSTs can be measured under a variety of solution conditions by imaging the light scattering in a set of parallel rectangular capillary tubes or microfluidic channels.^{83,84}

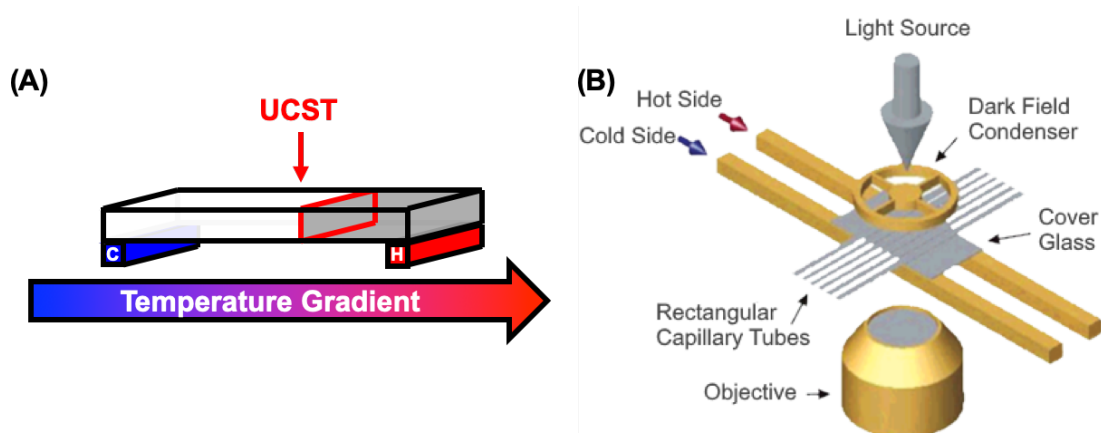


Figure 1-7: Schematic illustrations of the temperature gradient microfluidics technology. (A) Cartoon of a capillary containing a protein solution exhibiting UCST behavior on the temperature gradient, where the solution is cloudy on the cold side of the gradient. (B) Schematic of several capillary tubes on the temperature gradient device, which are imaged using a dark-field microscope.

Another key advantage to performing experiments on a temperature gradient is the ability to extract kinetic information by collecting images over time. The platform is particularly well-suited for measuring the conversion of cloudy droplet suspensions into an aqueous two-phase system (ATPS), as shown in Figure 1-8A.^{86,89,94} This device allows for temperature-dependent kinetics measurements that can be analyzed with the Arrhenius law. The apparent activation energies for ATPS formation obtained by this strategy can be measured in a high-throughput fashion because the kinetics measurements are collected across a range of temperatures, in just one experiment. The ability to measure apparent activation energies provides a unique tool to probe the landscape of the reaction coordinate diagram for ATPS formation as depicted schematically in Figure 1-8B and 1-8C.

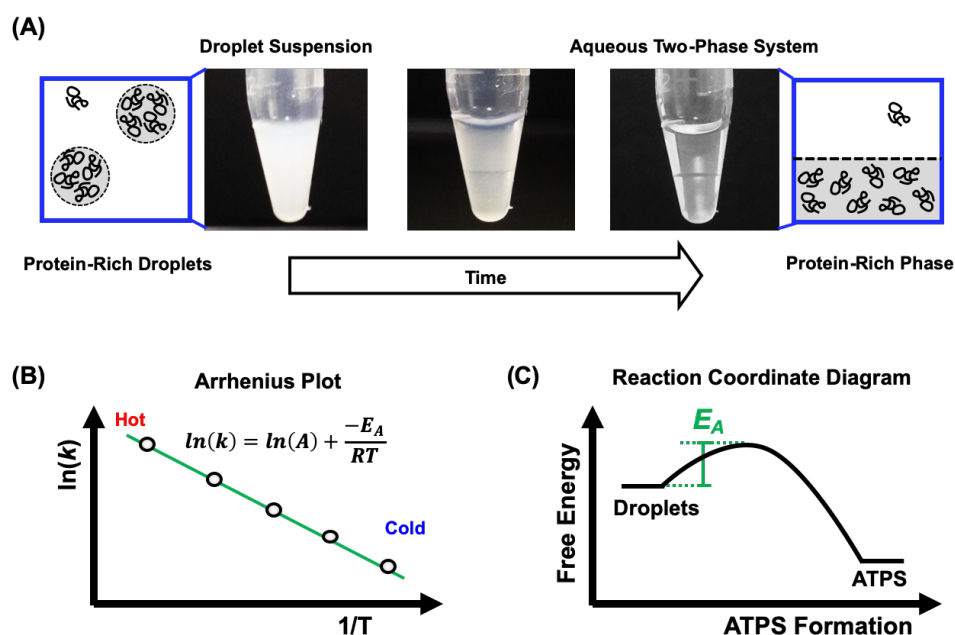


Figure 1-8: Kinetics of aqueous two-phase system (ATPS) formation. (A) Images of ATPS formation over time in a centrifuge tube. Schematics are provided to illustrate the structure of the initial protein-rich droplets and equilibrated ATPS. (B) Schematic illustration of the Arrhenius analysis of the temperature kinetics of ATPS formation. The apparent activation energy, $E_{A,app}$, extracted from the slope of the Arrhenius plot in (B) relates to the barrier for converting a droplet suspension into an ATPS formation, as illustrated schematic reaction coordinate diagram in (C).

Spectroscopic Tools for Ion-Protein Interactions and Water Structure

Phase transition temperatures and apparent activation energies are convenient metrics for systematically screening solution conditions; however, these light scattering measurements do not provide molecular-level information on the underlying non-covalent interactions. Where and how strongly do ions interact with the surface of protein macromolecule? How does water interact with the macromolecule surface? Answers to these questions can be explored with spectroscopic experiments that are sensitive to the local chemical environment, like nuclear magnetic resonance (NMR) and vibrational spectroscopies, which are depicted schematically in Figure 1-9.

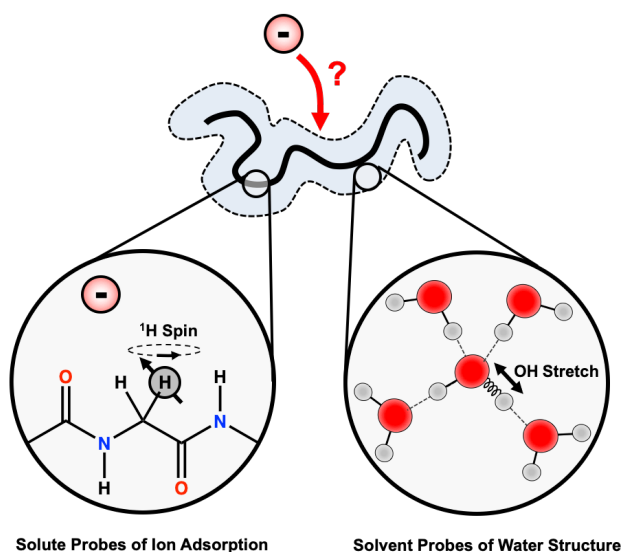


Figure 1-9: Schematics of ion-solute interactions and the hydration shell. The insets depict ^1H spin of nuclei along the polymer backbone and the OH stretch of water vibrational spectroscopies to study local chemical environments, like ion adsorption and hydrogen bonding architectures.

Considerable insights have been gained on the interaction of anions with model thermoresponsive polymers by combining LCST measurements and ^1H NMR spectroscopy. For example, weakly hydrated anions on the right-hand side of the Hofmeister series increase the LCST of elastin-like polypeptides.⁹⁰ It was proposed that these weakly hydrated anions inhibit hydrophobic collapse by adsorbing to the polymer surface.^{74,95} Several years later, NMR spectroscopy was performed on an elastin-like polypeptide to determine if and where anions bind.^{71,72} ^1H NMR spectroscopy employs radio waves to probe the nuclear spin of specific protons along the polymer chain, as illustrated in Figure 1-9, which reports on the electronic structure of the polymer and its local chemical environment. As weakly hydrated anions were titrated into the solution, the frequency of the peaks in the ^1H NMR spectrum changed.^{71,72} These salt-induced effects were modeled to determine the binding affinity to specific aliphatic moieties along the peptide backbone.^{71,72} In contrast, strongly hydrated anions on the left-hand side of the Hofmeister series did not exhibit signatures of direct interaction.^{71,72}

What drives the interaction between weakly hydrated anions and hydrophobic solutes? This interaction is expected to be weak in the gas phase, but both the anion and solute are surrounded by water molecules in solution. As such, the role of the hydration shell has been of significant interest in the fields of ion-specific effects and hydrophobic assembly.^{74,95-100} Vibrational spectroscopy is a valuable tool for probing the hydrogen bonding structure of water.^{101,102} For example, infrared spectroscopy uses infrared light to induce molecular vibrations. The vibrational energy of the OH stretch vibration of water is sensitive to the local hydrogen bonding environment, as illustrated in Figure 1-9. A major limitation to the use of vibrational spectroscopy has been its inability to distinguish the hydration shell from the bulk liquid. Indeed, both Raman and infrared spectroscopies measure the total response of water in an aqueous solution. In recent years, however, techniques have been developed to probe this thin layer of water at the surface of solutes. In particular, sum-frequency generation (SFG) spectroscopy and

multivariate curve resolution (MCR) algorithms have revolutionized the experimental techniques for exploring the structure of water in neat liquids versus salt solutions.^{103–112} The results from these experiments complement studies using natural probes on the polymer surface, like ^1H NMR.

Collectively, the thermodynamic and spectroscopic experiments support a mechanism for ion-specific effects called the solute-partitioning model, depicted schematically in Figure 1-10.^{6,49} Weakly hydrated anions partition to the macromolecule surface and drive denaturation. The adsorption to hydrophobic patches of the polymer surface lowers the energetic cost of exposing these patches to an aqueous environment. On the other hand, strongly hydrated anions are repelled from the surface and enhance the hydrophobic collapse. Indeed, folding or aggregation should reduce the exposure of the polymer surface to the repulsive interactions in solution.^{113,114}

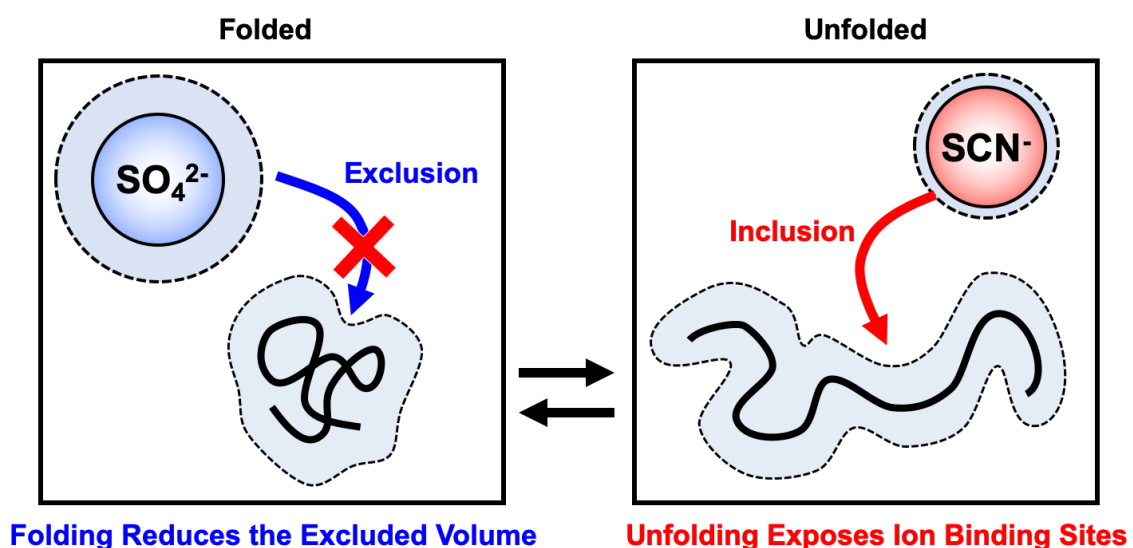


Figure 1-10: Schematic illustration of the solute partitioning model. The left-hand side of the schematic illustrates a folded protein, while the right-hand side depicts the protein in a denatured state. Strongly hydrated anions, like SO_4^{2-} , are repelled from the protein surface. As such, they are excluded from the region surrounding the macromolecule. This excluded volume is smaller for the folded state, rather than the extended. In contrast, weakly hydrated anions, like SCN^- , are attracted to the protein surface and are enriched or included in the polymer's hydration shell. These attractive ion-protein interactions shift the folding equilibrium toward the denatured state because this maximizes the binding site exposure to the solution.

Project Overview and Key Findings

Herein, two projects are presented that focus on distinct aspects of non-covalent interactions in aqueous solution. The first project expands the current mechanisms of ion-specific effects by taking a closer look at the interaction of weakly hydrated anions with hydrophobic solutes. In particular, this project assesses the quality of model systems for the study of ion-specific effects on protein denaturation. The affinity of weakly hydrated anions to model solutes and polymers of varying chain length is measured by LCSTs and ^1H NMR spectroscopies. It is discovered that the interaction strength is correlated with the surface curvature of the aliphatic binding site.¹¹⁵ This finding is significant as it connects Hofmeister chemistry to curvature-dependent hydrophobicity theories. The key relationship is that the structure of water at hydrophobic interfaces can modulate the binding affinity of weakly hydrated anions over several orders of magnitude. Direct evidence for the role of water structure is explored by a combination of vibrational spectroscopy and MCR algorithms that yield spectra of a solute's hydration shell.

The second project applies temperature gradient microfluidics to measure the colloidal stability of therapeutic antibody solutions. Polyethylene glycol was added to drug formulations to induce phase separation.⁹⁴ Analogous to the strongly hydrated SO_4^{2-} anion, polyethylene glycol is repelled from the protein surface and induces association by an excluded volume mechanism.^{46,116,117} It is demonstrated how high-throughput UCST measurements could be implemented for screening the colloidal stability of biopharmaceutical drug products. Moreover, the temperature gradient platform reveals that kinetics of ATPS formation in concentrated

antibody solutions is non-Arrhenius. A stepwise model for the reaction coordinate diagram is developed to interpret the kinetics data. Significantly, this model provides an apparent activation energy for the dissociation of protein monomers from the surface of protein-rich droplets and a metric for the structural fragility of a solid-like gel that forms at the coldest temperatures on the gradient.⁹⁴

Chapter 2

Ion-Specific Effects on the Hydrophobic Collapse of Thermoresponsive Polymers

The Hofmeister series was discovered almost 130 years ago.^{56,57} This series reoccurs for a variety of phenomena that occur in water. Over the years, numerous investigators have sought to come up with a unified, simple explanation for this effect. A particular area of interest has been the effect of ions on protein folding. Polymers that mimic protein folding have been vital to gaining molecular-level mechanisms of Hofmeister chemistry because they exhibit more controlled and simple chemistries than biological proteins. Moreover, the combination of spectroscopy and thermodynamic measurements have revealed fundamental insights. In this chapter, the use of polyethylene oxide (PEO) as a model system is demonstrated. The effects and interaction of ions with PEO are investigated using a combination of phase transition temperature measurements and proton nuclear magnetic resonance spectroscopy. Particular emphasis is placed on the interactions of weakly hydrated anions with PEO, which are known to act as strong chemical denaturants for proteins and model polymer systems.

Hydrophobic Collapse of Thermoresponsive Polymers

Proteins are polymers of amino acids Figure 2-1A. The specific sequence of side chains governs the self assembly of proteins into a compact native structure. A major driving force for protein folding is the clustering of aliphatic and aromatic side chains into the hydrophobic core of the protein.¹⁰ The hydrophobic effect can be studied with more control using non-ionic thermoresponsive polymers, the structures of which are summarized in Figure 2-1B. At low

temperatures, these polymers are hydrated and in an extended conformation. At higher temperatures, however, these polymers partially shed their hydration shell and undergo hydrophobic collapse. A range of polymers exhibit this lower critical solution temperature (LCST) behavior. Elastin-like polypeptides have the most similar structure to biological proteins, consisting of a protein backbone with all aliphatic side chains.^{118–120} Polymers like poly(*N*-isopropylacrylamide) and poly(ethylene oxide) also exhibit thermoresponsive properties and have the advantage of chemical simplicity.^{77,121} In fact, previous findings show that the amide NH group is not decisive for interactions between weakly hydrated anions and amide groups on polymers in aqueous solutions.⁷² Rather, the common motif is an α proton on a CH moiety that is electropositive due to a neighboring electron-withdrawing group of an amide carbonyl.^{71,72}

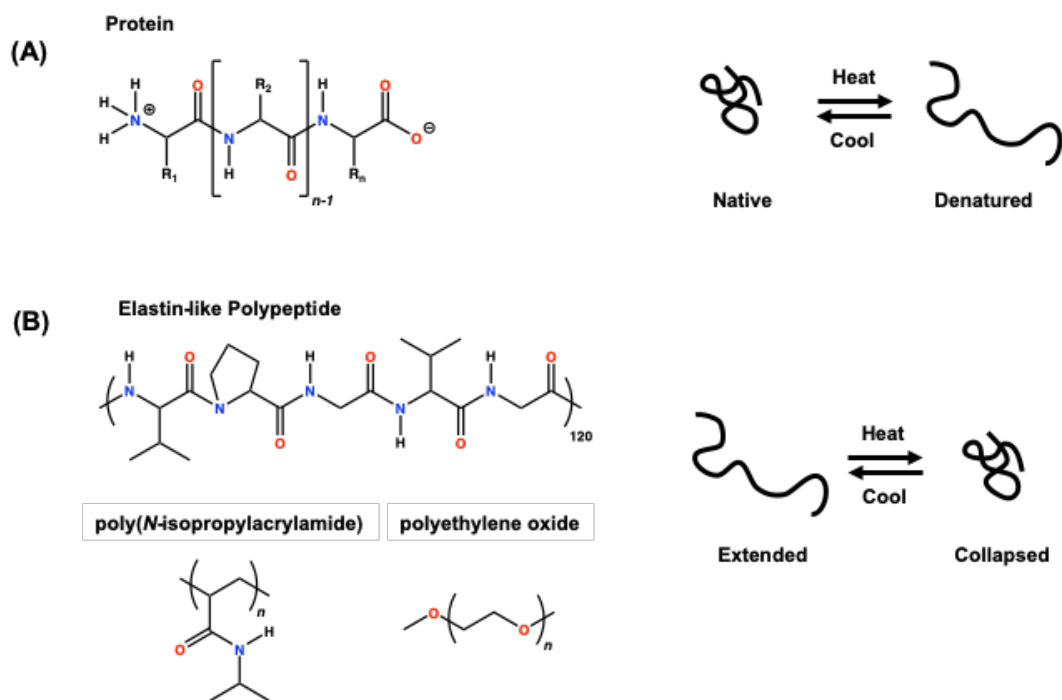


Figure 2-1: Structure and temperature-dependent conformations of proteins and thermoresponsive polymers (A) The bond-line structure of a protein and a schematic of the unfolding and folding of the chain. (B) Bond-line structures of several thermoresponsive polymers. The schematic on the right-hand side illustrates the hydrophobic collapse that occurs upon heating these polymer solutions.

Hydrophobic collapse can be easily monitored by measuring the light scattering from polymer solutions as a function of temperature. The solutions are clear at cold temperatures that are below the LCST, but at higher temperatures they become cloudy. Images of a solution of polyethylene oxide below and above its LCST are provided in Figure **2-2A**. Polyethylene oxide $M_v \sim 900,000$ (PEO-20k, Aldrich) was prepared at 0.5 M monomer stock solutions in 18 M Ω deionized water (22 mg/mL). The 0.5 M stocks were then aliquoted into microcentrifuge tubes in 0.5 mL quantities and dried under vacuum at 45 °C for 12 hours to remove water. The solid pellets formed by this procedure were then resuspended with water or salt solutions for further experiments. The quantitative measurements of LCSTs were performed using a melting point apparatus (Optimelt, Stanford Instruments). Specifically, 10 μ L of sample were loaded into glass capillary tubes open at one end. The light scattering was then recorded as a function of temperatures, at a ramp rate of 1 °C/min. The LCST was determined from the onset of scattering intensity relative to the flat and low intensity baseline observed at colder temperatures, as marked by the intersection of the two red lines in Figure **2-2B**.

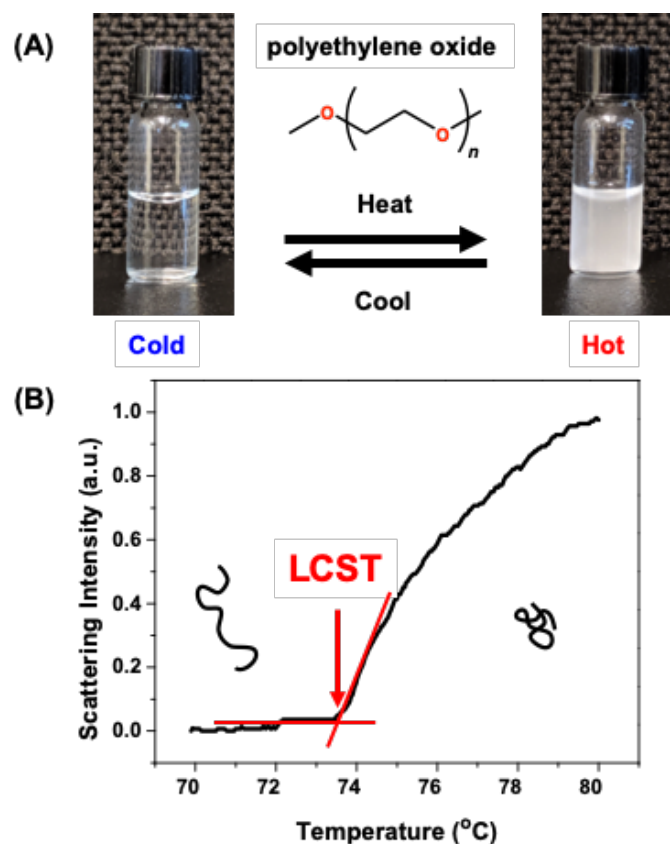


Figure 2-2: Light scattering measurements of hydrophobic collapse of PEO solutions. (A) Images of a PEO solution below and above the LCST. (B) Raw data from the melting point temperature apparatus for a solution containing 10 mg/mL PEO and 1 M NaCl. The LCST is determined from the onset of light scattering, which is marked by the red arrow and intersection of the two red lines.

Thermodynamic Investigations of Hofmeister Anion Interactions with PEO

The LCST provides a convenient metric for the influence of salt on the hydrophobic effect. All of the salts used in this study were at least 99% pure: sodium thiocyanate (NaSCN, 99.99%, Aldrich), sodium sulfate (Na_2SO_4 , $\geq 99\%$, Sigma-Aldrich), sodium chloride (NaCl, 99.999%, Aldrich), sodium iodide (NaI, 99.5%, Sigma-Aldrich), lithium iodide (LiI, 99.9%, Aldrich), and cesium iodide (CsI, 99.9%, Aldrich). All salts were used as received, with the exception of the hygroscopic NaSCN salt. The NaSCN salt was dried at 115 $^{\circ}\text{C}$ for 8 hours prior

to preparing solutions to remove adsorbed water. All of the stock salt solutions were prepared gravimetrically in volumetric flasks with 18 M Ω deionized water. To minimize oxidation of iodide, the iodide stock solutions were prepared with 18 M Ω deionized water that was purged with nitrogen gas for 1 hour. The NaSCN stock solution was prepared at 3.2 M. The Na₂SO₄ was prepared at 0.8 M due to its lower solubility at room temperature. The remaining salt stock solutions were prepared at 2.5 M.

The influence of NaCl on the LCST of PEO is summarized in Figure 2-3A. In pure water, the LCST of PEO is about 98 °C. As NaCl is added to the solution, the LCST decreases dramatically. In other words, the presence of salt enhances the hydrophobic collapse of PEO. This interpretation is depicted by the schematics in Figure 2-3A, where at a fixed temperature the addition of salt converts the polymer from an extended to a collapsed state. The advantage of using LCSTs for Hofmeister studies can be seen when this experiment is repeated for the strongly-hydrated SO₄²⁻ and the weakly-hydrated SCN⁻ anions. It should be noted that Na⁺ is used as the common cation. As can be seen, SO₄²⁻ decreases the LCST at a faster rate than NaCl, which indicates its pronounced enhancement of the hydrophobic effect. On the other hand, the addition of the NaSCN leads to an increase in the LCST. For the conditions where the LCST was above 90 °C, the temperature was ramped from 90 °C to 110 °C at a ramp rate of 2 °C/min. This quick ramp rate reduced the time before an LCST was induced, thus minimizing loss of water to evaporation while working near the boiling point of the solution.

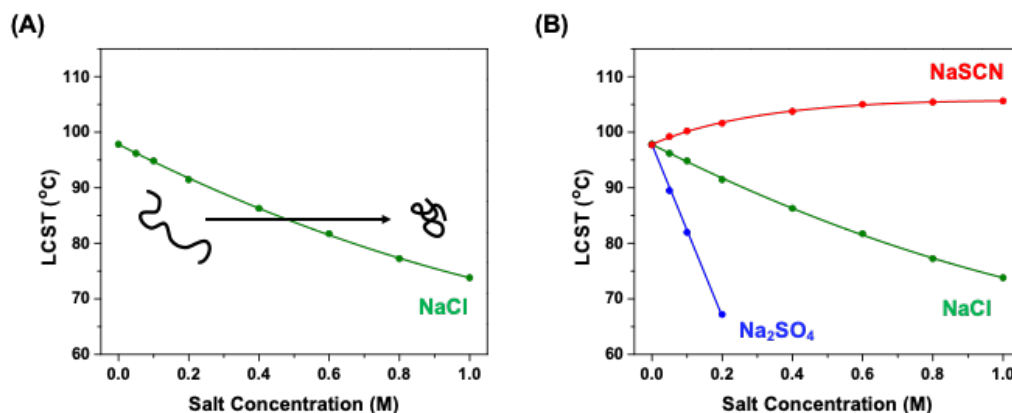


Figure 2-3: LCST phase diagrams for PEO as a function of various sodium salt concentrations. (A) The effects of NaCl on the LCST. A schematic is provided to illustrate the interpretation of the data. (B) Comparison of Na₂SO₄, NaCl, and NaSCN effects on the LCST of PEO. The circles are the LCST data points and the solid curves are best fits to the data using either Equations 2-1, 2-2, or 2-3 for Na₂SO₄, NaCl, and NaSCN, respectively.

The response of the LCST to salt concentration provides a metric for ability of salt to modulate the hydrophobic effect. Moreover, the shape of the phase diagrams reveals signatures of the ion-polymer interactions. The solid curves in Figure 2-3 are various functions that have been fit to the data. The Na₂SO₄ phase diagram was well modeled by a linear function described by Equation 2-1, where T_{LCST} is the LCST, T_0 is the LCST in pure water, a is the slope of the linear term, and c_{salt} is the concentration of salt.

$$T_{\text{LCST}} = T_0 + ac_{\text{salt}} \quad \text{Equation 2-1}$$

The large and negative value of a for Na₂SO₄ quantifies the strong “salting-out” effect on PEO. Similar to the Na₂SO₄ results, the dominant effect NaCl is also to decrease of the LCST; however, a third squared term was necessary to account for the nonlinearity of the data at higher salt concentration. The solid green curves in Figure 2-3 are fits to the data using Equation 2-2, where the coefficient b determines the magnitude of the empirical square term effect observed at

higher salt concentrations. The positive value of b for NaCl suggests that a second-order interaction may be present that gives rise to a “salting-in” effect.

$$T_{\text{LCST}} = T_0 + ac_{\text{salt}} + bc_{\text{salt}}^2 \quad \text{Equation 2-2}$$

The values of a have previously been shown to correlate with the hydration thermodynamics of anion.^{51,90} The strongly-hydrated anions lead to the most pronounced decrease in the LCST. As such, a common interpretation is that strongly-hydrated anions are excluded or repelled from the hydrophobic surfaces because they prefer to retain their hydration shell in bulk solution. As these salt ions are added into the solution, the polymer prefers to collapse and reduce its exposure to these repulsive interactions in the bulk aqueous solution. The collapse of the polymer also increases the translational entropy of the salt ions, because the collapse state occupies less volume than the extended. To a first approximation, the entropic and enthalpic contributions from the hydration shell should be insensitive to strongly-hydrated anions, since they remain hydrated in the bulk.

The NaSCN phase diagram, on the other hand, shows markedly different behavior. The LCST increases nonlinearly, approaching a maximum value at higher salt concentrations. This low-concentration nonlinearity is well modeled by a Langmuir isotherm contribution. The solid red curve in Figure 2-3B is the best fit to Equation 2-3, where K_D represents the apparent dissociation constant for NaSCN to the polymer and B_{max} quantifies the magnitude of the LCST increase due to the apparent binding interaction.

$$T_{\text{LCST}} = T_0 + ac_{\text{salt}} + B_{\text{max}} \frac{c_{\text{salt}}}{c_{\text{salt}} + K_D} \quad \text{Equation 2-3}$$

The phase diagram for PEO in the presence of NaSCN is replotted in Figure 2-4A for clarity. As can be seen, Equation 2-3 provides an excellent fit to the data. The physical meaning of the Langmuir isotherm contribution is depicted in Figure 2-4B. This contribution suggests that the SCN^- anions bind directly to the polymer. As a result, the polymer prefers to adopt an extended conformation, which present a greater portion of its surface area to the aqueous environment, thereby maximizing the number of binding interactions. At the highest salt concentration, the anions begin to saturate the surface of the polymer and the LCST approaches a maximum value. The salt concentration that produces half of this “salting-in” effect is quantified by the dissociation constant of $K_D = 0.6$ M.

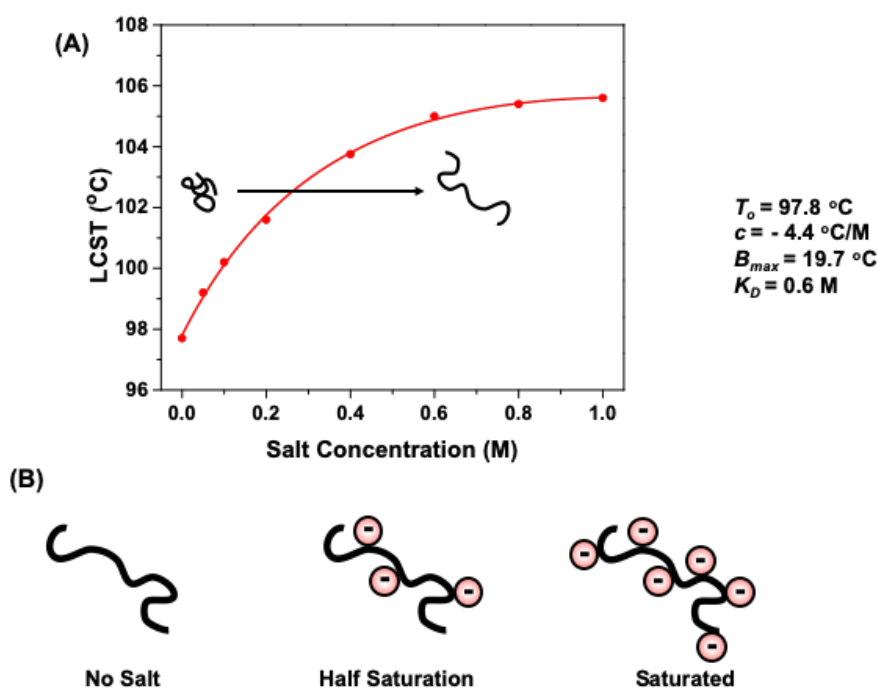


Figure 2-4: LCST phase diagram and proposed mechanism of anion-polymer interactions. (A) The data points are LCST values for PEO as a function of NaSCN concentration. The solid red curve is a fit to the data using Equation 2-3. (B) Cartoon illustration of the binding of anions to the polymer chain. The three cartoons are meant to represent increasing salt concentration from left to the right.

It is remarkable that these relatively simple equations can describe a salt's influence on the hydrophobic effect based on attractive or repulsive interactions with the polymer surface. The nature and strength of these interactions modulate the energetics of exposing hydrophobic portions of the polymer surface to the aqueous environment. The fitted parameters for the ^1H NMR titrations are summarized below in Table 2-1.

Table 2-1: Best fit parameters of Equations 2-1, 2-2, and 2-3 for the effect of sodium salts on the LCST of PEO-20k.

Salt	T_0 (ppm)	a (ppm M^{-1})	b (ppm M^{-2})	B_{max} (ppm)	K_D (M)
NaSCN	97.8	-4.3	-	19.6	0.61
NaCl	97.8	-31.9	7.9	-	-
Na_2SO_4	97.8	-153.8	-	-	-

Spectroscopic Investigations of Hofmeister Anion Interactions with PEO

Spectroscopic tools have provided strong support for the role of direct ion-macromolecule interactions in ion-specific effects. Proton nuclear magnetic resonance (^1H NMR) spectroscopy has been particularly useful because of its ability to measure a magnetic property of atoms called spin, as illustrated in Figure 2-5A.¹²² The spin of a nucleus generates a small magnetic field. When an external magnetic field is applied to a sample it places an energetic bias on the spin orientation. Spins that are aligned parallel to B_0 will be lower in energy than the antiparallel spin orientation, as shown in Figure 2-5B. Experimentally, large magnetic fields are applied to samples so that the energy difference is similar to the energy of radio waves, MHz. Figure 2-5C displays a cartoon version of this setup, where broadband pulses of radiofrequencies are sent into the sample to excite the spins into the antiparallel orientation.

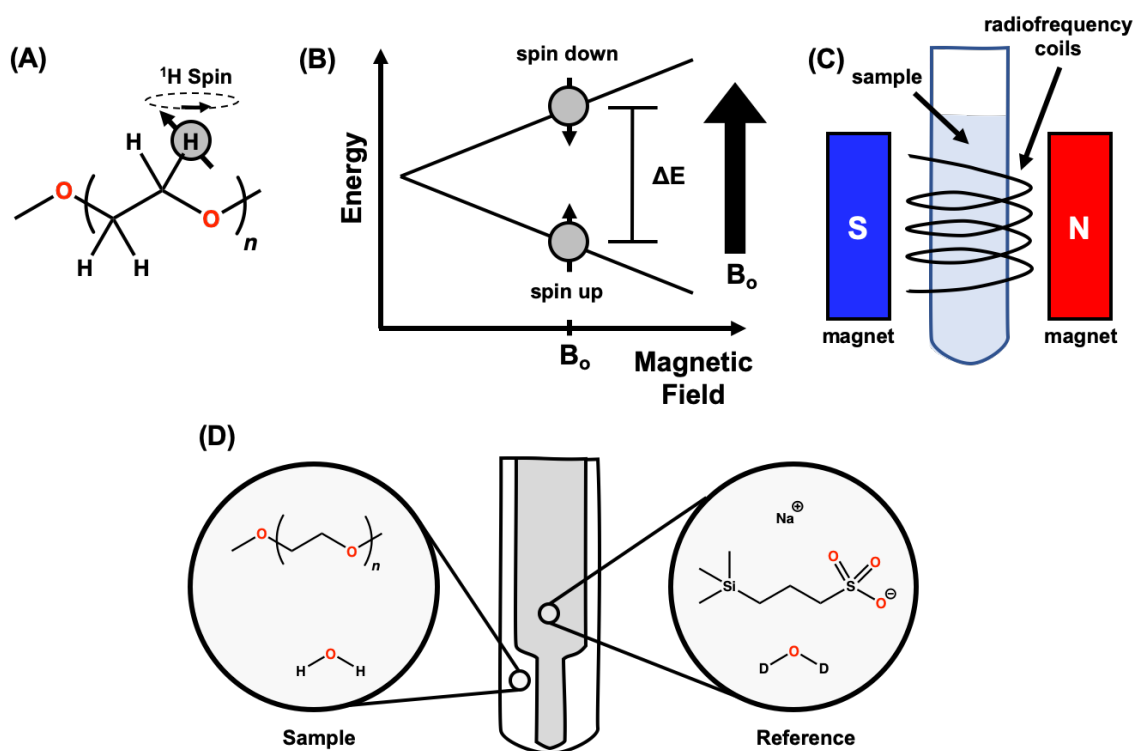


Figure 2-5: Schematic illustrations of nuclear magnetic resonance spectroscopy. (A) Cartoon of the spin property of nuclei covalent bound to the PEO chain. (B) The effect of magnetic fields on the energy of the spin up and spin down states. The diagram is drawn so that the external magnetic field, B_0 , is pointing in the up direction, as indicated by the thick black arrow. (C) A simplified cartoon illustration of the hardware used to perform a nuclear magnetic resonance experiment. (D) Sample geometry and composition used to acquire ^1H NMR spectra. Insets are provided to illustrate the general composition of the sample and reference solutions tested in this work.

The NMR experiments presented in this work focus on the energy required to flip the proton spin and use it to gather molecular-level insight into the chemical environment of the nuclei. As Figure 2-5B portrays, the energy difference between spin orientations depends on the strength of the external magnetic field. Significantly, the electrons orbiting a proton nucleus shield the nucleus from the full strength of the applied magnetic field. As such, a proton with a dense electron cloud will “experience” a weaker field at the core of the nucleus. The electron density is closely linked to the electron affinity of covalently bound atoms and its local chemical environment.

The external magnetic field strength can vary from spectrometer-to-spectrometer and from day-to-day use of the same spectrometer. As such, this energy difference is typically reported as a chemical shift, δ , which is referenced to the energy difference required to flip the spin of a proton on a reference molecule with very high electron density. The equation for the chemical shift is described by Equation 2-4, where ν_{sample} and $\nu_{\text{reference}}$ are the resonant radio frequencies for the protons on PEO versus those on the methyl groups of 4,4-dimethyl-4-silapentane-1-sulfonic acid (DSS).

$$\delta = \frac{\nu_{\text{sample}} - \nu_{\text{reference}}}{\nu_{\text{reference}}} \quad \text{Equation 2-4}$$

Herein, ^1H NMR experiments were performed with precision coaxial insert NMR tubes (Wilma LabGlass). The geometry of these tubes is illustrated in Figure 2-6A. The reference solution was loaded into a coaxial insert at volume of 150 μL . The external reference contained 2 mg/mL DSS and a locking agent of deuterium oxide (D_2O). The inserts were then positioned in the center of a 5 mm precision sample tube containing 400 μL the sample solution. The spectra were collected on a 500 MHz spectrometer (Bruker AVIII-HD-500) equipped with a Prodigy BBO cryoprobe. After introduction into the spectrometer, the samples were equilibrated to 298 K for 2 minutes, which is below the LCST of all of the tested PEO solutions. The ^1H spectra were acquired using an excitation sculpting pulse sequence to suppress the signal from the water protons.¹²³ TopSpin (Bruker) and Mnova (Santiago de Compostela, Spain) software packages were used for data processing. An example spectrum of PEO obtained using this method is provided in Figure 2-6. As can be seen, value of δ for the methylene proton of PEO is near 3.693 ppm, which indicates that the proton is deshielded relative to the methyl protons on DSS. This deshielding effect is expected because the methylene moiety is covalent bound to an ether

oxygen, which pulls electron density away from the protons. As such, it takes higher frequency radio waves to excite the spin. The spectrum of PEO-20k showed a methylene proton peak at $\delta = 3.6927 \pm 0.0008$ ppm, which was assigned to the methylene proton. The value of δ was determined from the average of the chemical shift on the shielded (δ_{upfield}) and deshielded ($\delta_{\text{downfield}}$) sides of the peak at the half-maximum intensity ($I_{\text{half max}}$), as demonstrated in Figure 2-6. We note that the resolution of the instrument was ~ 0.001 ppm (black data points in Figure 2-6). However, δ was determined using the data interpolated via zero point filling, as shown by the solid red curve in Figure 2-6. Additional trials with a similar analysis yielded standard deviations of 0.0002 ppm.

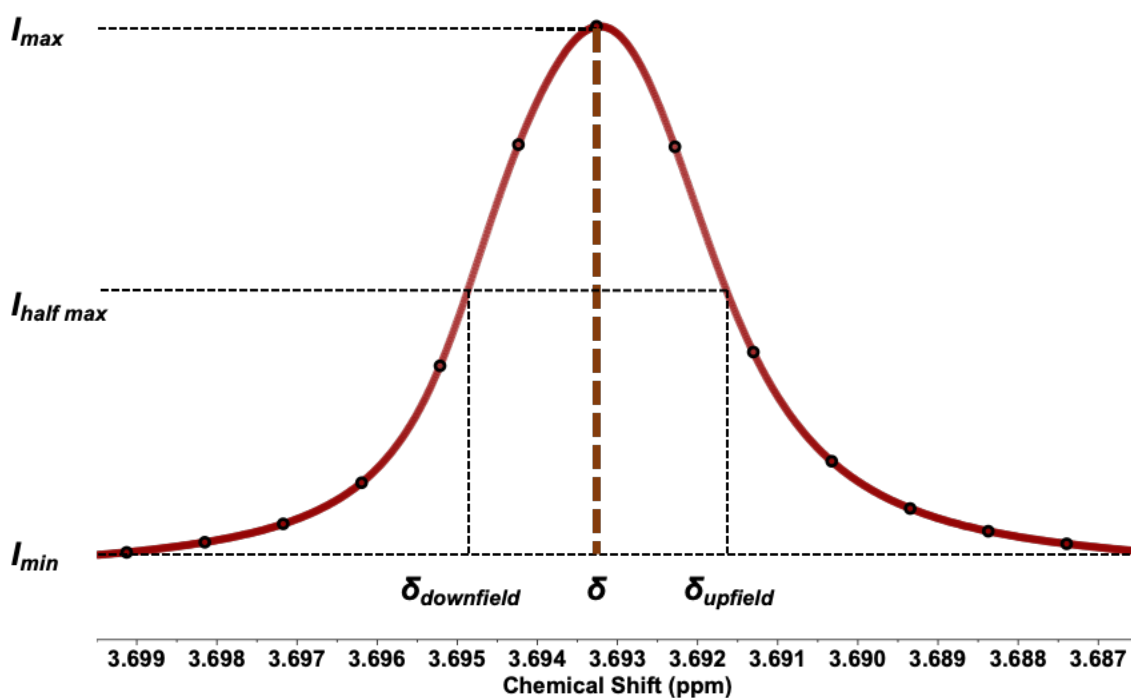


Figure 2-6: Spectrum of a PEO proton, where the chemical shift is marked by the vertical brown line. The black data points represent frequencies measured by the spectrometer, while the solid brown curve was obtained by zero-point filling in the Mnova software.

^1H NMR spectra were recorded as a function of salt concentration to search for signatures of ion-polymer interactions. As can be seen in Figure 2-7A, the peak corresponding to the PEO

protons shifted upfield as NaSCN was added to solution. The chemical shifts were extracted from these spectra and plotted in Figure 2-7B.

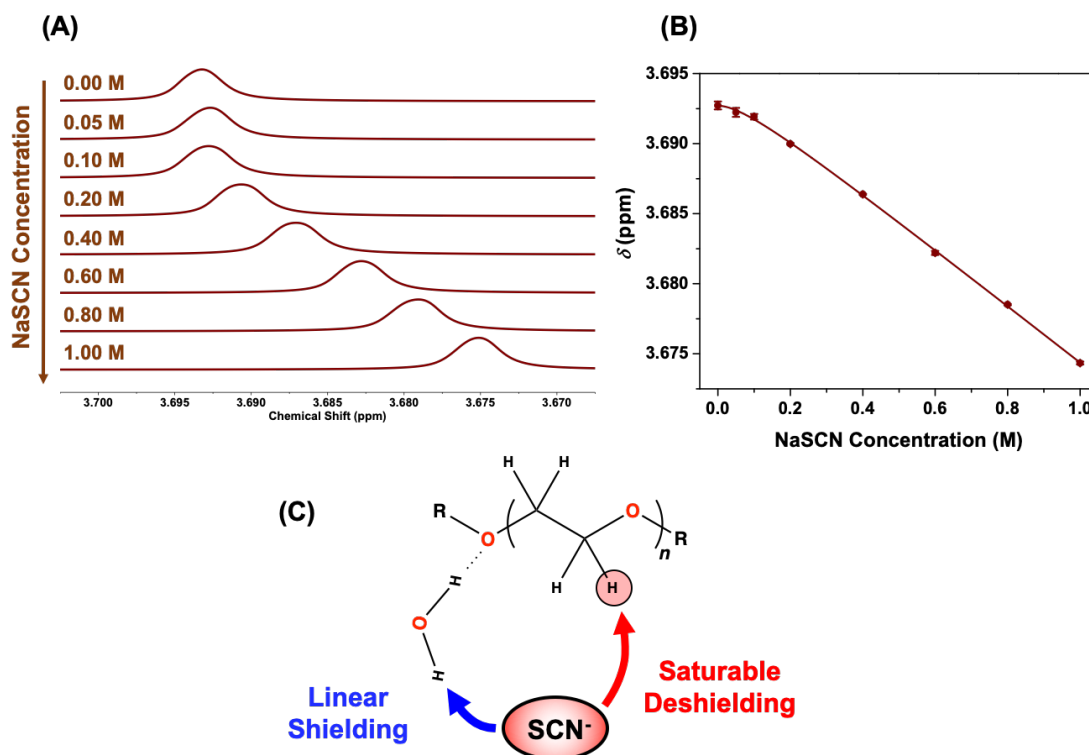


Figure 2-7: Salt-induced changes in the ^1H NMR spectrum of PEO. (A) Offset spectra acquired at different NaSCN concentrations. (B) The chemical shift of the methylene proton peak plotted as a function of salt concentration. The brown circles are the chemical shift data and the solid brown curve is a fit to the data using Equation 2-5. The error bars represent the standard deviation between 2-3 solutions preparations. (C) Schematic illustration of the physical interpretation of the model. The model describes the NaSCN effect with two contributions, including a dominant linear shielding effect that may involve indirect interactions and a smaller saturable deshielding contribution due direct adsorption of SCN^- anions to the aliphatic methylene units.

The dominant effect of adding NaSCN is a linear decrease in the chemical shift, or a deshielding effect. Careful assessment of the chemical shift's response to salt revealed nonlinearity at low concentration, which was reminiscent of the LCST phase diagram measured in the presence of NaSCN. In fact, the chemical shift data was well modeled by Equation 2-5, which has the same form as Equation 2-3 used to fit the LCST data. Here, the value of δ_{sample}

represents the chemical shift of the sample, δ_0 defines the chemical shift in pure water, a is the slope of the linear shielding effect and δ_{\max} is the small saturable deshielding effect observed at low concentration. The best fit to the data is plotted as the solid brown curve in Figure 2-7B.

$$\delta_{\text{sample}} = \delta_0 + ac_{\text{salt}} + \delta_{\max} \frac{c_{\text{salt}}}{c_{\text{salt}} + K_D} \quad \text{Equation 2-5}$$

Each condition was repeated at least two times and the standard deviation of the measurements was plotted as error bars in Figure 2-7B. On this scale, the error bars are smaller than the data points. The nonlinearity in the data is small; however, it becomes clear that the Langmuir isotherm contribution is necessary by comparing the fit to Equation 2-5 with a simple linear fit. A linear fit to the chemical shift is plotted in Figure 2-8A, the residual of the data versus the fit is plotted in Figure 2-8B. The residual chemical shift, δ_{residual} , was calculated using Equation 2-6, where the measured chemical shift data, δ_{sample} , can be compared to the chemical determined from the model's fit, δ_{model} .

$$\delta_{\text{residual}} = \delta_{\text{sample}} - \delta_{\text{model}} \quad \text{Equation 2-6}$$

The residual plot clearly shows that the data is nonlinear because a majority of the data points do not overlap with zero, which would indicate a perfect fit to the data. A horizontal dashed black line has been added at $\delta_{\text{residual}} = 0$ for clarity. The deviation is most pronounced at low concentration. Figure 2-8C displays a similar analysis for the model described by Equation 2-5. The residual chemical shift for this case is shown in Figure 2-8D, where nearly all of the data points overlap with zero. This simple residual analysis supports the notion that the data are more accurately described by a linear and a binding term.

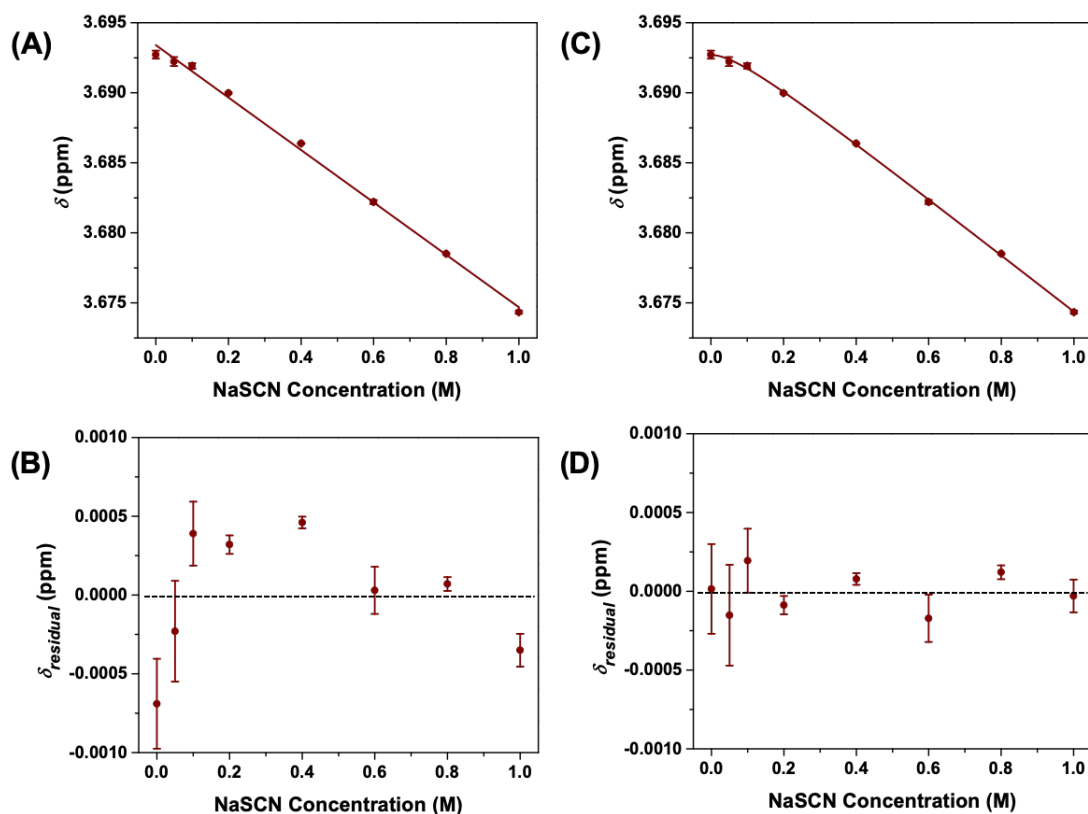


Figure 2-8: Comparisons of models for the NaSCN-induced chemical shift data of PEO-20k. (A) Chemical shift of the PEO-20k protons versus NaSCN concentration, where the solid brown curve is a fit to a line. (B) The residual chemical shift of (A) calculated using Equation 2-6. (C) Chemical shift of the PEO protons versus NaSCN concentration, where the solid brown curve is a fit to Equation 2-5. (D) The residual chemical shift of (C) calculated using Equation 2-6.

The effects of salts on chemical shifts have been investigated for water.^{124,125} In order to understand the origin of these two contributions to the chemical shift of PEO we first investigated the effect of polymer-water interactions by changing the temperature of the sample. As the temperature was increased the interactions with the polymer should be expected to be disrupted. Moreover, we expect that the dominant interaction between water and the PEO is through direct hydrogen bonding with the ether oxygen and hydrophobic hydration of the aliphatic methylene moieties. As can be seen in Figure 2-9, the chemical shift decreased with increasing temperature. This is consistent with the disruption of the hydrogen bonding between water and the ether

oxygen. At low temperatures, hydrogen bonding to water should provide a pathway to remove electron density from the polymer chain that produces the high value of δ_0 , depicted schematically in the lower left-hand part of Figure 2-9. Density functional theories suggest that the hydrogen bonds can transfer around 1/50 of an electron charge.¹²⁶ At higher temperatures, where this hydrogen bonding interaction is broken, the electron withdrawing pathway is broken and the electron cloud around the proton should be expected to become more dense, consistent with the observed shielding effect. This simple temperature-dependent experiment supports the idea that the slope of the linear salting out term may be related to the ability of salt ions to perturb the hydration shell of PEO.

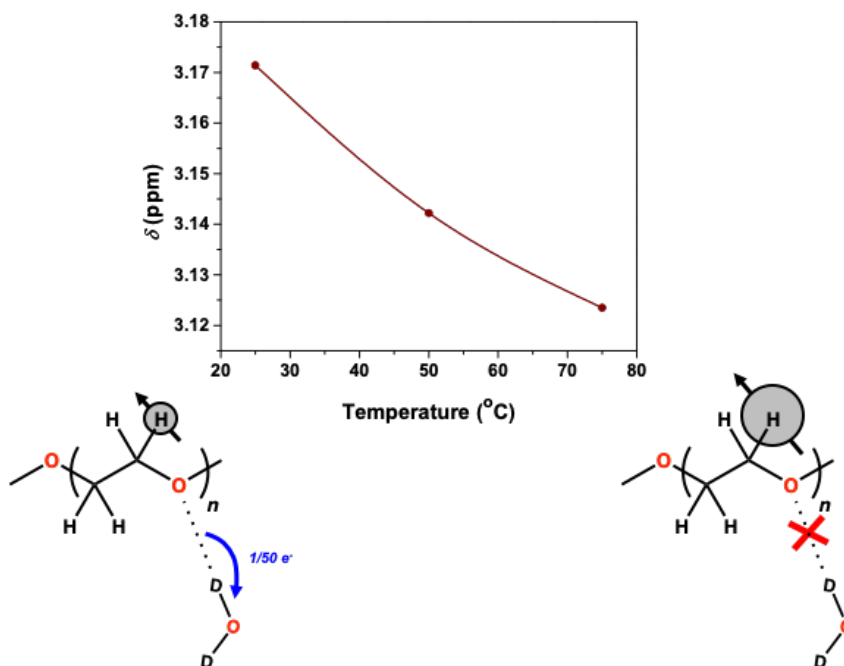


Figure 2-9: The temperature dependence of the chemical shift of PEO in D₂O. Two schematics are provided to illustrate the proposed mechanism for the decrease in the chemical shift.

The saturable deshielding effect of NaSCN was proposed to originate from direct adsorption of SCN⁻ to the polymer chain, as depicted in Figure 2-7C. Indeed, if the negatively charged anion were in direct contact with the methylene, then one should expect the electron

cloud to be pushed away from the proton and deshield the proton. In order to confirm this assignment, similar ^1H NMR experiments were performed for titrations of NaCl and Na_2SO_4 , as summarized in Figure 2-10.

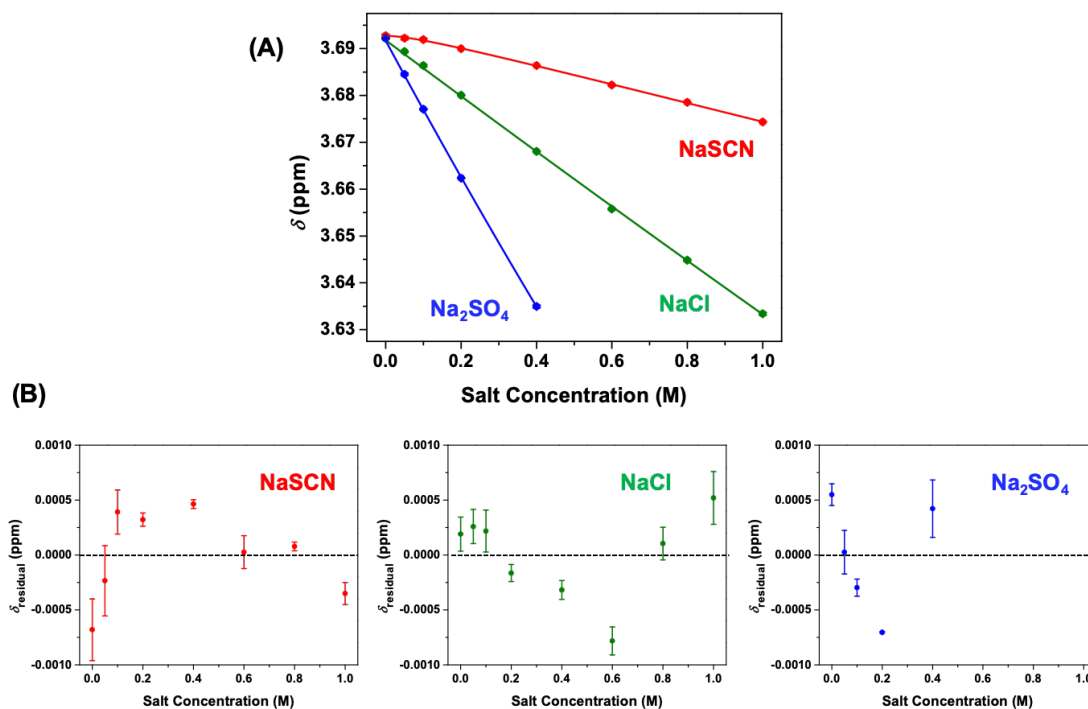


Figure 2-10: Salt-induced chemical shifts of PEO protons. (A) The chemical shift as a function of NaSCN, NaCl, and Na_2SO_4 . The data points are plotted as circles and the solid lines are fits to the data, using Equation 2-5 for NaSCN and Equation 2-7 for NaCl and Na_2SO_4 . (B) The residual chemical shifts for simple linear fits to each of the titration curves. The residual chemical shift data show distinct deviation for NaSCN in comparison the NaCl and Na_2SO_4 .

In comparison to NaSCN, the NaCl and Na_2SO_4 salts produced stronger shielding effects. That is the chemical shift decreased at a faster rate for these strongly hydrated anions. When an anion comes into proximity with the polymer chain one should expect it to reorient the hydrogen bonding architecture of the polymer's hydration shell, as depicted in Figure 2-7C; However, simple linear fits to the data were inadequate to describe the data. The residual chemical shift data after fitting the curves to simple lines is plotted in Figure 2-10B. The NaCl and Na_2SO_4 residuals

showed deviations at higher concentrations and the shape of the deviation was opposite to that of the NaSCN. In particular the NaCl and Na₂SO₄ data missed high, low, then high as salt was titrated into the solution. Similar to the LCST phase diagrams, the data were more accurately fit by including a squared term in the chemical shift Equation 2-7 as described by Equation 2-7. Here, the b parameter quantified the deshielding contribution that led to nonlinearity at high salt concentration. The square dependence of this contribution on salt concentration was empirical.

$$\delta_{\text{sample}} = \delta_0 + ac_{\text{salt}} + bc_{\text{salt}}^2 \quad \text{Equation 2-7}$$

The distinct nonlinearity observed for the weakly hydrated anions provides another piece of evidence for the assignment of this contribution to direct binding, since it can be modeled by a Langmuir isotherm. The fitted parameters for the ¹H NMR titrations are summarized below in Table 2-2.

Table 2-2: Best fit parameters of Equations 2-5 and 2-7 for the effect of sodium salts on the ¹H NMR chemical shift of PEO-20k.

Salt	δ_0 (ppm)	a (ppm M ⁻¹)	b (ppm M ⁻²)	δ_{max} (ppm)	K_D (M)
NaSCN	3.6918	-0.0203	-	0.0022	0.11
NaCl	3.6918	-0.0600	0.0015	-	-
Na ₂ SO ₄	3.6918	-0.1495	0.0188	-	-

The Role of Cations in the Adsorption of Weakly Hydrated Anions to PEO

The work presented thus far has largely attributed the effects on the LCST phase diagrams and the chemical shifts to the anion. Previous studies on cations chlorides by vibrational spectroscopy measurements have shown that interactions with the carbonyl oxygen of the amide are quite weak and show poor correlation with LCST measurements.¹²⁷ However, molecular

dynamics simulations have found that cations can bind with electronegative oxygen atoms of non-ionic solutes.^{128–130} In order to explore the role of the cations in these PEO studies, we performed similar experiments for a set of alkali iodide salts. An I⁻ anion was employed, rather than SCN⁻, due to the availability of commercial salts with a variety of cation identities. The LCST of PEO in the presence of LiI, NaI, and CsI is summarized in Figure 2-11. The results clearly demonstrate that all of these salts increase the LCST, indicating their ability to inhibit hydrophobic collapse. The solid curves in Figure 2-11 are fits to the data points. The LiI was fit to a linear function described by Equation 2-1, while the NaI and CsI were fit to a combination of linear and a Langmuir isotherm contribution as described by Equation 2-3.

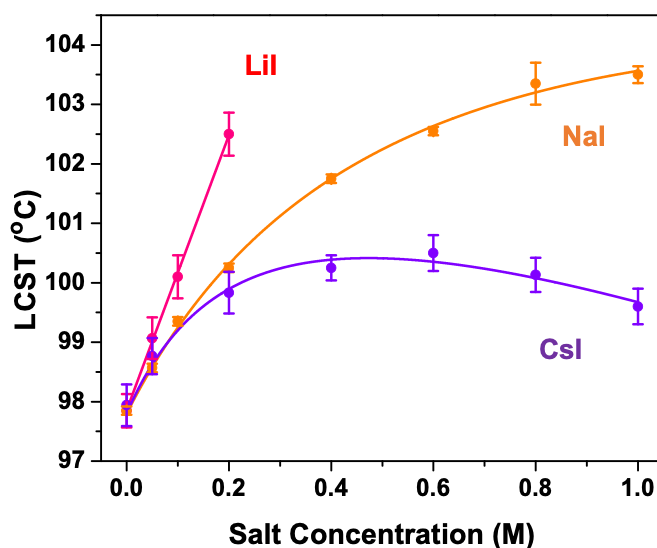


Figure 2-11: LCST phase diagrams for PEO in the presence of various alkali iodide salts. The data points are measurements of the LCST, while the solid curves are fits to the data.

The LCST data suggests that overall the effect of a salt comprised of a weakly hydrated anion is similar regardless of the identity of the alkali metal cation. It should be noted, however, that the magnitude of the “salting-in” effect, or increase in the LCST is influenced by the cation

identity. This effect may suggest cooperative interaction of the ions at the polymer surface. The best fit parameters for the LCST phase diagrams in the presence of alkali iodides is summarized in Table 2-3.

Table 2-3: Best fit parameters of Equation 2-3 for the effect of iodide salts on the LCST of PEO-20k.

Salt	T_0 (ppm)	a (ppm M ⁻¹)	b (ppm M ⁻²)	B_{\max} (ppm)	K_D (M)
LiI	97.8	23.1	-	-	-
NaI	97.8	-1.3	-	11.5	0.6
CsI	97.8	-3.5	-	6.9	0.3

In order to explore the molecular-level interactions of ions near PEO, we performed ¹H NMR titrations, which are summarized in Figure 2-12. The solid curves in Figure 2-12A represent best fits to Equation 2-5, involving a linear and binding term. Interestingly, the iodide salts produce a much stronger linear shielding effect than NaSCN. Figure 2-12B shows the residual chemical shifts for a simple linear fit, which revealed similar saturable deshielding effects to NaSCN. Again, we propose that this feature of nonlinearity arises from direct adsorption to the polymer surface. The data also show that the identity of the cation has a major effect on the linear shielding term. Larger cations produced more negative a parameters. According to the interpretation portrayed in Figure 2-7C, these results imply that Cs⁺ may perturb the hydration shell more than Na⁺ and Li⁺. This could be due to cation binding to the ether oxygen of PEO or due to ion-pairing between the cations and iodide. Future work exploring these effects on different polymers and with different anions may reveal the molecular-level interactions that give rise to the differences in the LCST phase behavior.

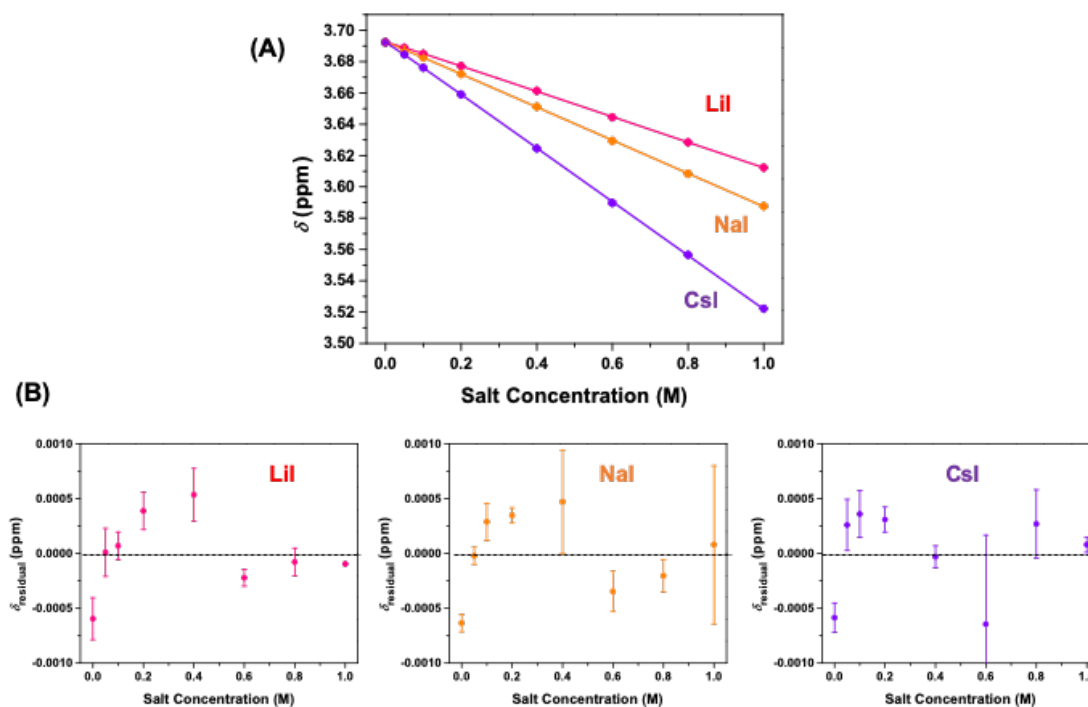


Figure 2-11: Salt-induced chemical shifts of PEO protons. (A) The chemical shift as a function of LiI, NaI, and CsI. The data points are plotted as circles and the solid lines are fits to the data, using Equation 2-5. (B) The residual chemical shifts for simple linear fits to each of the titration curves. The residual chemical shift data show similar nonlinearity as the NaSCN.

Table 2-4: Best fit parameters of Equation 2-5 for the effect of iodide salts on the ^1H NMR chemical shifts of PEO-20k.

Salt	δ_0 (ppm)	a (ppm M^{-1})	b (ppm M^{-2})	δ_{max} (ppm)	K_D (M)
LiI	3.6923	-0.0815	-	0.0015	0.07
NaI	3.6923	-0.1060	-	0.0012	0.03
CsI	3.6923	-0.1718	-	0.0015	0.06

Driving Forces for the Adsorption of Weakly Hydrated Anions to Polymer Chains

This chapter summarizes a set of LCST phase diagram measurements of PEO in the presence of various inorganic salt ions. Simple models are developed to fit the data on the basis of either attractive or repulsive interactions of the salt ions with the polymer surface. The key result

from these macroscopic experiments and models is that weakly hydrated anions appear to interact with the polymer leading to a “salting-in” effect that inhibits hydrophobic collapse. On the other hand, strongly hydrated anions drive the hydrophobic collapse because they are repelled from the polymer surface and retain their hydration shells in bulk solution.

In addition to the thermodynamic LCST measurements, ^1H NMR spectroscopy is employed to search for signatures of these interactions in the local chemical environment of the polymer surface. The basic principles of NMR and the chemical shift allow relationships to be made between the density of the electron cloud, hydration of the polymer, and direct interactions with weakly hydrated anions. Significantly, the interactions are elucidated by employing similar models to fit the changes in the chemical shift data as salt ions are titrated into the solution. In general, the major effect is a linear shielding. This contribution is argued to arise from the salt ions perturbation of hydrogen bonding between water and the ether oxygen of PEO. The magnitude of this linear contribution dependence on the anion and cation identity. The deviations from linearity, however, show two types of behavior that are distinct for weakly hydrated anions versus anions that are strongly hydrated.

These experiments add to the existing studies of the mechanisms of ion-specific effects. Despite the years of research invested to understand these interactions, fundamental questions relating to the driving forces for the interactions remain ambiguous. A particular area of interest is the driving force for weakly hydrated anions to adsorb to hydrophobic surfaces. This interaction is depicted schematically in Figure 2-12. In the gas phase, one should expect the interaction between an anion and an aliphatic surface to have attractions mainly due to ion-induced dipole forces. In solution, this interaction should be weaker than the ion-water and polymer-water interactions. Yet features of direct binding are observed by both thermodynamic and spectroscopic measurements, as demonstrated in this chapter. As such, these interactions should

be driven by a water-mediated effect. In Chapter 3, the role of interfacial water structure is investigated on a molecular level.

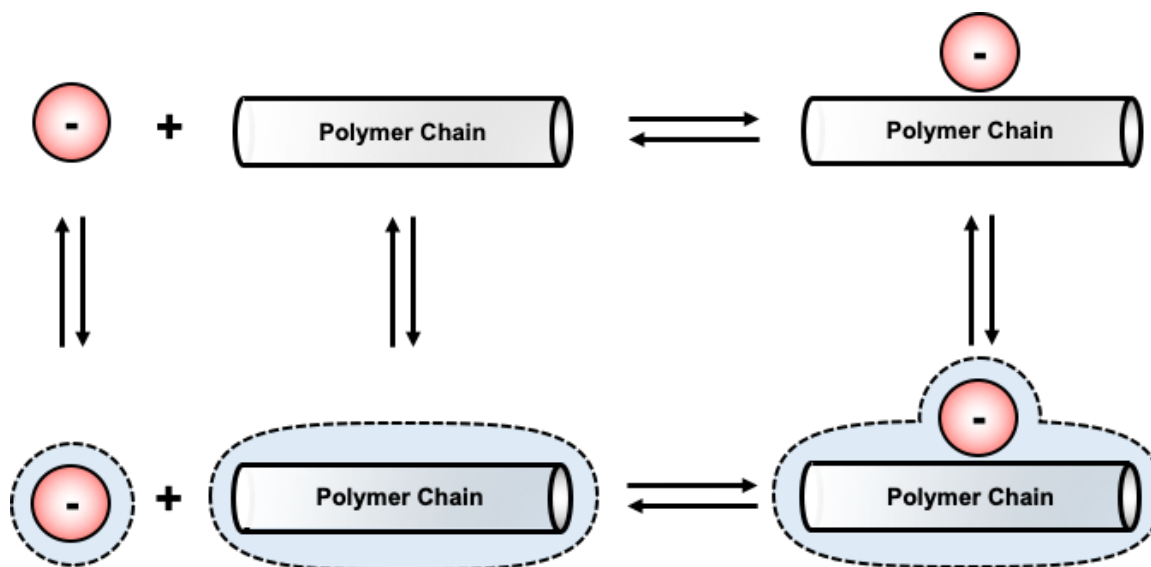


Figure 2-12: Schematic illustration of anion adsorption to a hydrophobic polymer chain. The top cartoons represent the interactions in vacuum, while the lower schematics highlight the importance of interfacial water structure in the process of adsorption.

Chapter 3

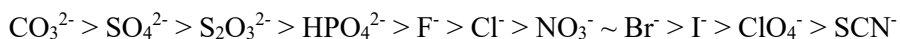
Surface Curvature and the Adsorption of Weakly Hydrated Anions to Hydrophobic Interfaces

The properties of aqueous solutions containing oil and salt are remarkably sensitive to the specific chemistry of their hydrophobic and ionic components.^{1,2,131-142} For example, longer polymer chains are generally less soluble in aqueous solutions than shorter ones, showing greater propensity to separate into oil-rich and water-rich phases.^{70,89,143} Also, longer chains exhibit distinct interactions with salt ions in solution compared to shorter chains or small molecules.¹⁴⁴⁻¹⁴⁷ Phenomena related to the hydrophobicity of polymers are ubiquitous, yet many of the molecular level mechanisms associated with ion specific hydrophobic effects are still not well understood. A fundamental understanding of hydrophobicity is of direct importance for the abstraction and purification of hydrocarbon fuels, the engineering of host-guest binding chemistry, the structuring and dynamics of self-assembled materials and emulsions, methane clathrate formation, the tuning of properties of ionic liquids, and even cleaning laundry.¹⁴⁸⁻¹⁵³

Weakly hydrated anions like SCN^- adsorb to hydrophobic regions of polymers and proteins in aqueous solutions, leading to unfolding and denaturation.⁷¹ Curiously, these same anions are repelled from the vicinity of small nonpolar molecules comprised of the same chemical constituents.⁹⁶ In this chapter, we explore the interactions of NaSCN with polyethylene glycols and polyethylene oxides of various molecular weights, ranging from monomers to polymers containing 1 million monomer units. A combination of ^1H NMR and vibrational spectroscopy measurements reveals that SCN^- accumulates near the surface of longer oligomeric chains but is excluded from shorter ones. This binding heterogeneity occurs because SCN^- preferentially binds to regions of low curvature, where ordered water structure in the macromolecule's hydration layer is disrupted. Significantly, the work presented in this chapter establishes a direct link between the size and shape of a hydrophobic entity, its water structure and Hofmeister chemistry.

Discrepancies in the Literature on the Adsorption of Weakly Hydrated Anions to Hydrophobic Surfaces

The anions on the left-hand side of the Hofmeister series are better hydrated and have been found to salt macromolecules out of solution. This is believed to occur via an excluded volume effect, whereby these ions are depleted from the polymer/water interface.¹⁵⁴ On the other hand, the ions to the right are more weakly hydrated and salt macromolecules into solution. Moreover, ions such as I^- , ClO_4^- and SCN^- are enriched at the polymer/water interface.^{51,74,95} At the molecular level, they are believed to shed their hydration shells in order to interact directly with hydrophobic moieties along the polymer chain. The Cl^- ion represents the dividing line for these behaviors, as shown in the anionic Hofmeister series below.



Weakly hydrated anions, such as I^- , SCN^- , and ClO_4^- , weaken the hydrophobic effect in aqueous solutions. These large, polarizable anions denature proteins, inhibit the formation of supramolecular host-guest complexes, and dissolve surfactant micelles.^{2,64,73} On the molecular level, weakly hydrated anions are believed to partially shed their hydration shells and adsorb to nonpolar interfaces, thereby inhibiting hydrophobic assembly.^{5,7,8} Surprisingly, measurements of the dissociation constants, K_D , of weakly hydrated anions to hydrophobic binding sites show substantial variation. In fact, the values vary over at least three orders magnitude (10 - 0.01 M), depending on the characteristics of the hydrophobe. For example, the adsorption of I^- to thermoresponsive polymers is well-characterized by millimolar equilibrium dissociation constant values, i.e. $K_D = 0.08\text{-}0.50\text{ M}$.^{51,71,72,90} Even tighter interactions have been observed at the air/water and graphene/water interfaces, $K_D = 0.03\text{-}0.26\text{ M}$, and inside supramolecular cavitands, $K_D = 0.09\text{ M}$.^{3,73,155-157} In stark contrast, however, I^- is repelled from small molecules, like *N*-

methyl acetamide and tert-butyl alcohol, where $K_D = 5-10 \text{ M}$.^{96,158} A summary of the structure of these solutes and the measured binding constants with I⁻ is provided in Figure 3-1.

Such results have called the direct binding mechanism into question and have inspired alternative explanations for core concepts of ion-specific effects on proteins. For example, apparent anion-backbone interactions have been rationalized by proposing new binding sites, such as aliphatic side chains.¹⁵⁸ Moreover, it has even been suggested that cations bind to proteins with higher affinities than anions. The continual recurrence of these debates exposes a critical gap in theories invoking a direct binding mechanism to explain anion-specific effects at nonpolar sites.⁶ Herein, it is argued that these apparent inconsistencies in the strength of weakly hydrated anion adsorption to polymers seem to be correlated with the curvature of the hydrophobic surface, as illustrated in Figure 3-1. Such results lead to the hypothesis that there should be a size-dependence and possibly a curvature-dependence for ion-hydrophobic interactions.

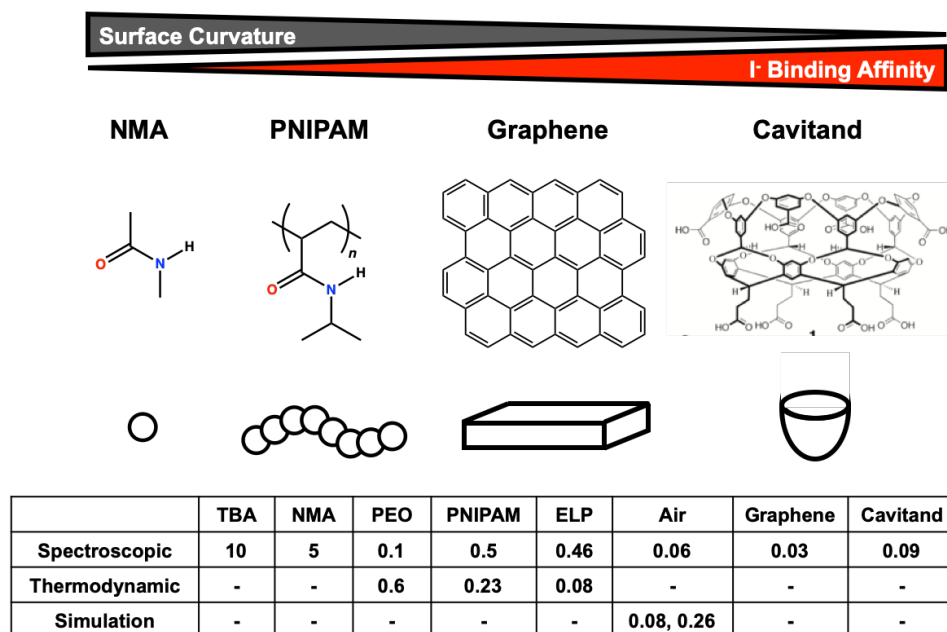


Figure 3-1: Surface curvature and binding affinity hypothesis. The structures of several molecules are provided along with cartoons to illustrate the general shapes. The binding constants determined for these molecules and others are summarized at the bottom of the figure. The values for the K_D are provided in molar units.

Surface curvature is known to affect other properties of nonpolar molecules, like solubility.¹⁵⁹ It is an age old adage that oil and water do not mix. This tendency of nonpolar substances to aggregate in aqueous solution is known as the hydrophobic effect. The term hydrophobic literally means “water-fearing” and misleadingly implies that oil and water repel one another. The forces that drive hydrophobic aggregation are more accurately ascribed to entropic (e.g. release of ordered water molecules) and enthalpic (e.g. maximized hydrogen bonds) contributions associated with strong and directional interactions of water with itself.¹⁶⁰ Although qualitative features of the hydrophobic effect were invoked as early as Irving Langmuir’s descriptions of the adsorption and orientation of nonpolar molecules to the air/water interface (1917), the formal concept of water-mediated hydrophobic interactions is generally attributed to Walter Kauzmann’s popular review on protein folding (1959).^{161,162} Kauzmann suggested that hydrophobic residues are buried within the interior of globular biomacromolecules in order to release water molecules from unfavorable configurations into the bulk solution. This idea was largely inspired by the “iceberg” model of nonpolar solvation proposed by Henry Frank (1945), which offered a pictorial illustration of ordered hydrogen bonding around hydrophobes based on the thermodynamic quantities of mixing.¹⁶³

In 1973, Frank Stillinger’s theoretical work established a significant physical basis for understanding the hydrophobic effect.¹⁶⁴ He related the structure of the hydrophobic/water interface to the macroscopic air/water interface. The idea was that bulk-like hydrogen bonding is preserved around small hydrophobic spheres ($r < 1$ nm), depicted in Figure 3-2. For large spheres ($r > 1$ nm), however, where the hydrophobic surface extends over areas greater than 1 nm^2 , it becomes impossible for the bulk-like hydrogen bonding network to be maintained, as illustrated in Figure 3-2. As such, Stillinger postulated that the surfaces of large hydrophobes in water were reminiscent of the air/water interface. Nearly thirty years later, Chandler calculated the enthalpic and entropic contributions to hydrophobic solvation as a function of solute size, which

consequently drive hydrophobic interactions.¹⁶⁰ The insights gleaned from these studies and others provide a fundamental basis for understanding hydrophobicity and the origins of water-mediated interactions based on the structure of the hydrophobic/water interface.^{165–169}

The molecular origins of curvature-dependent hydrophobicity relate to the formation of distinct water hydrogen bonding structures at the surface of positively curved solutes versus flat apolar interfaces.^{160,164,170} Water hydrogen bonding networks are able to wrap around small nonpolar solutes and maintain an ordered, bulk-like structure shown in Figure 3-2. Hydrophobic solutes that expose greater than 1 nm² of flat surface area, however, disrupt the hydrogen bonds between water molecules Figure 3-2. Large nonpolar solutes tend to cluster in solution to reduce the number of sites with broken hydrogen bonding. Signatures of this mechanism have been observed both experimentally and computationally in binary mixtures of hydrophobes in water.^{99,100}

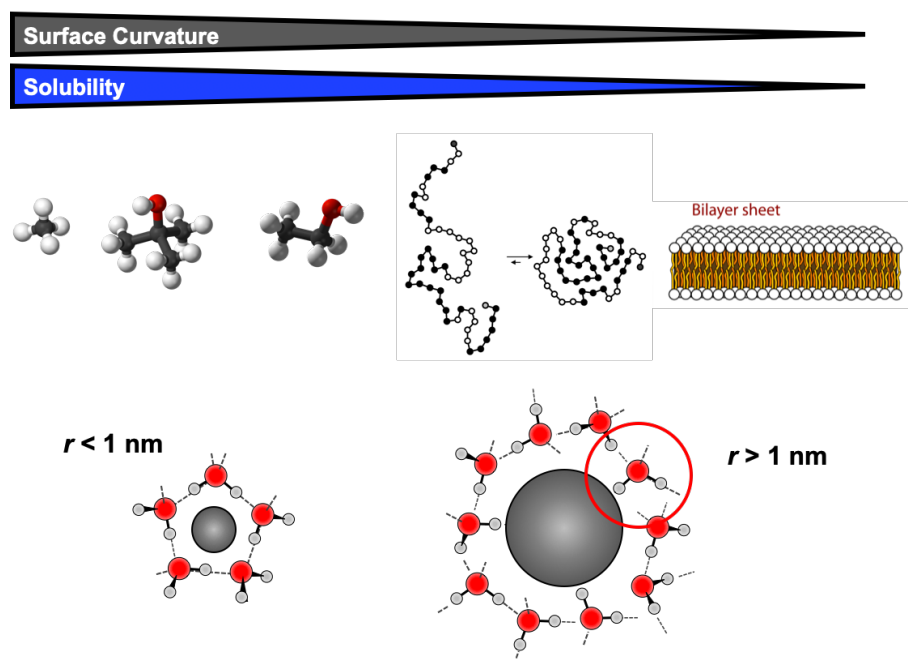


Figure 3-2: Surface curvature and solubility. The structure of several soluble small molecules are provided in contrast with polymers and lipids that self assemble in water. The origins of the difference in solubility can be understood by the structure of water-water hydrogen bonding at the surface of small, curved solutes versus larger solutes, whose surfaces appear locally more flat.

Herein, we show that sites with disrupted hydrogen bonding that drive hydrophobic self-assembly also constitute binding sites for the adsorption of weakly hydrated anions. More specifically, the geometric properties of the hydrophobic/aqueous interface, like solute size and surface curvature, can modulate the affinity of weakly hydrated anions over several orders of magnitude. This idea is depicted schematically in Figure 3-3.

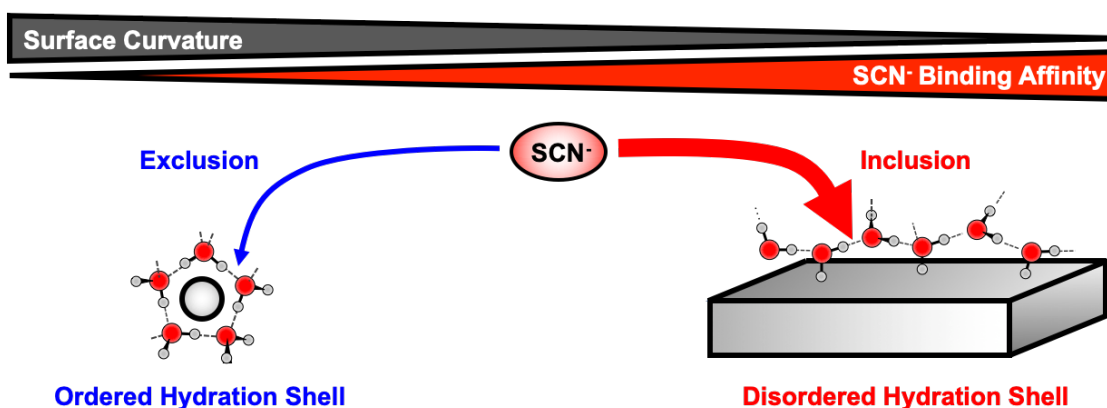


Figure 3-3: Proposed mechanism for the connection of hydrophobicity to ion-specific effects. Surface curvature impacts the order of the hydration shell. Weakly hydrated anions are excluded from the well-ordered hydration shells of small molecules. They readily adsorb to flat interfaces because they displace water molecules that exhibit broken hydrogen bonding. The Small solutes, depicted by the small grey sphere, exhibit positive curvature and have ordered hydration shells. The macroscopic interfaces, depicted by the grey slab, are flatter and contain sites of defective hydrogen bonding.

To test the effects of size and surface curvature on the adsorption of weakly hydrated anions to interfaces, we have measured the interaction of NaSCN with polyethers of varying chain length, n . We employed both polyethylene glycols, PEG- n , and polyethylene oxides, PEO- n , ranging in chain length from monomers to polymers. This idea is depicted schematically in Figure 3-4. We note that the monomer concentration was held constant in these experiments at 11 mg/mL or ~ 0.25 M. It was found that SCN^- is repelled from the surfaces of monomers, but binds increasingly more favorably to oligomers of increasing chain length. More importantly, SCN^- binds selectively to the central portions of oligomer chains, as opposed to the end groups as

drawn in the lower right-hand panel of Figure 3-4. There is a direct correlation between the degree of disordering of the water molecules in the hydration shell and the ability of SCN^- to bind. Namely, regions with more disrupted hydrogen bonding lead to more favorable interactions.

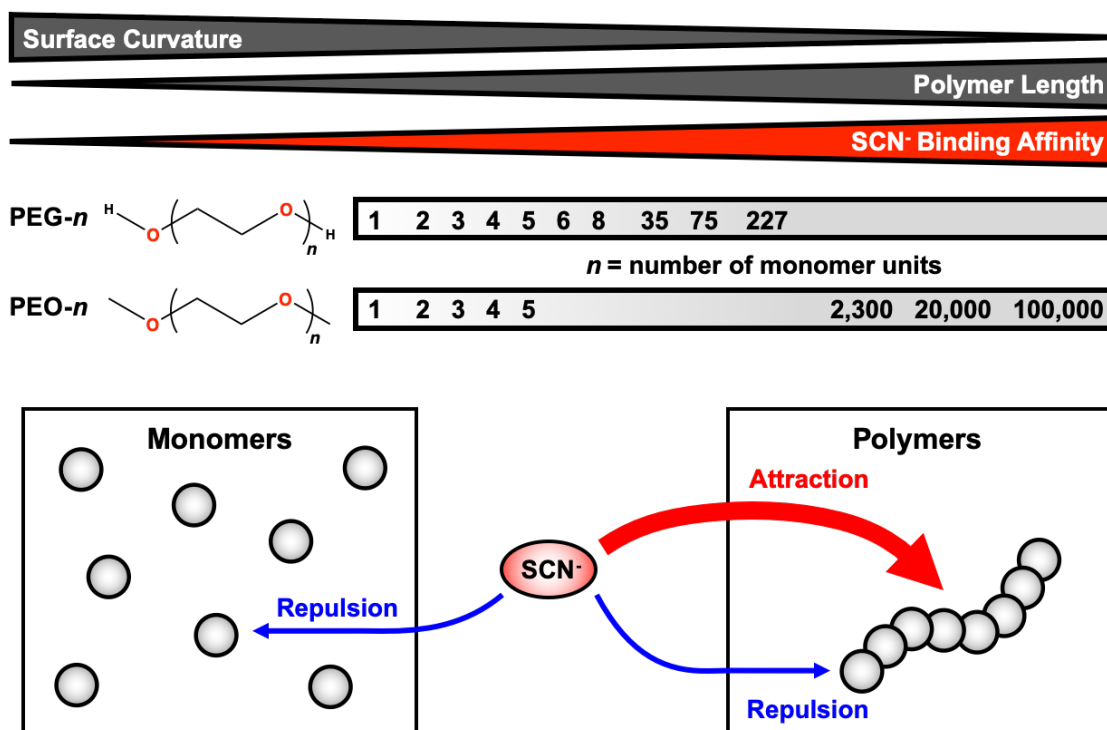


Figure 3-4: Schematic illustration of the experimental approach to systematically investigate the surface curvature hypothesis. Polymers of PEG and PEO were used as model systems ranging from monomers to 100,000 mers. The specific lengths used in these studies are summarized in the two grey horizontal bars. The key results from the study are summarized in the lower two panels. Namely, SCN^- anions are repelled from monomers and the termini of polymers, but are attracted to the middle of polymer chains, where the surface curvatures is locally more flat. Herein, it is shown that SCN^- is excluded from the termini of chains where the hydration shell is well-ordered (blue arrow). In contrast, SCN^- preferentially adsorbs to the center of polymer chains where the water structure is more disordered (red arrow).

The monomer and oligomers of polyethylene glycols (PEG- n) were of liquid form and at least 95% pure: Ethylene glycol (PEG-1, 99.8%, Sigma-Aldrich), Diethylene glycol (PEG-2, $\geq 99.0\%$, Sigma), Triethylene glycol (PEG-3, 99%, Sigma-Aldrich), Tetraethylene glycol (PEG-4, 99%, Aldrich), Pentaethylene glycol (PEG-5, 98%, Aldrich), Hexaethylene glycol (PEG-6, 97%, Aldrich), Octaethylene glycol (PEG-8, $\geq 95\%$, Aldrich). The monomer and oligomers of

polyethylene oxide (PEO-n) were also liquids with at least 99% pure: 1,2-dimethoxyethane (PEO-1, 99.9%, Sigma-Aldrich), Diethylene glycol dimethyl ether (PEO-2, 99.5%, Sigma-Aldrich), Triethylene glycol dimethyl ether (PEO-3, 99%, Sigma-Aldrich), Tetraethylene glycol dimethyl ether (PEO-4, $\geq 99\%$, Aldrich), Polyethylene glycol dimethyl ether Mn ~ 250 (PEO-5, n20/D 1.441, Aldrich). The longer chain PEGs and PEOs were of solid form: Polyethylene glycol Mw $\sim 1,500$ (PEG-35, Sigma-Aldrich), Polyethylene glycol Mw $\sim 3,350$ (PEG-75, Spectrum), Polyethylene glycol Mw $\sim 10,000$ (PEG-227, Sigma-Aldrich), Polyethylene oxide Mv $\sim 100,000$ (PEO-2k, Aldrich), Polyethylene oxide Mv $\sim 900,000$ (PEO-20k, Aldrich), and Polyethylene oxide Mv $\sim 5,000,000$ (PEO-100k, Aldrich).

Stock solutions of the polyethers were prepared in 18 M Ω deionized water to a monomer concentration of 2 M. The stock solutions for the polyethers in liquid form were prepared volumetrically by diluting a volume of the pure liquid with water. All of the 2 M stock solutions appeared soluble by visual inspection, with the exceptions of PEO-3, which appeared cloudy, and PEO-5, which appeared cloudy and exhibited a faint yellow color. Stock solutions of the solid PEGs were prepared gravimetrically to a monomer concentration of 2 M. The three longest polymers, the solid PEOs, were either insoluble or too viscous to be prepared at 2 M monomer concentrations. As such, 0.5 M stock solutions were prepared in 18 M Ω deionized water. The 0.5 M stocks were then aliquoted into microcentrifuge tubes in 0.5 mL quantities and dried under vacuum at 45 oC for 12 hours to remove water.

The salt and polyether stock solutions were mixed volumetrically with water to prepare the ternary solutions. The volumes of the three solutions were assumed to be additive. The same salt stock solution was used for all polyether solutes to reduce the sources of error. The ternary solutions were prepared in triplicate. For the ^1H NMR and LCST measurements, the salt concentrations ranged from 0 to 2 M, with the exception of sulfate, which ranged from 0 to 0.6 M. The monomer concentration of the polyethers was 0.25 M for ^1H NMR and LCST

measurements and 0.5 M for the Raman experiments, which contained no salt. For the three longest PEOs, the salt stock and water were added directly to the dried pellet and the volume of the polymer was assumed to be negligible. The solutions were stored in the dark to avoid exposure to light and avoid any photooxidation. Measurements were performed on the solutions no more than 2 months after their preparation.

¹H NMR Peak Assignments for Polyethers of Varying Chain Length

We observed multiple peaks in the ¹H NMR spectra of the polyethers. These peaks were assigned by comparing the spectra as a function of chain length in neat water. The spectra of the PEO-*n* mers are shown in Figure 3-5. We expected two peaks in the spectrum of PEO-1, one for the terminal methyl protons, highlighted in blue, and another for internal methylene protons, highlight in red, as indicated schematically by the colored circles in Figure 3-5. Indeed, the data for PEO-1, purple spectrum in Figure 3-5, showed two singlet peaks corresponding to the terminal methyl group, where $\delta = 3.3721 \pm 0.0002$ ppm, and central methylene units, where $\delta = 3.6074 \pm 0.0002$ ppm. The two circles above the PEO-1 spectrum, purple spectrum at the top of Figure 3-5, are a visual aid for the peak assignments, which correspond to the colored circles provided on the structure of the PEO-*n* mers in Figure 3-5. The spectra are offset to lower positions along the y-axis with increasing chain length, as indicated by the labels on the left-hand side of Figure 3-5. As the chain length was increased from PEO-1 to PEO-5, we found that the terminal methyl peak remained a singlet with a nearly constant peak frequency, at $\delta = 3.3728 \pm 0.0005$ ppm. On the other hand, the methylene proton peak showed more dramatic changes in splitting and peak frequency with increasing chain length, as marked by the peaks between the two dotted vertical red lines in Figure 3-5B.

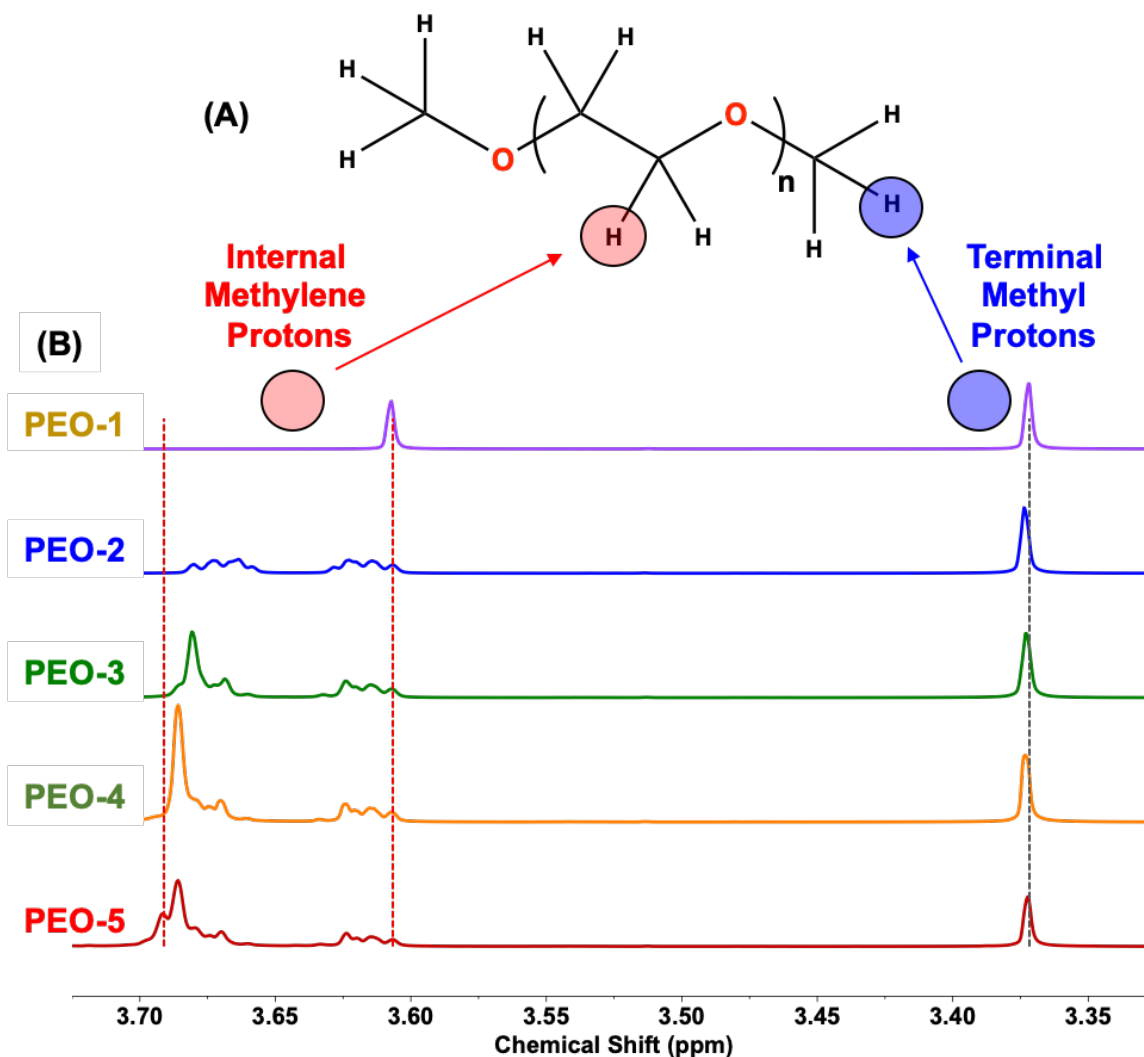


Figure 3-5: ^1H NMR spectra of PEO-*n* mers. (A) Bond-line structure of PEO-*n* mers. (B) ^1H NMR spectra of PEO-*n* mers, the solute length is labeled on the left-hand side of each spectrum. Two sets of peaks corresponding to the methyl termini and the central methylene are labeled with circles in (A) and dashed vertical lines in (B).

The spectra of the methylene protons can be seen more clearly in Figure 3-6A, where the x-axis has been contracted to the region of interest. The methylene protons for PEO-1, labeled by the purple circle above the purple spectrum at $\delta = 3.6074 \pm 0.0002$ ppm, exhibited no splitting, indicating that the two protons on the neighboring methylene moiety of the ethylene group are chemically equivalent. These internal methylene protons are labeled with purple circles on the PEO-1 structure in Figure 3-6B. The PEO-2 spectrum, however, exhibited two populations of

internal methylene protons that each had a complex splitting pattern, as can be seen in the blue spectrum of Figure 3-6A. The upfield population was centered near $\delta \sim 3.617$ ppm, labeled by the purple circle above the blue spectrum in Figure 3-6A, which was fairly similar in frequency to the methylene protons of PEO-1. As such, we assigned this upfield population to the pair of methylene units positioned at the ends of the chain, consisting of 4 protons labeled with purple circles on the PEO-2 structure in Figure 3-6B. The second population of internal methylene peaks in the PEO-2 spectrum was shifted downfield at $\delta \sim 3.670$ ppm, which is labeled by the blue circle above the blue spectrum in Figure 3-6A. This downfield population was assigned to the pair of methylene units, including the 4 protons positioned near the central ether oxygen of PEO-2, which are labeled with blue circles on the PEO-2 structure in Figure 3-6B.

The splitting pattern of the internal methylene protons on PEO-2 was complex, but it remained somewhat constant as the chain length was increased to PEO-3. For PEO-3, these protons should be located on the end-group monomers adjacent to the methyl termini. As such, we collectively refer to these upfield and downfield multiplets as the end-group protons. In addition to the end-group protons, we observed a new singlet peak in the PEO-3 spectrum at $\delta = 3.6807 \pm 0.0002$ ppm, which is labeled by the green circle above the green spectrum in Figure 3-6A. The frequency of this singlet was similar to the downfield protons of the end-group. Moreover, the apparent ratio of area under the singlet relative to the end-group peaks was $\sim 1:2$. These properties of the singlet are consistent with the methylene protons located on the central ethylene oxide monomer unit of PEO-3. These central 4 protons are labeled by green circles on the PEO-3 structure in Figure 3-6B. This singlet peak was also observed in the PEO-4 spectrum, which is marked by the orange circle above the orange spectrum in Figure 3-6A. This peak was more intense, relative to the end-group peaks with $\sim 1:1$ intensity ratio, and slightly deshielded at $\delta = 3.6859 \pm 0.0001$ ppm in comparison to the singlet of PEO-3. This frequency difference can be seen by comparing the dashed vertical green and orange lines in Figure 3-6A.

The longest oligomer employed for the methyl terminated polyethers was PEO-5. As can be seen, the spectrum looks similar to PEO-4, with the addition of a new deshielded singlet peak at $\delta = 3.6916 \pm 0.0001$ ppm, which is labeled by the red circle above the red spectrum in Figure **3-6A**. Considering the peak position and the apparent ratio of the new singlet to the old singlet and end-group peaks of $\sim 1:2:2$, we assigned the new, deshielded to the methylene protons located on the most central monomer unit of PEO-5. These 4 protons are labeled with red circles on PEO-5 in Figure **3-6B**. The PEO-5 spectrum thus consists of a central population of methylene protons, labeled by red circles in Figure **3-6B**, which are flanked immediately by a so-called penultimate population, labeled by orange circles in Figure **3-6B**, resembling the populations present in PEO-4 and PEO-3, and subsequently flanked by the end-groups, labeled by the purple and blue circles, which resemble the end-group populations present in the PEO-2, PEO-3, and PEO-4.

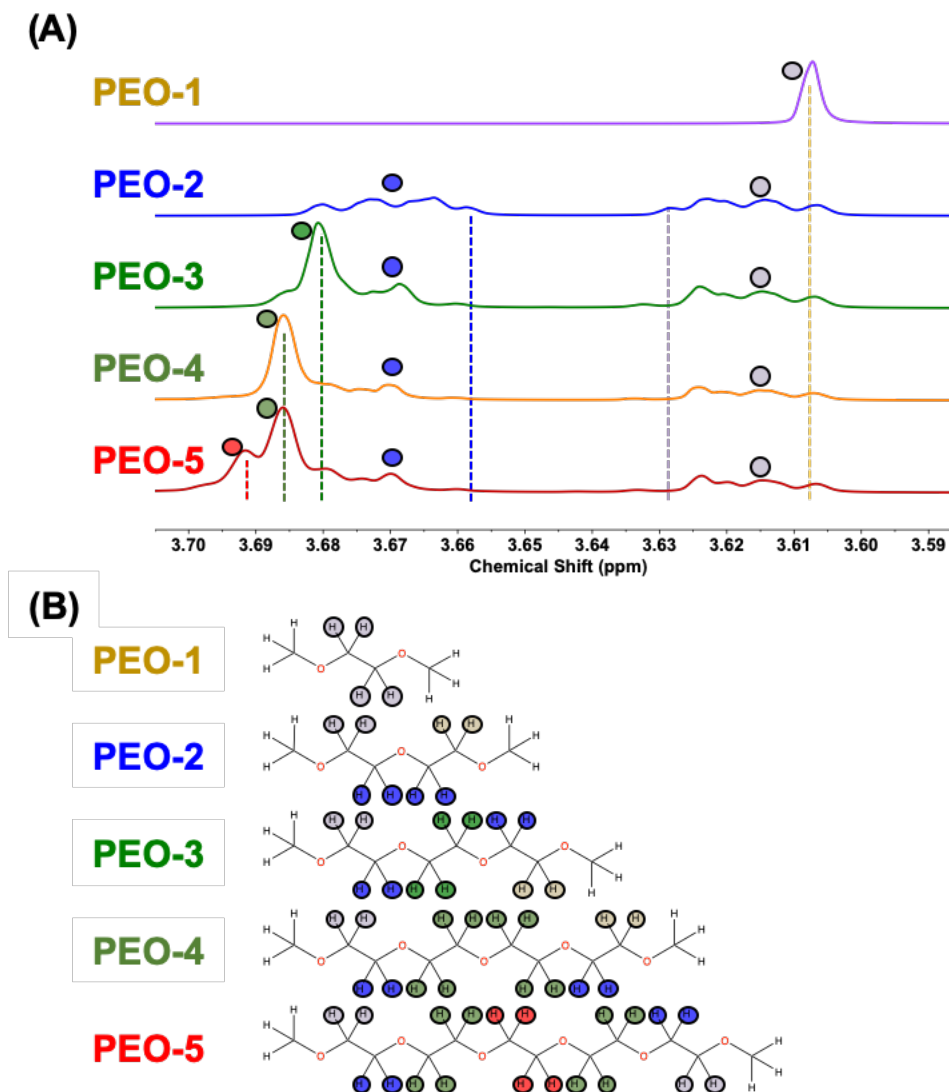


Figure 3-6: ^1H NMR spectra of the methylene protons as a function of PEO- n mer chain length (A) The spectral region corresponding to the methylene protons from Figure 3-5. The spectrum for each chain length is provided and labeled on the left-hand side. (B) Bond-line structures for the various chain lengths. The colored circles in (B) are assignments to specific peaks in the ^1H NMR spectra of (A).

Analogous “peak-to-proton” assignments were made for the PEG- n solutes. The spectra and structures of PEG-1 through PEG-8 are provided in Figure 3-7. Similar to PEO-1, the PEG-1 spectrum showed a singlet peak for the methylene protons at $\delta = 3.6583 \pm 0.0001$ ppm, which is labeled by the purple circle above the purple spectrum in Figure 3-7A. These protons are indicated with purple circles on the structure of PEG-1 in Figure 3-7B. The terminal hydroxyl

proton should exchange with the solvent. Upon lengthening to PEG-2, the singlet peak separated into two populations, which are labeled by the purple and blue circles above the blue spectrum in Figure 3-7A, each of which exhibited a complex splitting pattern that was reminiscent of the end-group protons for the PEO-*n* mers. As such, we assigned the upfield population to the terminal-most methylenes, marked by purple circles near $\delta \sim 3.635$ ppm, and the downfield population to the central-most methylenes, marked by blue circles near $\delta \sim 3.735$ ppm, on PEG-2. These assignments are illustrated schematically in Figure 3-7B. A new singlet peak at $\delta = 3.7028 \pm 0.0001$ ppm was apparent in the PEG-3 spectrum, labeled by the green circle above the green spectrum in Figure 3-7A. This singlet peak maintained nearly the same frequency at $\delta = 3.7018 \pm 0.0005$ ppm, but grew in intensity relative to the end-group peaks for PEG-4, which is marked by the green circle above the orange spectrum in Figure 3-7A. We assigned this singlet peak to the central methylene units for both the PEG-3 and PEG-4 oligomers. This assignment is visualized by the green circles on the PEG-3 and PEG-4 structures in Figure 3-7B.

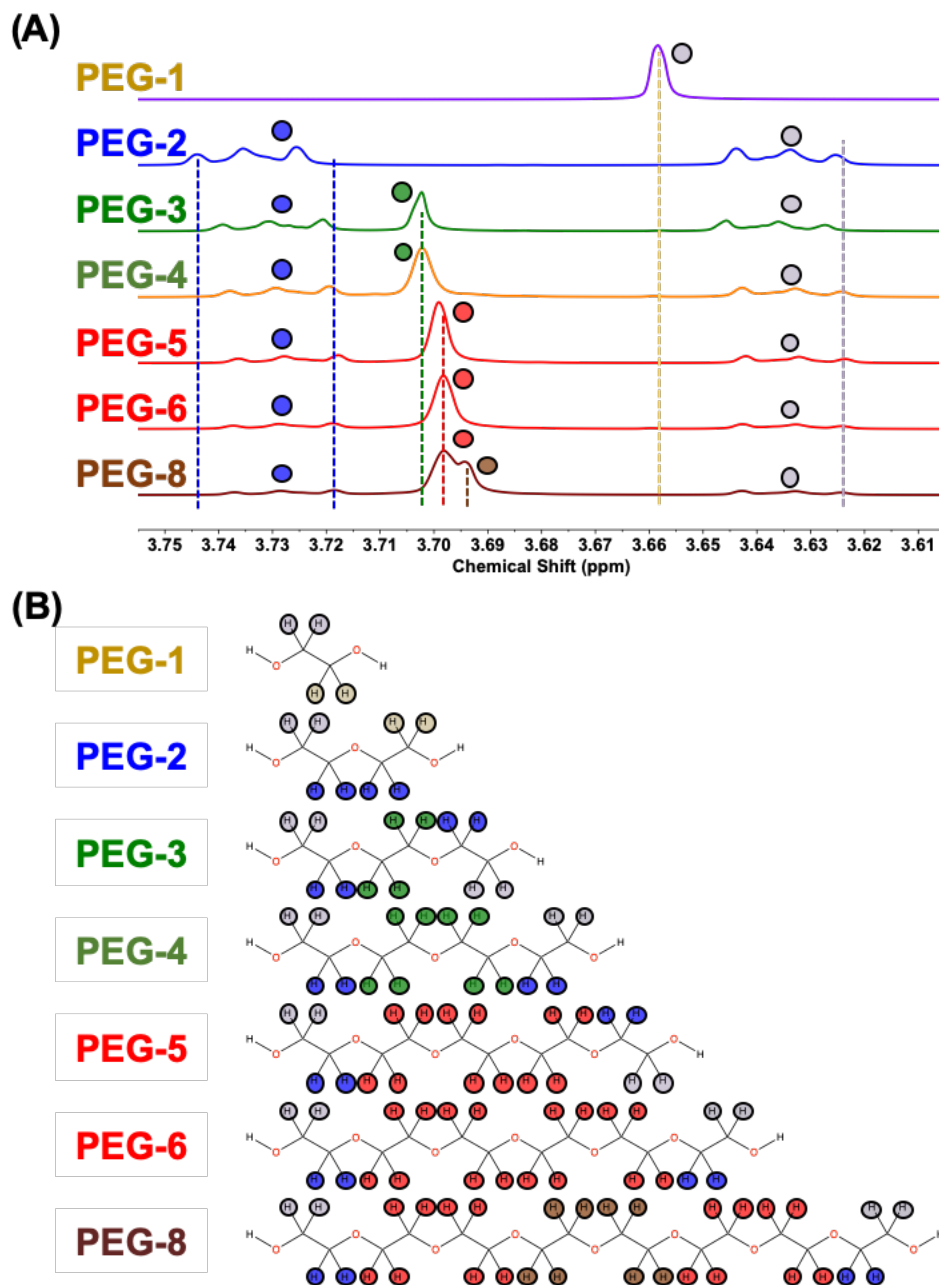


Figure 3-7: ^1H NMR spectra of the methylene protons as a function of PEG- n mer chain length (A) The spectral region corresponding to the methylene protons. The spectrum for each chain length is provided and labeled on the left-hand side. (B) Bond-line structures for the various chain lengths. The colored circles in (B) are assignments to specific peaks in the ^1H NMR spectra of (A).

The PEO-5 and PEG-6 oligomers were also dominated by a singlet peak corresponding to the internal methylene protons, indicated by the red circles above the red spectra in Figure 3-7A.

In contrast to PEO-5, the penultimate and central protons for PEG-5 and PEG-6 were

indistinguishable. The peak frequency, however, shifted upfield for PEG-5 to $\delta = 3.6989 \pm 0.0003$ ppm and even further upfield for PEG-6 where $\delta = 3.6975 \pm 0.0009$ ppm. As such, the singlet peaks observed for PEG-5 and PEG-6 should report on an average of both the penultimate and central methylene units, which is labeled by the red circles on the PEG-5 and PEG-6 structures in Figure 3-7B. Interestingly, the PEG-8 revealed an additional, distinct methylene population that was shifted upfield at $\delta = 3.6936 \pm 0.0009$ ppm, which is marked by the brown circle above the brown spectrum in Figure 3-7A. We assigned this upfield peak to the methylene protons on the central-most monomers of the chain, illustrated by the brown circles on the PEG-8 structure in Figure 3-7B.

For polyether chains that were longer than PEG-8, the peaks merge into a single peak Figure 3-8A. This is consistent with the spectrum being dominated by protons that resemble the central unit of the PEO-5 or PEO-8 mers. In summary, the ^1H NMR spectra distinguished 4 types of protons located at specific positions on the polyether chains, including (1) the terminal methyls, (2) the end-group methylenes, (3) the penultimate methylenes, and (4) the central methylenes. The central methylene protons positioned on monomer units located 3 or more units away from the end group are indistinguishable in the measured ^1H NMR spectra. The systems that have a distinct peak for the penultimate positions are limited to PEO-5 and PEG-8. These categories of protons are summarized in Table 3-1.

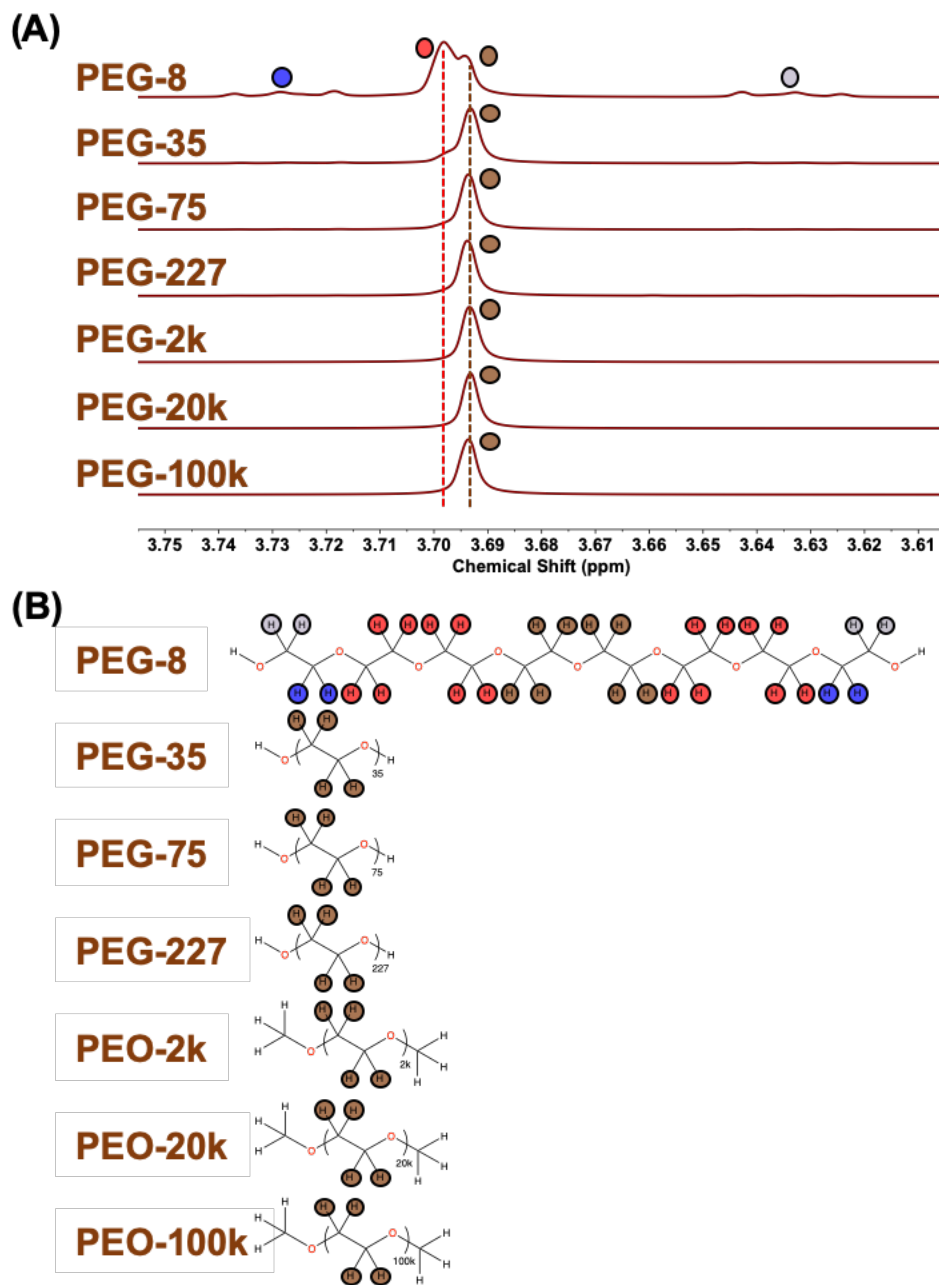


Figure 3-8: ^1H NMR spectra of the methylene protons as a function of PEG- n and PEO- n mer chain length (A) The spectral region corresponding to the methylene protons. The spectrum for each chain length is provided and labeled on the left-hand side. (B) Bond-line structures for the various chain lengths. The colored circles in (B) are assignments to specific peaks in the ^1H NMR spectra of (A).

Table 3-1: Summary of distinct proton populations observed in the ^1H NMR spectra of polyethylene oxides and polyethylene glycols of various chain length.

Chain Length (Monomer Units)	Proton Populations (Number)	Terminal CH_3 (Observable)	End $\text{CH}_2\text{-A}$ (Observable)	End $\text{CH}_2\text{-B}$ (Observable)	Penultimate CH_2 (Observable)	Middle CH_2 (Observable)
PEO-1	2	Yes	Yes	-	-	-
PEO-2	3	Yes	Yes	Yes	-	-
PEO-3	4	Yes	Yes	Yes	Yes	-
PEO-4	4	Yes	Yes	Yes	Yes	-
PEO-5	5	Yes	Yes	Yes	Yes	Yes
PEG-5	3	-	Yes	Yes	Yes	-
PEG-6	3	-	Yes	Yes	Yes	-
PEG-8	4	-	Yes	Yes	Yes	Yes
PEG-35	1	-	-	-	-	Yes
PEG-75	1	-	-	-	-	Yes
PEG-227	1	-	-	-	-	Yes
PEG-2,270	1	-	-	-	-	Yes
PEG-20,454	1	-	-	-	-	Yes

^1H NMR Measurements of SCN^- Interactions with Polyethers of Varying Chain Length

The effects of NaSCN on each of the peaks in the ^1H NMR spectra of the PEO and PEG oligomers was investigated. The salt-induced changes in the central-most methylene units of the PEO- n mers is discussed first, as shown in Figure 3-9A. The data are plotted as a change in chemical shift, $\Delta\delta$, since the values of the chemical shift in neat water, δ_0 , differ between the central-most protons on each oligomer.

$$\Delta\delta = \delta_{\text{sample}} - \delta_0 \quad \text{Equation 3-1}$$

As can be seen in Figure 3-9A, each data set for a given PEO- n mer exhibits non-linearity at low NaSCN concentration, below $c_{\text{salt}} = 0.5$ M. The solid curve for each data set in Figure 3-9A is a fit to Equation 3-2. The fitted parameters are summarized in Table S1.

$$\Delta\delta = ac_{\text{salt}} + \delta_{\text{max}} \frac{c_{\text{salt}}}{c_{\text{salt}} + K_{\text{D}}} \quad \text{Equation 3-2}$$

At higher NaSCN concentration, the salt-induced change in chemical shift is dominated by a decreasing linear trend. The values of $\Delta\delta$ as a function of NaSCN concentration for the central-most protons of PEG were well-modeled by Figure **3-9B**. Polyethers with chains longer than $n = 35$ have a similar titration profile as can be seen in the dark red curves in Figure **3-9C**. The PEO-20k titration data is plotted in all of the plots in Figure **3-9**, while PEG-35 is plotted in Figure **3-9B** and **3-9C** for visual reference.

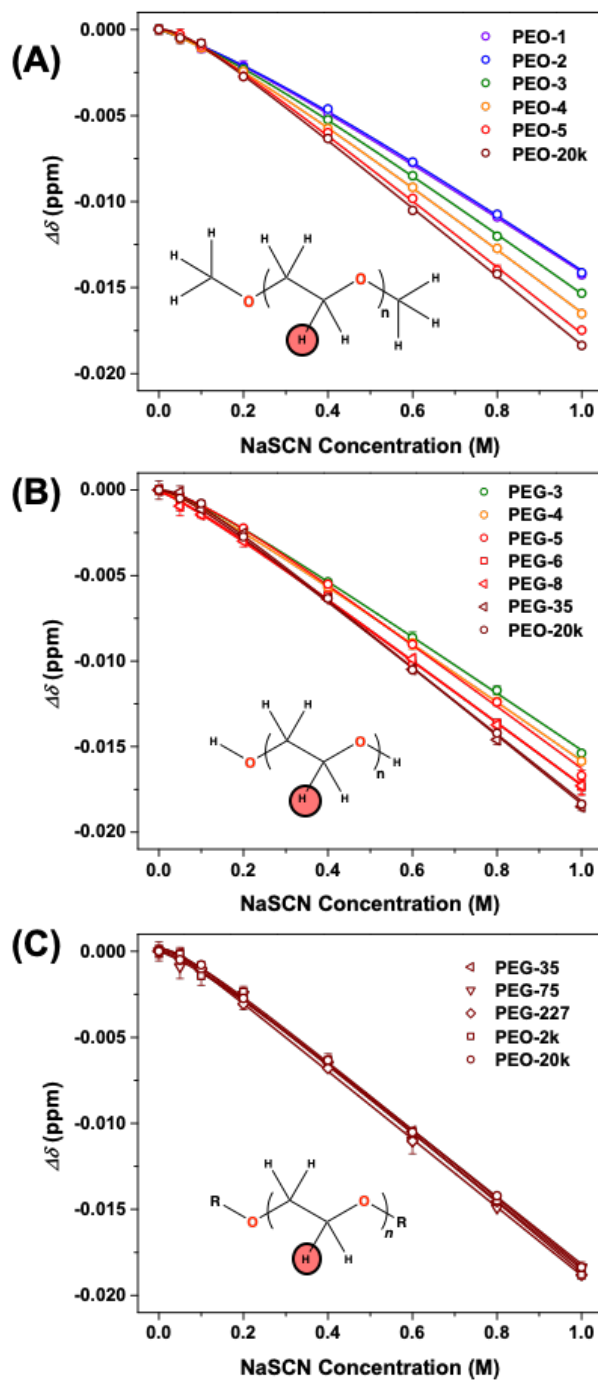


Figure 3-9: NaSCN-induced chemical shifts of the most central methylene proton on various polyether chains. The data is grouped into three panels for different solutes, including (A) PEO- n mers, (B) PEG- n mers from $n = 1$ to 35 monomer units, and (C) long chain PEO- n and PEG- n mers. The solid curves are fits to Equation 3-2.

We note that the PEG-1 and PEG-2 mer data are not included in Figure 3-9 because they could be fit to Equation 3-2. The titration data for these two systems are provided in Figure 3-10. As can be seen, the PEG-1 data shows non-linearity at higher concentrations, which is distinct from the non-linearity at low concentrations described by the Langmuir isotherm.

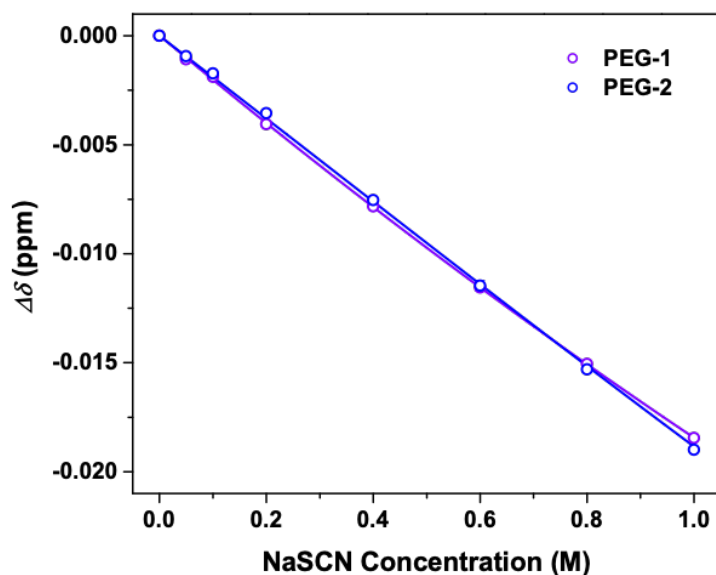


Figure 3-10: NaSCN-induced chemical shifts for PEG-1 and PEG-2. The solid curves are fits to the data using either Equation 3-3 or 3-4, for PEG-2 and PEG-1, respectively.

The data for PEG-2 could be fit to linear function described by Equation 3-3. PEG-1 on the other hand was best fit to a second-order polynomial described by Equation 3-4. We speculate that NaSCN is excluded from these locations and thus does not induce the deshielding non-linear effect described by the Langmuir isotherm. We note, however, that the hydroxyl end-group may complicate the interpretation of shifts in the methylene proton peak position.

$$\Delta\delta = ac_{\text{salt}}$$

Equation 3-3

$$\Delta\delta = ac_{\text{salt}} + bc_{\text{salt}}^2$$

Equation 3-4

In contrast to the central-most protons, the methyl terminal groups show a strikingly linear trend, regardless of chain length as summarized in Figure 3-11. Based on our interpretation of Equation 3-2, this indicates that no binding occurs at the end-group, while the salt ions adsorb readily to the central part of the chain. The nature of ion-polyether interactions is conserved with specific portions of the chain. Such a result, is consistent with the idea that the propensity of weakly hydrated anions to adsorb to surfaces is coupled to the curvature of the surface.

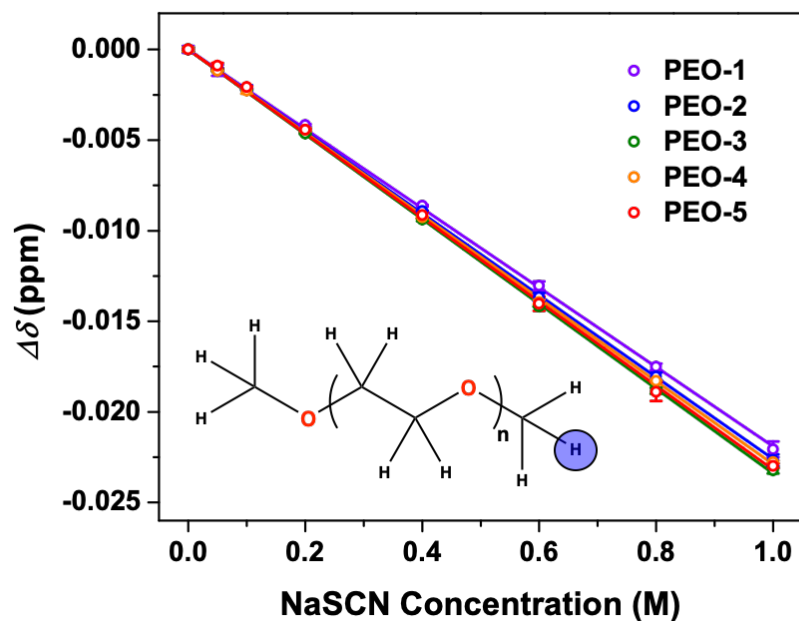


Figure 3-11: NaSCN-induced chemical shifts for protons located on the methyl termini of PEO-*n* mers.

In order to quantify this exclusion from the solute surface, we estimated the weakest measurable K_D value, which we denote as $K_{D,\text{limit}}$. The signature of anion binding in the ^1H NMR measurements is a saturable deshielding effect described by Langmuir isotherm contribution in

Equation **3-2**. As such, our approach to quantifying this contribution was to assess the shape of the residual chemical shift relative to a fit using a simple linear function. The slope of the linear contribution for the methyl termini data was $a \sim -0.0215$ ppm/M, while the average δ_{\max} parameter for the methylene protons was $\delta_{\max} = 0.003$ ppm. We generated a set of theoretical salt-induced chemical shifts using these parameters and a range of values for K_D , as shown in Figure **3-12A**. The data sets are offset for clarity. The nonlinearity for strong binding interactions, characterized by a low value of K_D , can be seen directly in chemical shift data; however, for weaker interactions the nonlinear deshielding effect becomes difficult to distinguish from the linear decrease. To test the limit of detection, each of these data sets was fit to linear function and the residual chemical shift was plotted in Figure **3-12B**. As can be seen, the low K_D data sets show clear deviation from a line, while the high K_D data sets are modeled quite well by a simple line.

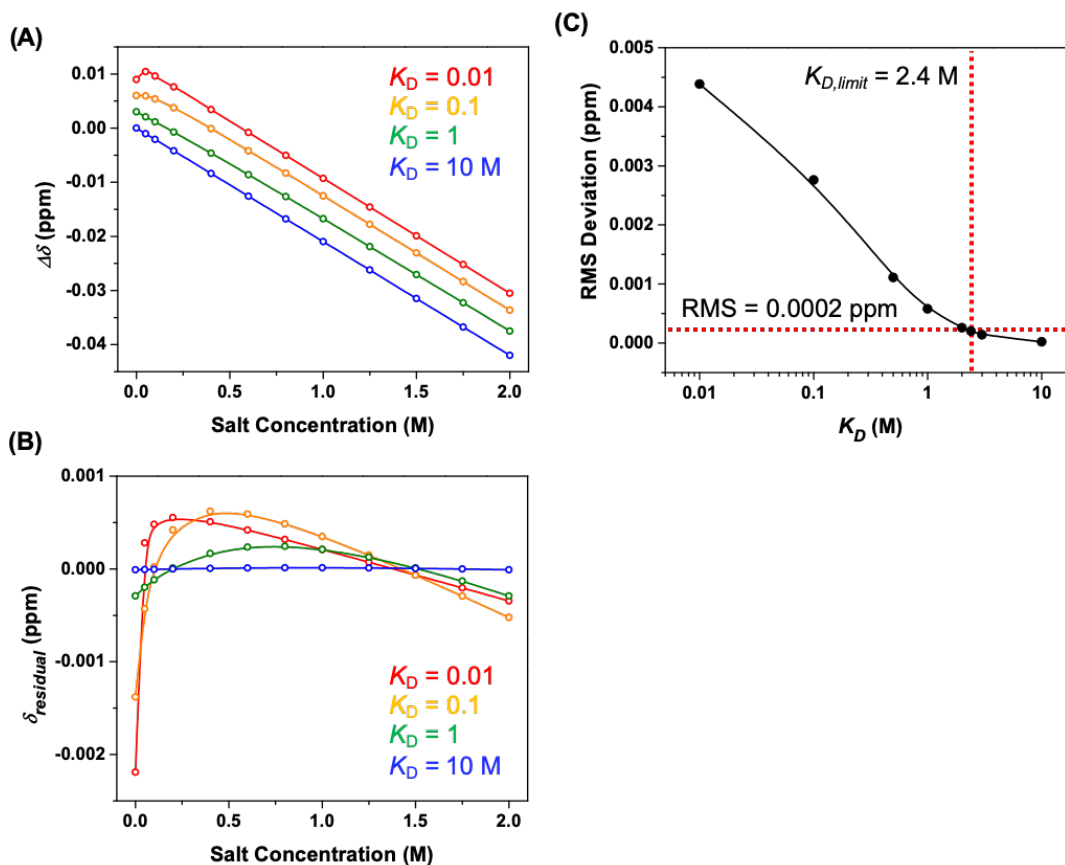


Figure 3-12: Estimates of the lower limit of detection for the Langmuir isotherm contribution to the salt-induced chemical shift effects. (A) Four theoretical titration curves simulated using parameters $a = -0.0215$ ppm M^{-1} , $\delta_{\text{max}} = 0.003$ ppm, and K_D values ranging from 0.01 M to 10 M. (B) The residual chemical shift effects relative to linear fits for the data in (A). (C) The RMSD calculated from residual chemical shifts plotted versus the K_D value used to generate the simulated data set. The dashed red lines in (C) mark the K_D value of 2.4 M that equaled the typical error of the chemical shift data in the experiments of 0.0002 ppm.

We assessed the limit of detection by calculating the average root mean squared deviation, *RMSD*, for each data set using Equation 3-5. The values of the *RMSD* were then plotted as a function of the K_D value in Figure 3-12C. From the experimental practice, a typical standard deviation for the chemical shift of a given conditions was ± 0.0002 ppm. The K_D value which yielded a *RMSD* equal to 0.0002 ppm was $K_{D, \text{limit}} = 2.4$ M. This value was assigned to the K_D for any proton that showed undetectable deshielding effect.

$$RMSD = \sqrt{\frac{\sum_{i=1}^{i=N} (\delta_{\text{sample},i} - \delta_{\text{model},i})^2}{N}}$$

Equation 3-5

The three parameters of Equation 3-2, including a , δ_{max} , and K_D , are plotted as a function of PEO and PEG chain length in Figure 3-13. The x-axis is plotted as the number of ethylene oxide monomer units on the chain, n .

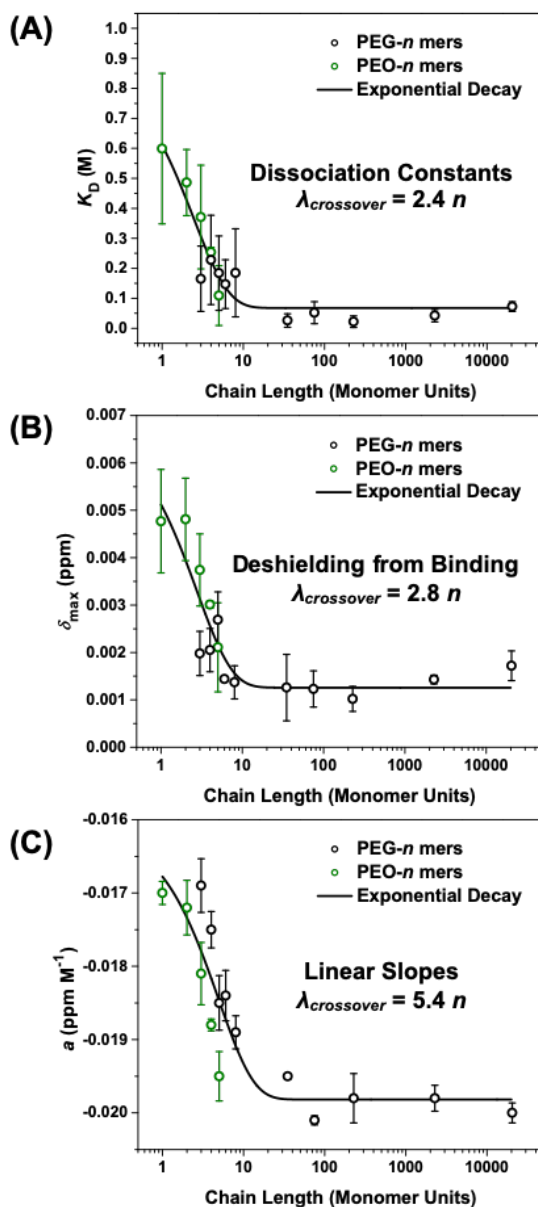


Figure 3-13: Summary of NaSCN-induced effects on the ^1H chemical shifts of the central-most methylene protons of PEO- n and PEG- n solutes obtained from fits to Equation 3-2. The fitted parameters are plotted as a function of chain length, including (A) K_D , (B) δ_{\max} , and (C) a . The data sets for PEG- n and PEO- n mers are plotted as black and green data points, respectively. The black curves are empirical fits to Equation 3-6. The crossover lengths obtained from these fits are provided on each panel.

The dark grey curves in Figure 3-13 are fits to the chain length dependence of each data set, which was modeled empirically to an exponential decay described by Equation 3-6, where as

the polyether chain is lengthened the ion-solute interaction parameters convert from a value relevant for an infinitely short molecule, y_0 , to that of an infinitely long chain, y_∞ , at a crossover length, λ . Above this length, the solute is large enough to facilitate favorable adsorption of SCN^- from the bulk solution.

$$y = y_0 \exp\left(\frac{-n}{\lambda}\right) + y_\infty \quad \text{Equation 3-6}$$

The crossover lengths obtained from the best fits to Equation 3-6 are summarized in Figure 3-11. Interestingly, the three data sets show a fairly similar crossover length at a monomer length of about a 3-mer. The length of a 3-mer should be expected to be near 1 nm, similar to the crossover predicted by Lum-Chandler-Weeks theory.¹⁷⁰

Consolidating the Heterogeneous Adsorption by Curvature of the Aliphatic Binding Site

In contrast to the central-most protons, the methyl terminal groups show a strikingly linear trend, regardless of chain length. Based on our interpretation of Equation 3-2, this indicates that no binding occurs at the end-group, while the salt ions adsorb readily to the central part of the chain. We provide the length dependent parameters of Equation 3-2 for the terminal methyl, end-group, penultimate groups of both PEO and PEG. Intriguingly, the nature of ion-polyether interactions is conserved with specific portions of the chain. Such a result, is consistent with the idea that the propensity of weakly hydrated anions to adsorb to surfaces is coupled to the curvature of the surface. The dissociation constant for each distinguishable position on each polymer is summarized in Table 3-2. This effect can be demonstrated by a detailed analysis of the ^1H NMR binding affinity results for the PEO-5 solute.

Table 3-2: Equilibrium dissociation constants, K_D , for the adsorption of NaSCN to polyether solutes. The data are organized by chain length and proximity to the termini.

		Middle	Penultimate	End (OH-Terminated)		End (CH ₃ -Terminated)		
		Mid CH ₂	Pen CH ₂	End CH ₂ -A	End CH ₂ -B	Term CH ₃	End CH ₂ -A	End CH ₂ -B
	Solute	K_D (M)	K_D (M)	K_D (M)	K_D (M)	K_D (M)	K_D (M)	K_D (M)
PEG- <i>n</i>	PEG-1	-	-	2.3 ± 1.2	-	-	-	-
	PEG-2	-	-	2.3 ± 1.2	2.3 ± 1.2	-	-	-
	PEG-3	-	0.18 ± 0.13	2.3 ± 1.2	2.3 ± 1.2	-	-	-
	PEG-4	-	0.21 ± 0.11	2.3 ± 1.2	2.3 ± 1.2	-	-	-
	PEG-5	-	0.20 ± 0.15	2.3 ± 1.2	2.3 ± 1.2	-	-	-
	PEG-6	-	0.23 ± 0.20	2.3 ± 1.2	2.3 ± 1.2	-	-	-
	PEG-8	0.26 ± 0.25	-	2.3 ± 1.2	2.3 ± 1.2	-	-	-
	PEG-35	0.02 ± 0.03	-	-	-	-	-	-
	PEG-75	0.27 ± 0.13	-	-	-	-	-	-
	PEG-227	0.02 ± 0.02	-	-	-	-	-	-
	PEG-2K	0.04 ± 0.02	-	-	-	-	-	-
PEG-20K	0.10 ± 0.05	-	-	-	-	-	-	
PEO- <i>n</i>	PEO-1	-	-	-	-	2.3 ± 1.2	0.52 ± 0.40	-
	PEO-2	-	-	-	-	2.3 ± 1.2	0.39 ± 0.09	0.34 ± 0.02
	PEO-3	-	0.37 ± 0.17	-	-	2.3 ± 1.2	0.24 ± 0.10	0.34 ± 0.08
	PEO-4	-	0.27 ± 0.03	-	-	2.3 ± 1.2	0.34 ± 0.18	0.38 ± 0.05
	PEO-5	0.11 ± 0.10	0.13 ± 0.10	-	-	2.3 ± 1.2	0.06 ± 0.06	0.13 ± 0.10
	Average	0.12 ± 0.06	0.23 ± 0.10	2.3 ± 0.64		2.3 ± 1.0	0.30 ± 0.14	

As with the previous measurements, the interaction of SCN⁻ with polyethers was monitored by changes in the chemical shift, $\Delta\delta$, of a solute's aliphatic protons with salt concentration, c_{salt} . A color-coded key for the identity of specific protons for PEO-5 is provided in Figure 3-14A and the corresponding $\Delta\delta$ values as a function of salt concentration are given in Figure 3-14B. The chemical shift of the central methylene protons, plotted as red data points, and the terminal methyl protons, plotted as blue data points, both become more negative with increasing NaSCN concentration. At the termini, this salt-induced shift was well characterized by a linear slope, α , as modeled by the first term in Equation 3-2. On the other hand, the central methylene protons showed significant deviation from linearity below 0.1 M NaSCN. This nonlinearity was modeled by a Langmuir isotherm, the second term in Equation 3-2, which quantified the small, saturable increase in the value of the chemical shift as SCN⁻ bound directly to the PEO-5 chain. The strength of the interaction was quantified by a dissociation constant, $K_D = 0.1$ M. Analysis of the methylene protons on the end and penultimate monomer units, as shown

in the green and orange data, showed similar behavior to the central monomer. These K_D values were converted to a free energy of adsorption using Equation 3-7.

$$\Delta G_{\text{ads}} = RT \ln(K_D) \quad \text{Equation 3-7}$$

The ΔG_{ads} measurements of all of the protons that could be distinguished in the ^1H NMR spectra, except PEG-1 and PEG-2, are plotted in Figure 3-14C. Here, the data are organized based on their location on the chain, rather than the total length of the chain. This analysis revealed a link between binding affinity and the proximity of the binding site to the termini of the chain, as illustrated schematically in Figure 3-14A. As can be seen, SCN^- was repelled from the termini, $K_D > 2.4 \text{ M}$, but attracted to the internal regions of the solute surface where $K_D \sim 0.1 \text{ M}$. Collectively, these results suggest that the adsorption of SCN^- to the polyether chain is heterogeneous with tighter binding in the middle and weaker binding near the ends. This is the case in spite of the fact that the monomer chemistry is essentially identical at each position. An important difference, however, is that the local surface curvature near the termini is large relative to the center of the chain. In fact, the internal segments of the chain should bare resemblance to a macroscopic interface due to the flat or concave curvature along the direction of the chain.

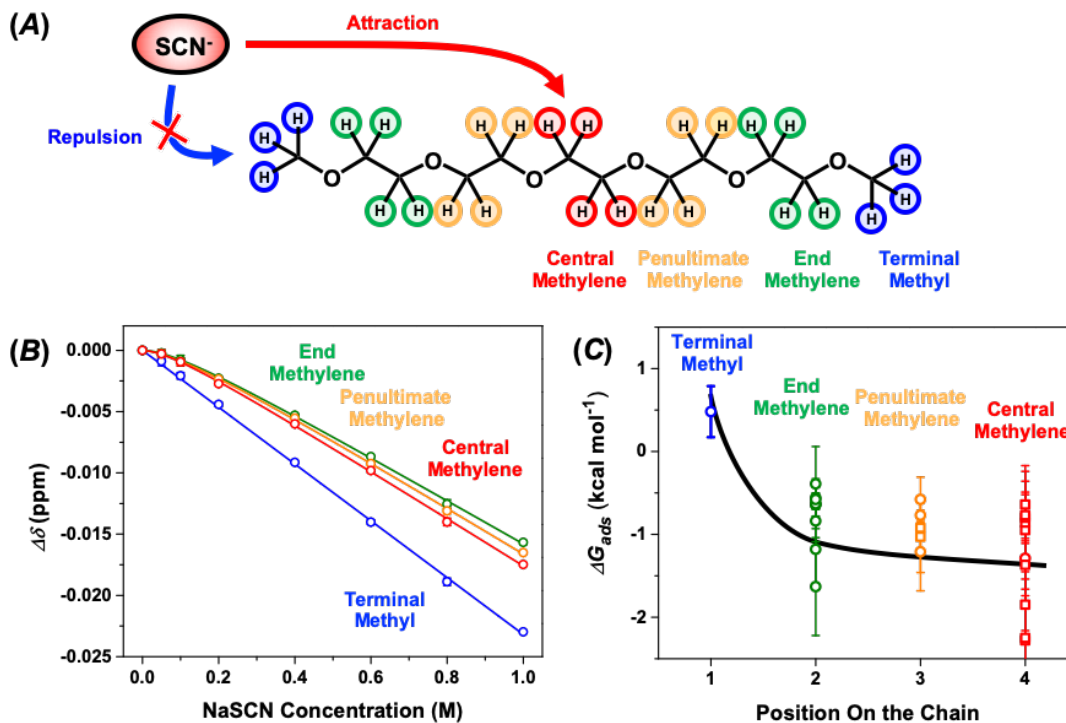


Figure 3-14: The interaction of SCN^- with polyether chains. (A) The bond line structure of PEO-5 and schematic of heterogeneous SCN^- adsorption. (B) The NaSCN-induced chemical shifts for the central methylene (red data points), penultimate methylene (orange data points), and end methylene (green data points), and terminal methyl (blue data points) protons of PEO-5 measured by ^1H NMR spectroscopy. The solid lines in (B) are fits to Equation 3-2. The location of each proton is circled in (A). (C) The free energy of adsorption for SCN^- -polymer interactions as a function of position along the chain. The black curve is a guide to the eye.

Measuring Water Structure by Vibrational Spectroscopy

Surface curvature is expected to influence the structure of water, as discussed earlier in this chapter. In order to test if these effects underly the apparent correlation of binding affinity with surface curvature, we devised experiments to probe the structure of water in the solute hydration shell. In particular, we employed vibrational spectroscopy to measure frequency required to make the OH bond of a water molecule stretch. This vibrational mode is depicted schematically in Figure 3-15A, where the OH bond is illustrated as a spring. At room

temperature, most of the molecules are found in the ground state, which has an average OH bond length of r_0 . With sufficient energy, typically in the infrared, IR, radiation wavelengths, this vibration can be excited into a state where the average bond length is extended to r_1 . The energy difference between these two transitions is dictated by the free energy of the oscillator as a function of the average bond length, r_{OH} , as illustrated in Figure **3-15B**. The oscillator can exist in distinct states defined by the horizontal black lines. In Raman spectroscopy, the energy difference between the ground and excited state is measured by shining a laser onto a sample and collecting the light that is scattered, as depicted in Figure **3-15C**. Most of the light is scattered off with the same energy, known as Rayleigh scattering; however, a small percentage of the light is scattered with less energy. These red-shifted photons are generated by Raman scattering. Remarkably, the energy difference between the laser and Raman photons is equal to the energy required to induce the OH stretch vibration. This idea is depicted schematically in by the green and red arrows in the Figure **3-15B**. The laser energy is much larger than the OH stretch energy and instantaneous excites the oscillator into a virtual state, shown as a dashed horizontal line in Figure **3-15B**. The photon induces vibrations, which instantaneously emit a photon with an energy with less energy than the laser light. By plotting the number of photons as a function of their energy, we obtain a spectrum of the vibrational modes of a sample. The Raman spectrum for liquid water is provided in Figure **3-15D**.

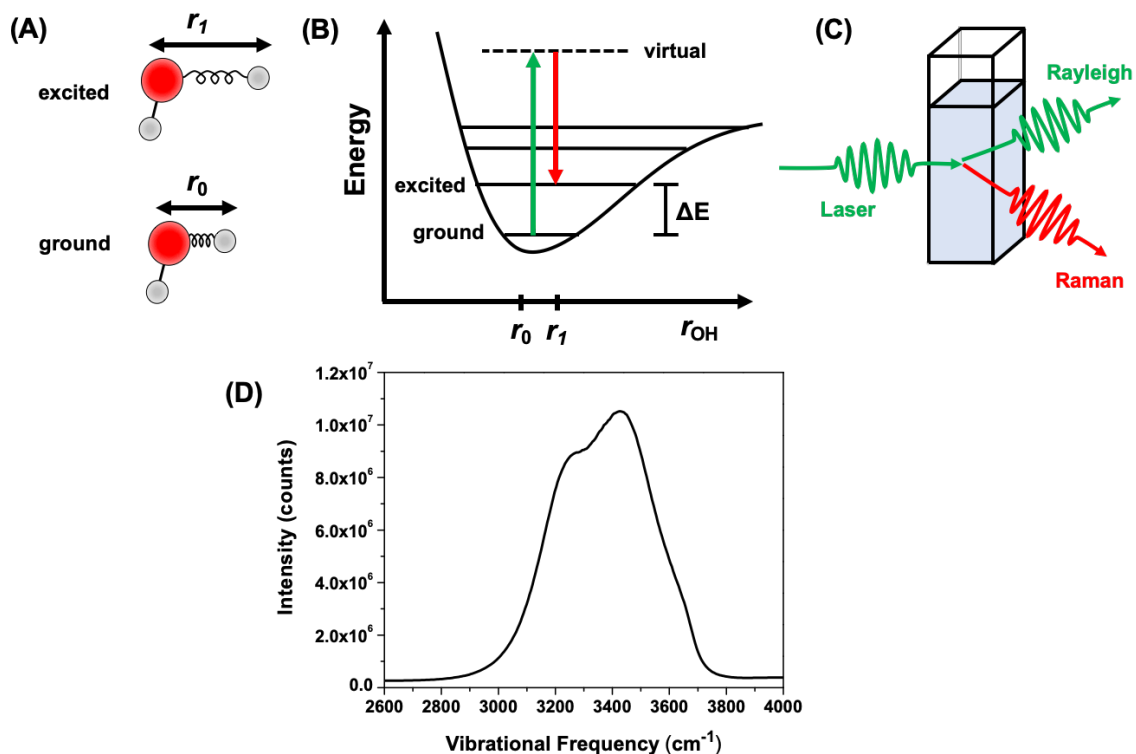


Figure 3-15: Basics of vibrational spectroscopy for the OH stretch of water. (A) Schematic illustration of the ground and excited states of the OH stretching vibration. The average bond length, r_{OH} , extends when the molecule is excited. (B) Energy landscape as a function of OH bond length. The Raman experiment is illustrated by the colored vertical arrows, which excite the molecules into a virtual state of very high energy that instantaneously scatter as a red-shifted photon due to the loss of energy via the vibration. (C) Schematic illustration of the experimental setup, where a laser is directed toward a sample and the scattered light is analyzed. (D) Raman spectrum of pure water at 20 °C.

Raman spectra were collected on a home-built instrument. The light source was the 514.5 nm line of a mixed Ar-Kr gas laser (2018-RM; Spectra-Physics, Mountain View, CA). The laser light was passed through a band-pass filter to spectrally narrow the laser line (FF01-514/3-25; Semrock, Rochester, NY). Moreover, the power and polarization were controlled by passing the light through a two half wave plates (1200-15; CVI Laser, Albuquerque, NM) separated by a beam splitter (CCM1-PDBS252; Thorlabs, Newton, NJ). The polarized light was then directed toward the sample using a series of high reflective mirrors (BB1-E02P; Thorlabs, Newton, NJ) and a 514 nm long-pass filter (LP02-514RE-25; Semrock, Rochester, NY). The laser light was

passed through a long working distance 10x objective (LU Plan, WD = 17.3mm, NA = 0.3; Nikon, Japan) to focus the laser to the center of a 1 cm quartz cuvette (5061-3387; Agilent Technologies) held in a temperature-controlled jacket (Versa 20; Quantum Northwest, Liberty Lake, WA).

The Raman signal was collected in a backscattering geometry through the same objective used to focus laser onto the sample. The backscattered light followed the reverse path of the incident light. The Stokes shifted Raman signal, however, passed through two of the long-pass filters, while the laser line was rejected. The Raman signal was then focused by a lens (AC254-050-A; Thorlabs, Newton, NJ) onto a custom 1x15 array fiber optics bundle (FiberTech-RoMack, Williamsburg, VA), which led the signal to the spectrometer (Isoplan-SCT320; Princeton Instruments, Trenton, NJ). The spectrometer was equipped with a 300 g/mm grating that spread the Raman signal onto a liquid nitrogen cooled 100x1340 CCD array camera (Pylon-100BR; Princeton Instruments, Trenton, NJ).

Unpolarized spectra of polyether solutions were collected using the 514.5 nm mode. The power of the incident light at the sample stage was adjusted to 50 mW. The exposure time for the CCD camera was adjusted to ensure that the signal did not saturate the detector (0.01-0.1 s) and number of exposures were adjusted accordingly for a total collection time of 5 min. Each solution was measured for a collection time of 5 min. Two spectra were recorded for each sample.

The structure of water has been investigated by vibrational spectroscopy since the 1960s. IR and Raman spectroscopies provide convenient measurements of the OH stretching bands. As can be seen in Figure **3-15D**, however, the spectrum of liquid water does not exhibit a gaussian shape. Rather, the spectrum appears to display at least two or three peaks. It is an understatement to say that researchers have argued over the interpretation of these peaks. The two most common interpretations are (1) that the peaks represent distinct populations of water hydrogen bonding networks and (2) that the multiple peaks are an artifact of coupling between the OH stretch and

HOH bending mode of water.^{171–175} Herein, we interpret the spectrum based on the population model. This interpretation is strongly supported by the temperature dependence of the Raman spectrum of pure water, as shown in Figure 3-16. The Raman spectra in Figure 3-16A are normalized to the area under the curve between 2600 and 3800 cm^{-1} .

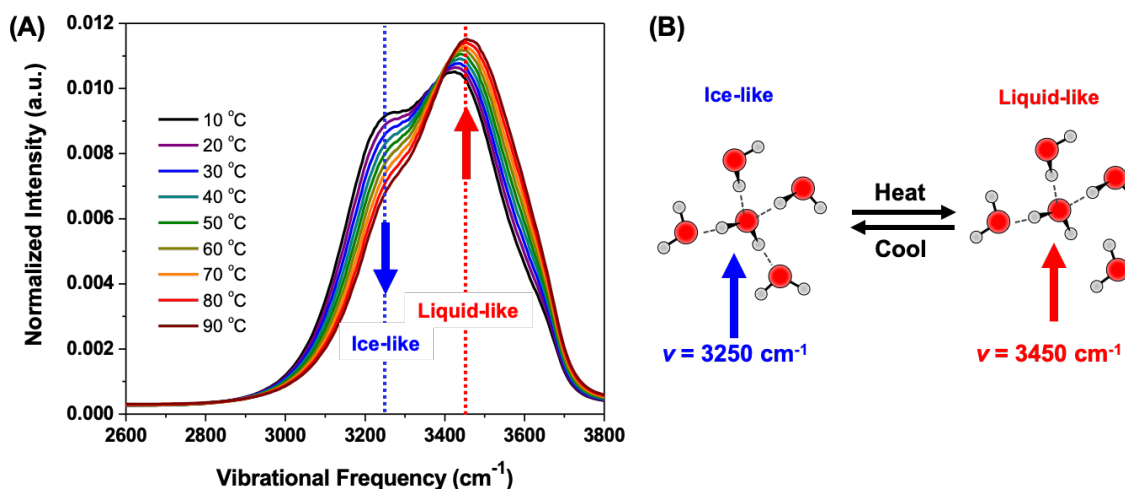


Figure 3-16. Two-state model interpretation for the Raman spectrum of liquid water. (A) Raman spectra of water measured as a function of temperature. The two peaks of the spectrum are labeled with dashed vertical lines. (B) Schematic illustration of the hydrogen bonding structures assigned to the two peaks of the Raman spectrum. The water molecule indicated by the colored arrows are intended to give rise to specific vibrational frequencies.

From 10 to 90 $^{\circ}\text{C}$, the Raman spectrum of water is dominated by two peaks, one near 3250 cm^{-1} and another at 3450 cm^{-1} . Upon increasing the temperature, the 3250 cm^{-1} peak decreases in intensity, while the 3450 cm^{-1} grows. This is consistent with the notion that one population is in equilibrium with another, a so-called two-state model. The two-state model assigns the low frequency peak to an ice-like hydrogen bonding population, while the higher frequency peak is attributed to a disordered, liquid-like population. The structure of these two states are illustrated schematically in Figure 3-16B. The two-state model is further supported by the fact that the spectra display an isosbestic point, near 3390 cm^{-1} , where all of the temperature-

dependent spectra appear to cross one another. The general idea that the frequency of the OH stretch depends on its local hydrogen bonding environment is consistent with gas phase spectra, which resonates at higher frequency than solid forms of water.^{176,177} Theoretical arguments attribute the red shift in the condensed phases to the transfer of electron density from the oxygen atom of the hydrogen bond acceptor into the low unoccupied molecular antibonding orbital of the hydrogen bond donor.^{178,179} This should weaken the effective bond order of the OH stretch leading to a decrease in the vibrational frequency.

Our hypothesis proposes that specific structural characteristics of the hydration shell modulate the affinity of weakly hydrated anions to bind to aliphatic surfaces. In order to study this, we need to remove the response of the bulk water, illustrated by the faded water molecules in Figure 3-17A. A major limitation to the use of Raman spectroscopy to study water at interfaces is the fact that most of the water in the sample is bulk. As such, the spectral characteristics of water in the hydration shells of molecules is buried in the spectrum. This idea is depicted in Figure 3-17B, which compares the spectrum of pure water to a solution containing 0.5 M PEG-1. As can be seen, the PEG-1 spectrum exhibits new sharp features at lower frequency that correspond to the CH stretching modes. More importantly, however, the OH stretching bands of the PEG-1 solution are nearly identical to the pure liquid. Indeed, the bands only show a small decrease upon the addition of the solute.

We expect the solution spectrum to be comprised of two major features: (1) bulk water and (2) solute-correlated vibrations. The latter should contain vibrational modes of the solute itself, like the sharp CH stretches, as well as any water molecules whose vibration is perturbed due to interaction with the solute. With this basic idea, we performed a “scaled” subtraction of the bulk water spectrum from the solution. Specifically, the raw Raman spectra were analyzed in IgorPro using a multivariate curve resolution algorithm generously provided by Dor Ben-Amotz (Purdue University, West Lafayette, IN).¹¹⁰ Each spectrum was referenced to a neat water

spectrum collected within 1 hour of the sample spectrum. Second order backgrounds were employed during the MCR analysis. In some cases, a third order function was necessary to fit a broad signal observed for long polymers. Unfortunately, the spectrum for the PEO-5 mer had significant “background” signal, which we speculate was from a fluorescent impurity. The MCR analysis yield the solute-correlated spectrum, which is a minimum area difference of a solution and a solvent spectrum. Each spectrum was normalized to the area under the CH stretching bands. MCR analysis allows the Raman spectrum of a solution to be separated into components corresponding to the solute hydration shell and the bulk water, as depicted schematically in 3-17A.

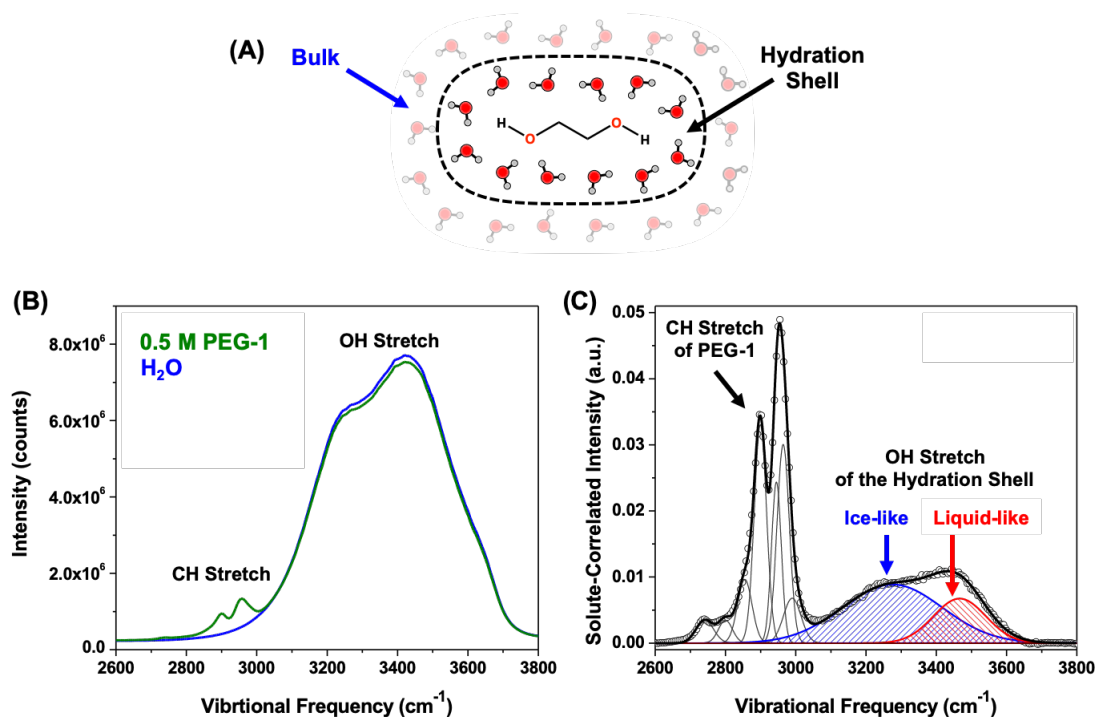


Figure 3-17: Basics of hydration shell spectroscopy by Raman-multivariate curve resolution. (A) Schematic illustration of PEG-1, its hydration shell, and bulk water residing beyond the first layer of water. (B) Raman spectra of pure water and a solution of 0.5 M PEG-1. (C) The solute-correlated spectrum of PEG-1 obtained via Raman-MCR. The black circles are the data points, while the solid black curve is the sum of a fit to multiple gaussian components. The CH stretch gaussians are colored in grey, while the two OH stretching modes are colored in blue or red to mark the 3250 cm⁻¹ and 3450 cm⁻¹, respectively.

The result of the MCR analysis is profound. The resulting SC spectrum contains the CH stretches of PEG-1 and two broad bands corresponding to the OH stretch. Based on the interpretation provided above, these OH stretches should be dominated by water molecules in the hydration shell. As can be seen, these water molecules also exhibit a two peak feature, corresponding to ice-like and liquid-like hydrogen bonding populations. In order to quantify the amount of these two populations the SC spectra were fit to a sum of gaussians using OriginLab to extract the area under the distinct OH stretch peaks, described by Equation 3-8. Here the intensity of the SC spectrum, I , as function of vibrational frequency, ν , is model by a baseline intensity, I_0 , and sum of n gaussian peaks, each of which are defined by a width parameter, w_i , a center frequency, $\nu_{c,i}$, and an area under the peak, A_i . Solute-correlated spectra and Gaussian fit parameters for the entire set of polyether solutes are summarized in Appendix A.

$$I = I_0 + \sum_{i=1}^{i=n} \frac{A_i}{w_i \sqrt{\pi/2}} \exp\left(\frac{-2(\nu - \nu_{c,i})^2}{w_i^2}\right) \quad \text{Equation 3-8}$$

Hydration Shell Water Structure for Polyethers of Varying Chain Length

The mechanism proposed in the introduction of this chapter postulates that the adsorption of weakly hydrated anions to interfaces should be modulated by the distinct hydration of curved versus flat surfaces. As such, Raman-MCR spectroscopy was employed to probe the structure of the polyether hydration shells.¹⁸⁰ The hydration shell spectrum of PEO-1, provided in Figure 3-18A, displayed narrow CH stretch bands at $\nu = 2600\text{-}3000 \text{ cm}^{-1}$ from the solute and broad OH stretch peaks at $\nu = 3000\text{-}3600 \text{ cm}^{-1}$ from water in the hydration shell. As described in the previous section, the OH stretch region was fit to two Gaussian bands, including a peak at 3250

cm^{-1} assigned to tetrahedrally ordered water molecules, and a peak around 3450 cm^{-1} corresponding to water molecules with broken hydrogen bonds.^{171,172,181–183} Similar experiments were performed on PEO-2k. The spectrum of this long polymer is dominated by the CH stretching modes of the methylene CH stretches. Moreover, the features of the OH stretches in the hydration shell appear different than its small molecule counterpart. In particular, the 3250 cm^{-1} peak decreased in intensity relative to the 3450 cm^{-1} .

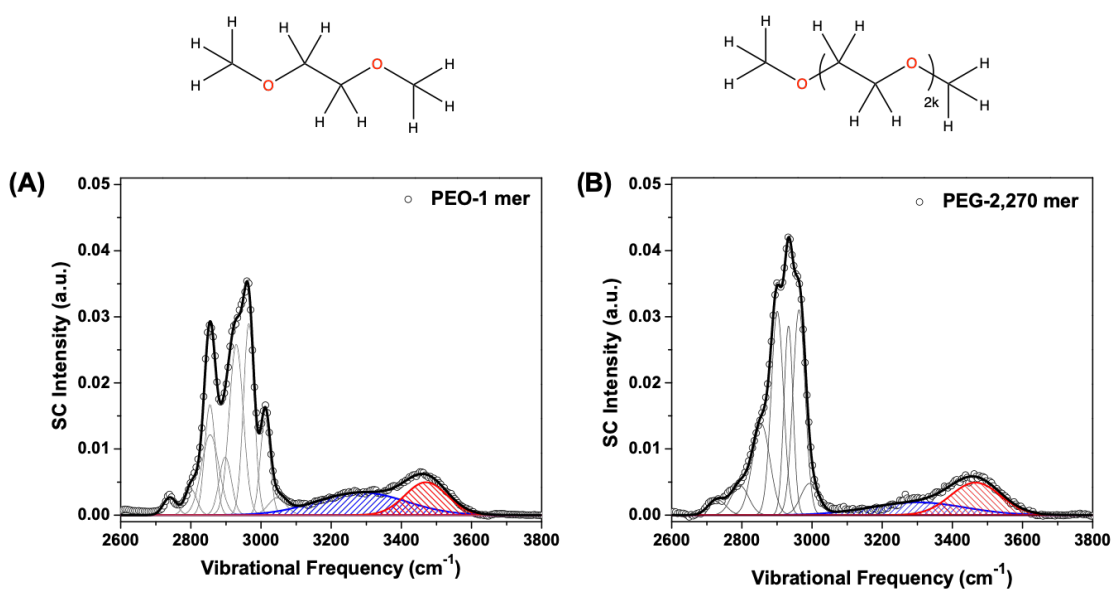


Figure 3-18: Solute correlated spectrum for (A) PEO-1 and (B) PEO-20k. Each spectrum is normalized to the area under the CH stretch bands.

The Raman-MCR measurements for the entire set of polyether solutes revealed a chain length induced structural transformation of the hydration shell. A set of spectra are shown in Figure 3-19A, where the data have been normalized to the intensity of the 3450 cm^{-1} peak. When plotted this way, the relative changes in the 3250 cm^{-1} can be easily seen.

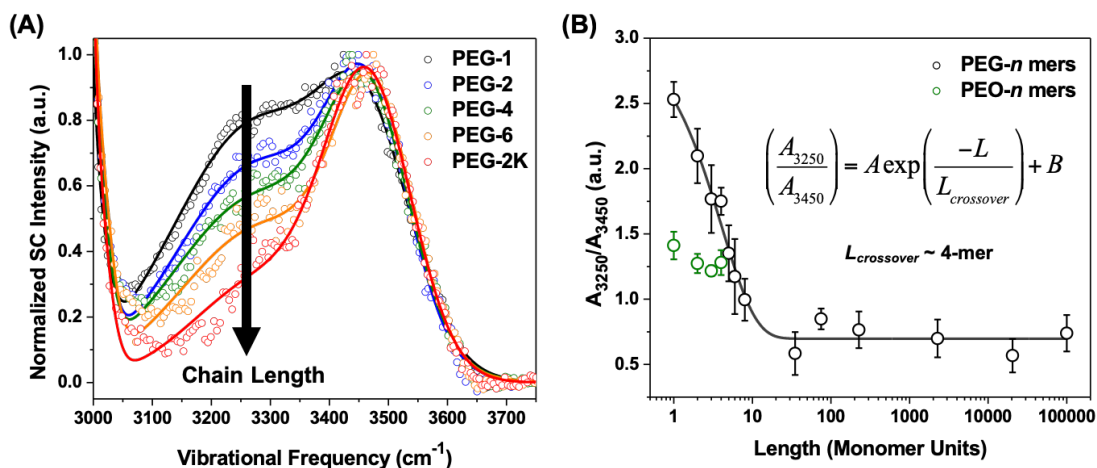


Figure 3-19: Chain length dependence of the OH stretch bands in the hydration shells of polyethers. (A) Solute correlated spectra for several PEG- n and PEO- n mers. The data have been normalized so that the intensity at 3450 cm^{-1} is equal to 1. The open circles are the measured spectra, while the solid curves are fits to Equation 3-8. (B) The ratio of the two OH stretch populations as a function of chain length. The data sets for the PEG- n and PEO- n mers are plotted in black and green, respectively. The solid black curve in (B) is a fit to Equation 3-6.

The ratio of ordered-to-disordered water, R , in the hydration shell was estimated by dividing the amplitude of the ordered peak by the amplitude of the disordered peak, as described by Equation 3-8.

$$R = \frac{A_{3250}}{A_{3450}} \quad \text{Equation 3-8}$$

The value of R decreased with chain length as shown in Figure 3-19B, suggesting a disruption of tetrahedral water structure at the center of the chain. Indeed, the hydration shells of long chains should be dominated by the water molecules solvating central groups, rather than the termini, since they constitute a majority of the solvent accessible surface area, *SASA*. The values of R exhibited crossover of $\lambda \sim 4$ monomer units, respectively, which bear remarkable similarity to those determined for the anion-polymer interactions parameters presented in Figure 3-13.

The differences in hydration shell architectures for the -OH and -CH₃ terminated polyethers are remarkably different, as can be seen from Figure 3-19. Indeed, one should expect the hydrogen bonding networks to differ for surfaces that can donate hydrogen bonds to the solvent, like PEG-*n* mers, versus those that cannot, like PEO-*n* mers. As such, using the two data sets complicates the surface curvature investigation. In order to study the effects of curvature we focus on the hydration shell measurements of the PEO-*n* mers. Although the difference between the monomer and the polymer is smaller than in the PEG-*n* mers, there is a clear difference between the ratio of the two OH stretch populations between PEO-1 and PEO-20k. Indeed, Figure 3-20 displays a comparison of these two spectra, which have been normalized so the intensity at 3450 cm⁻¹ is equal to 1.

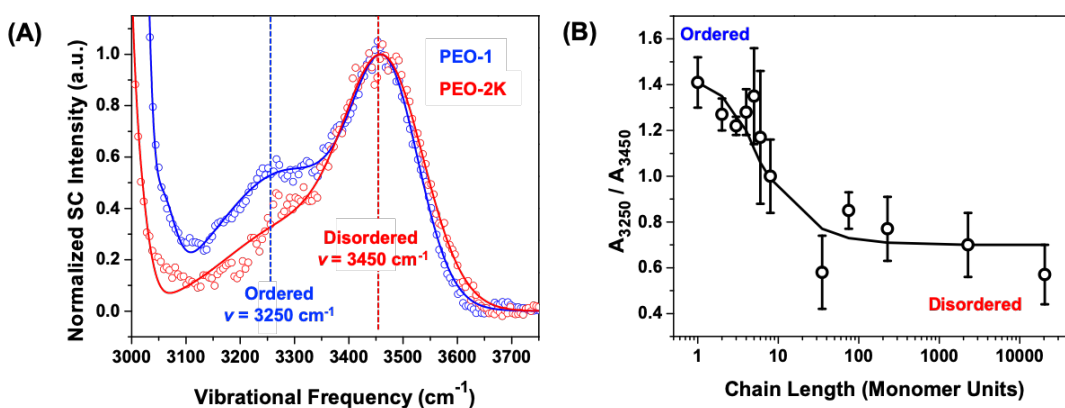


Figure 3-20: Chain length dependence of the OH stretch in the hydration shell of PEO-*n* mers. (A) Solute-correlated spectra for PEO-1 in blue and PEO-20k in red. The two OH stretch bands are marked with dashed vertical lines and labeled with their structure and frequency. (B) Ratio of the ordered-to-disordered areas of the two populations. The data are shown for PEO-1 to PEO-4 and then combined with the PEG-4 to PEG-227. The longest polymer chains were PEO-2k and PEO-20k. The solid black curve in (B) is a fit to the segmentation model described by Equation 3-9.

The ¹H NMR binding affinity measurements suggest that the surfaces of the methyl termini are distinct from the internal methylene-studded segments of the chain. Moreover, there are small differences between the binding affinity of SCN⁻ to the end, penultimate, and central

monomer units. In an effort to connect these results with the changes in the hydrogen bonding structures in the hydration shells measurements, we developed a simple model for the length dependence of the measured R values. The idea is that for a given solute, the measured R value is a sum of contributions from the 4 different portions of the surface. The contribution of these surfaces to the total signal should be proportional to the fraction of the surface. This idea is described by Equation 3-9, where the measured ratio, R , is a sum of the individual ratio contributions of different surface segments, R_i , that are weighted by the fraction of surface coverage determined by the solvent accessible surface area of a specific segment, $SASA_i$, over the total, $SASA_{total}$.

$$R = \sum_{i=1}^{i=n} R_i \frac{SASA_i}{SASA_{total}} \quad \text{Equation 3-9}$$

Considerable efforts were made to constrain the fits to Equation 3-9 considering that there are many parameters and only 12 data points. Our approach was to first estimate the $SASA$ by the number of protons and lone pairs that correspond to a specific segment of the solute surface. For PEO-5 for example, a methyl termini would be assigned a weight of 4, to account for the 3 for the protons of the methyl group and 1 lone pair of the neighboring ether oxygen. Since there are two termini per PEO-5, the $SASA_{termini}$ would be assigned a value of 8. Each monomer unit was assigned a value of 6, to account for the 4 methylene protons and 1 lone pair from each of the flanking ether oxygen atoms. As such, the $SASA$ values were 12, 12, and 6 for the end, penultimate and central groups of PEO-5. The total $SASA$ is the sum of these simple counting exercises, 38. The solid black line in Figure 3-20B appears choppy because the values of $SASA$ were only calculated for the solute lengths employed in the study. A more sophisticated model would be required to interpolate the data between each chain length. The segmentation model is

illustrated schematically in Figure 3-21A. By calculating these *SASA* contributions for each solute, we could begin testing the R_i values for specific segments.

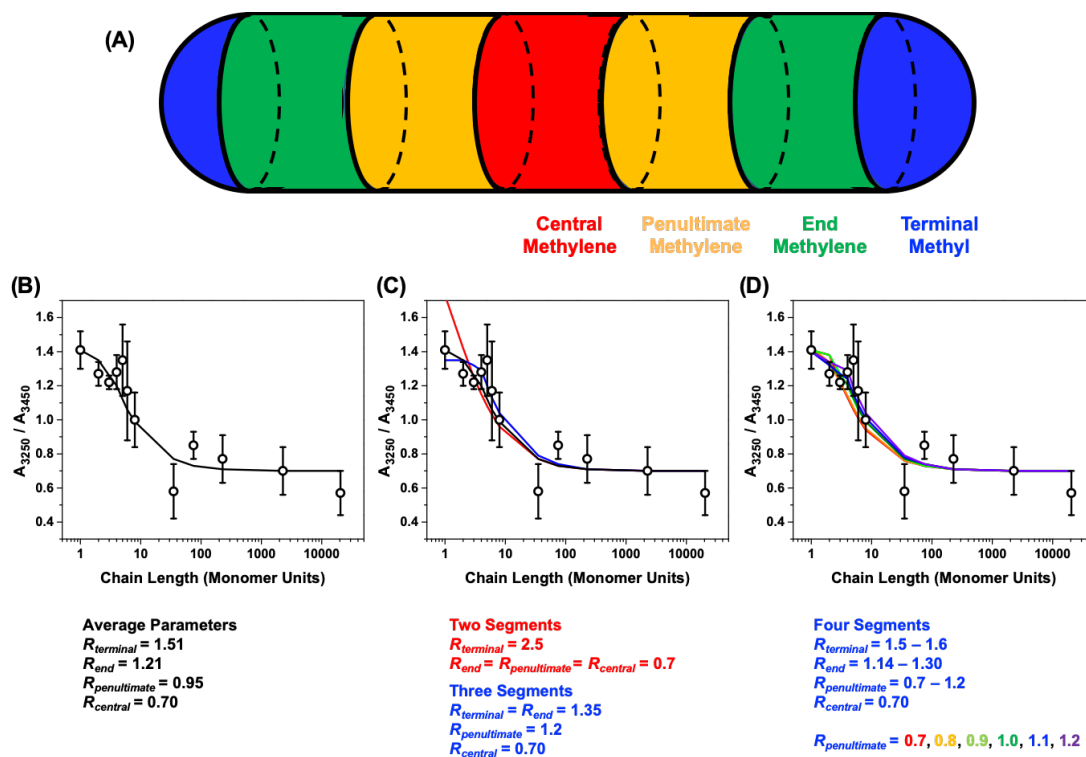


Figure 3-21: Fit assessment for the segmentation model describing the length dependence the OH stretch bands in the hydration shells of polyether solutes. (A) Schematic illustration of the segmentation model, where the PEO-5 solute has been segmented into four types of surfaces. The ratio of ordered-to-disordered peak areas is plotted as a function of chain length in (B-D). The black curve is the best fit to the four segment model, shown in (B-D) for comparison. The fits to two segments and three segments models are portrayed in (C). Lastly, in (D) the comparison of various fits to the four segments model using fixed parameters for the central and penultimate groups. The averages of these fits were used in the black curves shown in (B-D).

The best fit to Equation 3-9 using four different segments is displayed in Figure 3-21B. Moreover, the best fit parameters are summarized below the panel. The data sets were not well described by two segments, including the methyl termini and internal methylenes, as shown in the solid red curve of Figure 21-C. The three segment model does substantially better; however, the fit misses the data for small molecules. These subtleties can be captured by the four segment model; however, there are many solutions for the R_i values that can fit the data. Our approach was

to fit the values of the R_{central} to 0.7 because this is equal to value exhibited by long polymer chains. Next, we tested the best fitting parameters for R_{termini} and R_{end} for fixed values of $R_{\text{penultimate}}$. When $R_{\text{penultimate}}$ was varied from 0.7 to 1.2, the values of R_{termini} ranged from 1.5 to 1.6, while R_{end} ranged from 1.4 to 1.30. All of the fits model the data well. So we chose to use the average values of R_{termini} , R_{end} , and $R_{\text{penultimate}}$, which again were used to generate the black curves in Figure 3-21B.

Surface Curvature Connects Hydrophobicity and Hofmeister Chemistry

In order to quantify the relationship between the adsorption affinity and water structure, we plotted the free energy of adsorption versus the fraction of ordered water, as shown in Figure 3-22. The data were grouped according to the four binding site model, including the middle, penultimate, end, and termini. The end units for the OH-terminated are omitted from this correlation to avoid conflation of surface curvature and hydrogen bonding effects. The x-axis values were grouped based on the four segments model to the hydration shell ratio measurements. The error bars were assessed by the ranges of values used in Figure 3-21C. The y-axis data were grouped similarly to the plot shown in Figure 3-14C, which categorizes the binding site based on its proximity to the termini. The ΔG_{ads} values show was correlated with R in Figure 3-22. The hot spots for SCN^- adsorption occurred at aliphatic sites near the middle of the PEO-5 chain exhibiting zero (flat) or even negative (concave) curvature along the direction of the chain.

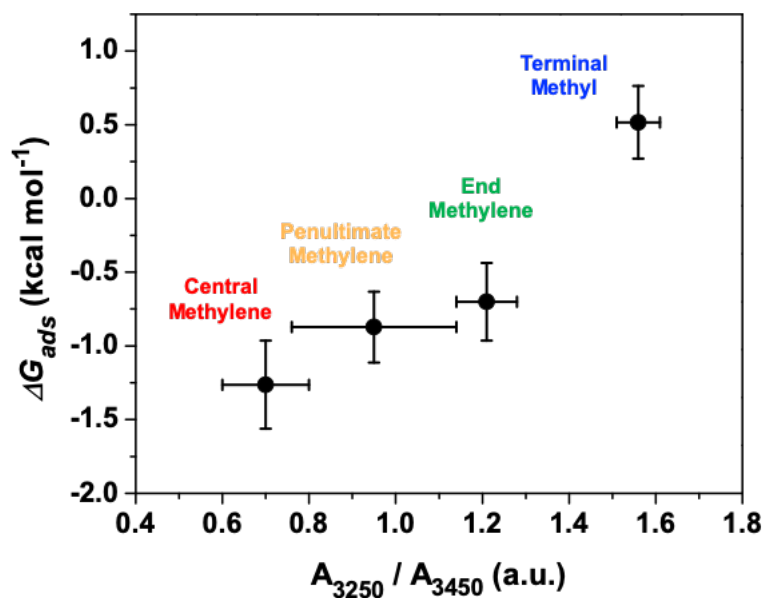


Figure 3-22: Correlation of the adsorption free energies measured via ^1H NMR spectroscopy and the ratio of ordered-to-disordered water structures near the surface of specific segments of polyether solutes. The data are grouped based on the four-segment model and labeled accordingly.

This result demonstrates that broken hydrogen bonds in the hydration shells of flatter regions along the polymer surface were readily displaced by weakly hydrated anions. On the other hand, the positive curvature (convex) of the termini and monomers facilitates tetrahedral hydrogen bonding networks, which in turn inhibits the adsorption of SCN^- . These ideas are captured in Figure 3-23, which illustrates the coupling of water structure and binding affinity based on the local curvature of the solute's surface.

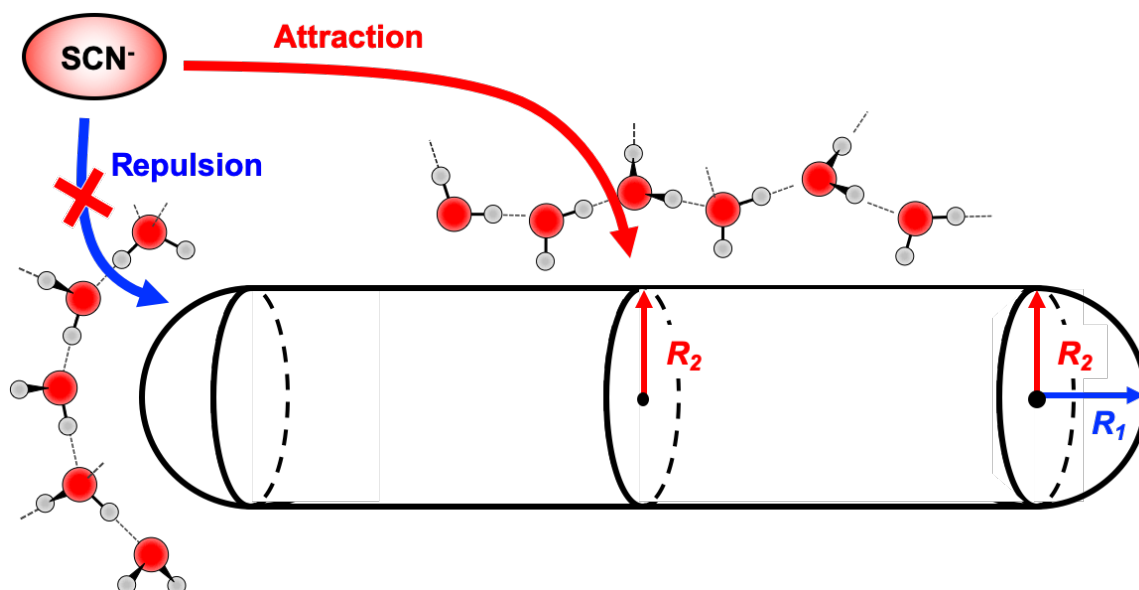


Figure 3-23: Schematic illustration of the mechanism for the surface curvature effect.

The mechanisms for the ion-specific effects of weakly hydrated anions in aqueous solutions have eluded researchers for over a century. In part, the confusion persists because the binding affinity of these anions varies substantially for molecular versus macroscopic surfaces. In this chapter, the systematic investigation of solutions containing NaSCN and polyethers of varying chain length revealed the critical role of surface topology in direct anion-solute interactions. ^1H NMR spectroscopy shows that the adsorption of SCN^- to the methylene backbone of polymers is enhanced relative to the identical chemical site on a monomer. No binding occurs at the methyl termini, regardless of the solute size. These results provide direct evidence for the attraction of weakly hydrated anions to flat portions of solute surfaces and repulsion from regions exhibiting positive curvature. Raman-MCR experiments suggest that the molecular origin of this surface curvature effect arises from the distinct hydrogen bonding of water near curved or flat interfaces. Remarkably, it was found that the driving force for SCN^- adsorption to a solute surface is modulated by the degree of tetrahedral ordering in the solute hydration layer. This work

demonstrates that weakly hydrated anions bind to interfaces at sites where the hydration shell is disordered and readily displaced upon anion adsorption.

The relationship between surface curvature and interfacial water structure is central to the hydrophobic effect. Indeed, small aliphatic molecules are more soluble than their larger counterparts, despite their chemical similarity. Stillinger envisioned that bulk-like hydrogen bonding of water should be preserved around small solutes, but disrupted near the surfaces of large solutes, which resemble the air/water interface. Quantitative theories and computer simulations predict a crossover between these two regimes at nanometer length scales.^{160,164} The vibrational hydration shell spectra of *n*-alcohols as a function of chain length and the solvation free energy of polymers with differently sized aromatic side chains both exhibit signatures of the predicted nanometer length scale.^{100,159} Comparison of the studies on small hydrophobic solutes with those at flat interfaces also support the notion of distinct interfacial water structures. Recent simulations have also advanced the knowledge of hydrogen bonding and dynamics at interfaces. Significantly, this work connects the consequences of surface curvature on water structure to the interactions at play in Hofmeister chemistry. Indeed, the chain length dependence of SCN⁻ adsorption displays a crossover length near 3 monomer units. The water structure in the hydration shells also displays an order-disorder transition at a similar length scale, ~ 4 monomer units. The crossover lengths obtained from the hydration shell metrics are larger because they represent an average over the entire solute surface, whereas the anion adsorption parameters report on local interactions for specific sites along the chain.

Such results are consistent with the idea that the center of the chain can be modeled as a cylinder, while the termini are modeled as half spheres as depicted in Figure 3-23. As such, the termini are curved about two axes while the center is curved about just one. Water is more tetrahedrally ordered near the end groups, which have positive curvature. Along the center of the chain, however, the surface is locally flatter or even concave, which restricts the formation of

bulk-like hydrogen bonding. It is at these sites of broken hydrogen bonding where the strongest affinity of SCN^- occurs. The correlation between ion affinity and the ordering of the hydration shell is evident from Figure 3-22. This correlation suggests that large solutes, which inhibit water-water hydrogen bonding at the surface, lead to anion adsorption. A surface with completely disordered hydrogen bonds this driving force is on the order of a water-water hydrogen bond, where ΔG_{ads} is favorable by several kcal mol^{-1} or $K_{\text{D}} \sim 0.001 \text{ M}$. The situation is quite different for small solutes, where the interfacial water molecules can more readily satisfy hydrogen bonding networks resembling those in bulk. In this case, there is no water-mediated driving force for SCN^- to interact with the solute and the ΔG_{ads} values are unfavorable with $K_{\text{D}} > 1 \text{ M}$.

We expect that this surface curvature effect is not restricted to PEG or PEO, but also applies to amide-rich polymers. Despite their chemical differences in hydrophobicity, hydrogen bonding capabilities, and partial charges on the aliphatic protons, this simple model based on surface curvature and water structure predicts the affinity of weakly hydrated anions to the chain as a function of solute size. This bifurcation in anion-hydrophobic interactions leads to divergent macroscopic consequences on the solubility of small molecules and polymers. Indeed, weakly hydrated anions salt small molecules out of solution. On the other hand, these same anions are known to inhibit the hydrophobic collapse of thermoresponsive polymers and denature proteins. The incorporation of these ideas into theoretical models should generate more accurate binding constants between anions and protein macromolecules. This relationship of water-mediated interactions and surface curvature may be important for a variety of phenomenon involving direct interactions with hydrophobic surfaces, ranging from methane clathrate formation to host-guest supramolecular complexation, and even cleaning laundry.

Chapter 4

Crowder-Induced Phase Separation of Therapeutic Antibody Solutions

Phase separation is the process by which homogeneous solutions demix into two phases. The schematic illustration at the center of Figure 4-1, illustrates the liquid-liquid phase separation (LLPS) of proteins in the monomeric state into protein-rich droplets, that can reach concentration up to 300 mg/mL protein.¹⁵ From a physical chemistry perspective, phase separation is not limited to protein solutions. In fact, phase separation is known to occur for mixtures of oil in water and for thermoresponsive polymers. The popularity of studying LLPS in the past 10 years has been motivated by the discovery of phase separated droplets in the cytoplasm of living cells. An example of a fluorescence image of a HeLa cell is provided in the lower left panel of Figure 4-1.¹⁶ In the image, the cytoplasm is stained green, while the nucleus is stain red. More important, a fluorescently label protein is shown in yellow, which forms locally concentrated regions called puncta. The organization of proteins and other macromolecules without the help of a lipid membrane has opened up a world of possibilities into how cells regulate reactions and function. These droplets can also serve as hubs for deleterious processes including irreversible aggregation and crystallization, as illustrated in the lower panel of Figure 4-1. This chapter will focus on the phase separation of therapeutic antibody solutions, highlighted by the red circle in the upper right-hand panel of Figure 4-1.

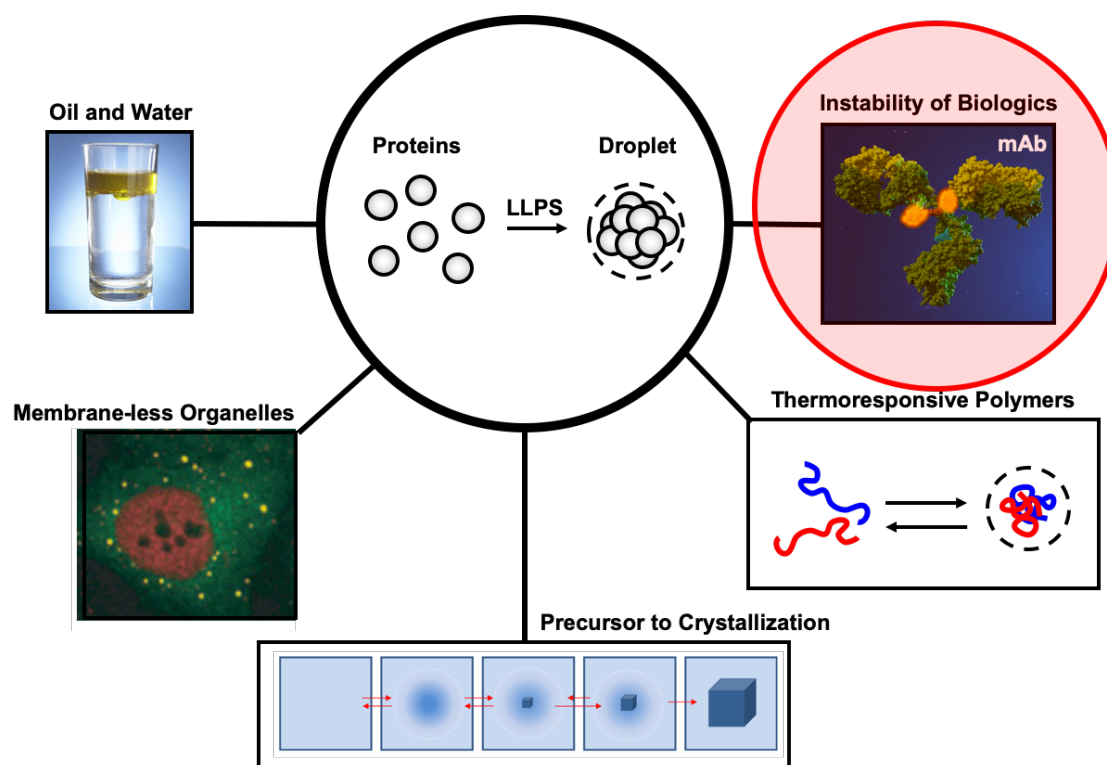


Figure 4-1: Literature overview of liquid-liquid phase separation. The center panel provides a cartoon depiction of the formation of protein-rich droplets, where each protein monomer is drawn as a grey sphere. The images that emanate from the central schematic provide examples of LLPS in other systems, including oil-water mixtures, inside of the cytoplasm of living cells, thermoresponsive polymers, and concentrated formulations of biologics. The behavior of macromolecules inside of these droplets, e.g. crystallization, has also become a topic of interest. Adapted from references 15 and 16.

In this chapter, a high-throughput temperature gradient microfluidics, TGM, device is employed to measure the phase separation of concentrated antibody solutions. This platform offers the potential to reduce the timescale for biopharmaceutical formulation screening from 1 month to just 1 day. Indeed, monoclonal antibodies, mAbs, are susceptible to protein aggregation and current stability testing involves long-term storage experiments that prolong drug development. In addition to high-throughput phase transition temperature measurements, the TGM allows the kinetics of the phase separation to be measured across a range of temperatures and solution conditions, simultaneously. The assays require only small volumes, below 10 μL , and can be performed concurrently on 10 to 100 samples in one experiment. This platform will

facilitate the rapid screening of solution conditions that induce or inhibit aggregation, including pH, salt, and buffer identity.

Challenges and Current Strategies for Formulating High Concentration Liquids

Therapeutic mAbs are large 150 kDa proteins that are engineered to bind to specific targets in the human body. Figure 4-2A schematically illustrates how an antibody might interact with the surface of a target. The ability to deliver drugs to specific sites in the body offers significant advantages over non-specific drugs. As a result, mAbs have become a major class of drug products, known as biopharmaceuticals. The timeline for developing a drug product and bringing it to market is a long and expensive process, requiring about 10 years and over 2 billion dollars, as illustrated in Figure 4-2B. The research and development portion of the development timeline begins by generating a library of millions of protein sequences that may bind to the target of interest. After screening for tight interactions, the number of candidates may be downselected to about 100 binders. From here, potency tests are performed to ensure that the binding events lead to the desired medicinal effects. The last stage of selection is to choose the candidate with the best stability. This is an important step in the process for guaranteeing that the drug product will remain stable and safe during storage. Moreover, the FDA requires that these drugs be stable for 2 years at 4 °C.

Protein-based drugs, including mAbs, are often formulated in aqueous solutions at high concentrations, e.g. above 100 mg/mL, for small-volume subcutaneous injections, as illustrated in Figure 4-2C. These protein-based drugs are susceptible to a range of degradation pathways depicted in Figure 4-2D. Indeed, concentrated protein solutions are susceptible to a range of deleterious condensation processes, including crystallization, aggregation, and LLPS, all driven by attractive protein-protein interactions.^{31,32,35,37-39,82} Preventing these events from occurring at

high concentrations is a critical challenge for improving the stability of liquid mAb formulations. The situation is particularly complex as temperature, pH, salts, surfactants, and crowders can each have a profound influence on mAb solution behavior.^{36,40–42,82} As such, understanding the mechanisms for protein condensation requires a detailed characterization of mAb phase behavior under a variety of solution conditions.

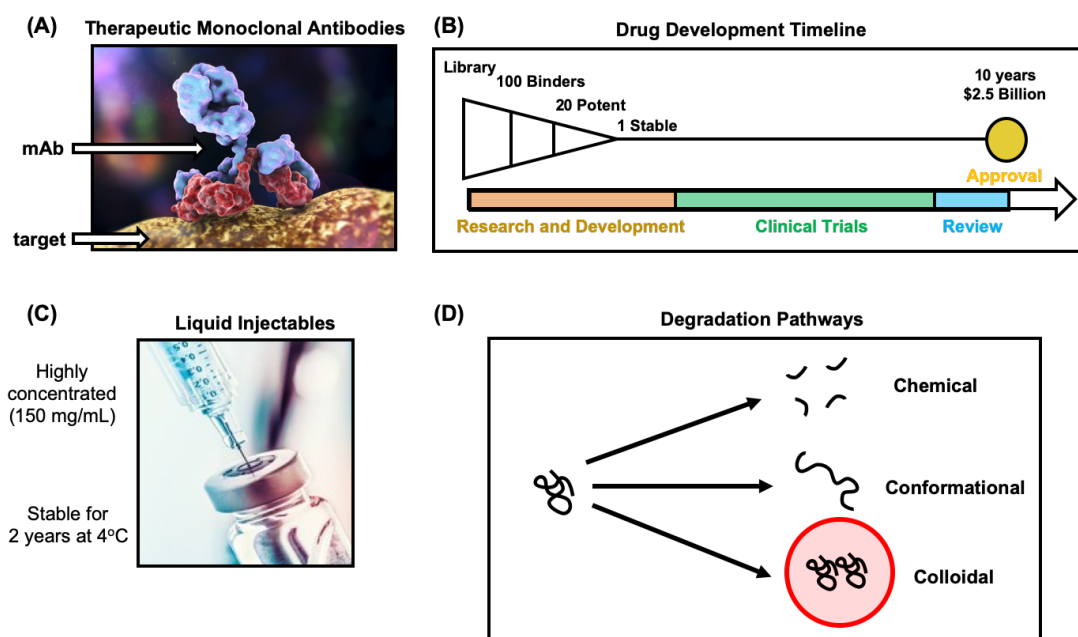


Figure 4-2: Development and degradation of mAb-based drug products. (A) Schematic cartoon illustrating the structure of a mAb, which is engineered to bind to specific medicinal targets. (B) Drug development timeline, where the funnel at the top of the figure portrays information about the stages of drug candidate selection. (C) Image of a liquid injectable modality for mAb therapeutics. (D) Degradation pathways for protein-based pharmaceutical drug products, including chemical, conformational, and colloidal interactions.

Protein aggregation can occur from reversible protein-protein interactions or through irreversible aggregation due to denaturation.^{14,15,19,26,184–187} Moreover, the former type of aggregation may eventually lead to the latter. The standard industrial approach for monitoring aggregation during long-term storage is to use size exclusion high pressure liquid chromatography, SE-HPLC.^{81,188–190} These measurements monitor the loss of monomers over time. Significantly, the method provides no detailed information as to the pathway or mechanism

of aggregation. Moreover, the HPLC method is painfully slow, with experiments typically performed over four to six weeks. Temperature stress experiments are performed at 40 °C to accelerate the degradation, but only cut this time down to one week. More importantly, aggregation pathways at 40 °C may differ substantially from the putative mechanisms that plague storage under more standard conditions at 4 °C.

In an effort to make better predictions of candidate stability on a short timeframe, a variety of methods are currently employed by the biopharmaceutical industry to predict the propensity for a formulation to proceed down each of these pathways.¹⁹¹ A common strategy to predict irreversible aggregation is to measure the protein melting temperatures, T_m , by chemical- or temperature-induced denaturation. Circular dichroism, CD, differential scanning calorimetry, DSC, and differential scanning fluorimetry, DSF are popular methods to measure T_m .¹⁹²⁻¹⁹⁴ Conventionally, these techniques have been low-throughput and are not advantageous for high-throughput formulation screening. Recently, however, label-free, high-throughput, small-volume nanoDSF assays have been commercialized by 2bind GmbH. Thermophoresis can also be employed to measure aggregates, but operates in the 1-100 nM protein concentration range (2bind and NanoTemper).^{195,196} There are also several techniques available to measure reversible protein-protein interactions. For example, static light scattering, SLS, and vapor pressure osmometry, VPO, can be used to obtain the second virial coefficient, B_2 .¹⁹⁷⁻²⁰⁰ A serious limitation for many of these techniques is the requirement of using very low protein concentrations, which is very different from the regime used in mAb formulations, which often exceeds 100 mg/mL, where very different aggregation mechanisms may be at work.

Colloidal protein-protein interactions can be evaluated with static light scattering (SLS), vapor pressure osmometry (VPO) and thermophoresis. A serious limitation for many of these techniques is the requirement of using very low protein concentrations. These concentrations are much lower than the regime in cells or pharmaceutical formulations, which often exceeds 100

mg/mL.^{201–203} LLPS can be measured under high protein concentrations and is representative of a reversible aggregation pathway. However, widespread use of LLPS measurements to evaluate PPIs have been limited by three major problems. First, conventional LLPS measurements are slow and low-throughput. When a protein solution is cooled below the liquid-liquid phase separation temperature, T_{ph} , monomers start to associate into an opaque suspension of protein-rich droplets. The value of T_{ph} reports on the strength of reversible protein-protein interactions.²⁰⁴ Typically, T_{ph} is measured by changes in light scattering intensity upon cooling.⁸⁰ These temperature quenches are performed on one solution at a time. Second, conventional LLPS measurements are impractical for measuring temperature-dependent kinetics. The kinetics of LLPS below T_{ph} contain rich information about the mechanism of phase separation.^{86,89,94} Exploring the effects of temperature on LLPS kinetics, however, is laborious as it requires numerous quenching measurements that are made by sequentially plunging a sample below T_{ph} . Indeed, kinetics have only been investigated in a limited number of labs with specialized equipment.²⁰⁵ Third, conventional LLPS measurements require separate experiments to measure a complete phase diagram. In addition to T_{ph} , the parameters of a LLPS phase diagram, such as the metastable, T_{meta} , and gelation, T_{gel} , temperatures, provide a more comprehensive description of protein-protein interactions.^{15,206} Currently, T_{meta} is typically extrapolated from static light scattering, SLS, measurements, while T_{gel} is measured as a function of concentration, rather than temperature.^{207–209} The required use of different techniques has impeded more thorough investigations of LLPS phase behavior.

Herein, a temperature gradient microfluidics device is employed to measure LLPS in antibody formulations. A schematic of the TGM device is shown in Figure 4-3. The critical advantage of TGM technology is the ability to measure protein phase behavior over a range of temperatures and solution conditions, simultaneously. Image analysis (i.e. light scattering obtained via dark-field microscopy) offers a novel metric for protein-protein interactions and

solution stability. The observables include the transition temperatures, including T_{ph} , T_{meta} , and T_{gel} , and most importantly the activation energies for protein-protein dissociation. These metrics would be extremely time consuming and tedious to obtain from conventional aggregation experiments or quenching assays where measurements are made sequentially.^{33,36,80,207} Indeed, the number of experiments that would need to be performed to obtain thermodynamic and kinetic parameters is simply impractical. Another advantage of the TGM technology is that it can be employed for high concentration protein solutions that are relevant to the exact formulation of interest. Also, the amount of material needed would be large.

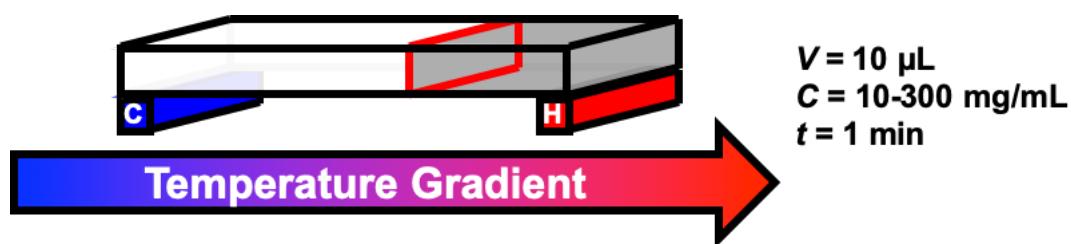


Figure 4-3: Schematic of a sample placed on the temperature gradient device. The primary advantages of this approach are summarized by the conditions on the right-hand side of the Figure.

The high-throughput and multiplexed nature of TGM experiments are key features of this technology that will make it a competitive analysis tool for mAb stability characterization. Biotech customers will benefit from the ability to rapidly screen solution conditions and drug candidates. The TGM device enables the use dark-field microscopy for measuring liquid-liquid phase separation along a temperature gradient. The central features of the apparatus are the application of a linear temperature along a sample and imaging the resulting light scattering. The instrument design employs hot and cold plates to rapidly generate a temperature gradient, a sample chamber to lower the humidity and damp convection currents that may disturb the temperature gradient, and a level to ensure that the device is oriented perpendicular to gravity.

The broader societal impact of this project is the streamlined production of therapeutic monoclonal antibodies. These protein-based drugs enable targeted drug delivery that has begun to

revolutionize modern medicine. Unfortunately, monoclonal antibodies are highly prone to instability, aggregation, and precipitation. The commercialization of the proposed TGM technology for the biopharmaceutical industry will enable rapid characterization of mAb stability, thereby reducing the time required for the research and development phase of the general drug development timeline.

Phase Separation Temperature Measurements on a Temperature Gradient

Conventionally, the phase separation of colloidal solutions is measured by temperature quenching. This method involves preparing a sample at warm temperatures, then slowly cooling it. Below a phase separation temperature, T_{ph} , the sample becomes turbid due to the formation of a cloudy suspension of protein-rich droplets. Images of the conventional temperature quenching assay are provided in Figure 4-4A and 4-4B. The value of T_{ph} represents a specific point on a colloidal phase diagram, depicted in Figure 4-4C. The collection of T_{ph} values defines the phase boundary between conditions that are homogeneous at warmer temperature versus conditions that lead to phase separation into two phases at colder temperatures. Phase diagrams have been measured for a variety of colloidal systems exhibiting UCST behavior, where T_{ph} reaches a maximum critical point, above which the system is soluble at all concentrations. The temperature quenching assay is depicted on the colloidal phase diagram by the black circles and black arrow in Figure 4-4C. These experiments are performed at fixed protein concentration, C_0 , and begin at warm temperatures that reside in the one phase region of the phase diagram. The temperature quench brings the solution into the two phase region of the phase diagram where the process of LLPS forms a cloudy suspension of protein-rich droplets.

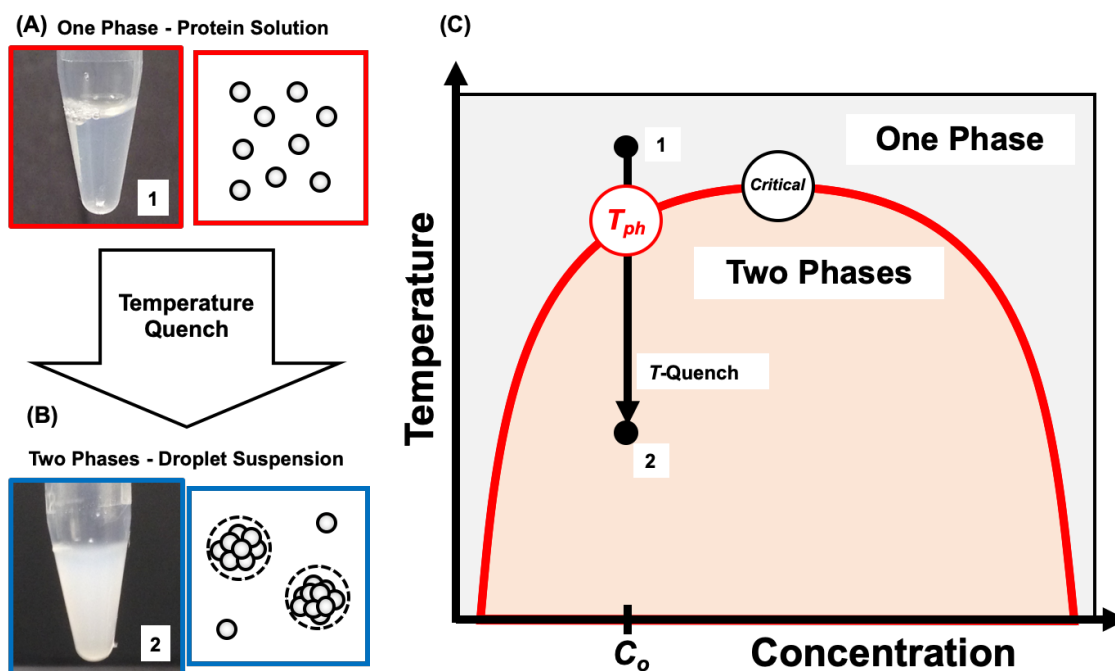


Figure 4-4: Images and schematics of temperature quenching. (A) Images and schematics of a protein solution, held at warm temperatures, marked by 1. Upon a temperature quench to colder conditions, labeled as 2 in (B), the solution becomes cloudy due to the formation of protein-rich droplets, which scatter light. (C) Colloid phase diagram exhibiting an upper critical solution temperature (UCST). The red curve delineates conditions where the system prefers to be in one or two phases. The temperature quench is depicted on the phase diagram with the black circles and arrows. The numbers on the black circles in (C) correspond to the images in (A) and (B).

The throughput of conventional temperature quenches is slow. Indeed, one measurement may take up to 20 minutes, giving rise to a throughput of 3 samples per hour. This is far too slow to be useful during the screening of drug candidates and solution conditions; however, by performing LLPS measurements along the temperature gradient device these phase separation temperatures can be measured in a high-throughput fashion. In these experiments, the temperature gradient is imaged from a top-view using a dark-field microscope, as depicted by the downward black arrow in Figure 4-5A. An image of a 90 mg/mL mAb solution in the presence of 20 mg/mL PEG is provided in Figure 4-5B. The left-hand side of the images corresponds to a temperature of 12.5 °C, while the right-hand side is 30.5 °C. The phase separation temperature can be easily seen as the point at which the solution transitions from a clear to cloudy, which is marked by the red

vertical arrow. The cloudy suspension appear bright on the dark-field microscope images, while the homogeneous solutions appear dark, since they do not scatter much light.

The value of T_{ph} can be measured quantitatively by extracting a line scan from the image, illustrated by the dashed horizontal red line. The data from the line scan is plotted below the sample image. As can be seen, the value of T_{ph} is defined by the onset of light scattering intensity as a solution is cooled, relative to the low, flat intensity baseline observed at higher temperatures. The critical advantage of the TGM approach is that this line scan could be measured in just 1 minute after placing a sample on the gradient. Moreover, dozens of capillaries can be imaged in just one experiment, yielding a throughput of 12 samples per minute, or ~ 300 samples per hour.

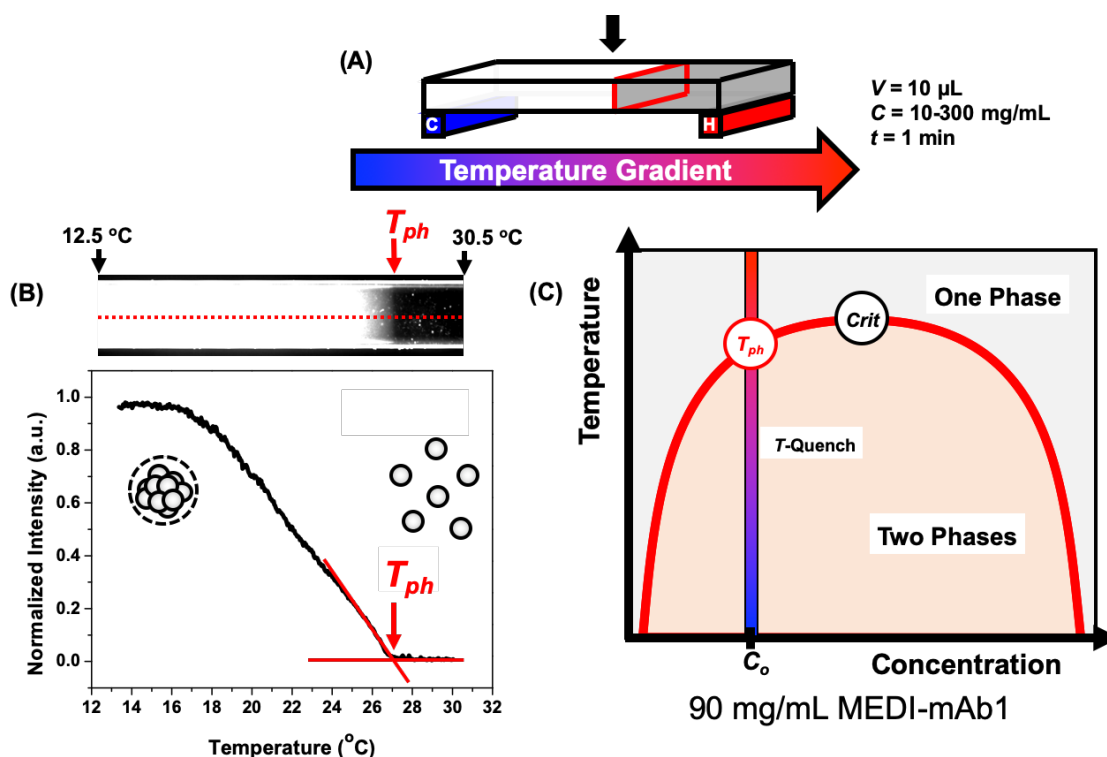


Figure 4-5: Measurements of T_{ph} on a temperature gradient. (A) Schematic of the temperature gradient device (B) Image of a 90 mg/mL mAb solution containing 20 mg/mL PEG. A line scan from the image is plotted to demonstrate how T_{ph} is quantitatively measured from the data. (C) The temperature gradient experiment probes a vertical slice of the phase diagram, unlike the temperature quenching assays described in Figure 4-4.

In most cases, protein solutions have intrinsic phase separation temperatures, $T_{ph,0}$, that are well below the freezing point of water. In order to study the colloidal properties of a system, LLPS can be induced by the addition of non-ionic crowding agents, like polyethylene glycol. A titration of PEG into a mAb solution is provided in Figure 4-6. PEG is believed to induce LLPS by enhancing the attractive protein-protein interactions via an excluded volume effect, illustrated by Figure 4-6A. In this mechanism the PEG chains are repelled from the protein surface. As such, the proteins are driven to interact to reduce the exposure of their surface to the aqueous environment.

An IgG1 mAb with an isoelectric point, pI, of 8.2 was produced, purified and formulated at 116 mg/mL in 10 mM sodium acetate at pH 4.8. Samples were diluted from this stock solution. NaCl (EMD Millipore), Na_2HPO_4 and NaH_2PO_4 (Sigma Aldrich) were at least 99% pure. PEG-3350 was purchased from Spectrum Chemical. All salts as well as PEG were used as received. 18.2 M Ω ·cm purified water from a Barnstead Nanopure water purification system (Thermo Scientific) was used to prepare solutions. Concentrated stock solutions were mixed volumetrically to achieve the desired concentrations. The samples were then incubated in a water bath at 318 K for 30 minutes along with periodic mixing to ensure homogeneity. To make temperature gradient measurements, the solutions were loaded into 12 mm x 1 mm x 0.1 mm rectangular borosilicate glass capillary tubes (VitroCom, Inc.), by capillary action, and sealed with wax to avoid sample evaporation and convection.

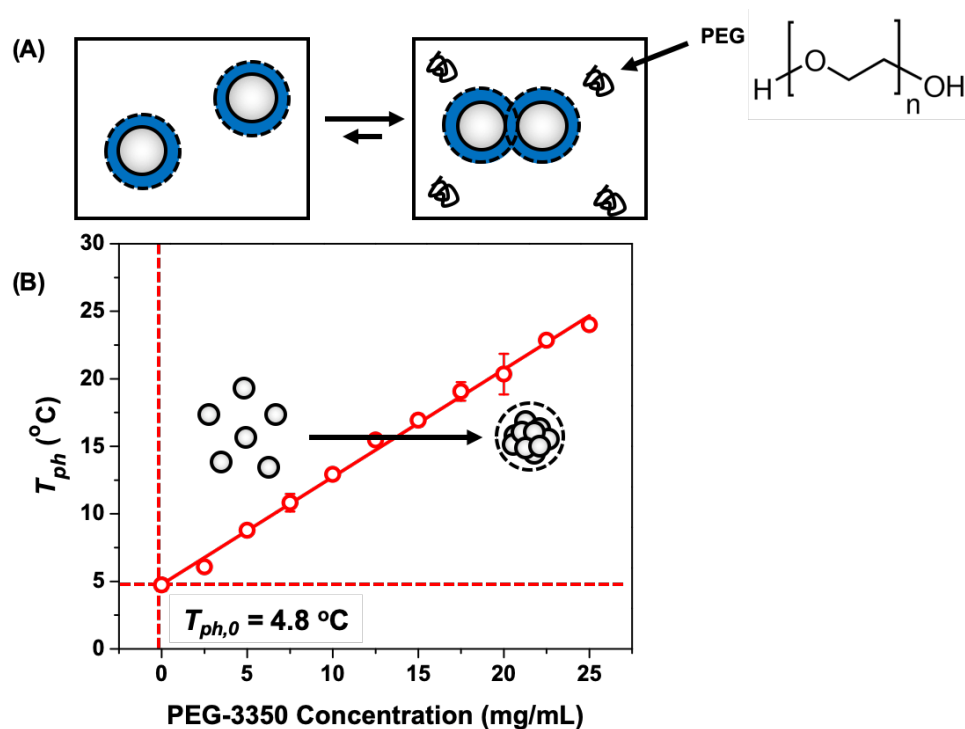


Figure 4-6: PEG-induced LLPS for a mAb solution containing 90 mg/mL mAb at pH 6.8. (A) Schematic illustration of the excluded volume mechanism by which PEG is believed to crowd proteins out of solution. (B) The values of T_{ph} measured as a function of the PEG concentration. The red circles are the T_{ph} measurements, while the red line is fit to Equation 4-1.

The increase of T_{ph} as a function of PEG concentration is remarkably linear as shown by the solid red line in Figure 4-6B, which is described by Equation 4-1 below. Here the phase transition temperature, T_{ph} , is modeled by an intrinsic temperature in pure water, $T_{ph,0}$, and a linear term, with a slope parameter, a , that quantifies the susceptibility of a protein to being crowded out of solution by PEG.

$$T_{ph} = T_{ph,0} + ac_{\text{PEG}} \quad \text{Equation 4-1}$$

The effects of salts on T_{ph} suggest that the attractive non-covalent interactions are electrostatic in nature. In 2009, TGM was used to explore ion-specific effects on reversible

protein-protein interactions between lysozyme molecules.⁴⁴ Upon cooling below the phase separation temperature, T_{ph} , lysozyme monomers associated and assembled into protein-rich droplets.^{43,210} As such, T_{ph} has been used to report on the strength of reversible protein-protein interactions.²⁰⁴ High-throughput measurements of T_{ph} by TGM revealed that salts modulate protein-protein interactions through ion-pairing between salt anions and cationic side chains of lysozyme.⁴⁴

The effect of NaCl on mAb-1 is shown in Figure 4-7. These experiments were performed at pH 6.8, which is below the pI of 8.2, and a fixed PEG concentration of 7.5 mg/mL. The solids lines are guides to the eye. As can be seen, the effect is non-monotonic. This data can be compared with other anions, like SCN^- and SO_4^{2-} in Figure 4-7B. We expect SCN^- and SO_4^{2-} anions to bind more strongly to positive patches of the mAb surface than Cl^- . As such, the data is consistent with anion binding neutralizing the total charge on the protein and enhancing protein-protein interactions. Moreover, this effect saturates at 10's of mM concentrations and then T_{ph} begins to decrease at higher salt concentration.

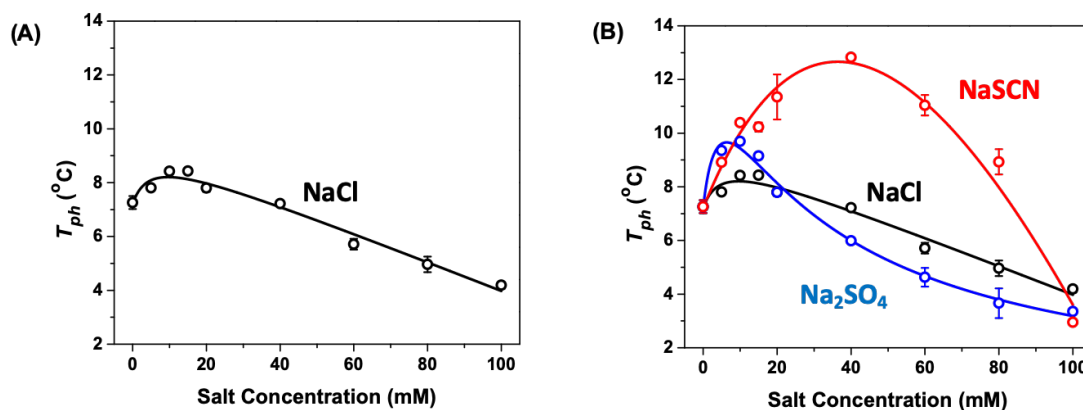


Figure 4-7: Hofmeister anion studies on the T_{ph} of a 90 mg/mL mAb-1 solution in 14 mM bis-tris at pH 6.8 and 7.5 mg/mL PEG.

The effect of surface charge on the protein was also explored by repeating the measurements at a pH value of 7.9, which is near the pI of 8.2. The two data sets are compared in Figure 4-8. As can be seen, near the pI the increase of T_{ph} at low salt concentration is much smaller than the data collected below the pI. This is consistent with the idea that the salt effects at low concentration are associated with ion-pairing interactions between salt anions and positive residues of the protein surface. At higher concentrations, apparently these ion-pairing interactions lead to the solubilization of the mAb.

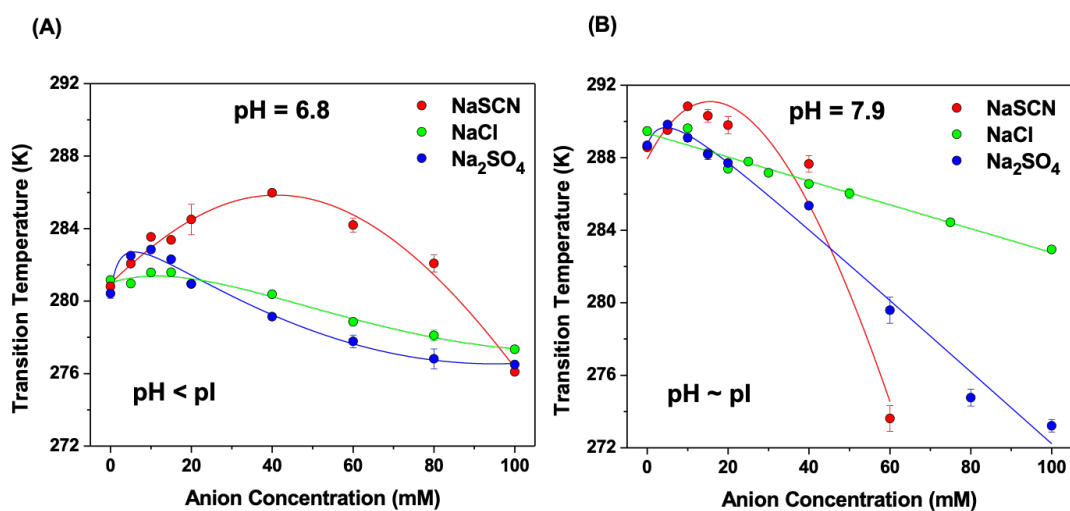


Figure 4-8: Hofmeister anion effects on T_{ph} of mAb-1. (A) Cloud point temperatures measured in 7.5 mg/mL PEG and 14 mM bis-tris at a solution pH of 6.8. (B) Cloud point temperature measured near the pI in 7.5 mg/mL PEG and 28 mM tris at a solution pH of 7.9. The mAb-1 concentration was held constant at 90 mg/mL for the experiments summarized in both (A) and (B). The solid curves are guides to the eye.

In the last set of Hofmeister studies, we compared the anionic Hofmeister effects with the cations. Figure 4-9A is the same data shown in Figure 4-8B, so that direct comparisons can be made the trends observed in Figure 4-9B, which plot the effects of different metal chloride salts on the T_{ph} value. The cation identity affects the slope of the trend, but no features that resemble the ion-pairing signature were observed. These results suggests that at pH conditions near or

below the pI of the mAb-1, the anion identity is critically important for the colloidal protein-protein interactions.

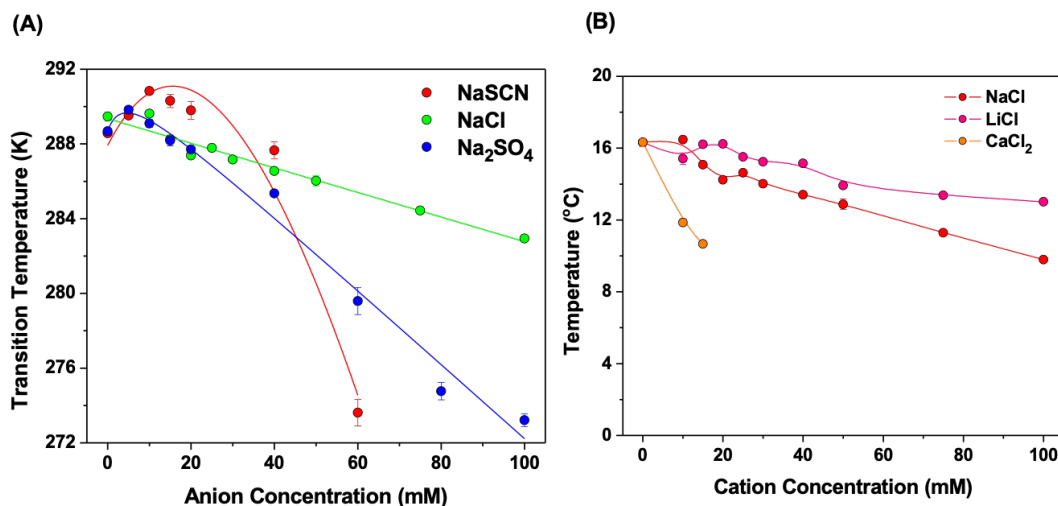


Figure 4-9: Hofmeister anion and cation effects on T_{ph} of mAb-1 with 7.5 mg/mL PEG and 28 mM tris at a solution pH of 7.9, which is near the pI of 8.2. The data are grouped by (A) sodium salt titrations and (B) chloride salt titrations.

In particular, the data suggest a mechanism depicted schematically in Figure 4-10. At pH values below the pI the protein should exhibit a net positive surface charge. Under these conditions there is a net electrostatic repulsion between the proteins, which makes them soluble. As salt is added to the solution, the anions bind to the positively charged side chains and begin to “neutralize” the surface, which decreases the electrostatic repulsion and the proteins and the phase separation occurs at higher temperatures. We propose that anions continue to bind with the macromolecule which generates a net negative charge, leading to a “salting in” effect at higher salt concentrations. Alternatively, the ion binding may begin to disrupt favorable charge-charge interactions between the proteins, thereby increasing their solubility. In either case the propensity to phase separate is strongly dependent on salt concentration, which suggests that the driving forces for the separation are electrostatic in nature.

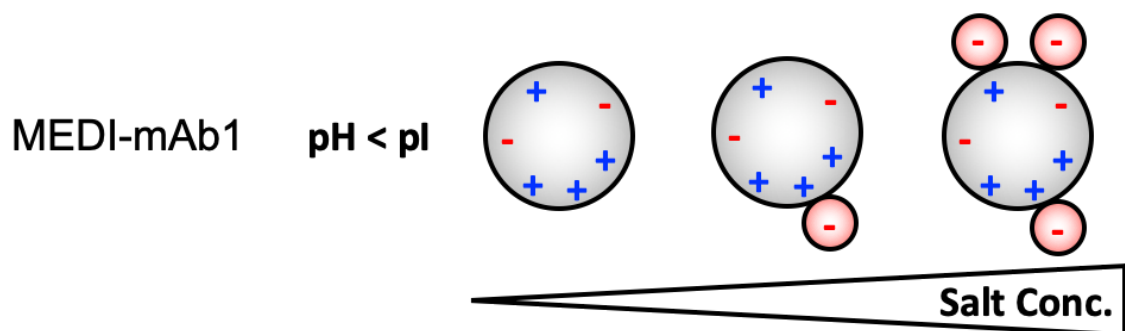


Figure 4-10: Proposed mechanism for the effects of salt on T_{ph} . The mAb is depicted as a grey sphere with charges representing ionic side chains. The adsorption of anions to positive charge sites first neutralizes the total charge of the protein leading to a “salting-out” effect. At higher salt concentrations additional binding of anions leads to overcharging and a “salting-in” effect.

In order to test the hypothesis of ion binding to the protein surface we employed attenuated total internal reflectance infrared, ATR-FTIR, spectroscopy. The basics of this method are illustrated in Figure 4-11. A broadband beam of IR radiation is directed to a ZnSe prism. The light is refracted through the surface of the ZnSe prism, where it totally internally reflects, then is refracted out of the other side of the crystal. During the reflection process, an evanescent wave forms and penetrates into the sample sitting above the ZnSe crystal. As such, the difference in the initial intensity, I_0 , and the final intensity, I , can be used to determine where the IR light was absorbed by the sample. For aqueous solutions, the penetration depth, $d_{\text{penetration}}$, is on the order of 0.5 to 2 μm .

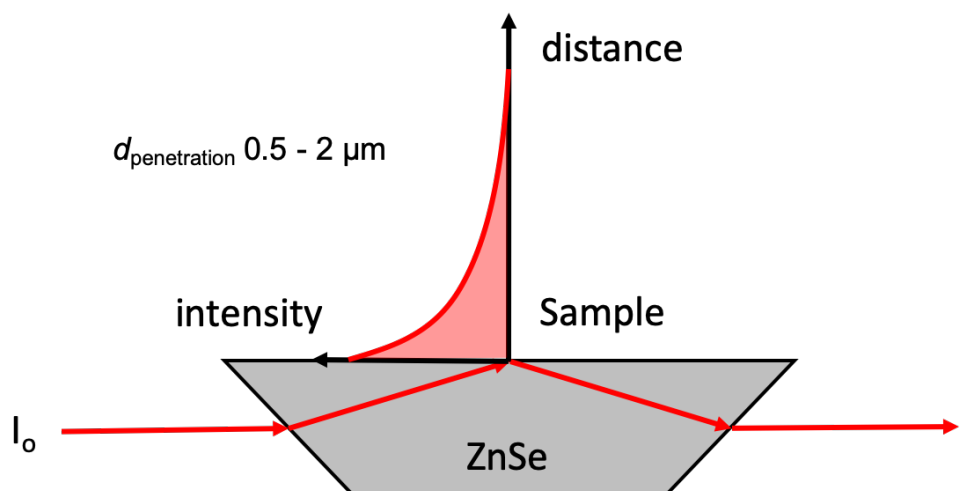


Figure 4-11: Basics of ATR-FTIR spectroscopy. The IR radiation is illustrated by the solid red arrows, while the evanescent field is depicted by the filled in red wave.

The phase separation of protein solutions presents a unique opportunity to measure the interaction of ions with the proteins. The idea behind this experiment is depicted schematically in Figure 4-12. The experiment begins by placing a homogeneous solution onto the sample stage. If the stage is held at a constant temperature, which is below T_{ph} , then the sample will begin to phase separate. With time the dense protein-rich droplets settle onto the stage. As a result, the proteins and any bound ions will fill the volume of the evanescent field and absorb more of the IR light.

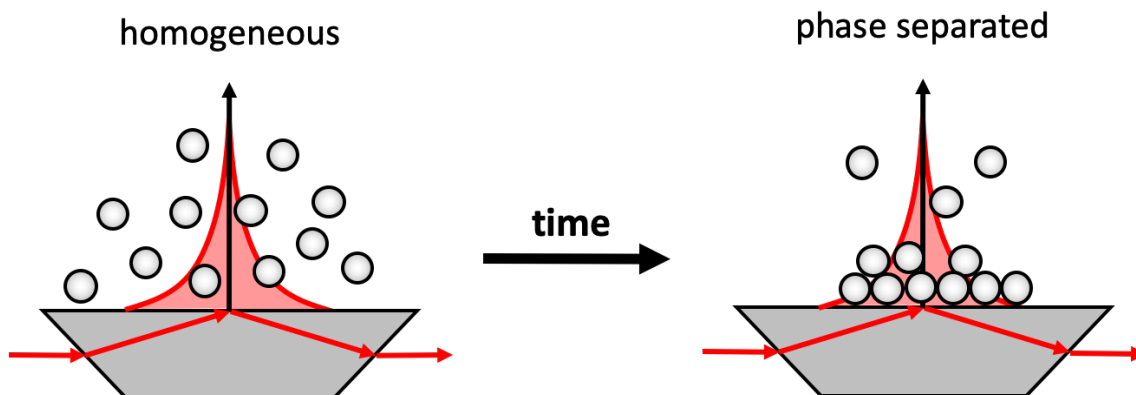


Figure 4-12: Schematic illustration of phase separation experiments on the ATR-FTIR stage. The proteins are depicted as grey spheres.

The IR spectra for a solution containing 90 mg/mL mAb-1 solution at pH 7.9 are summarized in Figure 4-13. The solution also contained 25 mg/mL PEG, 100 mM Na₂SO₄, and 14 mM bis-tris buffer. The spectra are focused on the amide I and amide II vibrations of the protein backbone. As can be seen, the bands grow over time, consistent with the sedimentation of protein-rich droplets onto the IR stage.

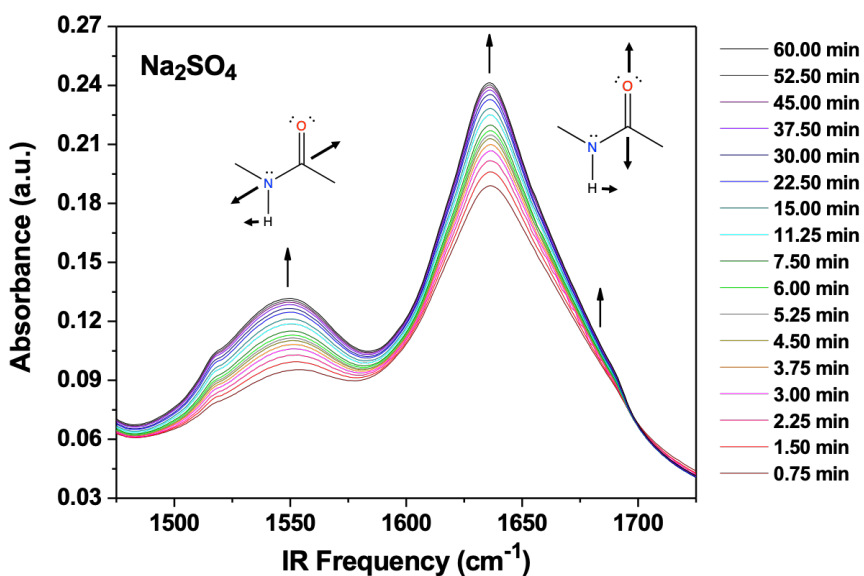


Figure 4-13: Amide I and amide II vibrational spectra of a 90 mg/mL mAb-1 sample in bis-tris buffer at pH 7.9. The solution also contained 25 mg/mL PEG and 100 mM Na₂SO₄.

A comparison of a similar experiment performed with 100 mM NaSCN is provided in Figure 4-14. As can be seen, the amide bands grow over time for both solution conditions. When plotted on the same y-axis scale, it is clear that the Na₂SO₄ condition leads to a more concentrated protein-rich phase than NaSCN, as marked by the dashed horizontal black line in Figure 4-14.

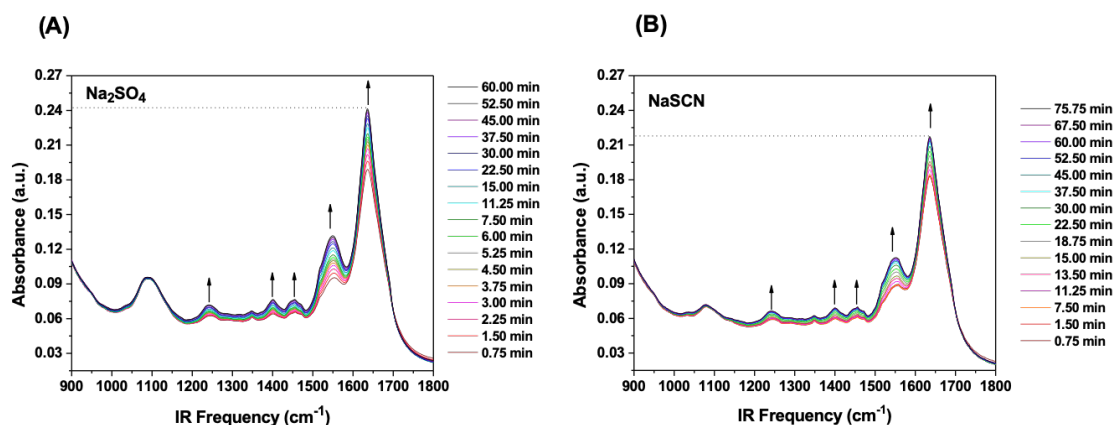


Figure 4-14: ATR-FTIR spectra of 90 mg/mL mAb-1 sample in bis-tris buffer at pH 7.9 and 25 mg/mL PEG. The two panels represent these conditions in addition to (A) 100 mM Na_2SO_4 and (B) 100 mM NaSCN .

Our expectation based on the hypothesis portrayed in Figure 4-10 was that the anion peaks would grow in with the protein peaks. Conveniently, these two anions have vibrational modes that could be assessed. The SO stretch of sulfate is in Figure 4-15A, while the CN stretch of thiocyanate is summarized in Figure 4-15B. To our surprise, there was little change in the intensity of these ion peaks, suggesting that the concentration did not vary much between the homogeneous and phase separated states. We note that the concentration of the protein-rich phase should be near ~ 300 mg/mL, which is still very well hydrated. As such, the measurements may simply be probing essentially the bulk aqueous solutions.

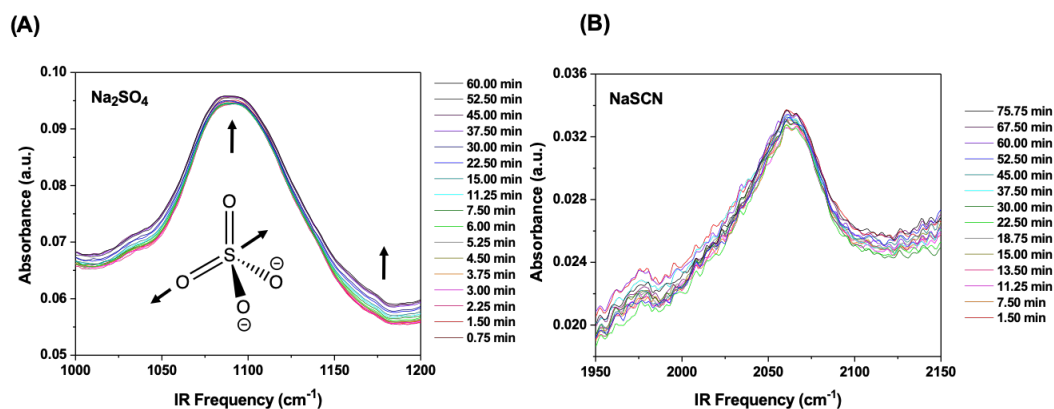


Figure 4-15: ATR-FTIR spectra of the ion peaks for solutions containing 90 mg/mL mAb-1 sample in bis-tris buffer at pH 7.9 and 25 mg/mL PEG. The two panels represent these conditions in addition to (A) 100 mM Na_2SO_4 and (B) 100 mM NaSCN .

In a final experiment to spectroscopically investigate the origins of protein-protein interactions, we employed Raman-MCR measurements to probe the mAb-1 hydration shell at various pH values. This range of pH spans the isoelectric point and gives rise to significant changes in the value of T_{ph} . As can be seen in Figure 4-16, however, there are only small changes in the OH stretch bands of the solute-correlated spectra. The Raman-MCR technique reports on the total population of perturbed water in the hydration shell, so apparently the changes in electrostatics that drive LLPS do not produce significant changes in the structure of water in the hydration shell of the protein.

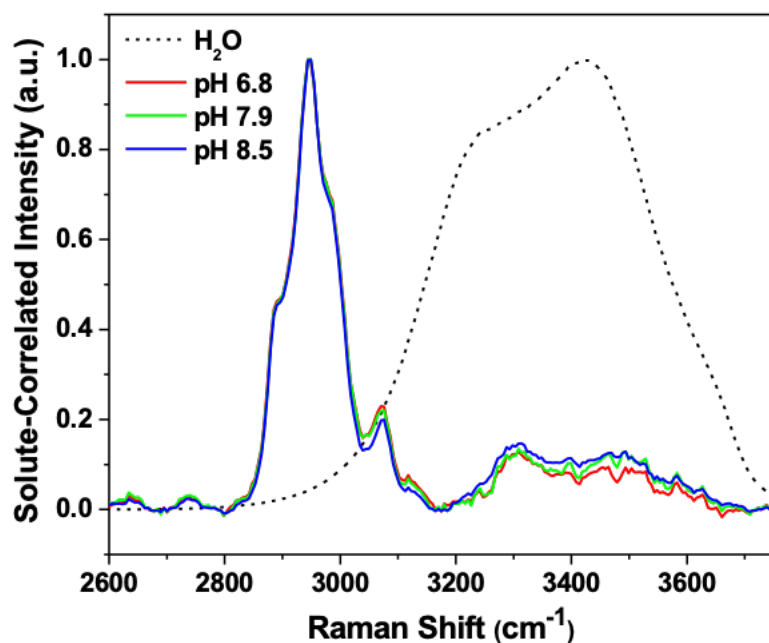


Figure 4-16: Solute-correlated spectra of a 90 mg/mL mAb-1 solution at various pH values.

Aqueous Two-Phase System Formation Measurements on a Temperature Gradient

The last type of experiment that we performed to explore the colloidal stability of mAb formulations were measurements of the kinetics of aqueous two-phase system (ATPS) formation. ATPS formation is the macroscopic stage of LLPS, where the protein-rich droplets sediment to form a large protein-rich phase on the bottom of the container. The process of ATPS formation is summarized in Figure 4-17. After quenching a mAb solution below T_{ph} it rapidly becomes turbid as protein-rich droplets form within seconds. With more time, the protein-rich droplets combine and settle to the bottom of the container to form a large protein-rich phase, that exists in equilibrium with a dilute protein-poor phase. At equilibrium both phases are large enough that they do not scatter much light and the solution is optically transparent. This process is illustrated

schematically on the phase diagram in in Figure 4-17C. At a final temperature below T_{ph} , the solution separates following the horizontal black arrows until reaching the red curve, which defines specific concentrations for the protein-rich and protein-poor phases.

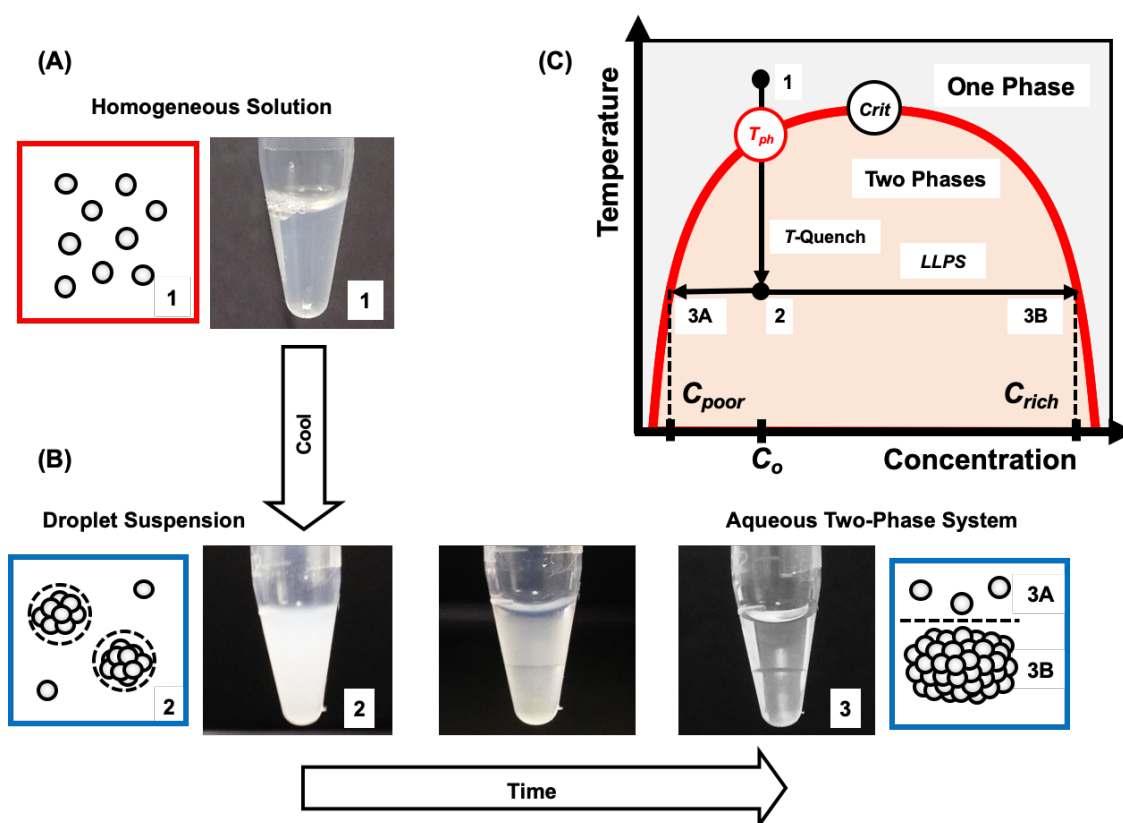


Figure 4-17: Images and schematics of ATPS formation.

By measuring ATPS rate on a temperature gradient, the rate constants can be determined across a range of temperatures, simultaneously. These measurements can then be analyzed by the Arrhenius law to determine an apparent activation energy for ATPS formation, which is depicted schematically in Figure 4-18D.

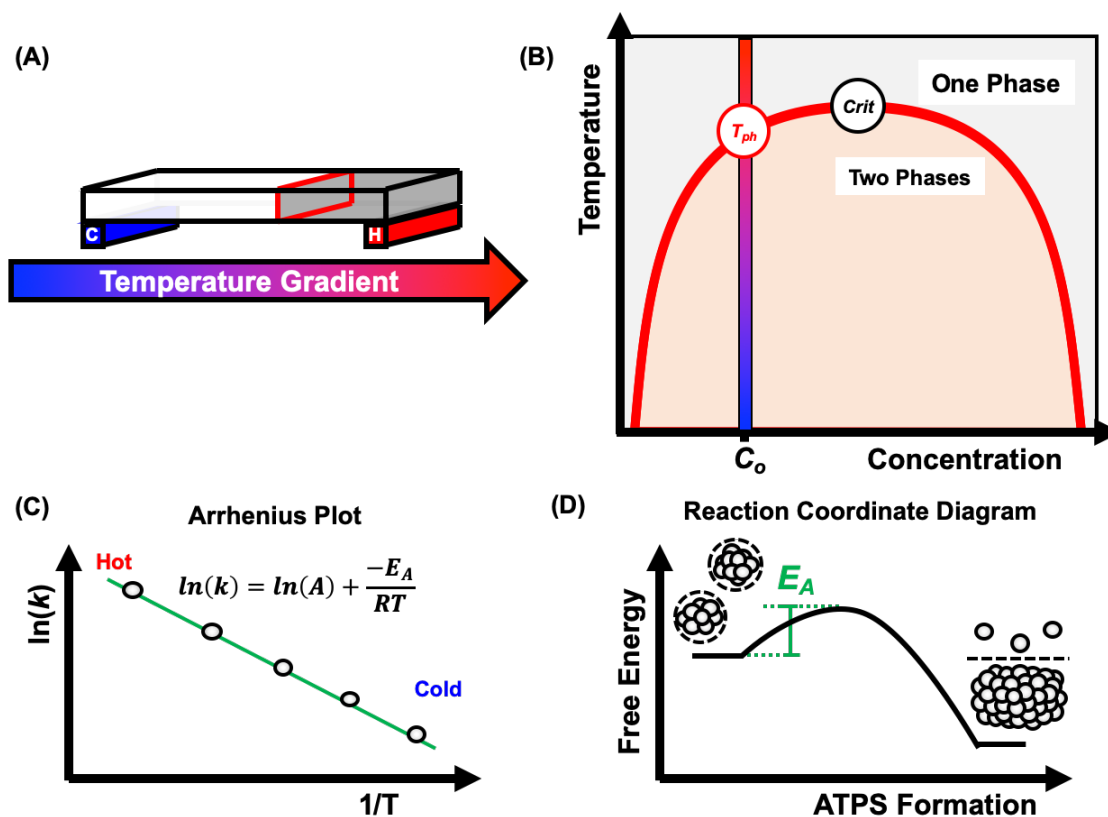


Figure 4-18: Schematic illustration of the temperature gradient and kinetics measurements that can be analyzed with the Arrhenius law.

The method employed to measure the rate constant for ATPS formation, k , on a temperature gradient is summarized in Figure 4-19. Again, the sample capillary tube is imaged from the top-view by dark-field microscopy. The images of a 90 mg/mL mAb sample over time are provided in Figure 4-19B. Portions of the sample that are initially cloudy become clear over the course of minutes as the droplet suspension transition into an ATPS. The rate constant of ATPS formation can be determined at specific temperatures, or positions, along the gradient. The data at an intermediate temperature of 25 °C is plotted in Figure 4-19C. The light scattering intensity was measured on the images at the location marked by the dashed, green line.

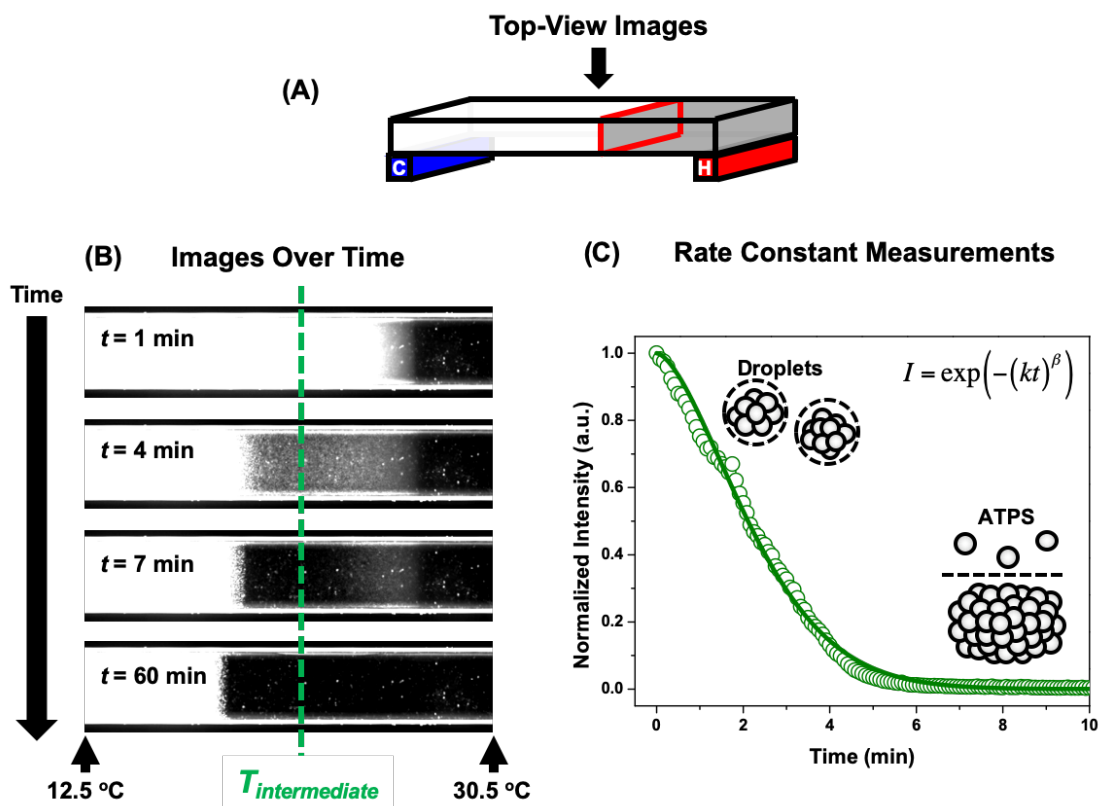


Figure 4-19: Measurements of the kinetics of ATPS formation on a temperature gradient. (A) TGM cartoon, reiterating the imaging of the capillary from a top-down orientation. (B) Dark-field images of a 90 mg/mL mAb-1 sample over time on the TGM device. (C) The rate constant of ATPS formation was measured by extracting the light scattering at specific temperatures. The open circles are the data from the dashed green line in (B) and the solid curve is a fit to the data using the model written in the top right of (C).

This analysis can be performed at every temperature or pixel position along the capillary tube to generate an Arrhenius plot. A typical Arrhenius plot from our measurements of ATPS formation in mAb formulation is shown in Figure 4-20A. The data are strikingly non-Arrhenius. That is, the data are not well described by a single line. Rather, the data are grouped into two general categories. At low temperatures, on the right-hand side of Figure 4-20A, the rate constant increases with heating as the Arrhenius law would predict. The region of the data is marked by the green line, which corresponds to an apparent activation energy of $E_{A,app} = 35\text{ kcal mol}^{-1}$. Based on previous studies of ATPS formation, we assigned this apparent activation energy to the coalescence of droplets into larger protein-rich phases, as portrayed by the green bar in Figure 4-

20B. With increasing temperature the rate constant reached a maximum then began decreasing as the temperature approached T_{ph} . Interestingly, this region of the data could be fit to the Arrhenius law, which yielded an apparent negative activation energy, $E_{A,app} = -28 \text{ kcal mol}^{-1}$. Negative activation energies are signatures that a reaction is not a simple, one-step process. In fact, as the temperature approached T_{ph} , one should expect the droplets to begin dissolving into the monomeric state. This impedes the formation of ATPS formation and gives rise to the negative value of $E_{A,app}$, as illustrated by the two red bars in Figure 4-20B.

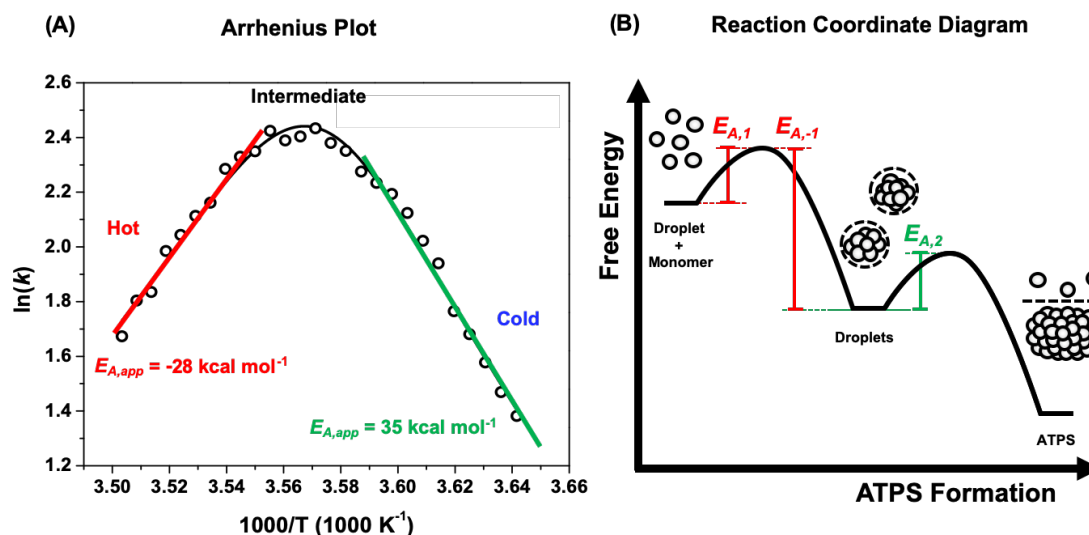


Figure 4-20: Non-Arrhenius kinetics of ATPS formation of mAb solutions. (A) Arrhenius plot and (B) the proposed reaction coordinate diagram to describe the data measured in (A). This figure is adapted from Reference 94.

Discussion of LLPS Assays to Monitor Colloidal Stability in Concentrated Protein Solutions

Basic physical chemistry tools offer remarkable molecular-level insight into the mechanisms of ion-specific effects on protein aggregation, as shown in Chapters 2 and 3. A key aspect of the TGM technology in this chapter is that it affords the large-scale and systematic

exploration of ion and protein chemistries on LLPS. The TGM device is a new high-throughput avenue for screening the effects of salt identity, pH, buffer conditions, crowders etc. on protein-protein interactions. Due to the complexity of these formulations, the phase space is extremely large and non-additive effects of co-solutes remain poorly understood. Analyses were developed to analyze the data and to extract relevant parameters for mAb stability. In particular, $E_{A,app}$ is a novel metric that may advance the characterization of protein-protein interactions in highly concentrated liquid mAb solutions developed to fight numerous diseases. These ideas are summarized schematically in Figure 4-21. Future experiments will be performed to investigate if these assays can explain phase separation in other systems. Parameters gathered from this type of experiment will be tested to see if they can predict stability and shelf-life of biologics.

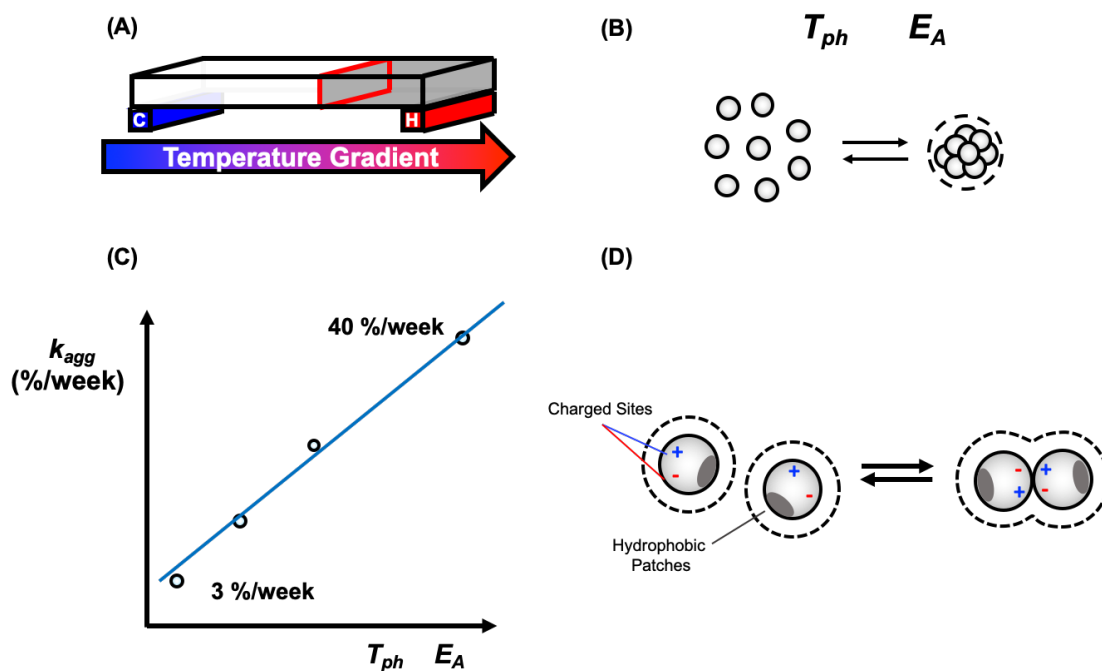


Figure 4-21: Schematic illustrations of (A) TGM apparatus, (B) parameters of colloid phase separation, (C) hypothesis of a correlation between the rate constant of long-term aggregation (k_{agg}) versus LLPS parameters, and (D) potential driving forces for reversible colloidal protein-protein interactions.

Chapter 5

A Stepwise Mechanism for Aqueous Two-Phase System Formation in Concentrated Antibody Solutions

Liquid phase separation, LLPS, is the process by which aqueous solutions demix into two distinct phases. In this chapter, we report the temperature-dependent kinetics of ATPS formation for solutions containing a monoclonal antibody and polyethylene glycol. Measurements are made by capturing dark-field images of protein-rich droplet suspensions as a function of time along a linear temperature gradient. The rate constants for ATPS formation fall into three kinetically distinct categories that are directly visualized along the temperature gradient. In the metastable region, just below the phase separation temperature, T_{ph} , ATPS formation is slow and has a large negative apparent activation energy. By contrast, ATPS formation proceeds more rapidly in the spinodal region, below the metastable temperature, T_{meta} , and a small positive apparent activation energy is observed. These region-specific apparent activation energies suggest that ATPS formation involves two steps with opposite temperature dependencies. Droplet growth is the first step, which accelerates with decreasing temperature as the solution becomes increasingly supersaturated. The second step, however, involves droplet coalescence and is proportional to temperature. It becomes the rate-limiting step in the spinodal region. At even colder temperatures, below a gelation temperature, T_{gel} , the proteins assemble into a kinetically trapped gel state that arrests ATPS formation. The kinetics of ATPS formation near T_{gel} is associated with a remarkably fragile solid-like gel structure, which can form below either the metastable or the spinodal region of the phase diagram.

Concentrated liquid formulations of therapeutic antibodies are susceptible to colloidal instability, including liquid-liquid phase separation, LLPS. Herein, we measure the kinetics of

aqueous two-phase system, ATPS, formation, the macroscopic stage of LLPS, along a linear temperature gradient device. These studies indicate that ATPS formation proceeds by the growth of protein-rich droplets and their subsequent coalescence. Droplet growth accelerates as the solution is cooled because protein-protein interactions become increasingly free energetically favorable. At lower temperatures, however, ATPS formation is rate-limited by a small barrier to droplet coalescence. A gel can form at the coldest temperatures, which arrest phase separation. We propose a simple two-step model that relates these results to a reaction coordinate diagram for ATPS formation.

Phase Separation and the Colloidal Stability of Therapeutic Protein Solutions

Therapeutic monoclonal antibodies, mAbs, are often formulated in aqueous solutions at high concentrations, e.g. above 100 mg/mL, for small-volume subcutaneous injections. Concentrated protein solutions, however, are susceptible to colloidal instability, which includes crystallization, aggregation, and liquid-liquid phase separation, LLPS, all driven by attractive protein-protein interactions.^{31,32,35,37–39,82} Preventing these events from occurring at high concentrations is a critical challenge for improving the stability of liquid mAb formulations. The situation is particularly complex as temperature, pH, salts, surfactants, and crowders can each have a profound influence on mAb solution behavior.^{36,40–42,82} As such, understanding the mechanisms involved in protein condensation requires a detailed characterization of both the kinetics and thermodynamics of mAb phase behavior under a variety of solution conditions.

LLPS occurs below the phase separation temperature, T_{ph} , and leads to an opaque suspension of protein-rich droplets. In the final stage of LLPS, the droplets macroscopically partition into an aqueous two-phase system, ATPS, consisting of protein-rich and protein-poor phases. The thermodynamics of LLPS provides a valuable tool for investigating protein-protein

interactions.²⁰⁴ Some proteins, however, undergo LLPS well below the freezing point of water.^{25,45,79,211} This experimental limitation can be circumvented by elevating T_{ph} with non-ionic crowding agents, like polyethylene glycol, PEG.^{25,34,45,46,79,211} High molecular weight PEG is typically believed to be excluded from the protein surface at low concentrations and therefore induces attraction by depleted volume effects.^{34,46,113,114,116,117,211} The values of T_{ph} have been routinely measured by the onset of turbidity as a solution is cooled.^{33,80,207} Alternatively, temperature quenching combined with centrifugation has also been employed.³⁶ Unfortunately, such methods are impractical for temperature-dependent kinetic analysis, as they would require a very large number of cooling experiments to study the separation below T_{ph} . Instead, we apply a novel method, temperature gradient microfluidics, to measure the kinetics of ATPS formation for mAb formulations in the presence of PEG.^{83,84,86,89,94}

A model colloidal phase diagram displaying an upper critical solution temperature is shown in Figure 5-1. Each of the experiments described herein provides continuous temperature-dependent information for a fixed mAb concentration, e.g. the vertical line at $C = C_0$ in Figure 5-1. The phase separation temperature is located on the binodal curve (red curve in Figure 5-1), above which the solution is homogenous. Below T_{ph} , LLPS is spontaneous and the solution separates into two phases. Just below T_{ph} , however, ATPS formation is slow because the homogenous solution is metastable with respect to LLPS. The lower temperature limit of the metastable region, T_{meta} , occurs on the spinodal curve (green curve in Figure 5-1), below which ATPS formation proceeds more rapidly. At even cooler temperatures, below the gel line (blue line in Figure 5-1), ATPS formation becomes arrested due to the assembly of proteins into a kinetically trapped gel state.

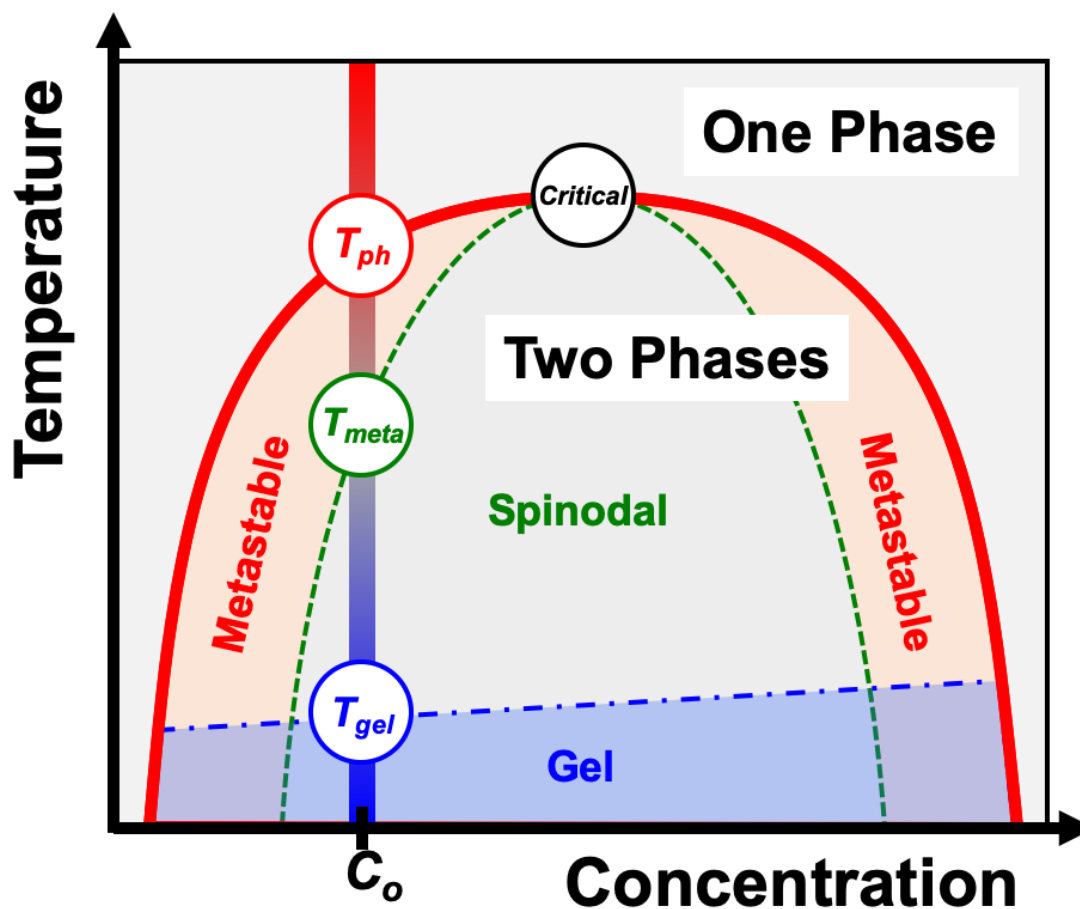


Figure 5-1: Schematic phase diagram of a colloidal system with attractive interactions displaying an upper critical solution temperature. The binodal (red), spinodal (green), and gelation (blue) curves delineate the various regions of the diagram. Temperature gradient experiments were performed at concentrations below the critical point (open black circle at the top of the binodal and spinodal curves), as illustrated by the vertical bar at C_0 (red to blue gradient with decreasing temperature). T_{ph} , T_{meta} , and T_{gel} values were extracted from each experiment and are denoted by open colored circles.

By measuring ATPS formation along a temperature gradient, we simultaneously visualize the three regions of the colloidal phase diagram below T_{ph} . Each region can be identified by its unique kinetics for ATPS formation. The regions are quantitatively delineated by discontinuities in the line scans of light scattering intensity versus temperature, as well as in the temperature dependence of the rate constant for ATPS formation. Using the Arrhenius law, we determined an apparent activation energy, $E_{A,app}$, for ATPS formation in the metastable region ($E_{A,app} \sim -35$ kcal

mol⁻¹) and in the spinodal region ($E_{A,app} \sim 1$ kcal mol⁻¹). A two-step model, involving reversible droplet growth followed by irreversible droplet coalescence, is proposed to explain the effects of temperature on $E_{A,app}$. In fact, we demonstrate that the kinetics of ATPS formation is governed by the thermodynamics of supersaturation in the metastable region but becomes rate-limited by droplet coalescence in the spinodal region. Furthermore, we employ the Vogel-Fulcher-Tammann law to characterize the astoundingly fragile structure of the mAb gel state (fragility index value of $D_{VFT} = 0.05$), which is consistent with a fractal-like network held together by weak protein-protein interactions. Significantly, our measurements show that gelation can occur below either the metastable or the spinodal region of the colloidal phase diagram, depending on the mAb concentration. Such results contradict the notion that gelation can only occur via arrested spinodal decomposition.

Measuring Aqueous Two-Phase System Formation on a Temperature Gradient

We investigated the phase behavior of a 90 mg/mL mAb solution containing 20 mg/mL PEG-3350, 15.5 mM NaCl, and 22.7 mM phosphate buffer at pH 6.8, which is below the antibody's isoelectric point of 8.2. Liquid formulations of therapeutic mAbs are typically prepared under conditions where the protein bears a net positive charge. As such, phosphate buffer was employed to achieve a pH of 6.8, which was below the pI. We note, however, that histidine and acetate buffers are more commonly employed in mAb formulations. NaCl was added to screen long-range electrostatic repulsions between the net positively charged mAbs. The PEG concentration was adjusted to induce phase separation at temperatures between 278 and 308 K. Throughout this chapter, PEG with a molecular weight of 3,350 g/mol. We found the final pH of mixed solutions to be dependent on the mAb concentration, due to the protein's buffer capacity. As such, 0.5 M phosphate buffer stock solutions were employed to maintain pH $6.8 \pm$

0.1 for all mAb concentrations. Our approach was to mix 2 sodium phosphate solutions, a 0.5 M NaH_2PO_4 solution and a 0.5 M Na_2HPO_4 solution, at various ratios to generate a series of buffer stock solutions and choose the ratio that matched the desired final pH upon mixing with the other solution components. In this method, appropriate amounts of H_3O^+ and OH^- were added to the sample to achieve the desired pH, while maintaining constant phosphate and chloride concentrations. This avoided tedious small volume additions of a strong acid, HCl, or base, NaOH. It should be noted that the total Na^+ ion concentration changed by less than ~ 7 mM between the 20 and 100 mg/mL mAb. In other words, the pH and ionic strength were held essentially constant for all of the solutions.

The experiment was initiated by introducing a clear, pre-heated sample, $T = 318$ K, onto a linear temperature gradient at a time designated as $t = 0$ min. Figure **5-2A** shows a set of dark-field images obtained at successive time points during the experiment. A schematic diagram from a side-on perspective of the rectangular sample capillary tube is provided in Figure **5-2B** to help illustrate the phase separation at each time point.

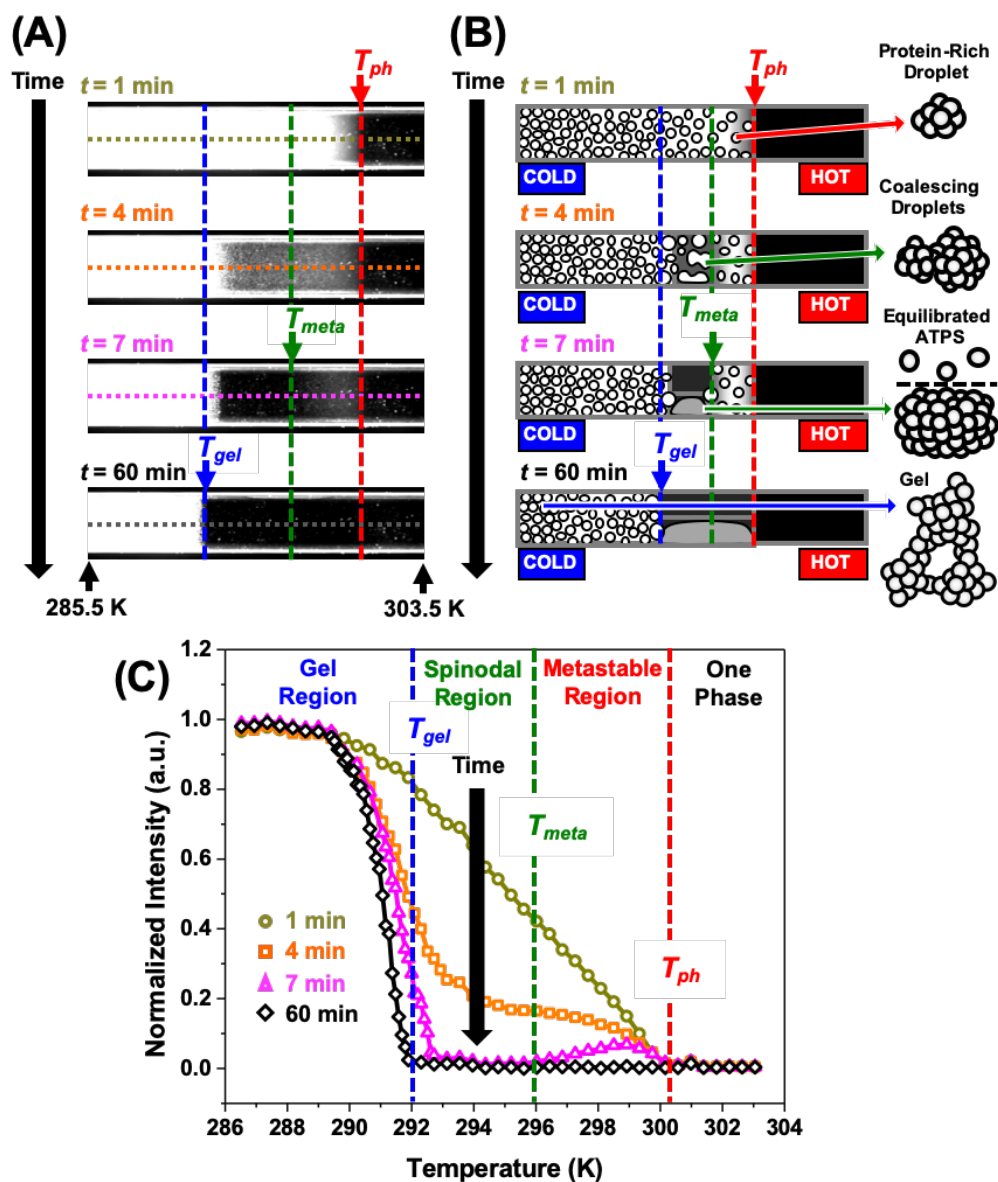


Figure 5-2: ATPS formation of a mAb solution on the temperature gradient device. (A) Dark-field images at time points ranging from $t = 1$ to $t = 60$ min during the experiment. The two, short upward-pointing black arrows at the bottom of the image denote the temperatures at each of these two points, respectively, while the colored arrows denote the positions of the three transition temperatures. (B) Schematic diagrams of ATPS formation along the temperature gradient device corresponding to the time points in (A). The schematics on the right are drawn from a side-on perspective of the rectangular capillary tube. The droplet cartoons on the far right side depict more detailed structures corresponding, in descending order, to a protein-rich droplet, two coalescing droplets, an equilibrated ATPS, and the gel state, respectively. The protein molecules are depicted as grey spheres in each droplet cartoon. (C) Line scans of scattering intensity versus temperature. The line scans plotted in (C) correspond to the dashed horizontal lines on the images in (A), which are color coded accordingly. The dashed vertical lines mark the phase transition temperatures.

The cooler side of the sample became cloudy almost immediately as protein-rich droplets formed and scattered the light. The phase separation temperature, T_{ph} , was determined at $t=1$ min from the onset of the scattering intensity near 300 K, marked by the red arrows in Figure 5-2A and 5-2B. A line scan of the scattering intensity versus temperature was measured from the dashed horizontal line in the $t = 1$ min image and plotted as gold data points in Figure 5-2C. As can be seen in the orange line scan measured after 4 minutes, the scattering intensity decreased between 292 and 300 K due to droplet growth and coalescence. The pink line scan at $t = 7$ min showed when the intensity had just reached a minimum and stopped changing between 293 and 296 K because the droplets settled to the bottom of the capillary tube to form a transparent ATPS. The scattering intensity between 296 and 300 K, however, was still decreasing due to slow droplet growth near T_{ph} . Using this time point, we could define the metastable temperature, T_{meta} , indicated by the vertical green line in Figure 5-2C. The value of T_{meta} divided the warmer, metastable region where ATPS formation was still occurring from the colder, spinodal region where it had just finished.

By $t = 60$ min, the separation yielded an equilibrated ATPS above a gelation temperature, T_{gel} . The equilibrated ATPS was optically homogeneous and did not scatter light. The line scans in Figure 5-2C reveal that T_{gel} continued to shift subtly and ever more slowly toward colder temperature over time. The time-dependent shift of T_{gel} was consistent with a pseudo phase transition, like a glass transition, which was kinetic rather than thermodynamic.²¹² Nonetheless, by $t = 60$ min, T_{gel} effectively stabilized on the timescale of the measurements and could be quantified by the onset of scattering relative to the completed ATPS, designated in Figure 5-2C by the vertical blue line.

We confirmed these interpretations for the decrease in light scattering by imaging ATPS formation in a larger sample, which is discussed further in Figure 5-3. In a control experiment, the 90 mg/mL mAb solution with 20 mg/mL PEG, 15.5 mM NaCl, and 22.7 mM phosphate

buffer at pH 6.8 was introduced onto the gradient at a constant temperature of 318 K, which is above T_{ph} (Figure 5-3A). The image appeared dark across the entire sample, confirming that the homogenous solution did not scatter very much light. In comparison, there was significant light scattering from the droplets that formed below T_{ph} , at $t = 1$ min, after being introduced onto a linear temperature gradient of 278 to 318 K (Figure 5-3B). As can be seen at 4 and 7 min, ATPS formation above T_{gel} resulted in a reduction of light scattering intensity (Figure 5-3C and 5-3D). Eventually, the ATPS formation yielded a completed ATPS above T_{gel} , e.g. 60 min (Figure 5-3E).

The reduction in light scattering intensity with time was attributed to the growth of droplets and the formation of a clear ATPS within the sample capillary. To confirm this interpretation, we acquired side-on images of macroscopic phase separation in a 1.5 mL microcentrifuge tube at constant temperature. These constant temperature experiments were also performed on a 90 mg/mL mAb solution with 20 mg/mL PEG, 15.5 mM NaCl, 22.7 mM phosphate buffer at pH 6.8. The sample was incubated and periodically mixed for 30 min at 318 K (Figure 5-3F). To initiate a temperature quench, the sample was removed from the water bath, 318 K, and placed at room temperature, 293 K, or in a cold room, 277 K. The images for the 293 K and 277 K quench experiments are shown in the upper and lower images of Figure 5-3F through 5-3I, respectively. The images were obtained over time to follow the macroscopic phase separation at 1, 15, and 60 minutes in Figure 5-3G, 5-3H, and 5-3I, respectively. As expected, the 293 K quench resulted in the formation of a clear ATPS after 60 minutes, while the deeper quench at 277 K formed a gel that did not macroscopically phase separate, even after several weeks.

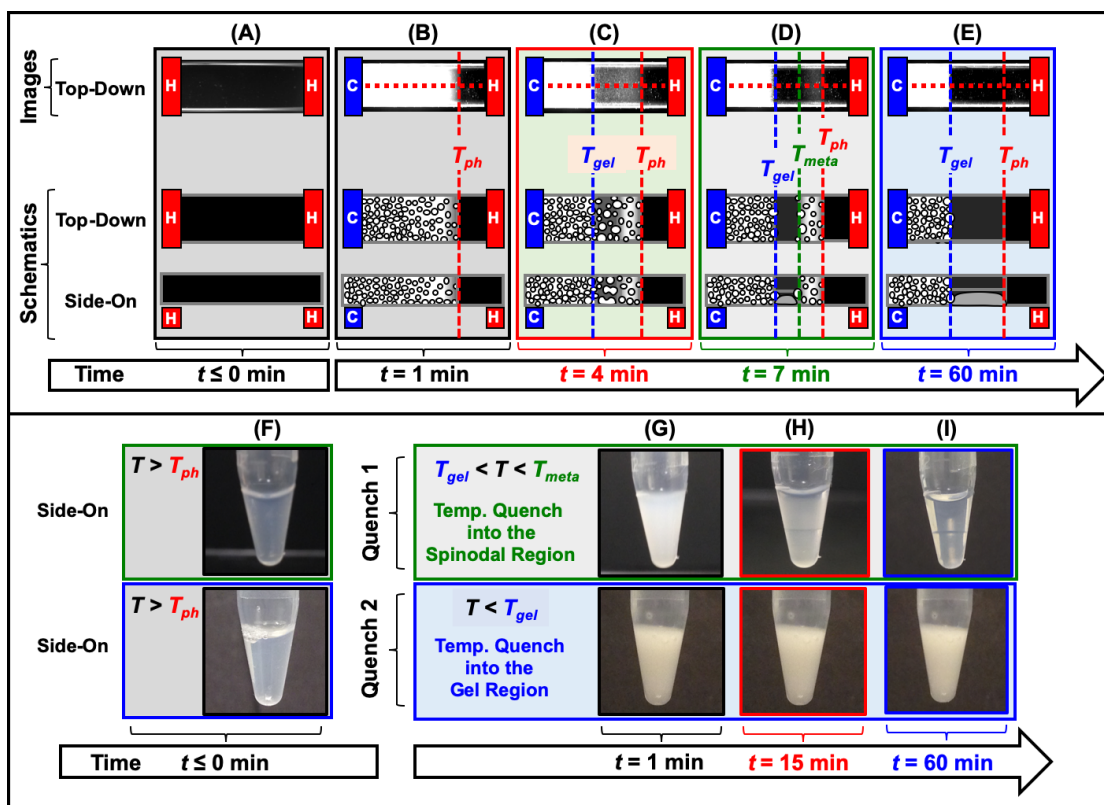


Figure 5-3: Dark-field images and schematics of phase separation on the temperature gradient device versus images of temperature quenches performed on macroscopic samples. The dark field images of the temperature gradient experiments are provided at five time points (columns A-E) during the separation of a solution containing 90 mg/mL mAb and 20 mg/mL PEG. Specifically, we show (A) an image of a sample exposed to a constant temperature (318 K) versus a linear temperature gradient (278 – 318 K) at (B) 1 min, (C) 5 min, (D) 7 min, and (E) 60 min after sample introduction. The white circles in the schematics represent protein-rich droplets, which scatter light (B-E). The droplets coalesce to form the clear protein-rich phase of an ATPS, as depicted by the large grey droplet (D-E). For comparison, we also recorded images of the phase separation process in centrifuge tubes upon temperature quenches at (Quench 1) 293 K and (Quench 2) 277 K, which reside in the spinodal and gel regions, respectively. We provide (F) an image recorded at 318 K, prior to the temperature quench, versus images captured at (G) 1 min, (H) 15 min, (I) 60 min after the temperature quench.

The procedures for determining the precise transition temperatures is summarized in Figure 5-4. The three transition temperatures were obtained quantitatively from line scans of scattering intensity as a function of temperature. The phase separation temperature, T_{ph} , was determined just after the temperature gradient stabilized, $t = 1$ min. The value of T_{ph} was defined as the onset of intensity, relative to the region of low and flat scattering intensity at high

temperature, as shown by the intersection of the two red tangent lines in Figure 5-4A. The metastable transition temperature, T_{meta} , was determined at the first time point where ATPS formation came to completion below T_{ph} . This time point occurred when the light scattering reached a minimum in intensity and did not change as more time past. In most cases, the time point for the metastable transition determination was around $t = 7$ min. The metastable transition temperature was determined by the onset of light scattering intensity, relative to the nearly completed ATPS at lower temperatures, as shown by the intersection of the two tangents shown with green lines in Figure 5-4B. Finally, the gelation temperature, T_{gel} , was determined from the line scan at $t = 60$ min, where ATPS formation had been completed or became kinetically trapped at all temperatures below T_{ph} . Specifically, the gelation transition temperature was determined by the onset of light scattering, relative to the completed ATPS baseline, as shown by the intersection of the two solid blue tangent lines in Figure 5-4C. We note that the four line scans provided in Figure 5-2 have been normalized to the highest and lowest intensities observed in temperature and time during the experiment. Specifically, the data for all four line scans were normalized by subtracting the lowest intensity data point and then dividing the line scan data by the difference between the highest and lowest intensity data points. As such, the normalized line scans have values that ranging from 1 to 0.

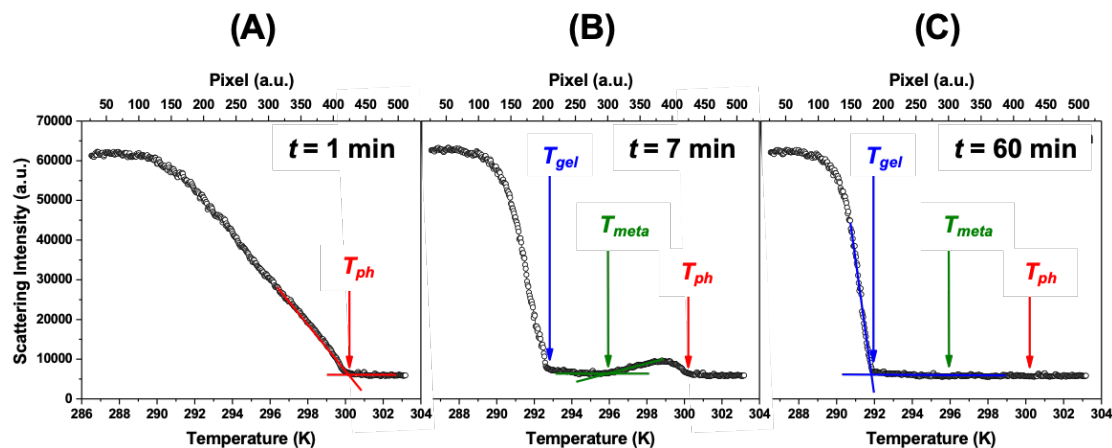


Figure 5-4: Line scans of scattering intensity as a function of temperature at three time points of phase separation for the 90 mg/mL mAb and 20 mg/mL PEG solution. The line scans were obtained from the dark field images shown in Figure 5-3. The line scans are given for (A) $t = 1$ min, (B) $t = 7$ min, and (C) $t = 60$ min. The solid lines are provided as visual aids for the transition temperature determinations of T_{ph} (red lines), T_{meta} (green lines), and T_{gel} (blue lines).

We measured the three transition temperatures as a function of mAb concentration at 20 mg/mL PEG-3350 to construct the phase diagram shown in Figure 5-5. As can be seen, T_{ph} increased sharply at low concentration, but began leveling-out by 100 mg/mL (red points in Figure 5-5). Below the binodal curve, we observed a metastable region that was bound by T_{meta} at low temperature, as shown by the green data points in Figure 5-5, for solutions containing more than 50 mg/mL mAb. T_{meta} increased with mAb concentration in a similar fashion to the binodal curve up to 100 mg/mL mAb and defined the spinodal curve, marked by the green curve in Figure 5-5. The spinodal should meet the binodal at the critical point, as shown schematically in Figure 5-1. This intersection was not observed in the employed concentration range, which may indicate that the critical concentration, C_{crit} , was located at higher mAb concentration. The presence of PEG, however, makes the system ternary, consisting of water, protein, and PEG. The ternary nature of the system could cause the phase diagram to have an asymmetric shape or move the critical point away from the binodal maximum.^{34,46,80,213} At lower concentrations, T_{meta} was not measurable due to gelation. Indeed, T_{meta} should be below T_{gel} for mAb concentrations between 20

and 50 mg/mL. We measured T_{gel} at all mAb concentrations to chart the gelation line, below which separation became arrested, marked by the blue curve in Figure 5-5. For all samples, gelation occurred at or below T_{ph} and T_{gel} increased only slightly with mAb concentration, with a linear slope of $0.05 \text{ K (mg/mL)}^{-1}$. These results suggest that the kinetic barrier associated with arrested ATPS formation is relatively independent of mAb concentration.

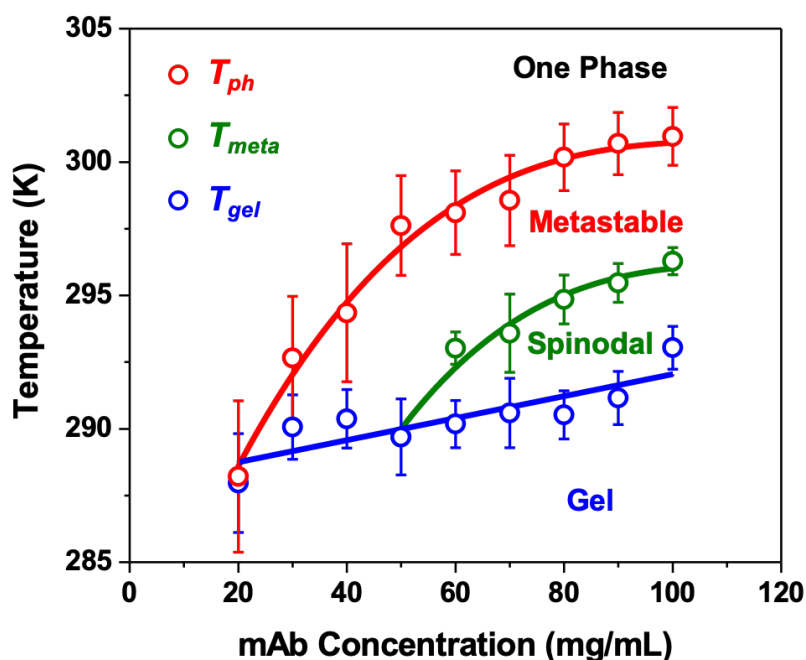


Figure 5-5: Colloidal phase diagram measured at 20 mg/mL PEG-3350. T_{ph} (red data points) and T_{gel} (blue data points) were measured at $t = 1$ min and $t = 60$ min, respectively; while T_{meta} (green data points) was measured at the first time point when ATPS formation had come to completion below T_{ph} . The red and green curves are guides to the eye, while the blue curve is a linear fit to the T_{gel} data.

The effect of PEG on the three transition temperatures was also measured. The results are summarized in Figure 5-6. As can be seen all of the transition temperatures increased linearly with PEG concentration, but with distinct slopes.

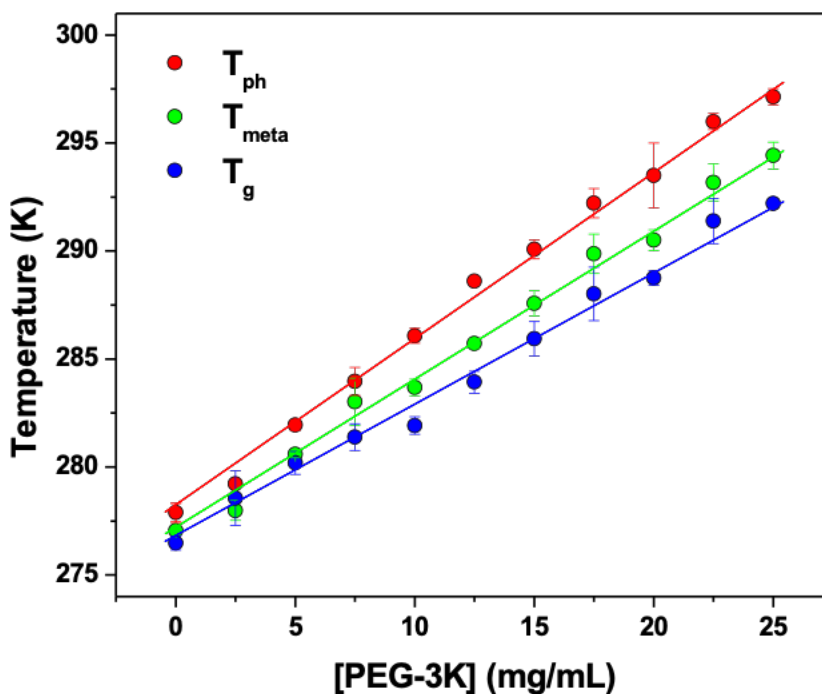


Figure 5-6: Phase transition temperatures measured as a function of PEG concentration at a fixed mAb concentration. The slopes of T_{ph} , T_{meta} , and T_{gel} were 0.80 , 0.71 , and 0.63 K (mg/mL) $^{-1}$, respectively.

Modeling the Kinetics of Aqueous Two-Phase System Formation

We analyzed the kinetics of ATPS formation as a function of temperature to probe the mechanism of the late stages of LLPS. Figure 5-7 displays the scattering intensity as a function of both temperature and time from the data shown in Figure 5-2. In the metastable region, slower ATPS formation gave rise to a low topographical ridge, denoted by the magenta region in Figure 5-7A, while the most rapid separation in the spinodal region produced a valley, indicated by the grey region in Figure 5-7A. Little or no scattering reduction was observed in the gel region at

colder temperatures, colored by the red region in Figure 5-7A. A characteristic scattering decay from each of the three kinetic regions is plotted in Figure 5-7B.

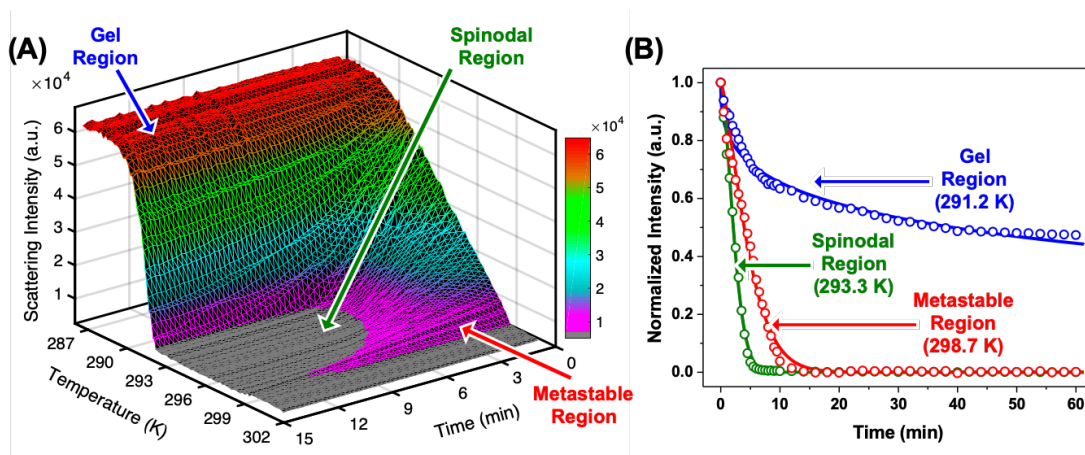


Figure 5-7: Kinetic analysis of the light scattering data obtained in Figure 5-2. (A) The scattering intensity is plotted as a function of both time and temperature. The data are shown at 15 s time intervals for clarity. (B) Three isothermal decays of the normalized scattering intensity as a function of time from the three distinct kinetic regions along the temperature gradient. The open circles are data points and the solid lines are fits to the data using Equation 5-1.

The normalized scattering intensity, I , for all temperatures was fit to the Kohlrausch-Williams-Watts (KWW) function provided in Equation 4-1: The KWW fits to the data points are shown as solid curves in Figure 5-7B.^{214,215}

$$I = \exp(-(kt)^\beta) \quad \text{Equation 5-1}$$

The time required to establish a steady-state linear temperature gradient across the sample capillary was estimated using two independent methods. First, we monitored the apparent position for the lower critical solution temperature, LCST, of PNIPAM as a function of time. A 10 mg/mL PNIPAM sample in 0.8 M NaCl was loaded into a capillary tube and then incubated at 4 °C, where the polymer was soluble. The sample was then introduced onto a pre-equilibrated temperature gradient, 278 – 318 K, and line scans of the light scattering intensity were measured

across the capillary as a function of time, as shown in Figure **5-8A**. At each time point, the line scans showed weak light scattering at cold temperatures and an onset of light scattering at the LCST located at hotter temperatures. Pixel number is proportional to temperature in Figure **5-8A**. The spatial position of the LCST shifted to a higher pixel position as time progressed and the sample capillary established a steady-state temperature gradient.

The apparent LCST pixel position is plotted over time in Figure **5-8B**, marked by blue data points. A schematic illustration of the PNIPAM experiment is provided in Figure **5-8C**. In a separate experiment, a thermocouple was used to acquire direct measurements of the external temperature of a capillary filled with DI water. The thermocouple was fastened to the capillary with a piece of scotch tape as shown in Figure **5-8D**. After introduction of the sample onto the temperature gradient, the temperature read out of the thermocouple was recorded at 1 second intervals. The red data points in Figure **5-8B** are the temperatures measured by the thermocouple over time. Both measurements provide an estimate of about 1 minute for the temperature equilibration of samples on the temperature gradient device.

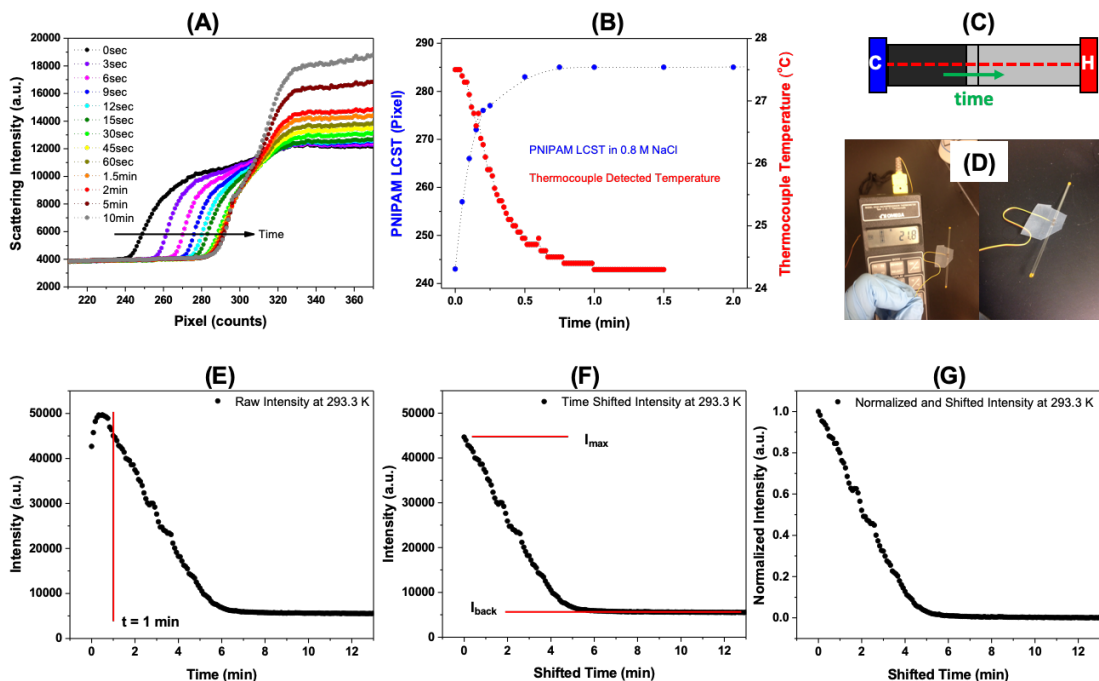


Figure 5-8: Control experiments on the establishment of a temperature gradient and a demonstration of the procedure for processing the light scattering kinetic data. (A) The line scans of a 10 mg/mL PNIPAM sample containing 0.8 M NaCl over time along a linear temperature gradient (278 – 318 K). The apparent LCST values (blue data points) determined from (A) are plotted in (B) along with a direct measurement of the temperature by a thermocouple (red data points) as a function of time. The shift of the LCST with time is illustrated schematically in (C). Two pictures demonstrate the thermocouple measurement technique (D). (E-G) The sequential processing of raw data is shown for an isotherm at 293.3 K of a 90 mg/mL mAb and 20 mg/mL PEG solution. The light scattering intensity is plotted as a function of time in (E). Note, the vertical red line denotes the time required to reach a steady-state temperature gradient. After discarding the first minute of raw data, the intensity was plotted as a function of shifted time in (F). The normalized data are provided in (G).

The isothermal light scattering decays, i.e. intensity versus time at a specific temperature along the temperature gradient, were processed by a standardized procedure prior to kinetic modeling. Here we provide a sequential demonstration of this procedure for an isotherm measured at 293.3 K for the 90 mg/mL mAb sample with 20 mg/mL PEG. The light scattering intensity, I , was plotted as a function of time, t , after placing the sample onto the temperature gradient, as shown in Figure 5-8E. The solid red vertical line denotes the equilibration time $t = 1$ min that was required to establish a steady-state heat flow and a stable, linear temperature

gradient. The data within this equilibration time window, i.e. $t < 1$ min, was discarded. Next, the remaining intensity data points were plotted as a function of shifted time, t_{shifted} , as shown in Figure 5-8F. The shifted time accounts for the discarded data by subtracting a temporal shift of 1 minute along the time axis, as shown in Equation 5-2. In the last step of data processing, the shifted time intensity data were background corrected by subtracting the residual scattering intensity, I_{back} , and normalized by division by the maximum intensity, I_{max} , as shown in Equation 5-3. The fully processed data, summarized in Figure 5-8G, was used for the fitting analyses and began at a normalized intensity, I_{norm} , of 1 at and decayed to 0.

$$t_{\text{shifted}} = t - 1 \text{ min} \quad \text{Equation 5-2}$$

$$I_{\text{norm}} = \frac{I - I_{\text{back}}}{I_{\text{max}} - I_{\text{back}}} \quad \text{Equation 5-3}$$

The process by which a thermodynamically unstable dispersion, i.e. liquid droplets of densely packed mAbs, could proceed toward an equilibrated ATPS generally should follow one of two possible mechanisms: coalescence or Ostwald ripening. For coalescence, there are two extreme cases. First, in a very dilute suspension of droplets, the collision rate between the droplets can be the rate-limiting step. In this situation, coalescence should resemble a second-order process. At higher concentrations of the droplets, however, the rupture of the interfacial water film between two droplets is the rate-limiting step. Under these circumstances, which are valid at the concentrations employed in the present experiments, the kinetics of droplet coalescence become first-order and follow a first-order reaction equation described by Equation 5-4, where the droplet number, N , decays from an initial number, N_0 , as a function of time, t , with a first-order rate constant, k .^{216,217}

$$N = N_0 \exp(-kt) \quad \text{Equation 5-4}$$

By contrast, Ostwald ripening is the growth of large droplets at the expense of smaller ones. The origins of this mechanism are understood by changes in solubility, $C(r)$, of a solute with the curvature of the droplet/solution interface or droplet radius, r . Specifically, there is a surface effect that decreases protein solubility with increasing particle radius, r , as can be shown through the Gibbs-Thompson equation, Equation 5-5.²¹⁸⁻²²⁰ Here, C_∞ is the protein solubility in the protein-poor phase of the completed ATPS, γ is the surface tension of the droplet/water interface, V_m is the molar volume of the protein in the protein-rich phase, r is the radius of a droplet, R is the ideal gas constant, and T is the absolute temperature.

$$C(r) = C_\infty \exp\left(\frac{2\gamma V_m}{rRT}\right) \sim C_\infty \left(1 + \frac{2\gamma V_m}{rRT}\right) \quad \text{Equation 5-5}$$

A decreasing concentration gradient in the radial direction extends out from the surface of sufficiently small droplets, while an increasing gradient exists near larger droplets.²²¹ Such gradients ultimately lead to diffusive transfer of material from small droplets to larger ones. Throughout this process, the average droplet radius increases with time as sufficiently large ones release fewer and fewer proteins per unit surface area into the bulk. The droplet number, N , in a system undergoing Ostwald ripening should follow second-order kinetics described by Equation 5-6.^{220,222}

$$\frac{1}{N} = \frac{1}{N_0} + kt \quad \text{Equation 5-6}$$

The idea that droplets grow via an Ostwald-like ripening process has been proposed for cluster growth in a variety of protein systems; however, the scattering decays were best fit to the Kohlrausch-Williams-Watts, KWW, model described by Equation 5-1.²²³⁻²²⁵ The normalized light scattering data and KWW fits for each isotherm are provided in Figure 5-9. The data are organized into three panels corresponding to the 90, 60, and 40 mg/mL mAb samples. Again, these fits to the KWW model provided an apparent rate constant for ATPS formation, k . The cooperativity exponent, β , accounts for cooperative, where $\beta > 1$, and anti-cooperative, where $\beta < 1$, features of the decays observed at high and low temperatures, respectively.

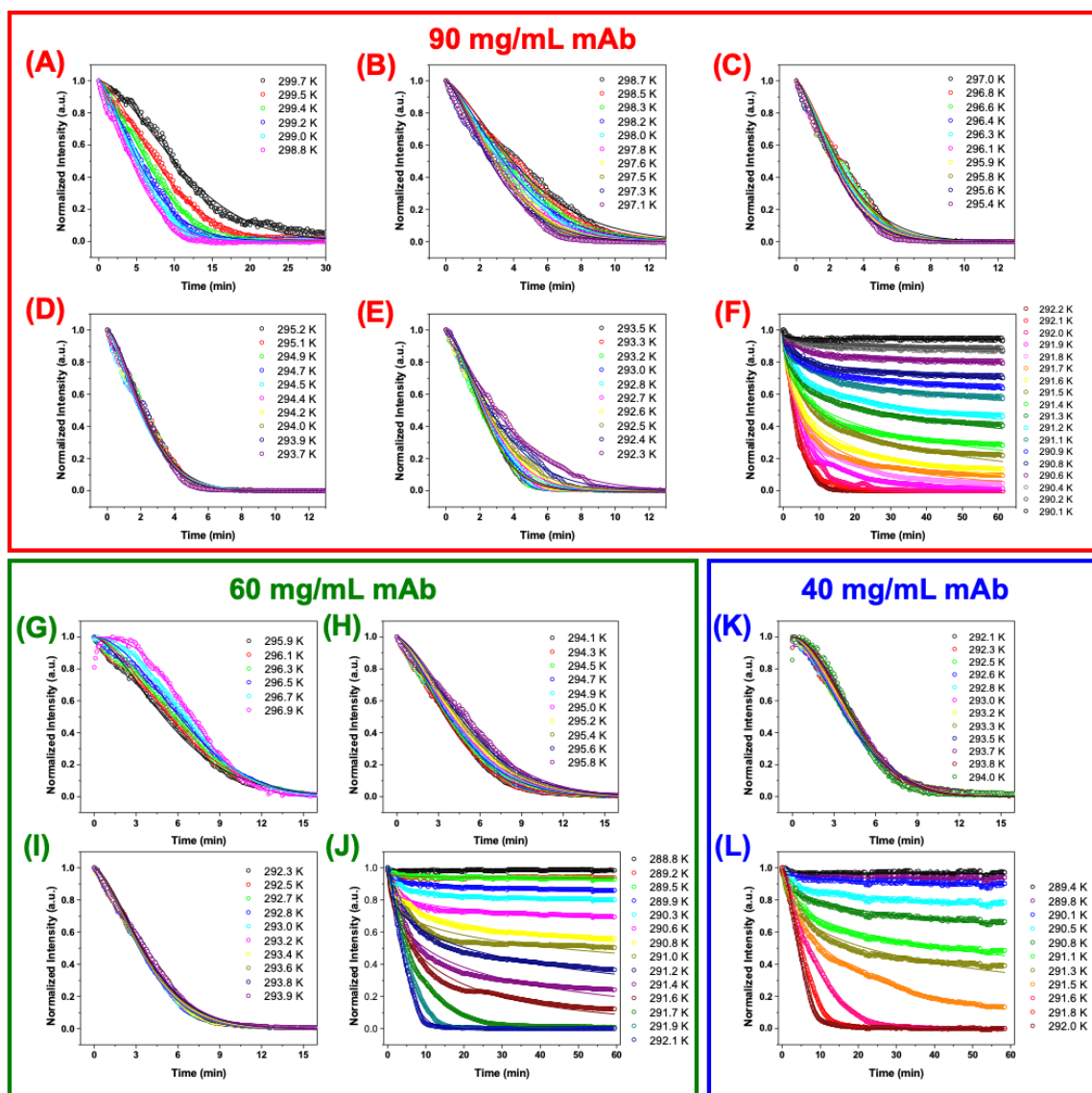


Figure 5-9: Normalized light scattering isotherms and KWW fits. The data are grouped into three panels corresponding to (red box) 90 mg/mL, (green box) 60 mg/mL, and (blue box) 40 mg/mL mAb concentrations all at 20 mg/mL PEG. The 90 mg/mL data are displayed in six plots with decreasing temperature: (A) 299.7 – 298.8 K, (B) 298.7 – 297.1 K, (C) 297.0 – 295.4 K, (D) 295.2 – 293.7 K, (E) 293.5 – 292.3 K, and (F) 292.2 – 290.1 K. The 60 mg/mL data are displayed in four plots with decreasing temperature: (G) 296.8 – 295.8 K, (H) 295.7 – 294.0 K, (I) 293.8 – 292.2 K, and (J) 292.0 – 288.7 K. The 40 mg/mL data are displayed in two plots with decreasing temperature: (K) 294.0 – 292.1 K and (L) 292.0 – 289.4 K.

Herein, the KWW equation empirically modeled the separation of a cloudy droplet dispersion into a clear, equilibrated APTS over time, t , by using a cooperativity exponent, β , and an apparent APTS formation rate constant, k . The fitted values of β for the 90 mg/mL mAb

sample are plotted as a function of temperature in **5-10**. As can be seen, ATPS formation was cooperative above T_{gel} with $\beta = \sim 1.5$, indicating that the reduction of scattering intensity was faster than a regular exponential decay. ATPS formation for a solution containing a high concentration of droplets should follow a standard exponential decay, where $\beta = 1$, if coalescence governs the separation, since the rate-limiting step is just the rupture of an interfacial water layer between two droplets.²¹⁶ However, the high density of protein droplets relative to water should cause them to fall to the bottom of the capillary tube via gravitational sedimentation, as depicted in Figure **5-2**. Therefore, as the droplets grew larger with time, they should have settled ever faster.²²⁶ Thus, the observed cooperativity was consistent with ATPS formation governed by droplet coalescence, but accelerated by sedimentation.

The temperature-dependent kinetics of ATPS formation provided further insight into the reaction mechanism. An Arrhenius plot of the fitted k values, i.e. $\ln(k)$ versus $1000/T$, is provided in Figure **5-10B**. As can be seen in the metastable region, ATPS formation accelerated as the temperature was lowered below T_{ph} . The fit to the Arrhenius law, drawn as solid black line over the red data points, revealed a negative apparent activation energy of $E_{\text{A,app}} = -35 \text{ kcal mol}^{-1}$, which was inconsistent with the positive $E_{\text{A,app}}$ expected for an elementary coalescence reaction. By contrast, $\ln(k)$ began to decrease modestly as the temperature was cooled below T_{meta} . The spinodal region could also be fit to the Arrhenius model, as drawn by the solid black line over the green data points, providing a slightly positive apparent activation energy of $E_{\text{A,app}} = 1 \text{ kcal mol}^{-1}$ that was smaller than the dissociation energy of typical water-water hydrogen bonds.^{227,228} The small, positive value of $E_{\text{A,app}}$ in the spinodal region was consistent with the energy required to rupture the aqueous film between two droplets and initiate coalescence.

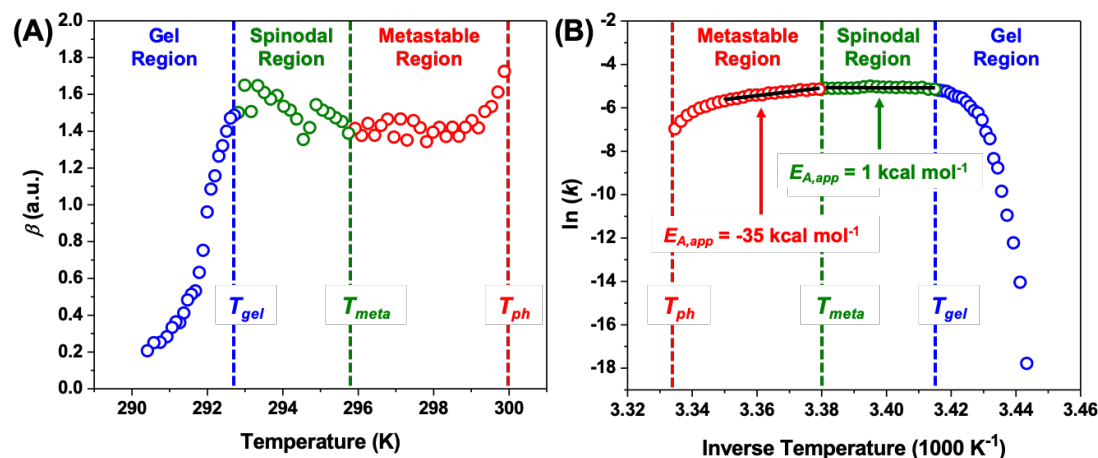


Figure 5-10: Temperature-dependent KWW parameters for the kinetics of ATPS formation in a solution of 90 mg/mL mAb and 20 mg/mL PEG. (A) The cooperativity exponent, β , is plotted as a function of temperature. The β values are colored to indicate the gel region from 290.4 to 292.8 K (blue data points), the spinodal region from 293.0 - 295.8 K (green data points), and the metastable region from 295.9 - 299.9 K (red data points). (B) The natural log of the rate constants, $\ln(k)$, are presented in an Arrhenius plot. The $\ln(k)$ data points are colored according to the regions defined in (A). The two solid black lines are linear fits to the data on either side of T_{meta} , which were used to determine the apparent activation energies, $E_{A,app}$, for ATPS formation in the metastable and spinodal regions.

The KWW parameter for additional concentrations of mAb are plotted in Figure 5-11.

The cooperativity exponents, β , and apparent rate constants, k , determined for the 90, 60, and 40 mg/mL mAb solutions with 20 mg/mL PEG are plotted as a function of temperature in Figure 5-11A and Figure 5-11B, respectively. Moreover, Arrhenius plots constructed from the measurements of k are provided in Figure 5-11C. We observed several generic features of temperature dependent phase separation kinetics for all mAb concentrations. Firstly, the reaction slowed down as the temperature approached T_{ph} , i.e. k decreased near T_{ph} . Secondly, the rate constant of the reactions reached a maximum at intermediate temperatures. Lastly, the phase separation became completely arrested at colder temperatures near T_{gel} .

Interestingly, k slows down near T_{ph} most dramatically under the 90 mg/mL conditions, as can be seen in the red data of Figure 5-11B. The hindrance of ATPS formation at the highest

temperature is consistent with an accelerated rate of dissociation. Indeed, T_{ph} occurs at a lower temperature for the 60 and 40 mg/mL mAb conditions, which prohibits measurements of ATPS formation at higher temperature where dissociation would be accelerated further. The attenuation of k near T_{ph} , is mirrored by an increase in β . For the 90 mg/mL sample, the nearly constant value of $\beta \sim 1.5$ at intermediate temperatures between 293 - 299 K increased slightly near T_{ph} , i.e. above 299 K. The more pronounced cooperativity in ATPS formation may indicate a prolonged lifetime of droplets due to enhanced protein dissociation from protein-rich droplets. The rate of ATPS formation was faster at higher mAb concentrations for all temperatures that did not gel, which can be seen by comparing the blue to green to red data in Figure **5-11B** at temperatures above $T \sim 292$ K. At lower mAb concentrations, the time required for droplet growth should be longer, thereby prolonging ATPS formation.

The natural log of the time constant for ATPS formation, $\ln(\tau)$, obtained from the negative of $\ln(k)$, represents a characteristic time scale for processes that contribute to ATPS formation. These time constants were found to lengthen dramatically as the temperature was lowered into the gel state for all mAb concentrations. The time constants are plotted on a natural log scale for the three protein concentrations in Figure **5-11D**.

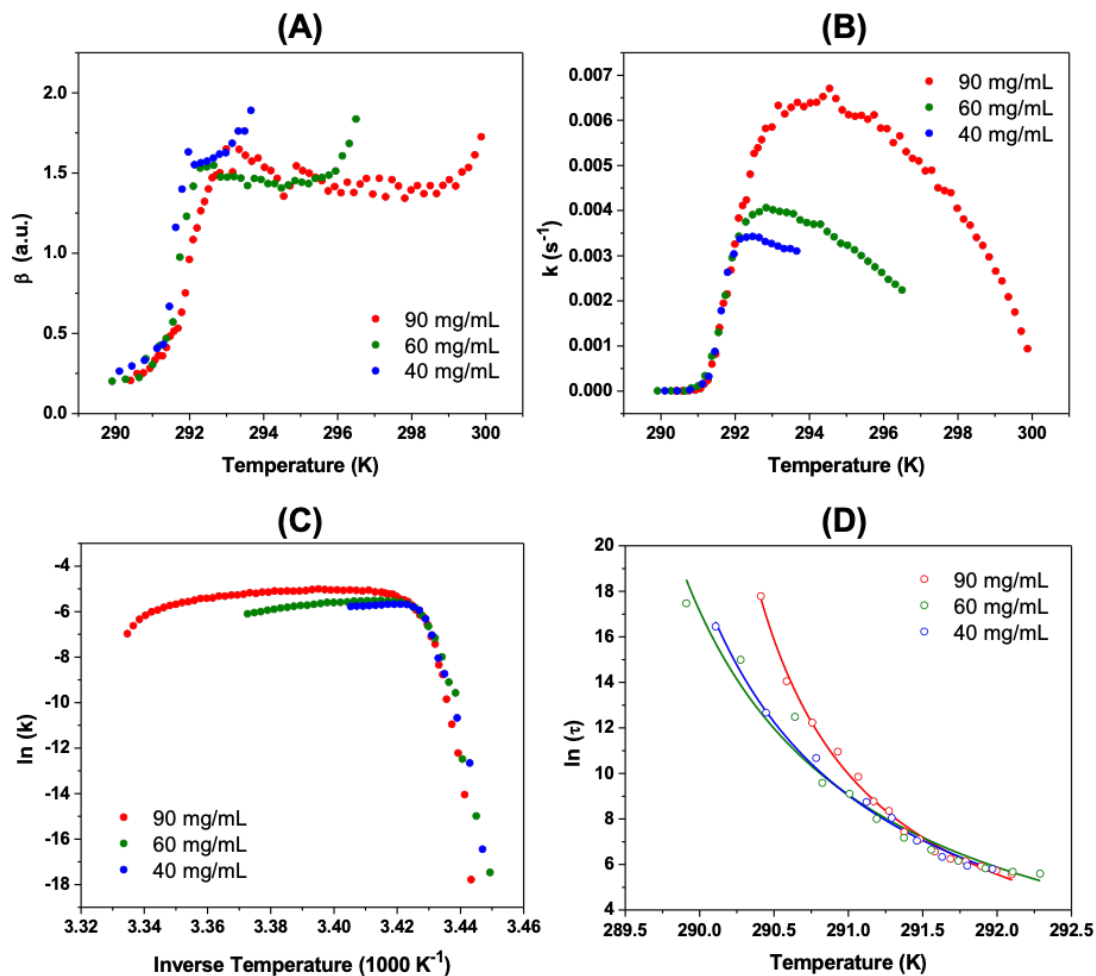


Figure 5-11: Summary of (A) the KWW cooperativity exponents and (B) the rate constants as a function of temperature for three mAb concentrations in 20 mg/mL PEG. (C) An Arrhenius plot of $\ln(k)$ vs. $1000/T$ and (D) a VFT plot of $\ln(\tau)$ versus T were prepared from the KWW parameters. The data points in (A-D) are colored according to the mAb concentration of either 40 mg/mL (blue), 60 mg/mL (green), or 90 mg/mL (red). The solid lines in (D) represent fits to the VFT model

We also observed distinct temperature-dependent regions in the kinetics of ATPS formation for 60 and 40 mg/mL mAb solutions, as shown in Figure 5-12. A spinodal region, however, was not present in the 40 mg/mL mAb solution as can be seen from the lack of a region characterized by a small, positive $E_{A,app}$ for the triangular data points.

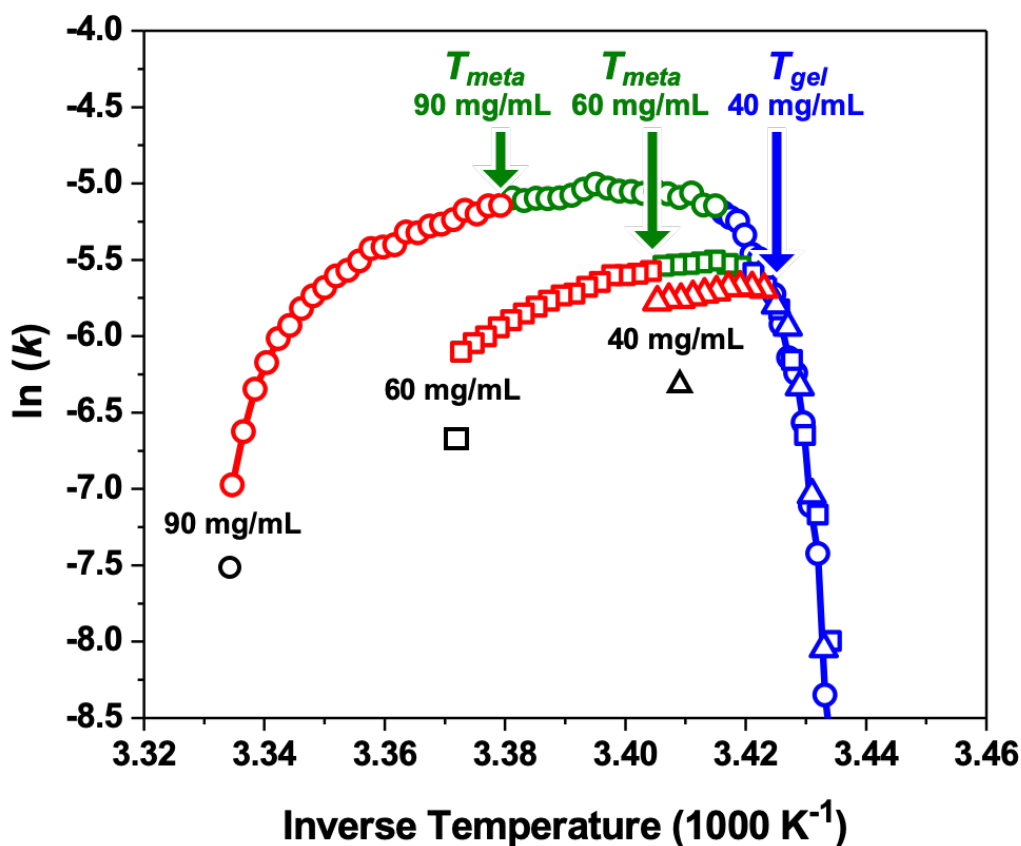


Figure 5-12: Arrhenius plots for the kinetics of ATPS formation in solutions containing 90 mg/mL (circle data points), 60 mg/mL (square data points), and 40 mg/mL (triangle data points) mAb in the presence of 20 mg/mL PEG. The natural log of the rate constants, $\ln(k)$, for each mAb concentration versus inverse temperature, $1000/T$, is divided into metastable (red data points), spinodal (green data points), and gel (blue data points) regions. The solid red and blue curves are provided as guides to the eye.

ATPS formation became anticooperative, i.e. $\beta < 1$, upon cooling below 292 K into the gel region, as can be seen in the blue data of Figure 5-12. This crossover occurred concomitantly with a dramatic reduction in $\ln(k)$, as depicted by the blue data points in Figure 5-12. As can be seen, $\ln(k)$ displayed an asymptotic decrease below T_{gel} that was reminiscent of changes in physical properties due to glass formation.²²⁹ To relate the abrupt deceleration of ATPS formation to the fragility of the arrested state formed below T_{gel} , the kinetics data in the gel region were

converted to time constants, τ , by taking the reciprocal of k . The $\ln(\tau)$ values for the 90 mg/mL mAb solution were plotted directly versus temperature in Figure 5-13, which could be fit to the Vogel-Fulcher-Tammann, VFT, law provided in Equation 5-7: The VFT fit to the data points is shown as a solid blue curve in Figure 5-13.²²⁹

$$\ln(\tau) = \ln(\tau_0) + \frac{D_{\text{VFT}} T_0}{T - T_0} \quad \text{Equation 5-7}$$

Here, the VFT law describes the melting of the kinetically arrested gel state by an ideal gelation temperature, T_0 , an intrinsic ATPS formation time constant, τ_0 , and a fragility index, D_{VFT} . The gel state formed below an ideal gelation temperature, $T_0 = 289.6$ K, where the time scale required for phase separation become infinitely slow, i.e. $\ln(\tau)$ approached infinity. As the temperature was increased toward the spinodal region, the ATPS formation time constants decreased rapidly and approached an intrinsic time constant, characterized by $\tau_0 = 0.6$ s, as T increased toward infinity. This extrapolated value for τ_0 provides an estimation of the time scale for collective protein reorganization during droplet coalescence and is on the order of the coalescence time period measured for oil droplet dispersions in water.²³⁰ The fragility index ($D_{\text{VFT}} = 0.05$) quantifies the weak resistance of the gel structure to accelerated phase separation as the temperature was increased above T_0 . Indeed, the measured fragility index was astoundingly weak in comparison to strong glass forming liquids like SiO_2 , which has been characterized by $D \sim$ 153.^{231–233}

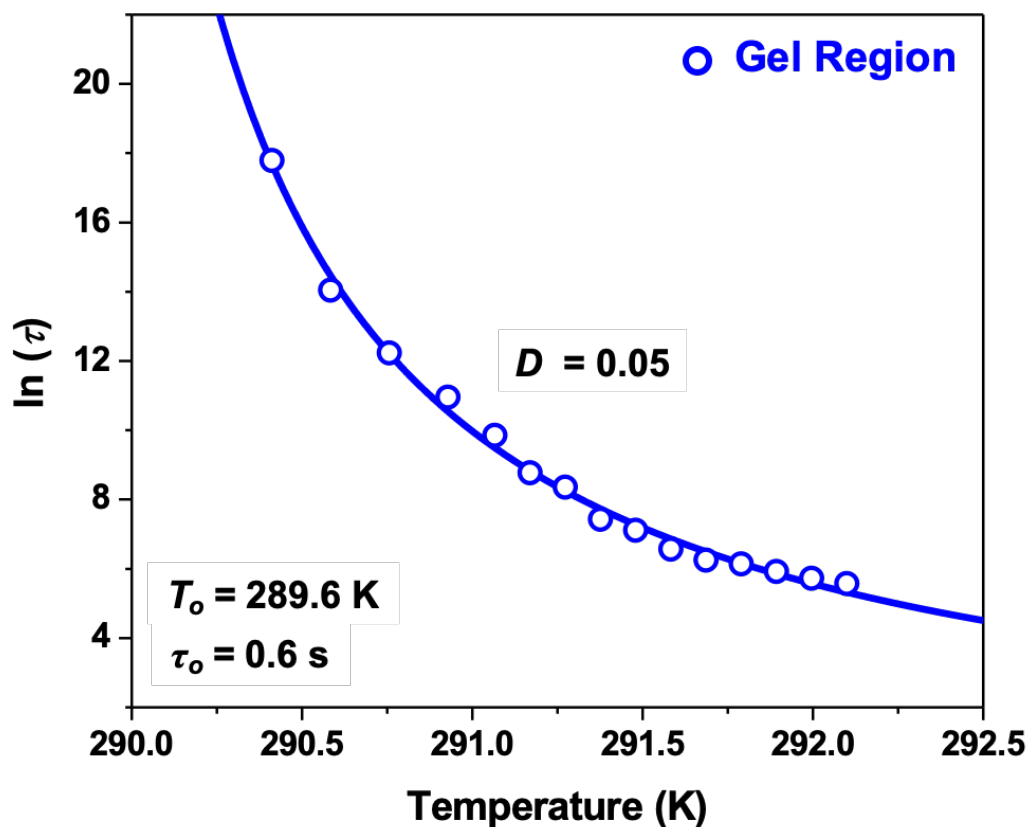


Figure 5-13: Time constants for ATPS formation as a function of temperature near T_{gel} for a solution of 90 mg/mL mAb and 20 mg/mL PEG. The natural log values of the time constants, $\ln(\tau)$, in the gel region, where $\beta < 1$, are plotted as blue data points along with the fit to the VFT model, shown as a solid blue curve.

It should be noted that the range of temperatures used in the VFT analysis were characterized by $\beta < 1$. The fitted parameters of gelation determined from fitting to the VFT model are provided in Appendix B. It would be informative to compare the fragility index, D_{VFT} , of the gels formed in mAb solutions to other soft colloidal systems. However, measurements of the fragility index for colloids are commonly based on concentration-dependent particle dynamics, rather than the temperature dependence of ATPS formation kinetics employed in this work.^{208,209} It should be note that the values of β for the 40 mg/mL sample lack a region of

intermediate temperatures where β is constant. This provides an additional indication that gelation occurs in the metastable region of the phase diagram at lower mAb concentrations.

The apparent activation energies for ATPS formation, $E_{A,app}$, were obtained from the Arrhenius plots in Figure **5-11C**. We calculated the values for $E_{A,app}$ by multiplying the first derivative of the Arrhenius plot by the negative of the ideal gas constant. The results are plotted as a function of temperature in Figure **5-14**. As can be seen in Figure **5-14A**, $E_{A,app}$ shows similar temperature dependence for all three mAb concentrations. At temperatures below 293 K, ATPS formation is hindered by a large positive $E_{A,app}$ due to gelation. On the other hand, at intermediate temperatures, $E_{A,app}$ shows an average close to 1 kcal mol⁻¹. With increasing temperature, $E_{A,app}$ clearly becomes negative with an average of ~ -35 kcal mol⁻¹. For clarity, the data are also plotted separately for each mAb concentration in Figure **5-14B**, **5-14C**, and **5-14D**. For each concentration, the average and standard deviation of the $E_{A,app}$ values are provided for the spinodal and metastable regions, which are labeled with green and red text, respectively.

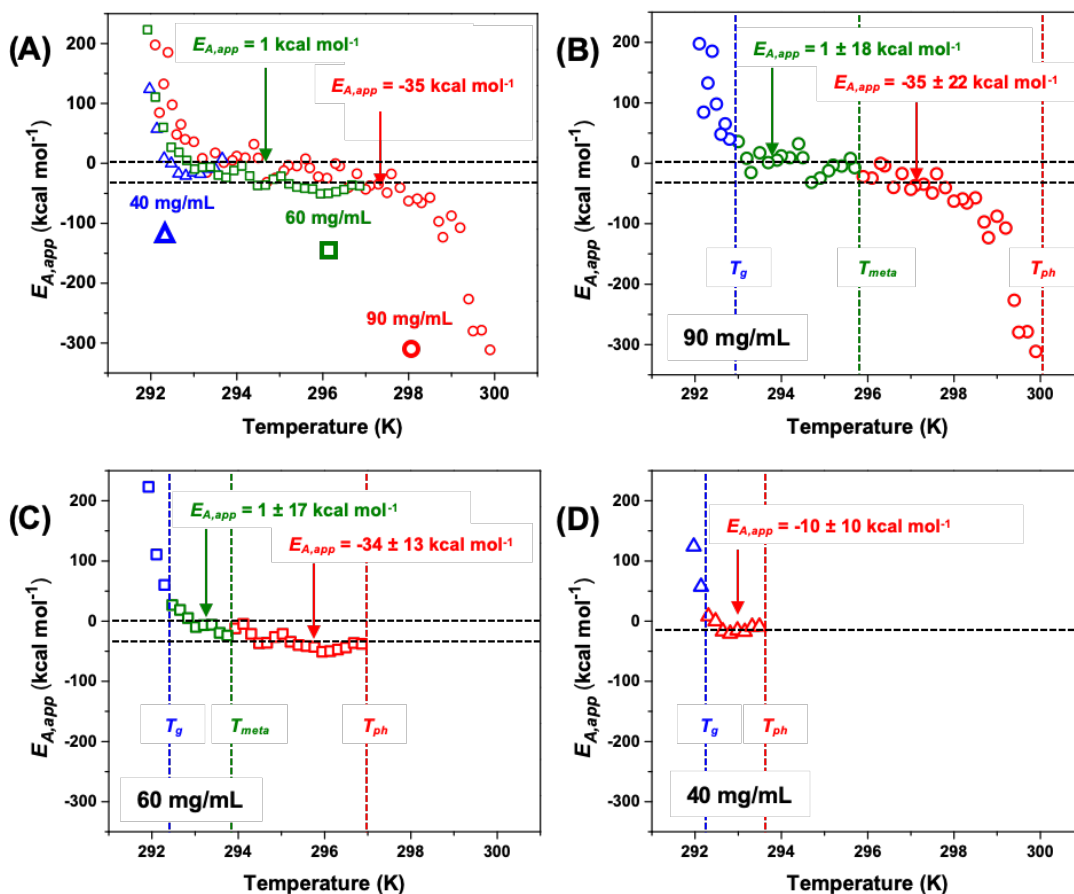


Figure 5-14: Point-by-point activation energy determinations as a function of temperature.

In order to explore the origins of gelation, we performed PEG titrations at various pH values. The data are plotted together in Figure 5-15. The data show that the PEG dependence of T_{gel} is similar for the two pH values. The effect of PEG on T_{ph} on the other hand changes dramatically. This data suggests that the driving force for gelation may not be the same as that for phase separation.

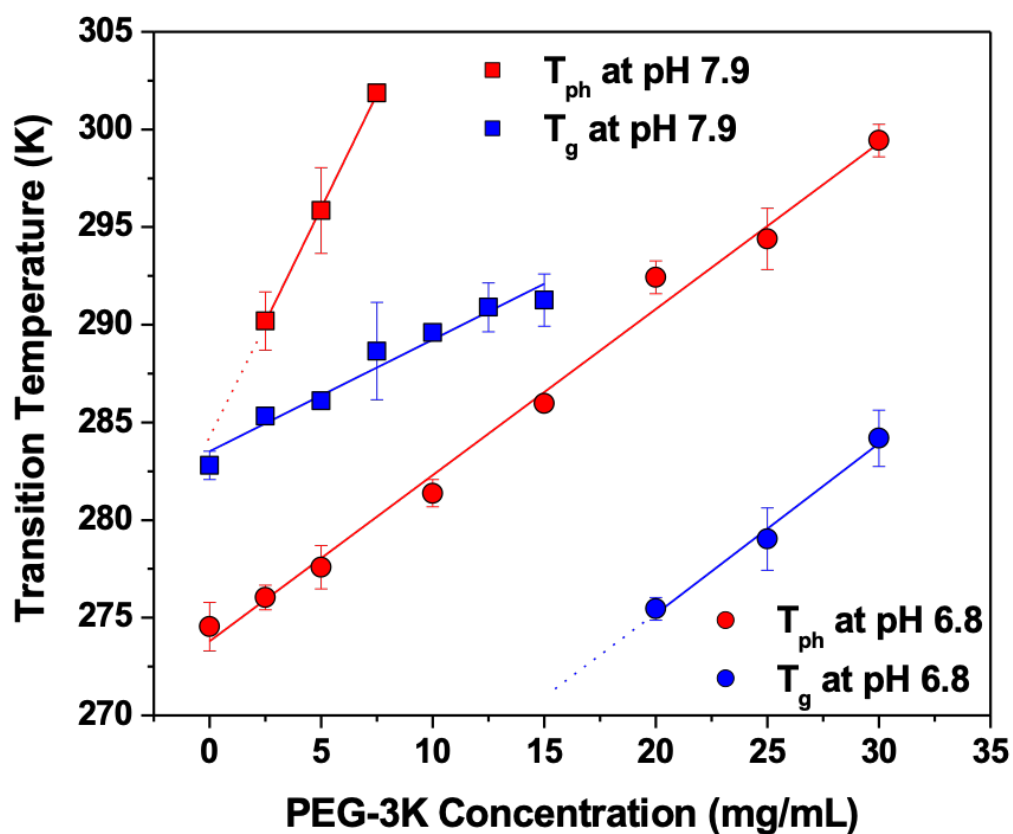


Figure 5-15: Phase separation and gelation temperatures versus PEG concentration at two pH values.

A Stepwise Mechanism to Explain the Non-Arrhenius Kinetics of ATPS Formation

The thermodynamics of colloidal phase diagrams have been measured for numerous systems that undergo LLPS and gelation.^{32,204,205,207,223,234–236} By measuring ATPS formation as a function of time along a temperature gradient, we directly visualized the metastable, spinodal, and gel regions of the phase diagram for mAb solutions containing PEG. This was possible because the temperature gradient measurements allowed the kinetics of ATPS formation to be extracted in

parallel over a range of temperatures. The kinetic measurements suggest a two-step mechanism for ATPS formation that is depicted schematically in Figure 5-16. After droplet nucleation has taken place, ATPS formation should continue via the first step of droplet growth, which involves the sequential, reversible addition of monomers into growing droplets, illustrated in Figure 5-16A, Step 1. Subsequently, ATPS formation is completed by the second step of irreversible droplet coalescence, illustrated by Figure 5-16A, Step 2. The rates of these two steps should have opposite temperature dependencies, which leads to a crossover in the rate-limiting step at T_{meta} . The distinct apparent activation energies measured in the metastable and spinodal regions can be related to the effects of temperature on the elementary activation energies of the two-step mechanism. This idea is depicted by the two reaction coordinate diagrams in Figure 5-16B that represent different temperatures below T_{ph} .

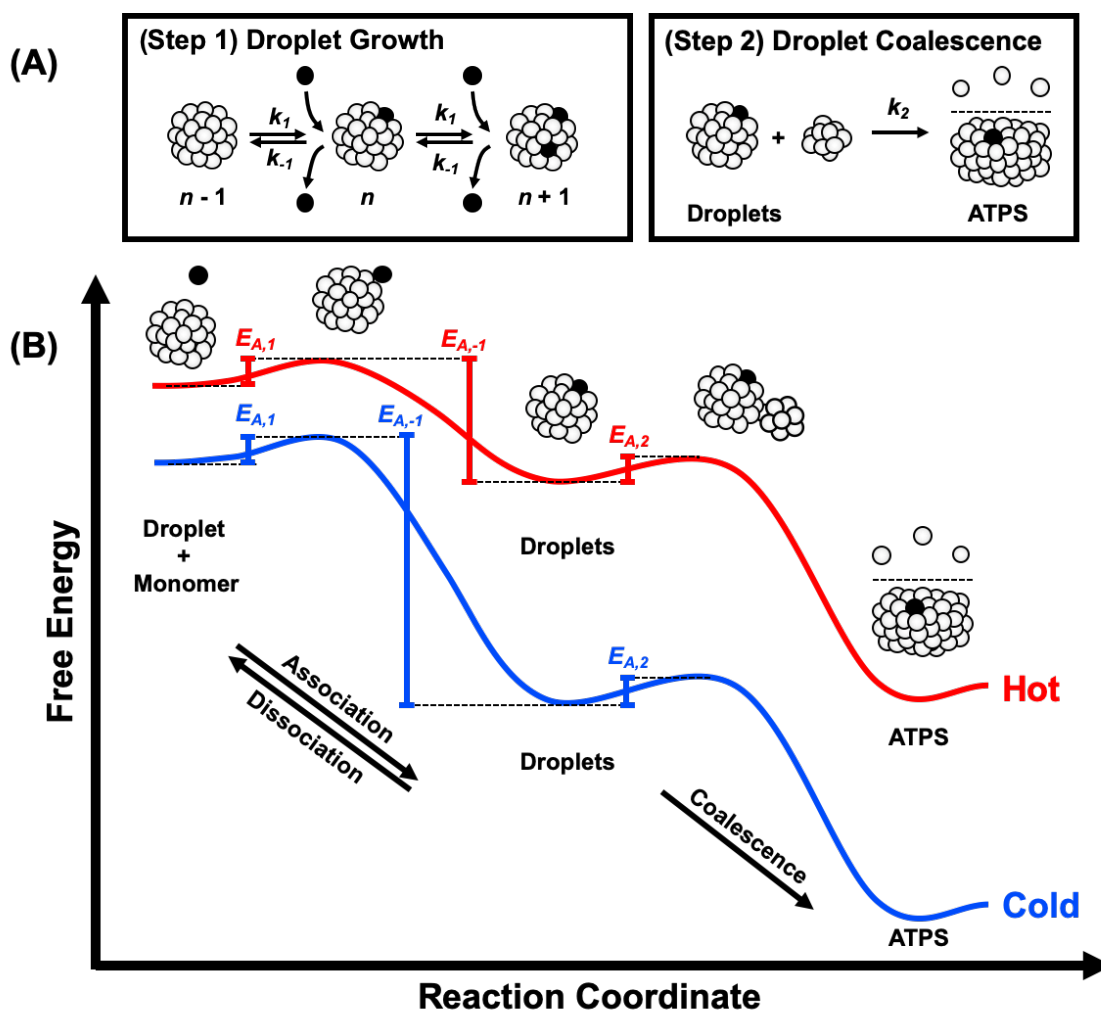


Figure 5-16: Two-step mechanism for ATPS formation. (A) ATPS formation begins with droplet growth (Step 1 in A) involving the sequential, reversible association of protein monomers with protein-rich droplets, characterized by the association, k_1 , and dissociation, k_{-1} . The circles represent folded protein monomers, several of which have been colored in black to highlight the growth mechanism. The number of monomers in the droplets, n , are not drawn to scale. The final stage of ATPS formation is the irreversible coalescence of droplets (Step 2 in A), characterized by the coalescence rate constant, k_2 . (B) The reaction coordinate diagrams for ATPS formation at hot (red curve) and cold (blue curve) temperatures relate the apparent activation energies measured in Figure 5-10 to the two-step mechanism in (A). The activation energies for the elementary steps are not drawn to scale in (B).

When a protein solution is cooled below T_{ph} , it rapidly becomes turbid as protein-rich droplets form within seconds.²⁰⁵ The cloudy droplet suspension slowly becomes transparent via ATPS formation on the order of minutes.^{86,89} Once a clear, macroscopic protein-rich phase forms, the system has reached equilibrium. The process of ATPS formation, as depicted in Figure 5-

16A, is reminiscent of a simple consecutive reaction with a reversible first step and an irreversible second step, as described by Equation **5-8**:



where A represents the initial droplet suspension. Over time, these droplets grow by reversible monomer addition into larger droplets, denoted by B . The larger droplets irreversibly coalesce to form an ATPS, represented by C . As growth and coalescence occur, the intensity of the light scattered by the initial droplet suspension decreases. Our analysis shows that the kinetics of ATPS formation in mAb solutions is well described by cooperative exponential decays with an apparent rate constant, k . Based on Equation **5-8**, however, k should be influenced by the elementary rate constants for monomer addition, k_1 , and dissociation, k_{-1} , as well as the elementary rate constant of coalescence, k_2 . The exact relationship of k to k_1 , k_{-1} , and k_2 is complex in these experiments because Equation **5-8** represents a simplification of the proposed mechanism illustrated in Figure **5-16A**. Nevertheless, the two-step mechanism provides a useful simplification for understanding the effects of temperature on the apparent value of k .

There are several experimental limitations of the measurements presented in the chapter. First is the time-scale of the measurements. To begin the experiment a sample-containing capillary is placed in contact with the hot and cold sides of the device at $t = 0$ s. As protein-rich droplets form, we expect the light scattering to increase. However, a time period of $t \sim 60$ s is required to form a steady-state temperature gradient across the sample. As such, the kinetic analysis was only performed on data collected after 60 s, after which the intensity decreases monotonically. This slow time scale ($\sim 10^1$ - 10^3 s) should be too slow to report on nucleation

events ($\sim 10^{-2}$ - 10^0 s).²⁰⁵ As such, we expect that changes in scattering intensity report on droplet growth and coalescence.

The scattering intensity measured on an optical dark-field microscope depends on both the concentration and size of the droplets inside of the sample-containing capillary. At early times after a sample has been cooled below T_{ph} , droplets should nucleate until a steady-state number of droplets have formed. We expect that by 60 s, the changes in the light scattering intensity should report on the growth rate of a steady-state concentration of droplets and their coalescence into an ATPS.

The effect of droplet size on the light scattering intensity depends on the ratio of the droplet radius, r , relative to the wavelength of the incident light, $\lambda \sim 350$ - 720 nm. Scattering from small droplets with $r < \sim 25$ nm should be weak and governed by Rayleigh scattering, which is dominated when the value of r/λ is less than 5. The light scattering from large droplets with a $r > \sim 2.5$ μm should also be weak and governed by the geometric scattering, which is relevant for values of r/λ that are greater than 5. Based on these arguments, the homogenous state, consisting mostly of protein monomers with $r \sim 5$ nm, and the equilibrated ATPS with $r \sim 5$ μm should both be nearly optically transparent. Thus, the intensity in TGM experiments should be dominated by Mie scattering, which dominates for values of $r/\lambda \sim 0.5$. These arguments suggest that droplets ranging from $r \sim 25$ nm to ~ 2.5 μm produce the signal observed in the TGM kinetics data. Indeed, nucleation events, which involve monomer, dimers, trimer, and higher order oligomers are small and should not scatter much light.

Our mechanistic interpretations are simplified and rely on the assumption that the scattering intensity reports on the number of droplets, N . In reality, however, the intensity depends on both the concentration and size of protein-rich droplets, as discussed above. We note that additional complications could arise from non-spherical droplet geometry (e.g. networks

formed in the gel state), variations in ensemble size distributions, multiple scattering, the collection of light over integrated scattering angles, and the use of a continuum light source.

Another important point of concern is the diffusion of material (e.g. proteins or droplets) along the sample capillary during an experiment. The diffusion coefficient of particle, D_{SE} , can be approximated by the Stokes-Einstein equation, provided in Equation 5-9, where k_B is the Boltzmann constant, T is the temperature, η is the viscosity, and r is the radius of the particle.

$$D_{SE} = \frac{k_B T}{6\pi\eta r} \quad \text{Equation 5-9}$$

The value of D_{SE} at 295 K for a mAb monomer is $\sim 5 \times 10^{-7}$ cm²/s, assuming $r = 5$ nm and the viscosity is that of pure water, 8.9×10^{-4} Pa s. Under the same solution conditions, a droplet with $r = 1$ μ m is expected to diffuse at a slower rate, $D_{SE} = 2.4 \times 10^{-9}$ cm²/s. The mean displacement, $\langle \Delta^2 x \rangle^{(1/2)}$, of these particles at various time points during the experiment can be estimated using Equation 5-10.

$$\langle \Delta^2 x \rangle^{1/2} = (6D_{SE}t)^{1/2} \quad \text{Equation 5-10}$$

The values of $\langle \Delta^2 x \rangle^{(1/2)}$, for the monomer at 1, 15, and 60 min were 0.132, 0.512, and 1.024 mm. The values of $\langle \Delta^2 x \rangle^{(1/2)}$, for the droplet at 1, 15, and 60 min were 0.009, 0.036, and 0.072 mm. Displacement along the temperature gradient has also been considered by multiplying the mean displacement by the temperature gradient (6.66 K/mm). The temperature displacement for the monomer at 1, 15, and 60 min were 0.881, 3.414, and 6.827 K. The temperature displacements for the droplet at 1, 15, and 60 min were 0.062, 0.241, and 0.483 K. As can be seen, the mAb monomer shows considerable diffusion during the experiment, while the droplets

are more localized. Since droplets form within 1 minute and ATPS formation is completed in about 15 minutes, only the lower end of these ranges need to be considered. Indeed, a growing droplet would probably experience less than a quarter of a degree temperature change before ATPS is completed.

Despite the limitations of monitoring the reaction by simple light scattering intensity under a dark-field microscope, the temperature dependence of the apparent rate constant for ATPS formation provides unique insight into the mechanism of the phase separation. The fact that ATPS formation slows down upon cooling below T_{meta} , which can be seen by the fact that the green data points decrease very slightly from left to right in Figure 5-10B, suggests that spinodal decomposition is rate-limited by the second step of coalescence, which is illustrated by Figure 5-16A, Step 2. Indeed, the rate constant for coalescence has previously been shown to be proportional to temperature.^{86,89} Based on this similarity, we assign the $E_{A,\text{app}}$ value for spinodal decomposition, marked by the black line over the green data in Figure 5-10B, to the activation energy for coalescence, $E_{A,2}$. This assignment is depicted schematically in Figure 5-16B. The acceleration of ATPS formation upon cooling through the metastable region, which can be seen by the fact that the red data points increase from left to right in Figure 5-10B, however, is distinct from coalescence. In fact, the negative $E_{A,\text{app}}$ value in the metastable region, marked by the black line over the red data in Figure 5-10B, indicates that ATPS formation is rate-limited by the first step of droplet growth and that there should be three activation energies to take into account: the first two corresponding to the reversible steps of the droplet growth, labeled by $E_{A,1}$ and $E_{A,-1}$ in Figure 5-16B, and the third for droplet coalescence in the forward direction, labeled by $E_{A,2}$ in Figure 5-16B. We expect the value of $E_{A,2}$ to be independent of temperature. Moreover, if droplet growth is diffusion-limited, then $E_{A,1}$ should also have a temperature-independent value.^{237,238} Based on these assumptions, the negative $E_{A,\text{app}}$ in the metastable region should reflect the

influence of temperature on the activation energy required to dissociate protein monomers from the surface of growing droplets, which again is illustrated by $E_{A,-1}$ in Figure 5-16.

Upon cooling below T_{ph} , the solution becomes supersaturated, i.e. the initial protein concentration is higher than the concentration in the protein-poor phase of the equilibrated ATPS. This concentration difference can be related to the degree of supersaturation, which quantifies the thermodynamic driving force for LLPS.²³⁹ At warmer temperatures near T_{ph} , the addition of a monomer to a droplet should be free energy favorable, but the absolute change in free energy should be small, which is illustrated by the red curve in Figure 5-16B. As the temperature is lowered, the supersaturation increases and the free energy difference for droplet growth becomes larger, which is exemplified by the blue curve in Figure 5-16B. As a consequence, $E_{A,-1}$ becomes higher at colder temperatures and droplet growth accelerates. This idea is supported by the linear dependence of k on supersaturation in the metastable region, which was estimated from the colloidal phase diagram in Figure 5-17.²³⁹⁻²⁴¹

Although droplets grow ever more rapidly at lower temperatures, the value of k begins to decrease below T_{meta} , marked by dashed vertical green line in Figure 5-10B, because droplet coalescence becomes the rate-limiting step. The gradual and continuous transition from the metastable region into the spinodal region, marked by the transition from the red to green data points in Figure 5-10B, should occur because droplet growth becomes faster at lower temperatures, while droplet coalescence is proportional to temperature. These ideas are consistent with the observation that T_{meta} is the first temperature at which ATPS formation comes to completion. Moreover, the two-step mechanism provides a simple framework for modeling the kinetics of both the metastable and spinodal regions.

We expect droplet growth to dominate the kinetics of ATPS formation in the metastable region, where we measured a negative $E_{A,app}$. Below, we consider 2 possibilities for the observed negative $E_{A,app}$. Case 1 is that the free energy of the thermodynamic states in Figure 5-16 change

with temperature. Classical nucleation theory predicts that the kinetics in the metastable region are controlled by Case 1.²³⁹ In particular, the theory predicts that the steady-state growth rate increases linearly with supersaturation, while the rate of nucleation should increase exponentially.^{15,239–241} We estimated the supersaturation at each temperature from the phase diagram to test the validity of Case 1 and also to test the idea that the apparent rate constants of ATPS formation, k , report on droplet growth, rather than nucleation. Supersaturation, s , was estimated using Equation 5-11,

$$s = \ln \left(\frac{C_0}{C_{\text{poor}}} \right) \quad \text{Equation 5-11}$$

where C_0 is the initial protein concentration, and C_{poor} is the equilibrium concentration of the protein-poor phase after a temperature quench. We obtained the values for C_{poor} at each temperature by fitting the binodal phase diagram, i.e. T_{ph} versus C , to Equation 5-11, where T_{crit} and C_{crit} are the critical temperature and concentration, while A and β are empirical parameters that determine the shape of the phase boundary.^{78,204,242,243} It should be emphasized that T_{crit} and C_{crit} are nominal values as the measurements were only made up to 100 mg/mL and Equation 5-12 assumes that the binodal curve is symmetric despite the ternary nature of the system, which has been shown to influence the shape of colloidal phase diagrams.^{34,46,80,204,213,243} Nevertheless, the data below 100 mg/mL was well-modeled by Equation 5-12.

$$T_{\text{ph}} = T_{\text{crit}} \left[1 - A \left(\frac{C_{\text{crit}} - C}{C_{\text{crit}}} \right)^{1/\beta} \right] \quad \text{Equation 5-12}$$

This analysis for estimating the supersaturation is depicted schematically in Figure 5-17A. Remarkably, the dependence of k on s , provided in Figure 5-17B, is approximately linear in

the metastable region, marked by the black line over the red data points in Figure **5-17B**, until reaching a maximum value at T_{meta} . At even higher values of s , i.e. lower temperature, the rate constant became arrested due to gelation, as shown in the blue data points. As described in the main text, this analysis suggests that the negative value of $E_{A,\text{app}}$ is related to the enhanced thermodynamic driving force for demixing as the temperature of the solution is decreased below T_{ph} .

In other words, the value of $E_{A,\text{app}}$ is related to the change in free energy with respect to temperature. Supersaturation should be related to the change in free energy upon forming protein-protein interactions, e.g. adding a protein to a droplet. The concept of supersaturation is included in Figure **5-16** by the difference in free energy between the initial state, involving a monomer and a droplet, and the intermediate state, involving a droplet. Based on Figure **5-17**, the change in free energy should be larger at lower temperatures. As a consequence, we expect the activation energy required for dissociation to increase and droplet growth to accelerate.

One could imagine a second case involving thermodynamic states that are fixed. Under Case 2, the reaction coordinate is again a multi-step process involving a reversible first step and an irreversible second step. The negative $E_{A,\text{app}}$ would imply that the reverse reaction in the first step has a large activation energy. As the temperature is lowered, the rate of the reverse reaction decreases sharply and the reversibility of the first step, i.e. droplet growth, is impeded, leading to an accumulation of intermediate droplets. As such, the observed rate of ATPS formation increases with cooling, until eventually it becomes limited by the second step of droplet coalescence in the spinodal region.

The negative $E_{A,\text{app}}$ in the metastable region, marked by the black line over the red data in Figure **5-10B**, would support the idea that LLPS is limited by a pre-equilibrium step in a multistep reaction, as drawn in Figure **5-16**.²⁴⁴ In fact, when k is collectively influenced by k_1 , k_{-1} , and k_2 , there should be 3 activation energies to take into account: 2 corresponding to the

reversible steps of the pre-equilibrium ($E_{A,1}$ and $E_{A,-1}$ in Figure **5-16**) and 1 for droplet coalescence in the forward direction ($E_{A,2}$ in Figure **5-16**). The relative magnitudes of the forward and reverse activation energies determine whether the overall apparent activation energy is positive or negative ($E_{A,app} = E_{A,1} + E_{A,2} - E_{A,-1}$). To estimate the value of $E_{A,-1}$ for the Case 2 scenario, we assumed that the association reaction was essentially diffusion-limited. Under diffusion-limited conditions, k_1 should exhibit a weak temperature dependence, proportional to the diffusion coefficient.^{237,238} Based on the small barrier for coalescence ($E_{A,2} = 1$ kcal mol⁻¹) measured in the spinodal region and the assumption of diffusion-limited association ($E_{A,1} \sim 0$ kcal mol⁻¹), the apparent activation energy measured in the metastable region provides an approximate barrier for the dissociation of protein monomers from protein-rich droplets ($E_{A,-1} \sim 35$ kcal mol⁻¹). This is in agreement with the apparent activation energy for dissociating protein-protein complexes by electrospray mass spectrometry.²⁴⁵

Although Case 2 might appear to offer a plausible interpretation for the negative $E_{A,app}$ in the metastable region, the supersaturation analysis presented in Figure **5-17** suggests the thermodynamic states do change with temperature. Thus, the temperature-dependent kinetics of ATPS formation are more accurately described by Case 1.

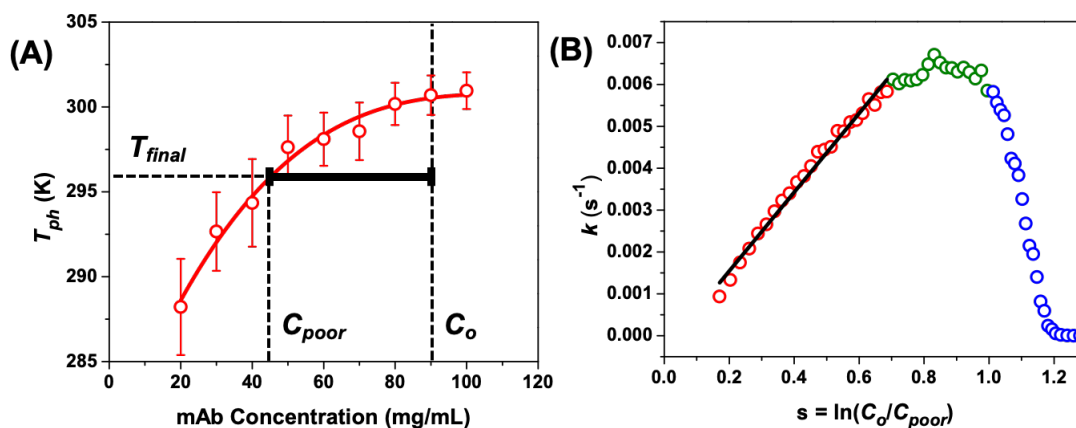


Figure 5-17: Analysis of the kinetics data, which was inspired by classical nucleation theory. (A) Binodal phase diagram, reproduced from Figure 5-5. The method for estimating the supersaturation is illustrated with the dashed and solid black lines in (A). The dashed vertical black line on the right hand side of the figure marks the initial protein concentration, C_0 . After a temperature quench to a final temperature, T_{final} . The equilibrium concentration of the protein-poor phase, C_{poor} , should be defined by the dashed vertical black line on the left hand side of (A). (B) The measured rate constants for ATPS formation plotted against the supersaturation. The solid black line in (B) is a linear fit to the data measured in the metastable region, consistent with growth kinetics as opposed to the exponential dependence expected for nucleation.

At even colder temperatures, ATPS formation becomes arrested by the formation of a kinetically trapped gel (blue data points in Figure 5-10B). Gelation should occur under conditions where the proteins assemble into an expansive fractal-like network of poorly packed protein clusters that cannot undergo coalescence to complete ATPS formation, as depicted in the droplet cartoon at 60 min in Figure 5-2.²⁰⁶ Indeed, the extremely fragile structure of the gel, as determined by the VFT model in Figure 5-13, $D_{VFT} = 0.05$, is consistent with a fractal-like network held together by a collection of weak and poorly optimized protein-protein interactions. The value of T_{gel} is rather insensitive to the concentration of the protein, as shown by the blue data points in Figure 5-15. T_{gel} occurs below the spinodal curve at high mAb concentration, e.g. $C = 90$ mg/mL mAb in Figure 5-2, which is consistent with previously proposed gelation mechanisms involving arrested spinodal decomposition.^{234-236,246} The phase diagram provided in Figure 5-5, however, demonstrates that gelation can also occur below the metastable region at

lower mAb concentrations. In fact, the location of T_{gel} relative to T_{meta} as a function of mAb concentration can be directly observed in the three Arrhenius plots provided in Figure 5-12. The fastest rate of ATPS formation occurs near T_{meta} for both the 90 and 60 mg/mL mAb samples, as indicated by the green arrows in Figure 5-12, where T_{meta} is above T_{gel} . The 40 mg/mL mAb solution, however, shows a maximum value for $\ln(k)$ at T_{gel} , which is marked by the blue arrow in Figure 5-12. This result demonstrates that T_{gel} can occur at the boundary of the metastable and gel regions of the phase diagram. As such, gelation in mAb solutions may occur by diffusion-limited cluster aggregation in the metastable region as opposed to arrested spinodal decomposition.²⁴⁷

Conclusion and Implications

Herein, it was shown that the kinetics of ATPS formation in mAb solutions containing PEG exhibits unique temperature-dependent signatures that correspond to distinct regions of a colloidal phase diagram. Analysis of these signatures suggests that the late stages of phase separation proceed in two steps, beginning with droplet growth and ending with droplet coalescence. The kinetics of ATPS formation is controlled by droplet growth in the metastable region, which accelerates with decreasing temperature due to a growing activation energy required for dissociating a protein from the surface of a droplet. The kinetics for spinodal decomposition, however, is distinct because the reaction pathway is limited by the second step of coalescence. The ability to explore the reaction coordinate diagram for ATPS formation via temperature gradient microfluidics may help to provide insights into the effects of solution conditions, e.g. crowders, salts, surfactants, buffers and pH, and protein properties on the phase behavior of mAb formulations, as illustrated in Figure 5-18. In a broader sense, the two-step mechanism should help provide insight into the phase behavior of colloids and polymers, as well as the phase separation of biomacromolecules inside living cells.¹⁹

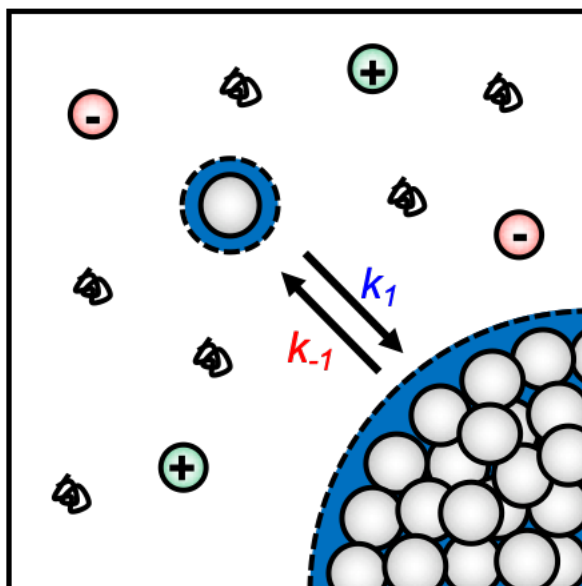


Figure 5-18: Schematic illustration of the effects of non-ionic crowders and salt ions on the association and dissociation of protein monomers to phase separated protein-rich droplets.

References

- (1) Collins, K. D.; Washabaugh, M. W. The Hofmeister Effect and the Behaviour of Water at Interfaces. *Q. Rev. Biophys.* **1985**, *18* (4), 323–422.
<https://doi.org/10.1017/S0033583500005369>.
- (2) Baldwin, R. L. How Hofmeister Ion Interactions Affect Protein Stability. *Biophys. J.* **1996**, *71* (4), 2056–2063.
- (3) Jungwirth, P.; Tobias, D. J. Ions at the Air/Water Interface. *J. Phys. Chem. B* **2002**, *106* (25), 6361–6373. <https://doi.org/10.1021/jp020242g>.
- (4) Omta, A. W.; Kropman, M. F.; Woutersen, S.; Bakker, H. J. Negligible Effect of Ions on the Hydrogen-Bond Structure in Liquid Water. *Sci. Wash.* **2003**, *301* (5631), 347–349.
- (5) Zhang, Y.; Cremer, P. S. Interactions between Macromolecules and Ions: The Hofmeister Series. *Curr. Opin. Chem. Biol.* **2006**, *10* (6), 658–663.
<https://doi.org/10.1016/j.cbpa.2006.09.020>.
- (6) Pegram, L. M.; Record, M. T. Thermodynamic Origin of Hofmeister Ion Effects. *J. Phys. Chem. B* **2008**, *112* (31), 9428–9436. <https://doi.org/10.1021/jp800816a>.
- (7) Zhang, Y.; Cremer, P. S. Chemistry of Hofmeister Anions and Osmolytes. *Annu. Rev. Phys. Chem.* **2010**, *61* (1), 63–83.
<https://doi.org/10.1146/annurev.physchem.59.032607.093635>.
- (8) Okur, H. I.; Hladílková, J.; Rembert, K. B.; Cho, Y.; Heyda, J.; Dzubiella, J.; Cremer, P. S.; Jungwirth, P. Beyond the Hofmeister Series: Ion-Specific Effects on Proteins and Their Biological Functions. *J. Phys. Chem. B* **2017**, *121* (9), 1997–2014.
<https://doi.org/10.1021/acs.jpcc.6b10797>.
- (9) Kuhlman, B.; Dantas, G.; Ireton, G. C.; Varani, G.; et al. Design of a Novel Globular Protein Fold with Atomic-Level Accuracy. *Sci. Wash.* **2003**, *302* (5649), 1364–1368.

- (10) Baase, W. A.; Liu, L.; Tronrud, D. E.; Matthews, B. W. Lessons from the Lysozyme of Phage T4. *Protein Sci.* **2010**, *19* (4), 631–641. <https://doi.org/10.1002/pro.344>.
- (11) Shoichet, B. K.; Baase, W. A.; Kuroki, R.; Matthews, B. W. A Relationship between Protein Stability and Protein Function. *Proc. Natl. Acad. Sci.* **1995**, *92* (2), 452–456. <https://doi.org/10.1073/pnas.92.2.452>.
- (12) Fabrizio Chiti; Christopher M. Dobson. Protein Misfolding, Amyloid Formation, and Human Disease: A Summary of Progress Over the Last Decade. *Annu. Rev. Biochem.* **2017**, *86*, 27–68. <https://doi.org/10.1146/annurev-biochem-061516-045115>.
- (13) Roberts, C. J. Therapeutic Protein Aggregation: Mechanisms, Design, and Control. *Trends Biotechnol.* **2014**, *32* (7), 372–380. <https://doi.org/10.1016/j.tibtech.2014.05.005>.
- (14) G. Vekilov, P. Phase Transitions of Folded Proteins. *Soft Matter* **2010**, *6* (21), 5254–5272. <https://doi.org/10.1039/C0SM00215A>.
- (15) Vekilov, P. G. Phase Diagrams and Kinetics of Phase Transitions in Protein Solutions. *J. Phys. Condens. Matter* **2012**, *24* (19), 193101. <https://doi.org/10.1088/0953-8984/24/19/193101>.
- (16) Brangwynne, C. p; Tompa, P.; Pappu, R. v. Polymer Physics of Intracellular Phase Transitions. *Nat. Phys. Lond.* **2015**, *11* (11), 899–904. <http://dx.doi.org.ezaccess.libraries.psu.edu/10.1038/nphys3532>.
- (17) Raut, A. S.; Kalonia, D. S. Pharmaceutical Perspective on Opalescence and Liquid–Liquid Phase Separation in Protein Solutions. *Mol. Pharm.* **2016**, *13* (5), 1431–1444. <https://doi.org/10.1021/acs.molpharmaceut.5b00937>.
- (18) An, S.; Kumar, R.; Sheets, E. D.; Benkovic, S. J. Reversible Compartmentalization of de Novo Purine Biosynthetic Complexes in Living Cells. *Science* **2008**, *320* (5872), 103–106. <https://doi.org/10.1126/science.1152241>.

- (19) Brangwynne, C. P.; Eckmann, C. R.; Courson, D. S.; Rybarska, A.; Hoege, C.; Gharakhani, J.; Jülicher, F.; Hyman, A. A. Germline P Granules Are Liquid Droplets That Localize by Controlled Dissolution/Condensation. *Science* **2009**, *324* (5935), 1729–1732. <https://doi.org/10.1126/science.1172046>.
- (20) Dolgin, E. What Lava Lamps and Vinaigrette Can Teach Us about Cell Biology. *Nature* **2018**, *555* (7696), 300–302. <https://doi.org/10.1038/d41586-018-03070-2>.
- (21) Riback, J. A.; Katanski, C. D.; Kear-Scott, J. L.; Pilipenko, E. V.; Rojek, A. E.; Sosnick, T. R.; Drummond, D. A. Stress-Triggered Phase Separation Is an Adaptive, Evolutionarily Tuned Response. *Cell* **2017**, *168* (6), 1028–1040.e19. <https://doi.org/10.1016/j.cell.2017.02.027>.
- (22) Larson, A. G.; Elnatan, D.; Keenen, M. M.; Trnka, M. J.; Johnston, J. B.; Burlingame, A. L.; Agard, D. A.; Redding, S.; Narlikar, G. J. Liquid Droplet Formation by HP1 α Suggests a Role for Phase Separation in Heterochromatin. *Nature* **2017**, *547* (7662), 236–240. <https://doi.org/10.1038/nature22822>.
- (23) Franzmann, T. M.; Janel, M.; Pozniakovsky, A.; Mahamid, J.; Holehouse, A. S.; Nüske, E.; Richter, D.; Baumeister, W.; Grill, S. W.; Pappu, R. V.; et al. Phase Separation of a Yeast Prion Protein Promotes Cellular Fitness. *Science* **2018**, *359* (6371), eaao5654. <https://doi.org/10.1126/science.aao5654>.
- (24) Molliex, A.; Temirov, J.; Lee, J.; Coughlin, M.; Kanagaraj, A. P.; Kim, H. J.; Mittag, T.; Taylor, J. P. Phase Separation by Low Complexity Domains Promotes Stress Granule Assembly and Drives Pathological Fibrillization. *Cell* **2015**, *163* (1), 123–133. <https://doi.org/10.1016/j.cell.2015.09.015>.
- (25) Annunziata, O.; Ogun, O.; Benedek, G. B. Observation of Liquid–Liquid Phase Separation for Eye Lens Γ S-Crystallin. *Proc. Natl. Acad. Sci. U. S. A.* **2003**, *100* (3), 970–974. <https://doi.org/10.1073/pnas.242746499>.

- (26) Eaton, W. A.; Hofrichter, J. Sick Cell Hemoglobin Polymerization. In *Advances in Protein Chemistry*; Anfinsen, C. B., Edsall, J. T., Richards, F. M., Eisenberg, D. S., Eds.; Academic Press, 1990; Vol. 40, pp 63–279. [https://doi.org/10.1016/S0065-3233\(08\)60287-9](https://doi.org/10.1016/S0065-3233(08)60287-9).
- (27) Patel, A.; Lee, H. O.; Jawerth, L.; Maharana, S.; Jahnel, M.; Hein, M. Y.; Stoyanov, S.; Mahamid, J.; Saha, S.; Franzmann, T. M.; et al. A Liquid-to-Solid Phase Transition of the ALS Protein FUS Accelerated by Disease Mutation. *Cell* **2015**, *162* (5), 1066–1077. <https://doi.org/10.1016/j.cell.2015.07.047>.
- (28) Wegmann, S.; Eftekhazadeh, B.; Tepper, K.; Zoltowska, K. M.; Bennett, R. E.; Dujardin, S.; Laskowski, P. R.; MacKenzie, D.; Kamath, T.; Commins, C.; et al. Tau Protein Liquid–Liquid Phase Separation Can Initiate Tau Aggregation. *EMBO J.* **2018**, *37* (7), e98049. <https://doi.org/10.15252/embj.201798049>.
- (29) Boulay, G.; Sandoval, G. J.; Riggi, N.; Iyer, S.; Buisson, R.; Naigles, B.; Awad, M. E.; Rengarajan, S.; Volorio, A.; McBride, M. J.; et al. Cancer-Specific Retargeting of BAF Complexes by a Prion-like Domain. *Cell* **2017**, *171* (1), 163–178.e19. <https://doi.org/10.1016/j.cell.2017.07.036>.
- (30) Alberti, S.; Hyman, A. A. Are Aberrant Phase Transitions a Driver of Cellular Aging? *Bioessays* **2016**, *38* (10), 959–968. <https://doi.org/10.1002/bies.201600042>.
- (31) Asherie, N. Protein Crystallization and Phase Diagrams. *Methods* **2004**, *34* (3), 266–272. <https://doi.org/10.1016/j.ymeth.2004.03.028>.
- (32) Ahamed, T.; Esteban, B. N. A.; Ottens, M.; van Dedem, G. W. K.; van der Wielen, L. A. M.; Bisschops, M. A. T.; Lee, A.; Pham, C.; Thömmes, J. Phase Behavior of an Intact Monoclonal Antibody. *Biophys. J.* **2007**, *93* (2), 610–619. <https://doi.org/10.1529/biophysj.106.098293>.

- (33) Wang, Y.; Lomakin, A.; Latypov, R. F.; Benedek, G. B. Phase Separation in Solutions of Monoclonal Antibodies and the Effect of Human Serum Albumin. *Proc. Natl. Acad. Sci.* **2011**, *108* (40), 16606–16611. <https://doi.org/10.1073/pnas.1112241108>.
- (34) Wang, Y.; Lomakin, A.; Latypov, R. F.; Laubach, J. P.; Hideshima, T.; Richardson, P. G.; Munshi, N. C.; Anderson, K. C.; Benedek, G. B. Phase Transitions in Human IgG Solutions. *J. Chem. Phys.* **2013**, *139* (12), 121904. <https://doi.org/10.1063/1.4811345>.
- (35) Wang, Y.; Lomakin, A.; Hideshima, T.; Laubach, J. P.; Ogun, O.; Richardson, P. G.; Munshi, N. C.; Anderson, K. C.; Benedek, G. B. Pathological Crystallization of Human Immunoglobulins. *Proc. Natl. Acad. Sci. U. S. A.* **2012**, *109* (33), 13359–13361. <https://doi.org/10.1073/pnas.1211723109>.
- (36) Mason, B. D.; Zhang-van Enk, J.; Zhang, L.; Remmele, R. L.; Zhang, J. Liquid-Liquid Phase Separation of a Monoclonal Antibody and Nonmonotonic Influence of Hofmeister Anions. *Biophys. J.* **2010**, *99* (11), 3792–3800. <https://doi.org/10.1016/j.bpj.2010.10.040>.
- (37) Trilisky, E.; Gillespie, R.; Osslund, T. D.; Vunnum, S. Crystallization and Liquid-Liquid Phase Separation of Monoclonal Antibodies and Fc-Fusion Proteins: Screening Results. *Biotechnol. Prog.* **2011**, *27* (4), 1054–1067. <https://doi.org/10.1002/btpr.621>.
- (38) Dumetz, A. C.; Chockla, A. M.; Kaler, E. W.; Lenhoff, A. M. Protein Phase Behavior in Aqueous Solutions: Crystallization, Liquid-Liquid Phase Separation, Gels, and Aggregates. *Biophys. J.* **2008**, *94* (2), 570–583. <https://doi.org/10.1529/biophysj.107.116152>.
- (39) Lewus, R. A.; Darcy, P. A.; Lenhoff, A. M.; Sandler, S. I. Interactions and Phase Behavior of a Monoclonal Antibody. *Biotechnol. Prog.* **2011**, *27* (1), 280–289. <https://doi.org/10.1002/btpr.536>.

- (40) Latypov, R. F.; Hogan, S.; Lau, H.; Gadgil, H.; Liu, D. Elucidation of Acid-Induced Unfolding and Aggregation of Human Immunoglobulin IgG1 and IgG2 Fc. *J. Biol. Chem.* **2012**, *287* (2), 1381–1396. <https://doi.org/10.1074/jbc.M111.297697>.
- (41) Budyak, I. L.; Doyle, B. L.; Weiss, W. F. Technical Decision-Making with Higher Order Structure Data: Specific Binding of a Nonionic Detergent Perturbs Higher Order Structure of a Therapeutic Monoclonal Antibody. *J. Pharm. Sci.* **2015**, *104* (4), 1543–1547. <https://doi.org/10.1002/jps.24293>.
- (42) Zhang, L.; Zhang, J. Specific Ion-Protein Interactions Dictate Solubility Behavior of a Monoclonal Antibody at Low Salt Concentrations. *Mol. Pharm.* **2012**, *9* (9), 2582–2590. <https://doi.org/10.1021/mp300183a>.
- (43) Taratuta, V. G.; Holschbach, Andreas.; Thurston, G. M.; Blankschtein, Daniel.; Benedek, G. B. Liquid-Liquid Phase Separation of Aqueous Lysozyme Solutions: Effects of PH and Salt Identity. *J. Phys. Chem.* **1990**, *94* (5), 2140–2144. <https://doi.org/10.1021/j100368a074>.
- (44) Zhang, Y.; Cremer, P. S. The Inverse and Direct Hofmeister Series for Lysozyme. *Proc. Natl. Acad. Sci.* **2009**, *106* (36), 15249–15253. <https://doi.org/10.1073/pnas.0907616106>.
- (45) Wang, Y.; Annunziata, O. Comparison between Protein-Polyethylene Glycol (PEG) Interactions and the Effect of PEG on Protein-Protein Interactions Using the Liquid-Liquid Phase Transition. *J. Phys. Chem. B* **2007**, *111* (5), 1222–1230. <https://doi.org/10.1021/jp065608u>.
- (46) Annunziata, O.; Asherie, N.; Lomakin, A.; Pande, J.; Ogun, O.; Benedek, G. B. Effect of Polyethylene Glycol on the Liquid-Liquid Phase Transition in Aqueous Protein Solutions. *Proc. Natl. Acad. Sci.* **2002**, *99* (22), 14165–14170. <https://doi.org/10.1073/pnas.212507199>.

- (47) Cacace, M. G.; Landau, E. M.; Ramsden, J. J. The Hofmeister Series: Salt and Solvent Effects on Interfacial Phenomena. *Q. Rev. Biophys.* **1997**, *30* (3), 241–277.
<https://doi.org/10.1017/S0033583597003363>.
- (48) Kunz, W.; Lo Nostro, P.; Ninham, B. W. The Present State of Affairs with Hofmeister Effects. *Curr. Opin. Colloid Interface Sci.* **2004**, *9* (1), 1–18.
<https://doi.org/10.1016/j.cocis.2004.05.004>.
- (49) Record, M. T.; Guinn, E.; Pegram, L.; Capp, M. Introductory Lecture: Interpreting and Predicting Hofmeister Salt Ion and Solute Effects on Biopolymer and Model Processes Using the Solute Partitioning Model. *Faraday Discuss.* **2013**, *160* (0), 9–44.
<https://doi.org/10.1039/C2FD20128C>.
- (50) Kunz, W. Specific Ion Effects in Colloidal and Biological Systems. *Curr. Opin. Colloid Interface Sci.* **2010**, *15* (1), 34–39. <https://doi.org/10.1016/j.cocis.2009.11.008>.
- (51) Zhang, Y.; Furyk, S.; Bergbreiter, D. E.; Cremer, P. S. Specific Ion Effects on the Water Solubility of Macromolecules: PNIPAM and the Hofmeister Series. *J. Am. Chem. Soc.* **2005**, *127* (41), 14505–14510. <https://doi.org/10.1021/ja0546424>.
- (52) Robinson, D. R.; Jencks, W. P. The Effect of Compounds of the Urea-Guanidinium Class on the Activity Coefficient of Acetyltetraglycine Ethyl Ester and Related Compounds1. *J. Am. Chem. Soc.* **1965**, *87* (11), 2462–2470. <https://doi.org/10.1021/ja01089a028>.
- (53) Von Hippel, P. H.; Schleich, T. Ion Effects on the Solution Structure of Biological Macromolecules. *Acc. Chem. Res.* **1969**, *2* (9), 257–265.
<https://doi.org/10.1021/ar50021a001>.
- (54) Von Hippel, P. H.; Peticolas, V.; Schack, L.; Karlson, L. Model Studies on the Effects of Neutral Salts on the Conformational Stability of Biological Macromolecules. I. Ion Binding to Polyacrylamide and Polystyrene Columns. *Biochemistry* **1973**, *12* (7), 1256–1264. <https://doi.org/10.1021/bi00731a003>.

- (55) Collins, K. D. Sticky Ions in Biological Systems. *Proc. Natl. Acad. Sci. U. S. A.* **1995**, *92* (12), 5553–5557.
- (56) Hofmeister, F. Zur Lehre von der Wirkung der Salze. *Arch. Für Exp. Pathol. Pharmacol.* **1888**, *24* (4), 247–260. <https://doi.org/10.1007/BF01918191>.
- (57) Kunz, W.; Henle, J.; Ninham, B. W. ‘Zur Lehre von Der Wirkung Der Salze’ (about the Science of the Effect of Salts): Franz Hofmeister’s Historical Papers. *Curr. Opin. Colloid Interface Sci.* **2004**, *9* (1), 19–37. <https://doi.org/10.1016/j.cocis.2004.05.005>.
- (58) Wilson, E. K. A Renaissance for Hofmeister. *Chem. Eng. News Arch.* **2007**, *85* (48), 47–49.
- (59) Hofmeister Still Mystifies. *Chem. Eng. News Arch.* **2012**, *90* (29), 42–43. <https://doi.org/10.1021/cen-09029-scitech1>.
- (60) Jungwirth, P.; Cremer, P. S. Beyond Hofmeister. *Nat. Chem.* **2014**, *6*, 261–263. <https://doi.org/10.1038/nchem.1899>.
- (61) Chen, Y.; Okur, H. I.; Gomopoulos, N.; Macias-Romero, C.; Cremer, P. S.; Petersen, P. B.; Tocci, G.; Wilkins, D. M.; Liang, C.; Ceriotti, M.; et al. Electrolytes Induce Long-Range Orientational Order and Free Energy Changes in the H-Bond Network of Bulk Water. *Sci. Adv.* **2016**, *2* (4), e1501891. <https://doi.org/10.1126/sciadv.1501891>.
- (62) Okur, H. I.; Drexler, C. I.; Tyrode, E.; Cremer, P. S.; Roke, S. The Jones–Ray Effect Is Not Caused by Surface-Active Impurities. *J. Phys. Chem. Lett.* **2018**, *9* (23), 6739–6743. <https://doi.org/10.1021/acs.jpcclett.8b02957>.
- (63) Effect of Electrolytes on Bubble Coalescence. *Nat. Lond.* **1993**, *364* (6435), 317. <http://dx.doi.org.ezaccess.libraries.psu.edu/10.1038/364317a0>.
- (64) Ray, A.; Nemethy, G. Effects of Ionic Protein Denaturants on Micelle Formation by Nonionic Detergents. *J. Am. Chem. Soc.* **1971**, *93* (25), 6787–6793. <https://doi.org/10.1021/ja00754a014>.

- (65) Islam, Md. N.; Sarker, K. C.; Sharker, K. K. Influence of Some Hofmeister Anions on the Krafft Temperature and Micelle Formation of Cetylpyridinium Bromide in Aqueous Solution. *J. Surfactants Deterg.* **2015**, *18* (1), 9–16. <https://doi.org/10.1007/s11743-014-1642-x>.
- (66) Abezgauz, L.; Kuperkar, K.; Hassan, P. A.; Ramon, O.; Bahadur, P.; Danino, D. Effect of Hofmeister Anions on Micellization and Micellar Growth of the Surfactant Cetylpyridinium Chloride. *J. Colloid Interface Sci.* **2010**, *342* (1), 83–92. <https://doi.org/10.1016/j.jcis.2009.08.045>.
- (67) Pinna, M. C.; Salis, A.; Monduzzi, M.; Ninham, B. W. Hofmeister Series: The Hydrolytic Activity of *Aspergillus Niger* Lipase Depends on Specific Anion Effects. *J. Phys. Chem. B* **2005**, *109* (12), 5406–5408. <https://doi.org/10.1021/jp050574w>.
- (68) Bauduin, P.; Nohmie, F.; Touraud, D.; Neueder, R.; Kunz, W.; Ninham, B. W. Hofmeister Specific-Ion Effects on Enzyme Activity and Buffer PH: Horseradish Peroxidase in Citrate Buffer. *J. Mol. Liq.* **2006**, *123* (1), 14–19. <https://doi.org/10.1016/j.molliq.2005.03.003>.
- (69) Ninham, B. W.; Yaminsky, V. Ion Binding and Ion Specificity: The Hofmeister Effect and Onsager and Lifshitz Theories. *Langmuir* **1997**, *13* (7), 2097–2108. <https://doi.org/10.1021/la960974y>.
- (70) Zhang, Y.; Furyk, S.; Sagle, L. B.; Cho, Y.; Bergbreiter, D. E.; Cremer, P. S. Effects of Hofmeister Anions on the LCST of PNIPAM as a Function of Molecular Weight. *J. Phys. Chem. C* **2007**, *111* (25), 8916–8924. <https://doi.org/10.1021/jp0690603>.
- (71) Rembert, K. B.; Paterová, J.; Heyda, J.; Hilty, C.; Jungwirth, P.; Cremer, P. S. Molecular Mechanisms of Ion-Specific Effects on Proteins. *J. Am. Chem. Soc.* **2012**, *134* (24), 10039–10046. <https://doi.org/10.1021/ja301297g>.

- (72) Rembert, K. B.; Okur, H. I.; Hilty, C.; Cremer, P. S. An NH Moiety Is Not Required for Anion Binding to Amides in Aqueous Solution. *Langmuir* **2015**, *31* (11), 3459–3464. <https://doi.org/10.1021/acs.langmuir.5b00127>.
- (73) Gibb, C. L. D.; Gibb, B. C. Anion Binding to Hydrophobic Concavity Is Central to the Salting-in Effects of Hofmeister Chaotropes. *J. Am. Chem. Soc.* **2011**, *133* (19), 7344–7347. <https://doi.org/10.1021/ja202308n>.
- (74) Chen, X.; Yang, T.; Kataoka, S.; Cremer, P. S. Specific Ion Effects on Interfacial Water Structure near Macromolecules. *J. Am. Chem. Soc.* **2007**, *129* (40), 12272–12279. <https://doi.org/10.1021/ja073869r>.
- (75) Hladílková, J.; Heyda, J.; Rembert, K. B.; Okur, H. I.; Kurra, Y.; Liu, W. R.; Hilty, C.; Cremer, P. S.; Jungwirth, P. Effects of End Group Termination on Salting-Out Constants for Triglycine. *J. Phys. Chem. Lett.* **2013**, *4* (23), 4069–4073. <https://doi.org/10.1021/jz4022238>.
- (76) Kherb, J.; Flores, S. C.; Cremer, P. S. Role of Carboxylate Side Chains in the Cation Hofmeister Series. *J. Phys. Chem. B* **2012**, *116* (25), 7389–7397. <https://doi.org/10.1021/jp212243c>.
- (77) Halperin, A.; Kröger, M.; Winnik, F. M. Poly(N-isopropylacrylamide) Phase Diagrams: Fifty Years of Research. *Angew. Chem. Int. Ed.* **2015**, *54* (51), 15342–15367. <https://doi.org/10.1002/anie.201506663>.
- (78) Muschol, M.; Rosenberger, F. Liquid–Liquid Phase Separation in Supersaturated Lysozyme Solutions and Associated Precipitate Formation/Crystallization. *J. Chem. Phys.* **1997**, *107* (6), 1953–1962. <https://doi.org/10.1063/1.474547>.
- (79) Annunziata, O.; Pande, A.; Pande, J.; Ogun, O.; Lubsen, N. H.; Benedek, G. B. Oligomerization and Phase Transitions in Aqueous Solutions of Native and Truncated

Human BB1-Crystallin. *Biochemistry* **2005**, *44* (4), 1316–1328.

<https://doi.org/10.1021/bi048419f>.

- (80) Liu, C.; Asherie, N.; Lomakin, A.; Pande, J.; Ogun, O.; Benedek, G. B. Phase Separation in Aqueous Solutions of Lens γ -Crystallins: Special Role of FS. *Proc. Natl. Acad. Sci. U. S. A.* **1996**, *93* (1), 377–382.
- (81) Hong, P.; Koza, S.; Bouvier, E. S. P. Size-Exclusion Chromatography for the Analysis of Protein Biotherapeutics and Their Aggregates. *J. Liq. Chromatogr. Relat. Technol.* **2012**, *35* (20), 2923–2950. <https://doi.org/10.1080/10826076.2012.743724>.
- (82) Mason, B. D.; Zhang, L.; Remmele, R. L.; Zhang, J. Opalescence of an IgG2 Monoclonal Antibody Solution as It Relates to Liquid-Liquid Phase Separation. *J. Pharm. Sci.* **2011**, *100* (11), 4587–4596. <https://doi.org/10.1002/jps.22650>.
- (83) Mao, H.; Yang, T.; Cremer, P. S. A Microfluidic Device with a Linear Temperature Gradient for Parallel and Combinatorial Measurements. *J. Am. Chem. Soc.* **2002**, *124* (16), 4432–4435. <https://doi.org/10.1021/ja017625x>.
- (84) Mao, H.; Holden, M. A.; You, M.; Cremer, P. S. Reusable Platforms for High-Throughput on-Chip Temperature Gradient Assays. *Anal. Chem.* **2002**, *74* (19), 5071–5075. <https://doi.org/10.1021/ac025851z>.
- (85) Mao, H.; Li, C.; Zhang, Y.; Bergbreiter, D. E.; Cremer, P. S. Measuring LCSTs by Novel Temperature Gradient Methods: Evidence for Intermolecular Interactions in Mixed Polymer Solutions. *J. Am. Chem. Soc.* **2003**, *125* (10), 2850–2851. <https://doi.org/10.1021/ja029691k>.
- (86) Zhang, Y.; Mao, H.; Cremer, P. S. Probing the Mechanism of Aqueous Two-Phase System Formation for α -Elastin on-Chip. *J. Am. Chem. Soc.* **2003**, *125* (50), 15630–15635. <https://doi.org/10.1021/ja037869c>.

- (87) Mao, H.; Li, C.; Zhang, Y.; Furyk, S.; Cremer, P. S.; Bergbreiter, D. E. High-Throughput Studies of the Effects of Polymer Structure and Solution Components on the Phase Separation of Thermoresponsive Polymers. *Macromolecules* **2004**, *37* (3), 1031–1036. <https://doi.org/10.1021/ma035590a>.
- (88) Furyk, S.; Zhang, Y.; Ortiz-Acosta, D.; Cremer, P. S.; Bergbreiter, D. E. Effects of End Group Polarity and Molecular Weight on the Lower Critical Solution Temperature of Poly(N-Isopropylacrylamide). *J. Polym. Sci. Part Polym. Chem.* **2006**, *44* (4), 1492–1501. <https://doi.org/10.1002/pola.21256>.
- (89) Zhang, Y.; Trabbic-Carlson, K.; Albertorio, F.; Chilkoti, A.; Cremer, P. S. Aqueous Two-Phase System Formation Kinetics for Elastin-like Polypeptides of Varying Chain Length. *Biomacromolecules* **2006**, *7* (7), 2192–2199. <https://doi.org/10.1021/bm060254y>.
- (90) Cho, Y.; Zhang, Y.; Christensen, T.; Sagle, L. B.; Chilkoti, A.; Cremer, P. S. Effects of Hofmeister Anions on the Phase Transition Temperature of Elastin-like Polypeptides. *J. Phys. Chem. B* **2008**, *112* (44), 13765–13771. <https://doi.org/10.1021/jp8062977>.
- (91) Cho, Y.; Sagle, L. B.; Iimura, S.; Zhang, Y.; Kherb, J.; Chilkoti, A.; Scholtz, J. M.; Cremer, P. S. Hydrogen Bonding of β -Turn Structure Is Stabilized in D₂O. *J. Am. Chem. Soc.* **2009**, *131* (42), 15188–15193. <https://doi.org/10.1021/ja9040785>.
- (92) Sagle, L. B.; Zhang, Y.; Litosh, V. A.; Chen, X.; Cho, Y.; Cremer, P. S. Investigating the Hydrogen-Bonding Model of Urea Denaturation. *J. Am. Chem. Soc.* **2009**, *131* (26), 9304–9310. <https://doi.org/10.1021/ja9016057>.
- (93) Gage, S. H. Modern Dark-Field Microscopy and the History of Its Development. *Trans. Am. Microsc. Soc.* **1920**, *39* (2), 95–141. <https://doi.org/10.2307/3221838>.
- (94) Rogers, B. A.; Rembert, K. B.; Poyton, M. F.; Okur, H. I.; Kale, A. R.; Yang, T.; Zhang, J.; Cremer, P. S. A Stepwise Mechanism for Aqueous Two-Phase System Formation in

- Concentrated Antibody Solutions. *Proc. Natl. Acad. Sci.* **2019**, *116* (32), 15784–15791. <https://doi.org/10.1073/pnas.1900886116>.
- (95) Chen, X.; Flores, S. C.; Lim, S.-M.; Zhang, Y.; Yang, T.; Kherb, J.; Cremer, P. S. Specific Anion Effects on Water Structure Adjacent to Protein Monolayers. *Langmuir* **2010**, *26* (21), 16447–16454. <https://doi.org/10.1021/la1015862>.
- (96) Rankin, B. M.; Ben-Amotz, D. Expulsion of Ions from Hydrophobic Hydration Shells. *J. Am. Chem. Soc.* **2013**, *135* (24), 8818–8821. <https://doi.org/10.1021/ja4036303>.
- (97) Scheu, R.; Rankin, B. M.; Chen, Y.; Jena, K. C.; Ben-Amotz, D.; Roke, S. Charge Asymmetry at Aqueous Hydrophobic Interfaces and Hydration Shells. *Angew. Chem.* **2014**, *126* (36), 9714–9717. <https://doi.org/10.1002/ange.201310266>.
- (98) Duboué-Dijon, E.; Laage, D. Characterization of the Local Structure in Liquid Water by Various Order Parameters. *J. Phys. Chem. B* **2015**, *119* (26), 8406–8418. <https://doi.org/10.1021/acs.jpcc.5b02936>.
- (99) Hande, V. R.; Chakrabarty, S. Structural Order of Water Molecules around Hydrophobic Solutes: Length-Scale Dependence and Solute–Solvent Coupling. *J. Phys. Chem. B* **2015**, *119* (34), 11346–11357. <https://doi.org/10.1021/acs.jpcc.5b03449>.
- (100) Davis, J. G.; Gierszal, K. P.; Wang, P.; Ben-Amotz, D. Water Structural Transformation at Molecular Hydrophobic Interfaces. *Nature* **2012**, *491* (7425), 582–585. <https://doi.org/10.1038/nature11570>.
- (101) Skinner, J. L.; Pieniazek, P. A.; Gruenbaum, S. M. Vibrational Spectroscopy of Water at Interfaces. *Acc. Chem. Res.* **2012**, *45* (1), 93–100. <https://doi.org/10.1021/ar200122a>.
- (102) Perakis, F.; De Marco, L.; Shalit, A.; Tang, F.; Kann, Z. R.; Kühne, T. D.; Torre, R.; Bonn, M.; Nagata, Y. Vibrational Spectroscopy and Dynamics of Water. *Chem. Rev.* **2016**, *116* (13), 7590–7607. <https://doi.org/10.1021/acs.chemrev.5b00640>.

- (103) Fan, Y.; Chen, X.; Yang, L.; Cremer, P. S.; Gao, Y. Q. On the Structure of Water at the Aqueous/Air Interface. *J. Phys. Chem. B* **2009**, *113* (34), 11672–11679.
<https://doi.org/10.1021/jp900117t>.
- (104) Du, Q.; Freysz, E.; Shen, Y. R. Surface Vibrational Spectroscopic Studies of Hydrogen Bonding and Hydrophobicity. *Science* **1994**, *264* (5160), 826–828.
- (105) Shen, Y. R.; Ostroverkhov, V. Sum-Frequency Vibrational Spectroscopy on Water Interfaces: Polar Orientation of Water Molecules at Interfaces. *Chem. Rev.* **2006**, *106* (4), 1140–1154. <https://doi.org/10.1021/cr040377d>.
- (106) Tian, C. S.; Shen, Y. R. Structure and Charging of Hydrophobic Material/Water Interfaces Studied by Phase-Sensitive Sum-Frequency Vibrational Spectroscopy. *Proc. Natl. Acad. Sci.* **2009**, *106* (36), 15148–15153. <https://doi.org/10.1073/pnas.0901480106>.
- (107) Messmer, M. C.; Conboy, J. C.; Richmond, G. L. Observation of Molecular Ordering at the Liquid-Liquid Interface by Resonant Sum Frequency Generation. *J. Am. Chem. Soc.* **1995**, *117* (30), 8039–8040. <https://doi.org/10.1021/ja00135a032>.
- (108) Scatena, L. F.; Brown, M. G.; Richmond, G. L. Water at Hydrophobic Surfaces: Weak Hydrogen Bonding and Strong Orientation Effects. *Science* **2001**, *292* (5518), 908–912.
<https://doi.org/10.1126/science.1059514>.
- (109) Wang *, H.-F.; Gan † ‡, W.; Lu † ‡ §, R.; Rao † ‡ ¶, Y.; Wu †, B.-H. Quantitative Spectral and Orientational Analysis in Surface Sum Frequency Generation Vibrational Spectroscopy (SFG-VS). *Int. Rev. Phys. Chem.* **2005**, *24* (2), 191–256.
<https://doi.org/10.1080/01442350500225894>.
- (110) Perera, P.; Wyche, M.; Loethen, Y.; Ben-Amotz, D. Solute-Induced Perturbations of Solvent-Shell Molecules Observed Using Multivariate Raman Curve Resolution. *J. Am. Chem. Soc.* **2008**, *130* (14), 4576–4577. <https://doi.org/10.1021/ja077333h>.

- (111) Perera, P. N.; Browder, B.; Ben-Amotz, D. Perturbations of Water by Alkali Halide Ions Measured Using Multivariate Raman Curve Resolution. *J. Phys. Chem. B* **2009**, *113* (7), 1805–1809. <https://doi.org/10.1021/jp808732s>.
- (112) Perera, P. N.; Fega, K. R.; Lawrence, C.; Sundstrom, E. J.; Tomlinson-Phillips, J.; Ben-Amotz, D. Observation of Water Dangling OH Bonds around Dissolved Nonpolar Groups. *Proc. Natl. Acad. Sci.* **2009**, *106* (30), 12230–12234. <https://doi.org/10.1073/pnas.0903675106>.
- (113) Asakura, S.; Oosawa, F. On Interaction between Two Bodies Immersed in a Solution of Macromolecules. *J. Chem. Phys.* **1954**, *22* (7), 1255–1256. <https://doi.org/10.1063/1.1740347>.
- (114) Asakura, S.; Oosawa, F. Interaction between Particles Suspended in Solutions of Macromolecules. *J. Polym. Sci.* **1958**, *33* (126), 183–192. <https://doi.org/10.1002/pol.1958.1203312618>.
- (115) Bradley A. Rogers; Halil I. Okur; Chuanyu Yan; Tinglu Yang; Jan Heyda; Paul S. Cremer. Surface Curvature and the Adsorption of Weakly Hydrated Anions to Hydrophobic Interfaces. *Prep.*
- (116) Arakawa, T.; Timasheff, S. N. Mechanism of Polyethylene Glycol Interaction with Proteins. *Biochemistry* **1985**, *24* (24), 6756–6762. <https://doi.org/10.1021/bi00345a005>.
- (117) Bhat, R.; Timasheff, S. N. Steric Exclusion Is the Principal Source of the Preferential Hydration of Proteins in the Presence of Polyethylene Glycols. *Protein Sci.* **1992**, *1* (9), 1133–1143. <https://doi.org/10.1002/pro.5560010907>.
- (118) Urry, D. W. Entropic Elastic Processes in Protein Mechanisms. I. Elastic Structure Due to an Inverse Temperature Transition and Elasticity Due to Internal Chain Dynamics. *J. Protein Chem.* **1988**, *7* (1), 1–34.

- (119) Urry, D. W. Physical Chemistry of Biological Free Energy Transduction As Demonstrated by Elastic Protein-Based Polymers. *J. Phys. Chem. B* **1997**, *101* (51), 11007–11028. <https://doi.org/10.1021/jp972167t>.
- (120) Urry, D. W.; Peng, S. Q.; Parker, T. M. Hydrophobicity-Induced PK Shifts in Elastin Protein-Based Polymers. *Biopolymers* **1992**, *32* (4), 373–379. <https://doi.org/10.1002/bip.360320413>.
- (121) Janchristeerriksson, R. Salt Effects on the Cloud Point of the Poly(Ethylene Oxide)+ Water System. 22.
- (122) The Basics of NMR <https://www.cis.rit.edu/htbooks/nmr/inside.htm> (accessed Sep 20, 2019).
- (123) Stott, K.; Stonehouse, J.; Keeler, J.; Hwang, T.-L.; Shaka, A. J. Excitation Sculpting in High-Resolution Nuclear Magnetic Resonance Spectroscopy: Application to Selective NOE Experiments. *J. Am. Chem. Soc.* **1995**, *117* (14), 4199–4200. <https://doi.org/10.1021/ja00119a048>.
- (124) Shoolery, J. N.; Alder, B. J. Nuclear Magnetic Resonance in Concentrated Aqueous Electrolytes. *J. Chem. Phys.* **1955**, *23*, 805–811. <https://doi.org/10.1063/1.1742126>.
- (125) Ma, V. Effect of Ions on the ^{17}O and ^1H NMR Chemical Shifts of Water. *J Chem Soc* **1998**, *9*.
- (126) Lee, A. J.; Rick, S. W. The Effects of Charge Transfer on the Properties of Liquid Water. *J. Chem. Phys.* **2011**, *134* (18), 184507. <https://doi.org/10.1063/1.3589419>.
- (127) Okur, H. I.; Kherb, J.; Cremer, P. S. Cations Bind Only Weakly to Amides in Aqueous Solutions. *J. Am. Chem. Soc.* **2013**, *135* (13), 5062–5067. <https://doi.org/10.1021/ja3119256>.
- (128) Heyda, J.; Vincent, J. C.; Tobias, D. J.; Dzubiella, J.; Jungwirth, P. Ion Specificity at the Peptide Bond: Molecular Dynamics Simulations of N-Methylacetamide in Aqueous Salt

- Solutions. *J. Phys. Chem. B* **2010**, *114* (2), 1213–1220.
<https://doi.org/10.1021/jp910953w>.
- (129) Algaer, E. A.; van der Vegt, N. F. A. Hofmeister Ion Interactions with Model Amide Compounds. *J. Phys. Chem. B* **2011**, *115* (46), 13781–13787.
<https://doi.org/10.1021/jp208583w>.
- (130) Du, H.; Wickramasinghe, R.; Qian, X. Effects of Salt on the Lower Critical Solution Temperature of Poly (N-Isopropylacrylamide). *J. Phys. Chem. B* **2010**, *114* (49), 16594–16604. <https://doi.org/10.1021/jp105652c>.
- (131) Collins, K. D. Why Continuum Electrostatics Theories Cannot Explain Biological Structure, Polyelectrolytes or Ionic Strength Effects in Ion–Protein Interactions. *Biophys. Chem.* **2012**, *167*, 43–59. <https://doi.org/10.1016/j.bpc.2012.04.002>.
- (132) Collins, K. D.; Neilson, G. W.; Enderby, J. E. Ions in Water: Characterizing the Forces That Control Chemical Processes and Biological Structure. *Biophys. Chem.* **2007**, *128* (2), 95–104. <https://doi.org/10.1016/j.bpc.2007.03.009>.
- (133) Poul B. Petersen; Richard J. Saykally. On the Nature of Ions at the Liquid Water Surface. *Annu. Rev. Phys. Chem.* **2006**, *57*, 333–364.
- (134) Petersen, P. B.; Saykally, R. J. Adsorption of Ions to the Surface of Dilute Electrolyte Solutions: The Jones–Ray Effect Revisited. *J. Am. Chem. Soc.* **2005**, *127* (44), 15446–15452. <https://doi.org/10.1021/ja053224w>.
- (135) Tanford, C. Protein Denaturation. *Adv. Protein Chem.* **1968**, *23*, 121–282.
- (136) Auton, M.; Bolen, D. W. Predicting the Energetics of Osmolyte-Induced Protein Folding/Unfolding. *Proc. Natl. Acad. Sci.* **2005**, *102* (42), 15065–15068.
<https://doi.org/10.1073/pnas.0507053102>.

- (137) Dexter, A. F.; Malcolm, A. S.; Middelberg, A. P. J. Reversible Active Switching of the Mechanical Properties of a Peptide Film at a Fluid–Fluid Interface. *Nat. Mater.* **2006**, *5* (6), 502–506. <https://doi.org/10.1038/nmat1653>.
- (138) Hu, L.; Chen, M.; Fang, X.; Wu, L. Oil–Water Interfacial Self-Assembly: A Novel Strategy for Nanofilm and Nanodevice Fabrication. *Chem Soc Rev* **2012**, *41* (3), 1350–1362. <https://doi.org/10.1039/C1CS15189D>.
- (139) Tsionsky, M.; Bard, A. J.; Mirkin, M. V. Long-Range Electron Transfer through a Lipid Monolayer at the Liquid/Liquid Interface. *J. Am. Chem. Soc.* **1997**, *119* (44), 10785–10792. <https://doi.org/10.1021/ja972134r>.
- (140) Leunissen, M. E.; Blaaderen, A. van; Hollingsworth, A. D.; Sullivan, M. T.; Chaikin, P. M. Electrostatics at the Oil–Water Interface, Stability, and Order in Emulsions and Colloids. *Proc. Natl. Acad. Sci.* **2007**, *104* (8), 2585–2590. <https://doi.org/10.1073/pnas.0610589104>.
- (141) Riter, R. E.; Undiks, E. P.; Levinger, N. E. Impact of Counterion on Water Motion in Aerosol OT Reverse Micelles. *J. Am. Chem. Soc.* **1998**, *120* (24), 6062–6067. <https://doi.org/10.1021/ja980087c>.
- (142) Holden, M. A.; Needham, D.; Bayley, H. Functional Bionetworks from Nanoliter Water Droplets. *J. Am. Chem. Soc.* **2007**, *129* (27), 8650–8655. <https://doi.org/10.1021/ja072292a>.
- (143) Meyer, D. E.; Chilkoti, A. Quantification of the Effects of Chain Length and Concentration on the Thermal Behavior of Elastin-like Polypeptides. *Biomacromolecules* **2004**, *5* (3), 846–851. <https://doi.org/10.1021/bm034215n>.
- (144) Heyda, J.; Okur, H. I.; Hladílková, J.; Rembert, K. B.; Hunn, W.; Yang, T.; Dzubiella, J.; Jungwirth, P.; Cremer, P. S. Guanidinium Can Both Cause and Prevent the Hydrophobic

- Collapse of Biomacromolecules. *J. Am. Chem. Soc.* **2017**, *139* (2), 863–870.
<https://doi.org/10.1021/jacs.6b11082>.
- (145) Uemura, T.; Ohba, M.; Kitagawa, S. Size and Surface Effects of Prussian Blue Nanoparticles Protected by Organic Polymers. *Inorg. Chem.* **2004**, *43* (23), 7339–7345.
<https://doi.org/10.1021/ic0488435>.
- (146) Sinha, K.; Wang, W.; Winey, K. I.; Maranas, J. K. Dynamic Patterning in PEO-Based Single Ion Conductors for Li Ion Batteries. *Macromolecules* **2012**, *45* (10), 4354–4362.
<https://doi.org/10.1021/ma300051y>.
- (147) Bouchet, R.; Phan, T. N. T.; Beaudoin, E.; Devaux, D.; Davidson, P.; Bertin, D.; Denoyel, R. Charge Transport in Nanostructured PS–PEO–PS Triblock Copolymer Electrolytes. *Macromolecules* **2014**, *47* (8), 2659–2665.
<https://doi.org/10.1021/ma500420w>.
- (148) Asumana, C.; Haque, M. R.; Yu, L.; Wu, X.; Chen, X.; Yu, G. Desulfurization of Real Fuel Oils by Extraction with Ionic Liquids. *Sep. Sci. Technol.* **2013**, *48* (17), 2582–2588.
<https://doi.org/10.1080/01496395.2013.804559>.
- (149) Fox, J. M.; Kang, K.; Sherman, W.; Héroux, A.; Sastry, G. M.; Baghbanzadeh, M.; Lockett, M. R.; Whitesides, G. M. Interactions between Hofmeister Anions and the Binding Pocket of a Protein. *J. Am. Chem. Soc.* **2015**, *137* (11), 3859–3866.
<https://doi.org/10.1021/jacs.5b00187>.
- (150) Cui, H.; Chen, Z.; Zhong, S.; Wooley, K. L.; Pochan, D. J. Block Copolymer Assembly via Kinetic Control. *Science* **2007**, *317* (5838), 647–650.
<https://doi.org/10.1126/science.1141768>.
- (151) Østergaard, K. K.; Anderson, R.; Llamedo, M.; Tohidi, B. Hydrate Phase Equilibria in Porous Media: Effect of Pore Size and Salinity. *Terra Nova* **2002**, *14* (5), 307–312.
<https://doi.org/10.1046/j.1365-3121.2002.00433.x>.

- (152) Constantinescu, D.; Weingärtner, H.; Herrmann, C. Protein Denaturation by Ionic Liquids and the Hofmeister Series: A Case Study of Aqueous Solutions of Ribonuclease A. *Angew. Chem. Int. Ed.* **2007**, *46* (46), 8887–8889.
<https://doi.org/10.1002/anie.200702295>.
- (153) Wong, T.-S.; Kang, S. H.; Tang, S. K. Y.; Smythe, E. J.; Hatton, B. D.; Grinthal, A.; Aizenberg, J. Bioinspired Self-Repairing Slippery Surfaces with Pressure-Stable Omniphobicity. *Nature* **2011**, *477* (7365), 443–447. <https://doi.org/10.1038/nature10447>.
- (154) Arakawa, T.; Timasheff, S. N. Preferential Interactions of Proteins with Salts in Concentrated Solutions. *Biochemistry* **1982**, *21* (25), 6545–6552.
<https://doi.org/10.1021/bi00268a034>.
- (155) Otten, D. E.; Shaffer, P. R.; Geissler, P. L.; Saykally, R. J. Elucidating the Mechanism of Selective Ion Adsorption to the Liquid Water Surface. *Proc. Natl. Acad. Sci.* **2012**, *109* (3), 701–705. <https://doi.org/10.1073/pnas.1116169109>.
- (156) Dang, L. X. Computational Study of Ion Binding to the Liquid Interface of Water. *J. Phys. Chem. B* **2002**, *106* (40), 10388–10394. <https://doi.org/10.1021/jp021871t>.
- (157) McCaffrey, D. L.; Nguyen, S. C.; Cox, S. J.; Weller, H.; Alivisatos, A. P.; Geissler, P. L.; Saykally, R. J. Mechanism of Ion Adsorption to Aqueous Interfaces: Graphene/Water vs. Air/Water. *Proc. Natl. Acad. Sci.* **2017**, *114* (51), 13369–13373.
<https://doi.org/10.1073/pnas.1702760114>.
- (158) Balos, V.; Kim, H.; Bonn, M.; Hunger, J. Dissecting Hofmeister Effects: Direct Anion–Amide Interactions Are Weaker than Cation–Amide Binding. *Angew. Chem. Int. Ed.* **55** (28), 8125–8128. <https://doi.org/10.1002/anie.201602769>.
- (159) Li, I. T. S.; Walker, G. C. Signature of Hydrophobic Hydration in a Single Polymer. *Proc. Natl. Acad. Sci.* **2011**, *108* (40), 16527–16532.
<https://doi.org/10.1073/pnas.1105450108>.

- (160) Chandler, D. Interfaces and the driving force of hydrophobic assembly
<https://www.nature.com/articles/nature04162> (accessed Jun 4, 2018).
<https://doi.org/10.1038/nature04162>.
- (161) Langmuir, I. THE CONSTITUTION AND FUNDAMENTAL PROPERTIES OF SOLIDS AND LIQUIDS. II. LIQUIDS.1. *J. Am. Chem. Soc.* **1917**, *39* (9), 1848–1906.
<https://doi.org/10.1021/ja02254a006>.
- (162) Kauzmann, W. Some Factors in the Interpretation of Protein Denaturation11The Preparation of This Article Has Been Assisted by a Grant from the National Science Foundation. In *Advances in Protein Chemistry*; Anfinsen, C. B., Anson, M. L., Bailey, K., Edsall, J. T., Eds.; Academic Press, 1959; Vol. 14, pp 1–63.
[https://doi.org/10.1016/S0065-3233\(08\)60608-7](https://doi.org/10.1016/S0065-3233(08)60608-7).
- (163) Frank, H. S.; Evans, M. W. Free Volume and Entropy in Condensed Systems III. Entropy in Binary Liquid Mixtures; Partial Molal Entropy in Dilute Solutions; Structure and Thermodynamics in Aqueous Electrolytes. *J. Chem. Phys.* **1945**, *13* (11), 507–532.
<https://doi.org/10.1063/1.1723985>.
- (164) Stillinger, F. H. Structure in Aqueous Solutions of Nonpolar Solutes from the Standpoint of Scaled-Particle Theory. *J. Solut. Chem.* **1973**, *2* (2), 141–158.
<https://doi.org/10.1007/BF00651970>.
- (165) Pangali, C.; Rao, M.; Berne, B. J. Hydrophobic Hydration around a Pair of Apolar Species in Water. *J. Chem. Phys.* **1979**, *71* (7), 2982–2990.
<https://doi.org/10.1063/1.438702>.
- (166) Pratt, L. R.; Chandler, D. Effects of Solute–Solvent Attractive Forces on Hydrophobic Correlations. *J. Chem. Phys.* **1980**, *73* (7), 3434–3441. <https://doi.org/10.1063/1.440541>.

- (167) Smith, D. E.; Zhang, L.; Haymet, A. D. J. Entropy of Association of Methane in Water: A New Molecular Dynamics Computer Simulation. *J. Am. Chem. Soc.* **1992**, *114* (14), 5875–5876. <https://doi.org/10.1021/ja00040a068>.
- (168) Guillot, B.; Guissani, Y. A Computer Simulation Study of the Temperature Dependence of the Hydrophobic Hydration. *J. Chem. Phys.* **1993**, *99* (10), 8075–8094. <https://doi.org/10.1063/1.465634>.
- (169) Lazaridis, T.; Paulaitis, M. E. Entropy of Hydrophobic Hydration: A New Statistical Mechanical Formulation. *J. Phys. Chem.* **1992**, *96* (9), 3847–3855. <https://doi.org/10.1021/j100188a051>.
- (170) Lum, K.; Chandler, D.; Weeks, J. D. Hydrophobicity at Small and Large Length Scales. *J. Phys. Chem. B* **1999**, *103* (22), 4570–4577. <https://doi.org/10.1021/jp984327m>.
- (171) Walrafen, G. E.; Fisher, M. R.; Hokmabadi, M. S.; Yang, W. -H. Temperature Dependence of the Low- and High-frequency Raman Scattering from Liquid Water. *J. Chem. Phys.* **1986**, *85* (12), 6970–6982. <https://doi.org/10.1063/1.451384>.
- (172) Morawietz, T.; Marsalek, O.; Pattenaude, S. R.; Streacker, L. M.; Ben-Amotz, D.; Markland, T. E. The Interplay of Structure and Dynamics in the Raman Spectrum of Liquid Water over the Full Frequency and Temperature Range. *J. Phys. Chem. Lett.* **2018**, *9* (4), 851–857. <https://doi.org/10.1021/acs.jpcclett.8b00133>.
- (173) Sovago, M.; Campen, R. K.; Wurpel, G. W. H.; Müller, M.; Bakker, H. J.; Bonn, M. Vibrational Response of Hydrogen-Bonded Interfacial Water Is Dominated by Intramolecular Coupling. *Phys. Rev. Lett.* **2008**, *100* (17), 173901. <https://doi.org/10.1103/PhysRevLett.100.173901>.
- (174) Tian, C. S.; Shen, Y. R. Comment on ‘‘Vibrational Response of Hydrogen-Bonded Interfacial Water Is Dominated by Intramolecular Coupling’’. *Phys. Rev. Lett.* **2008**, *101* (13), 139401. <https://doi.org/10.1103/PhysRevLett.101.139401>.

- (175) Sovago, M.; Campen, R. K.; Wurfel, G. W. H.; Müller, M.; Bakker, H. J.; Bonn, M. Sovago et al. Reply: *Phys. Rev. Lett.* **2008**, *101* (13), 139402. <https://doi.org/10.1103/PhysRevLett.101.139402>.
- (176) Minceva-Sukarova, B.; Sherman, W. F.; Wilkinson, G. R. The Raman Spectra of Ice (Ih, II, III, V, VI and IX) as Functions of Pressure and Temperature. *J. Phys. C Solid State Phys.* **1984**, *17* (32), 5833–5850. <https://doi.org/10.1088/0022-3719/17/32/017>.
- (177) Avila, G.; Fernández, J. M.; Maté, B.; Tejada, G.; Montero, S. Ro-Vibrational Raman Cross Sections of Water Vapor in the OH Stretching Region. *J. Mol. Spectrosc.* **1999**, *196* (1), 77–92. <https://doi.org/10.1006/jmsp.1999.7854>.
- (178) Soniat, M.; Rick, S. W. Charge Transfer Effects of Ions at the Liquid Water/Vapor Interface. *J. Chem. Phys.* **2014**, *140* (18), 184703. <https://doi.org/10.1063/1.4874256>.
- (179) Vácha, R.; Rick, S. W.; Jungwirth, P.; de Beer, A. G. F.; de Aguiar, H. B.; Samson, J.-S.; Roke, S. The Orientation and Charge of Water at the Hydrophobic Oil Droplet–Water Interface. *J. Am. Chem. Soc.* **2011**, *133* (26), 10204–10210. <https://doi.org/10.1021/ja202081x>.
- (180) Ben-Amotz, D. Hydration-Shell Vibrational Spectroscopy. *J. Am. Chem. Soc.* **2019**, *141* (27), 10569–10580. <https://doi.org/10.1021/jacs.9b02742>.
- (181) D'Arrigo, G.; Maisano, G.; Mallamace, F.; Migliardo, P.; Wanderlingh, F. Raman Scattering and Structure of Normal and Supercooled Water. *J. Chem. Phys.* **1981**, *75* (9), 4264–4270. <https://doi.org/10.1063/1.442629>.
- (182) Sun, Q. Local Statistical Interpretation for Water Structure. *Chem. Phys. Lett.* **2013**, *568–569*, 90–94. <https://doi.org/10.1016/j.cplett.2013.03.065>.
- (183) Harada, Y.; Miyawaki, J.; Niwa, H.; Yamazoe, K.; Pettersson, L. G. M.; Nilsson, A. Probing the OH Stretch in Different Local Environments in Liquid Water. *J. Phys. Chem. Lett.* **2017**, *8* (22), 5487–5491. <https://doi.org/10.1021/acs.jpcclett.7b02060>.

- (184) Mahler, H.-C.; Friess, W.; Grauschopf, U.; Kiese, S. Protein Aggregation: Pathways, Induction Factors and Analysis. *J. Pharm. Sci.* **2009**, *98* (9), 2909–2934.
<https://doi.org/10.1002/jps.21566>.
- (185) Gunton, J. D.; Shiryayev, A.; Pagan, D. L. *Protein Condensation: Kinetic Pathways to Crystallization and Disease*; Cambridge University Press, 2007.
- (186) Berland, C. R.; Thurston, G. M.; Kondo, M.; Broide, M. L.; Pande, J.; Ogun, O.; Benedek, G. B. Solid-Liquid Phase Boundaries of Lens Protein Solutions. *Proc. Natl. Acad. Sci. U. S. A.* **1992**, *89* (4), 1214–1218.
- (187) Dodson, G.; Steiner, D. The Role of Assembly in Insulin's Biosynthesis. *Curr. Opin. Struct. Biol.* **1998**, *8* (2), 189–194. [https://doi.org/10.1016/S0959-440X\(98\)80037-7](https://doi.org/10.1016/S0959-440X(98)80037-7).
- (188) Fekete, S.; Beck, A.; Veuthey, J.-L.; Guillarme, D. Theory and Practice of Size Exclusion Chromatography for the Analysis of Protein Aggregates. *J. Pharm. Biomed. Anal.* **2014**, *101*, 161–173. <https://doi.org/10.1016/j.jpba.2014.04.011>.
- (189) Woodbury, R. L.; Hardy, S. J. S.; Randall, L. L. Complex Behavior in Solution of Homodimeric SecA. *Protein Sci. Publ. Protein Soc.* **2002**, *11* (4), 875–882.
- (190) Pan, J.; Han, J.; Borchers, C. H.; Konermann, L. Structure and Dynamics of Small Soluble A β (1–40) Oligomers Studied by Top-Down Hydrogen Exchange Mass Spectrometry. *Biochemistry* **2012**, *51* (17), 3694–3703.
<https://doi.org/10.1021/bi3002049>.
- (191) Tatford, O. C.; Gomme, P. T.; Bertolini, J. Analytical Techniques for the Evaluation of Liquid Protein Therapeutics. *Biotechnol. Appl. Biochem.* **2004**, *40* (1), 67–81.
<https://doi.org/10.1042/BA20030183>.
- (192) Greenfield, N. J. Using Circular Dichroism Collected as a Function of Temperature to Determine the Thermodynamics of Protein Unfolding and Binding Interactions. *Nat. Protoc.* **2006**, *1* (6), 2527–2535. <https://doi.org/10.1038/nprot.2006.204>.

- (193) Johnson, C. M. Differential Scanning Calorimetry as a Tool for Protein Folding and Stability. *Arch. Biochem. Biophys.* **2013**, *531* (1), 100–109.
<https://doi.org/10.1016/j.abb.2012.09.008>.
- (194) Huynh, K.; Partch, C. L. Current Protocols in Protein Science. *Curr. Protoc. Protein Sci. Editor. Board John E Coligan Al* **2015**, *79*, 28.9.1-28.9.14.
<https://doi.org/10.1002/0471140864.ps2809s79>.
- (195) Jerabek-Willemsen, M.; Wienken, C. J.; Braun, D.; Baaske, P.; Duhr, S. Molecular Interaction Studies Using Microscale Thermophoresis. *ASSAY Drug Dev. Technol.* **2011**, *9* (4), 342–353. <https://doi.org/10.1089/adt.2011.0380>.
- (196) Asmari, M.; Ratih, R.; Alhazmi, H. A.; El Deeb, S. Thermophoresis for Characterizing Biomolecular Interaction. *Methods* **2018**, *146*, 107–119.
<https://doi.org/10.1016/j.ymeth.2018.02.003>.
- (197) Debye, P. Light Scattering in Solutions. *J. Appl. Phys.* **1944**, *15* (4), 338–342.
<https://doi.org/10.1063/1.1707436>.
- (198) Zimm, B. H. Molecular Theory of the Scattering of Light in Fluids. *J. Chem. Phys.* **1945**, *13* (4), 141–145. <https://doi.org/10.1063/1.1724013>.
- (199) Zimm, B. H. The Scattering of Light and the Radial Distribution Function of High Polymer Solutions. *J. Chem. Phys.* **1948**, *16* (12), 1093–1099.
<https://doi.org/10.1063/1.1746738>.
- (200) Schweinfus, J. J.; Checkal, C.; Saksa, B.; Baka, N.; Modi, K.; Rivera, C. Molar Mass and Second Virial Coefficient of Polyethylene Glycol by Vapor Pressure Osmometry. *J. Chem. Educ.* **2015**, *92* (12), 2157–2160. <https://doi.org/10.1021/acs.jchemed.5b00369>.
- (201) Zimmerman, S. B.; Trach, S. O. Estimation of Macromolecule Concentrations and Excluded Volume Effects for the Cytoplasm of Escherichia Coli. *J. Mol. Biol.* **1991**, *222* (3), 599–620. [https://doi.org/10.1016/0022-2836\(91\)90499-V](https://doi.org/10.1016/0022-2836(91)90499-V).

- (202) Shire, S. J.; Shahrokh, Z.; Liu, J. Challenges in the Development of High Protein Concentration Formulations. *J. Pharm. Sci.* **2004**, *93* (6), 1390–1402.
<https://doi.org/10.1002/jps.20079>.
- (203) Schermeyer, M.-T.; Wöll, A. K.; Kokke, B.; Eppink, M.; Hubbuch, J. Characterization of Highly Concentrated Antibody Solution - A Toolbox for the Description of Protein Long-Term Solution Stability. *mAbs* **2017**, *9* (7), 1169–1185.
<https://doi.org/10.1080/19420862.2017.1338222>.
- (204) Petsev, D. N.; Wu, X.; Galkin, O.; Vekilov, P. G. Thermodynamic Functions of Concentrated Protein Solutions from Phase Equilibria. *J. Phys. Chem. B* **2003**, *107* (16), 3921–3926. <https://doi.org/10.1021/jp0278317>.
- (205) Shah, M.; Galkin, O.; Vekilov, P. G. Smooth Transition from Metastability to Instability in Phase Separating Protein Solutions. *J. Chem. Phys.* **2004**, *121* (15), 7505–7512.
<https://doi.org/10.1063/1.1792156>.
- (206) Lu, P. J.; Weitz, D. A. Colloidal Particles: Crystals, Glasses, and Gels. *Annu. Rev. Condens. Matter Phys.* **2013**, *4* (1), 217–233. <https://doi.org/10.1146/annurev-conmatphys-030212-184213>.
- (207) Thomson, J. A.; Schurtenberger, P.; Thurston, G. M.; Benedek, G. B. Binary Liquid Phase Separation and Critical Phenomena in a Protein/Water Solution. *Proc. Natl. Acad. Sci.* **1987**, *84* (20), 7079–7083. <https://doi.org/10.1073/pnas.84.20.7079>.
- (208) Mattsson, J.; Wyss, H. M.; Fernandez-Nieves, A.; Miyazaki, K.; Hu, Z.; Reichman, D. R.; Weitz, D. A. Soft Colloids Make Strong Glasses. *Nature* **2009**, *462* (7269), 83–86.
<https://doi.org/10.1038/nature08457>.
- (209) van der Scheer, P.; van de Laar, T.; van der Gucht, J.; Vlassopoulos, D.; Sprakel, J. Fragility and Strength in Nanoparticle Glasses. *ACS Nano* **2017**, *11* (7), 6755–6763.
<https://doi.org/10.1021/acsnano.7b01359>.

- (210) Ishimoto, C.; Tanaka, T. Critical Behavior of a Binary Mixture of Protein and Salt Water. *Phys. Rev. Lett.* **1977**, *39* (8), 474–477. <https://doi.org/10.1103/PhysRevLett.39.474>.
- (211) Wang, Y.; Latypov, R. F.; Lomakin, A.; Meyer, J. A.; Kerwin, B. A.; Vunnum, S.; Benedek, G. B. Quantitative Evaluation of Colloidal Stability of Antibody Solutions Using PEG-Induced Liquid–Liquid Phase Separation. *Mol. Pharm.* **2014**, *11* (5), 1391–1402. <https://doi.org/10.1021/mp400521b>.
- (212) Stillinger, F. H. A Topographic View of Supercooled Liquids and Glass Formation. *Science* **1995**, *267* (5206), 1935–1939. <https://doi.org/10.1126/science.267.5206.1935>.
- (213) Wang, Y.; Lomakin, A.; McManus, J. J.; Ogun, O.; Benedek, G. B. Phase Behavior of Mixtures of Human Lens Proteins Gamma D and Beta B1. *Proc. Natl. Acad. Sci.* **2010**, *107* (30), 13282–13287. <https://doi.org/10.1073/pnas.1008353107>.
- (214) Kohlrausch, R. Theorie Des Elektrischen Rückstandes in Der Leidener Flasche. *Ann. Phys.* **1854**, *167* (2), 179–214. <https://doi.org/10.1002/andp.18541670203>.
- (215) Williams, G.; Watts, D. C. Non-Symmetrical Dielectric Relaxation Behaviour Arising from a Simple Empirical Decay Function. *Trans. Faraday Soc.* **1970**, *66* (0), 80–85. <https://doi.org/10.1039/TF9706600080>.
- (216) Florence, A. T.; Rogers, J. A. Emulsion Stabilization by Non-Ionic Surfactants: Experiment and Theory. *J. Pharm. Pharmacol.* **1971**, *23* (4), 233–251. <https://doi.org/10.1111/j.2042-7158.1971.tb08653.x>.
- (217) Buscall, R. The Properties of O/W Emulsions Stabilised with a Non-Ionic Surfactant and Surfactant-Polymer Mixtures. In *Emulsions*; Weiss, A., Ed.; Progress in Colloid and Polymer Science; Steinkopff, 1978; pp 15–26.
- (218) Talapin, D. V.; Rogach, A. L.; Haase, M.; Weller, H. Evolution of an Ensemble of Nanoparticles in a Colloidal Solution: Theoretical Study. *J. Phys. Chem. B* **2001**, *105* (49), 12278–12285. <https://doi.org/10.1021/jp012229m>.

- (219) Kabalnov, A. S.; Shchukin, E. D. Ostwald Ripening Theory: Applications to Fluorocarbon Emulsion Stability. *Adv. Colloid Interface Sci.* **1992**, *38*, 69–97. [https://doi.org/10.1016/0001-8686\(92\)80043-W](https://doi.org/10.1016/0001-8686(92)80043-W).
- (220) Taylor, P. Ostwald Ripening in Emulsions. *Adv. Colloid Interface Sci.* **1998**, *75* (2), 107–163. [https://doi.org/10.1016/S0001-8686\(98\)00035-9](https://doi.org/10.1016/S0001-8686(98)00035-9).
- (221) Fortelný, I.; Živný, A.; Jůza, J. Coarsening of the Phase Structure in Immiscible Polymer Blends. Coalescence or Ostwald Ripening? *J. Polym. Sci. Part B Polym. Phys.* **1999**, *37* (3), 181–187. [https://doi.org/10.1002/\(SICI\)1099-0488\(19990201\)37:3<181::AID-POLB1>3.0.CO;2-I](https://doi.org/10.1002/(SICI)1099-0488(19990201)37:3<181::AID-POLB1>3.0.CO;2-I).
- (222) Buscall, R.; Davis, S. S.; Potts, D. C. The Effect of Long-Chain Alkanes on the Stability of Oil-in-Water Emulsions. The Significance of Ostwald Ripening. *Colloid Polym. Sci.* **1979**, *257* (6), 636–644. <https://doi.org/10.1007/BF01548833>.
- (223) Pan, W.; Vekilov, P. G.; Lubchenko, V. Origin of Anomalous Mesoscopic Phases in Protein Solutions. *J. Phys. Chem. B* **2010**, *114* (22), 7620–7630. <https://doi.org/10.1021/jp100617w>.
- (224) Li, Y.; Lubchenko, V.; Vorontsova, M. A.; Filobelo, L.; Vekilov, P. G. Ostwald-Like Ripening of the Anomalous Mesoscopic Clusters in Protein Solutions. *J. Phys. Chem. B* **2012**, *116* (35), 10657–10664. <https://doi.org/10.1021/jp303316s>.
- (225) Streets, A. M.; Quake, S. R. Ostwald Ripening of Clusters during Protein Crystallization. *Phys. Rev. Lett.* **2010**, *104* (17), 178102. <https://doi.org/10.1103/PhysRevLett.104.178102>.
- (226) Parkinson, L.; Sedev, R.; Fornasiero, D.; Ralston, J. The Terminal Rise Velocity of 10–100 Mm Diameter Bubbles in Water. *J. Colloid Interface Sci.* **2008**, *322* (1), 168–172. <https://doi.org/10.1016/j.jcis.2008.02.072>.

- (227) Curtiss, L. A.; Frurip, D. J.; Blander, M. Studies of Molecular Association in H₂O and D₂O Vapors by Measurement of Thermal Conductivity. *J. Chem. Phys.* **1979**, *71* (6), 2703–2711. <https://doi.org/10.1063/1.438628>.
- (228) Feyereisen, M. W.; Feller, D.; Dixon, D. A. Hydrogen Bond Energy of the Water Dimer. *J. Phys. Chem.* **1996**, *100* (8), 2993–2997. <https://doi.org/10.1021/jp952860l>.
- (229) Scherer, G. W. Editorial Comments on a Paper by Gordon S. Fulcher. *J. Am. Ceram. Soc.* **1992**, *75* (5), 1060–1062. <https://doi.org/10.1111/j.1151-2916.1992.tb05537.x>.
- (230) Krebs, T.; Schroen, K.; Boom, R. A Microfluidic Method to Study Demulsification Kinetics. *Lab. Chip* **2012**, *12* (6), 1060–1070. <https://doi.org/10.1039/C2LC20930F>.
- (231) Angell, C. A. Perspective on the Glass Transition. *J. Phys. Chem. Solids* **1988**, *49* (8), 863–871. [https://doi.org/10.1016/0022-3697\(88\)90002-9](https://doi.org/10.1016/0022-3697(88)90002-9).
- (232) Angell, C. A. Relaxation in Liquids, Polymers and Plastic Crystals — Strong/Fragile Patterns and Problems. *J. Non-Cryst. Solids* **1991**, *131–133*, 13–31. [https://doi.org/10.1016/0022-3093\(91\)90266-9](https://doi.org/10.1016/0022-3093(91)90266-9).
- (233) Nascimento, M. L. F.; Aparicio, C. Viscosity of Strong and Fragile Glass-Forming Liquids Investigated by Means of Principal Component Analysis. *J. Phys. Chem. Solids* **2007**, *68* (1), 104–110. <https://doi.org/10.1016/j.jpcs.2006.09.013>.
- (234) Cardinaux, F.; Gibaud, T.; Stradner, A.; Schurtenberger, P. Interplay between Spinodal Decomposition and Glass Formation in Proteins Exhibiting Short-Range Attractions. *Phys. Rev. Lett.* **2007**, *99* (11), 118301. <https://doi.org/10.1103/PhysRevLett.99.118301>.
- (235) Gibaud, T.; Schurtenberger, P. A Closer Look at Arrested Spinodal Decomposition in Protein Solutions. *J. Phys. Condens. Matter* **2009**, *21* (32), 322201. <https://doi.org/10.1088/0953-8984/21/32/322201>.

- (236) Lu, P. J.; Zaccarelli, E.; Ciulla, F.; Schofield, A. B.; Sciortino, F.; Weitz, D. A. Gelation of Particles with Short-Range Attraction. *Nature* **2008**, *453* (7194), 499–503.
<https://doi.org/10.1038/nature06931>.
- (237) Smoluchowski, M. V. Drei Vortrage Uber Diffusion, Brownsche Bewegung Und Koagulation von Kolloidteilchen. *Z. Phys.* **1916**, *17*, 557–585.
- (238) Tempel, M. van den. Stability of oil-in-water emulsions II: Mechanism of the coagulation of an emulsion. *Recl. Trav. Chim. Pays-Bas* **1953**, *72* (5), 433–441.
<https://doi.org/10.1002/recl.19530720508>.
- (239) Mullin, J. W. *Crystallization*, 4th ed.; Butterworth-Heinemann: Oxford ; Boston, 2001.
- (240) Berthoud, A. Théorie de la formation des faces d'un cristal. *J. Chim. Phys.* **1912**, *10*, 624–635. <https://doi.org/10.1051/jcp/1912100624>.
- (241) Valeton, J. . J. . P. . I. Wachstum Und Auflösung Der Kristalle. III. *Z. Für Krist. - Cryst. Mater.* **1924**, *60* (1–6), 1–38. <https://doi.org/10.1524/zkri.1924.60.1.1>.
- (242) Heller, P. Experimental Investigations of Critical Phenomena. *Rep. Prog. Phys.* **1967**, *30* (2), 731–826. <https://doi.org/10.1088/0034-4885/30/2/307>.
- (243) Broide, M. L.; Berland, C. R.; Pande, J.; Ogun, O. O.; Benedek, G. B. Binary-Liquid Phase Separation of Lens Protein Solutions. *Proc. Natl. Acad. Sci. U. S. A.* **1991**, *88* (13), 5660–5664.
- (244) Atkins, P.; Paula, J. de. The Rates of Chemical Reactions. In *Physical Chemistry*; W. H. Freeman: New York, 2009; pp 782–830.
- (245) Yefremova, Y.; Melder, F.; Danquah, B.; Opuni, K.; Koy, C.; Ehrens, A.; Frommholz, D.; Illges, H.; Koelbel, K.; Sobott, F.; et al. Apparent Activation Energies of Protein-Protein Complex Dissociation in the Gas-Phase Determined by Electrospray Mass Spectrometry. *Anal. Bioanal. Chem.* **2017**, *409* (28), 6549–6558.
<https://doi.org/10.1007/s00216-017-0603-4>.

- (246) Zaccarelli, E.; Lu, P. J.; Ciulla, F.; Weitz, D. A.; Sciortino, F. Gelation as Arrested Phase Separation in Short-Ranged Attractive Colloid–Polymer Mixtures. *J. Phys. Condens. Matter* **2008**, *20* (49), 494242. <https://doi.org/10.1088/0953-8984/20/49/494242>.
- (247) Zaccarelli, E. Colloidal Gels: Equilibrium and Non-Equilibrium Routes. *J. Phys. Condens. Matter* **2007**, *19* (32), 323101. <https://doi.org/10.1088/0953-8984/19/32/323101>.

Appendix A

Supporting Information for Chapters 2-3

Solute-correlated spectra were measured and fit using the strategies described in Chapter 3. Here, we show the data and fits for the different polyether solutes at 0.5 M monomer concentrations, ~ 22 mg/mL solute, in Figures A-1 through A-16.

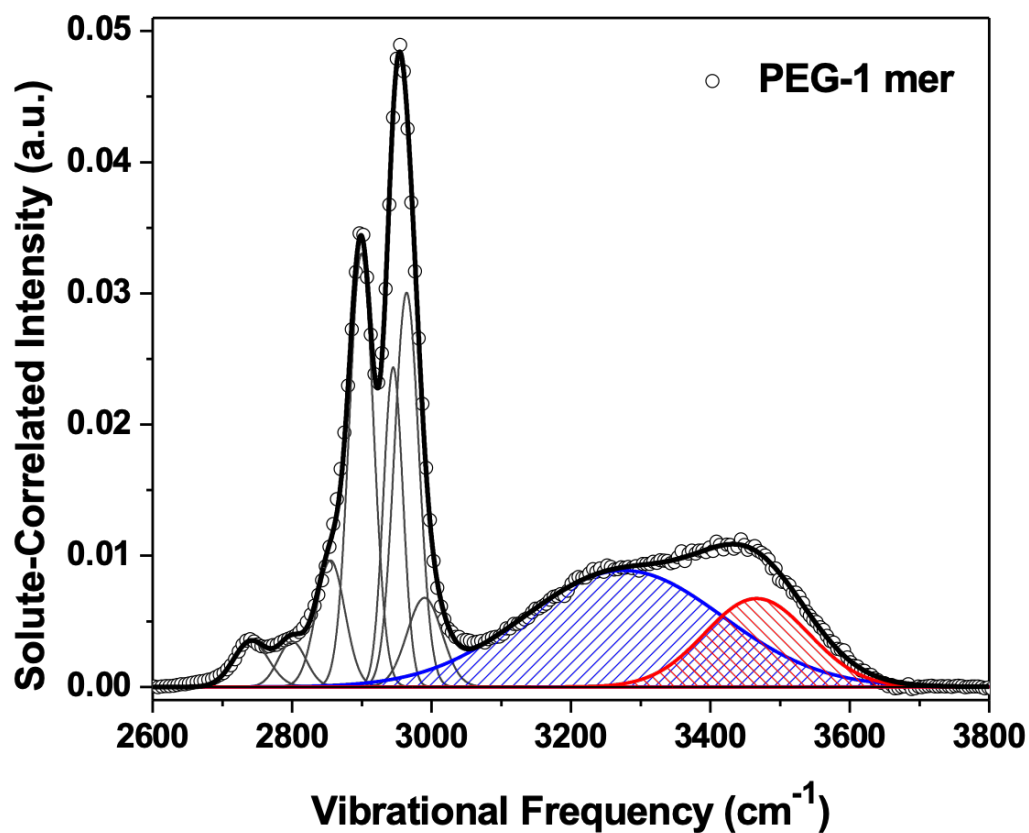


Figure A-1: Solute-correlated spectrum for PEG-1. The spectrum is normalized to the area under the CH stretches from 2600 to 3050 cm^{-1} .

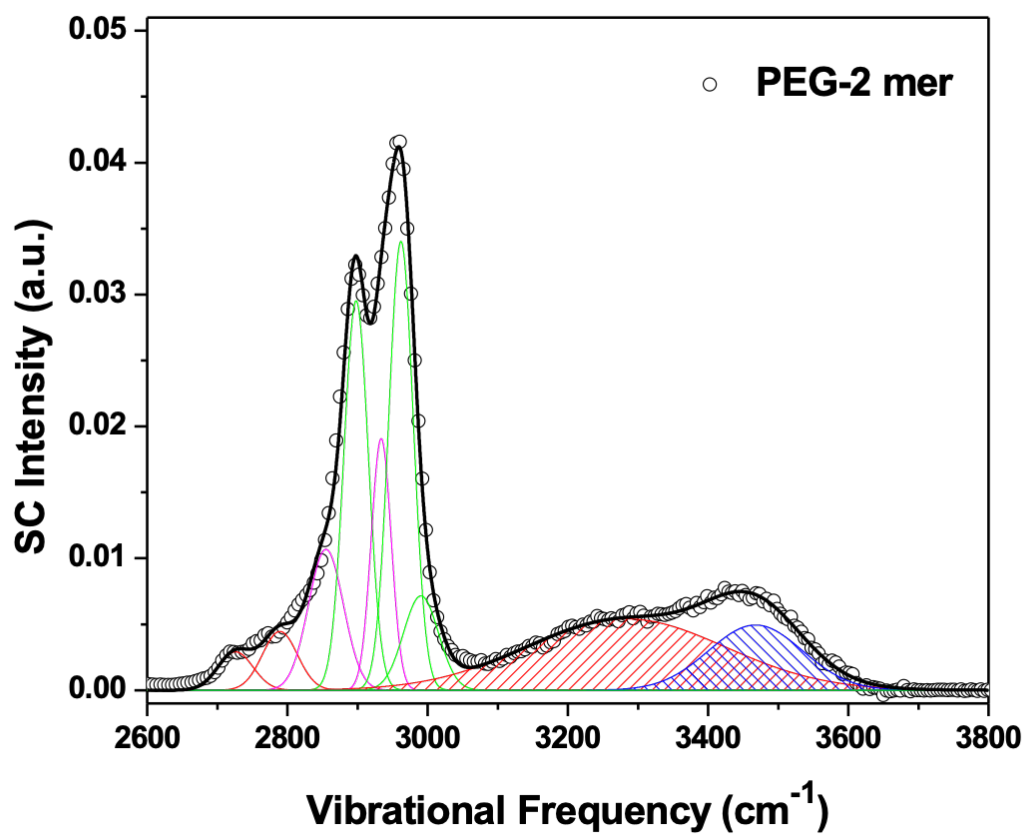


Figure A-2: Solute-correlated spectrum for PEG-2. The spectrum is normalized to the area under the CH stretches from 2600 to 3050 cm⁻¹.

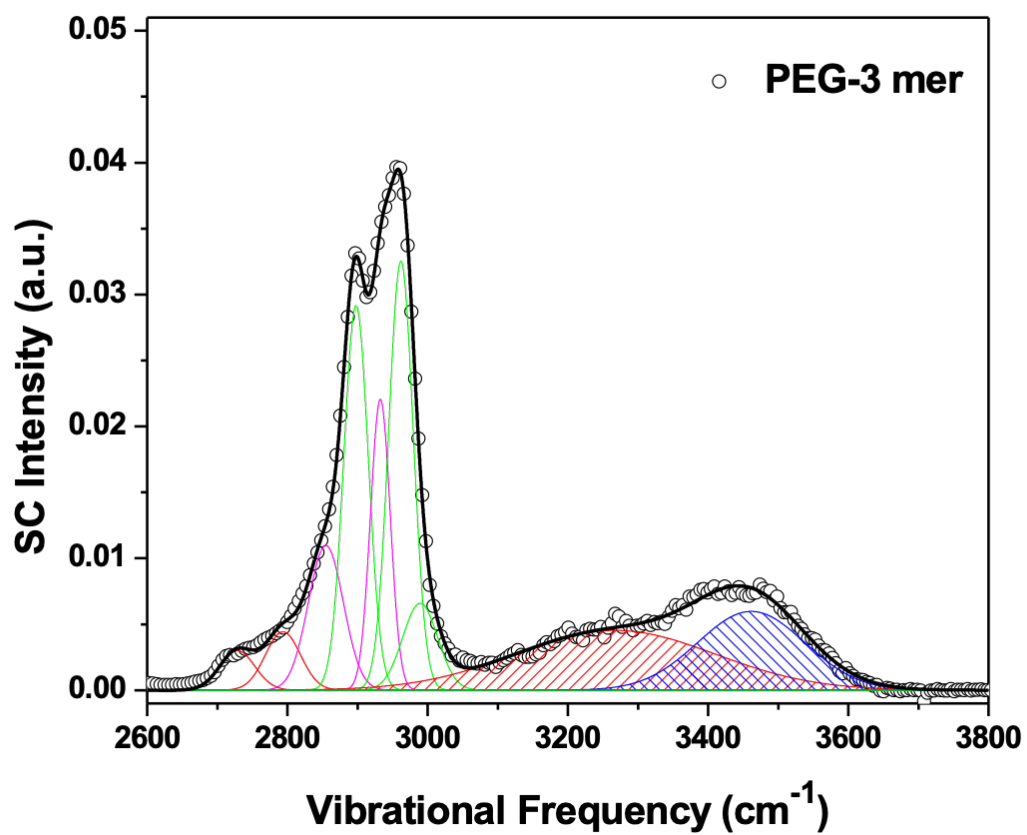


Figure A-3: Solute-correlated spectrum for PEG-3. The spectrum is normalized to the area under the CH stretches from 2600 to 3050 cm⁻¹.

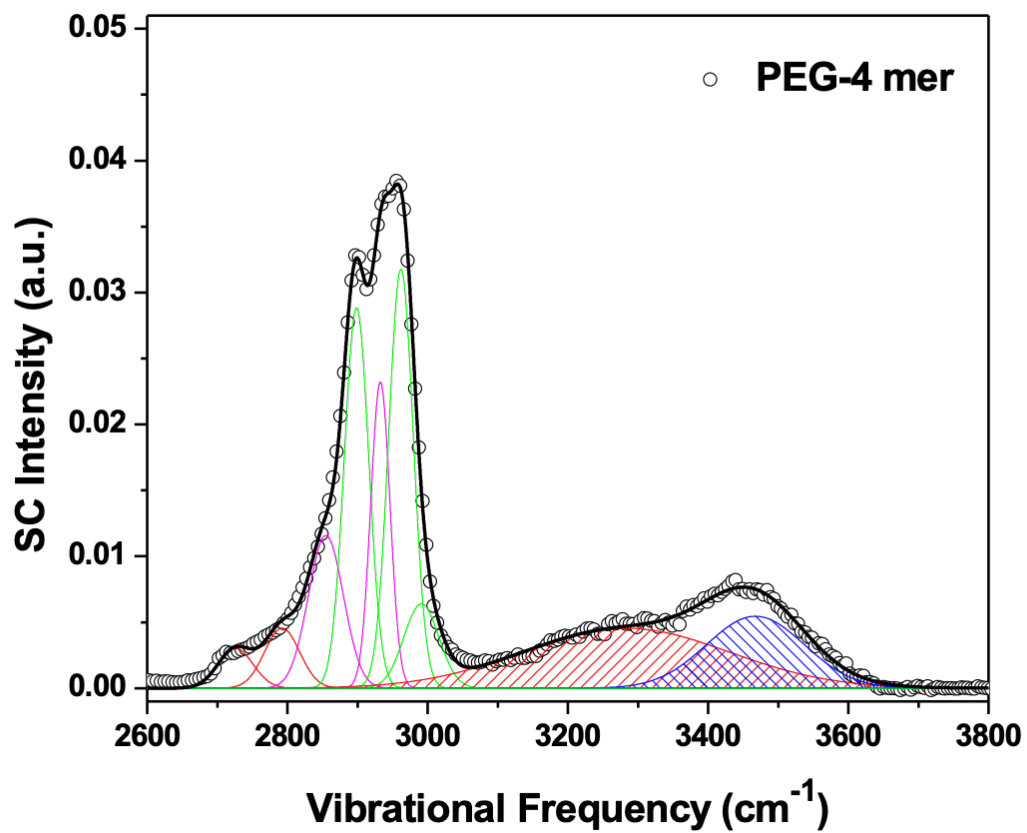


Figure A-4: Solute-correlated spectrum for PEG-4. The spectrum is normalized to the area under the CH stretches from 2600 to 3050 cm⁻¹.

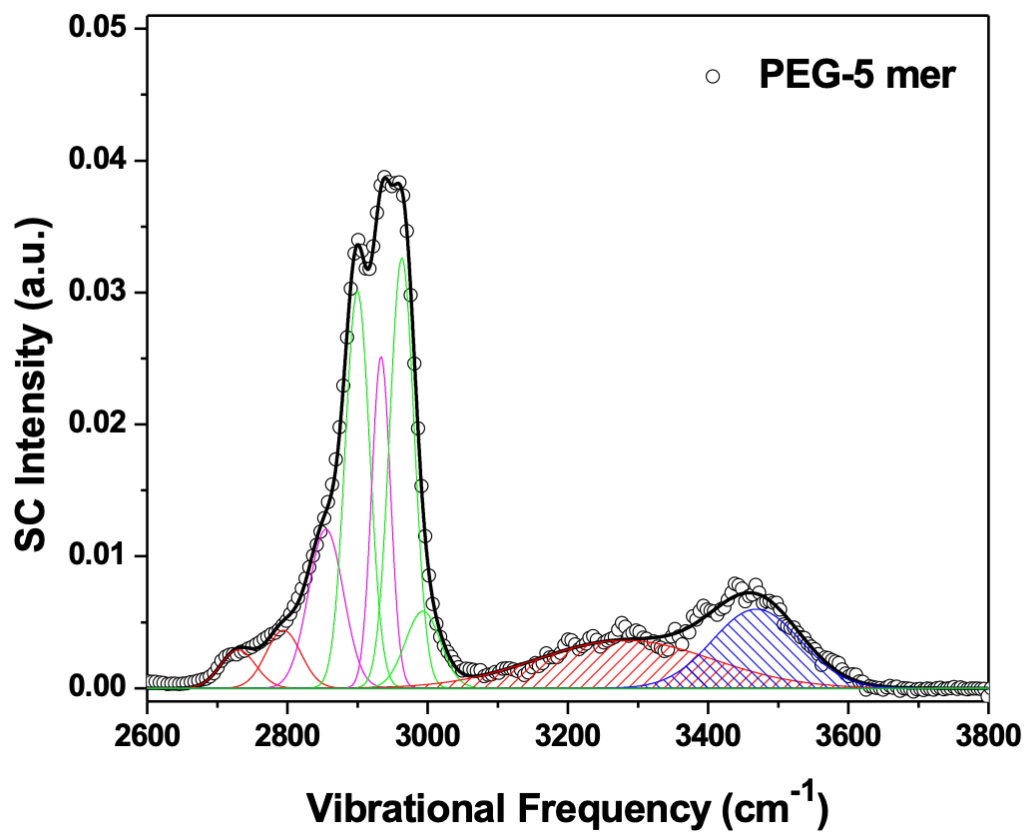


Figure A-5: Solute-correlated spectrum for PEG-5. The spectrum is normalized to the area under the CH stretches from 2600 to 3050 cm⁻¹.

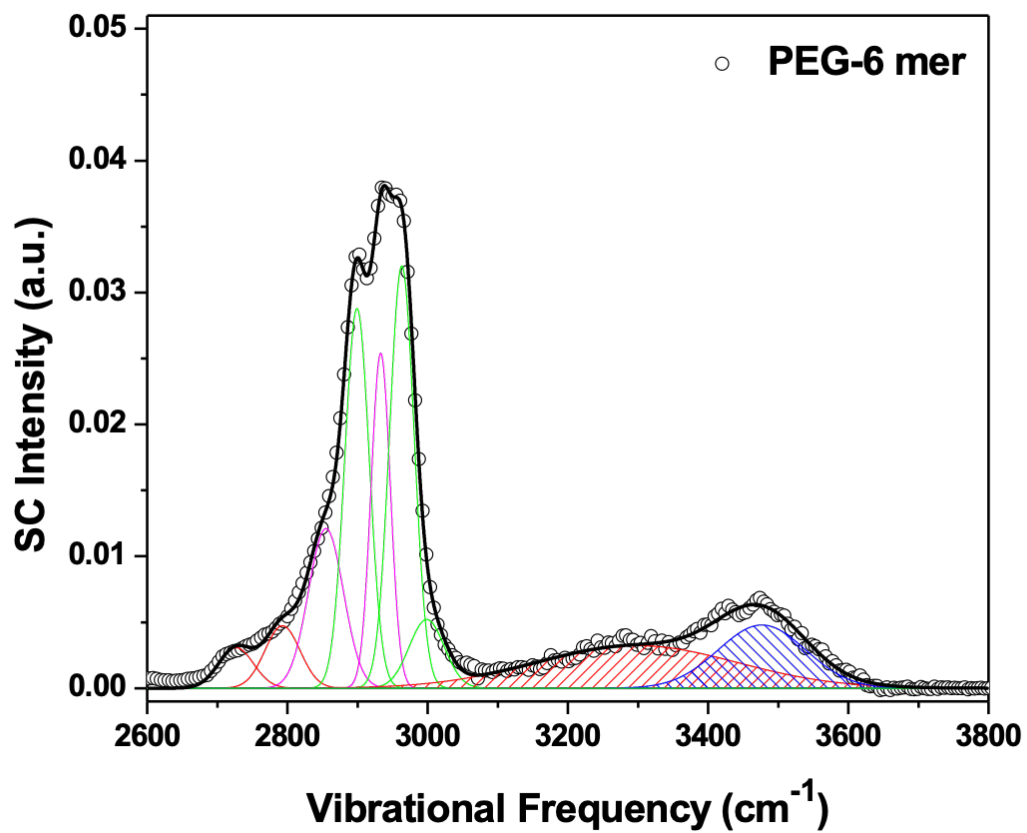


Figure A-6: Solute-correlated spectrum for PEG-6. The spectrum is normalized to the area under the CH stretches from 2600 to 3050 cm⁻¹.

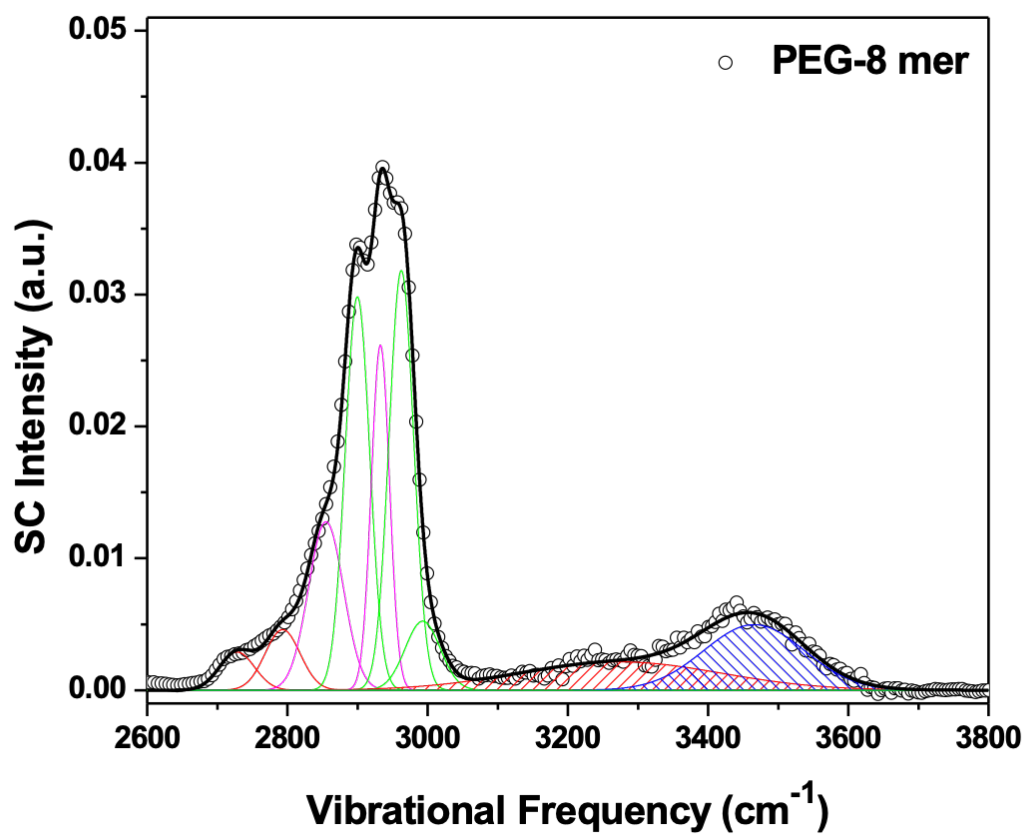


Figure A-7: Solute-correlated spectrum for PEG-8. The spectrum is normalized to the area under the CH stretches from 2600 to 3050 cm⁻¹.

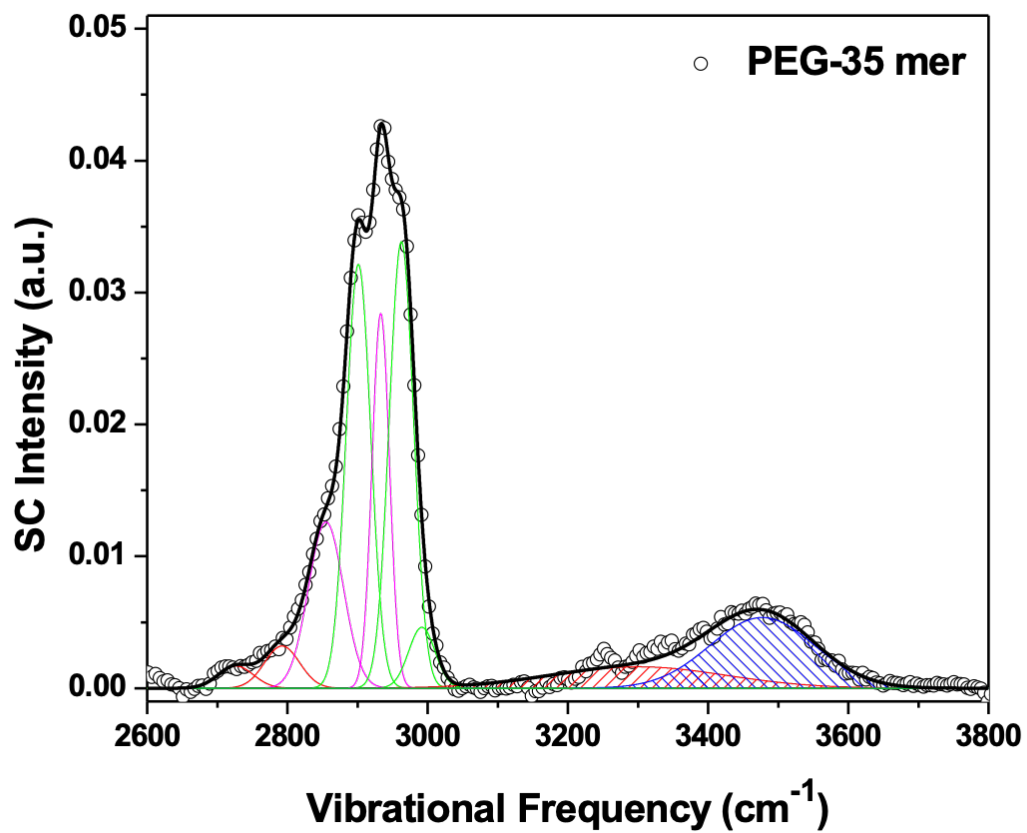


Figure A-8: Solute-correlated spectrum for PEG-35. The spectrum is normalized to the area under the CH stretches from 2600 to 3050 cm⁻¹.

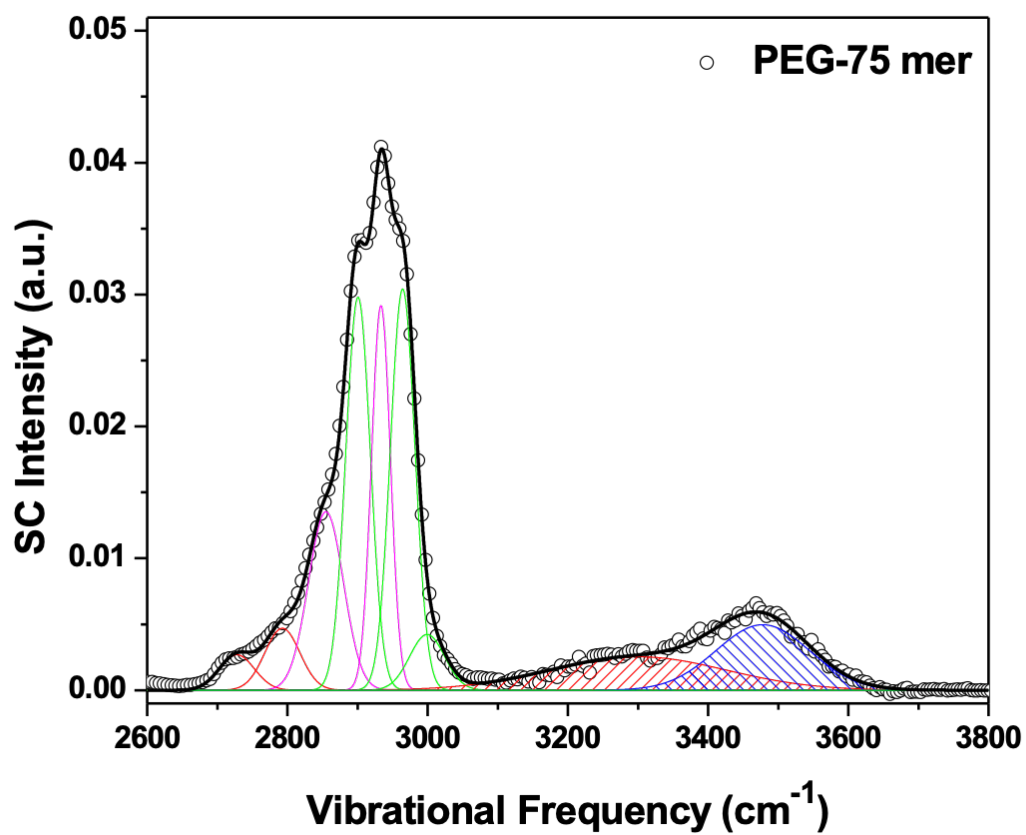


Figure A-9: Solute-correlated spectrum for PEG-75. The spectrum is normalized to the area under the CH stretches from 2600 to 3050 cm⁻¹.

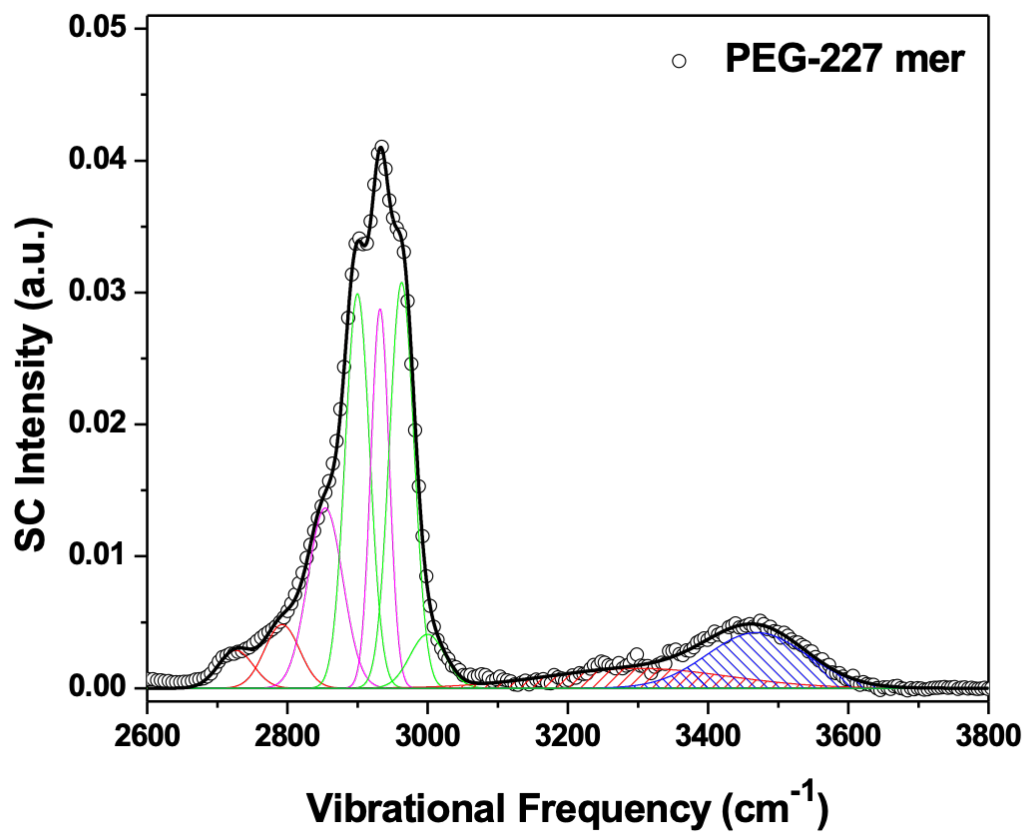


Figure A-10: Solute-correlated spectrum for PEG-227. The spectrum is normalized to the area under the CH stretches from 2600 to 3050 cm⁻¹.

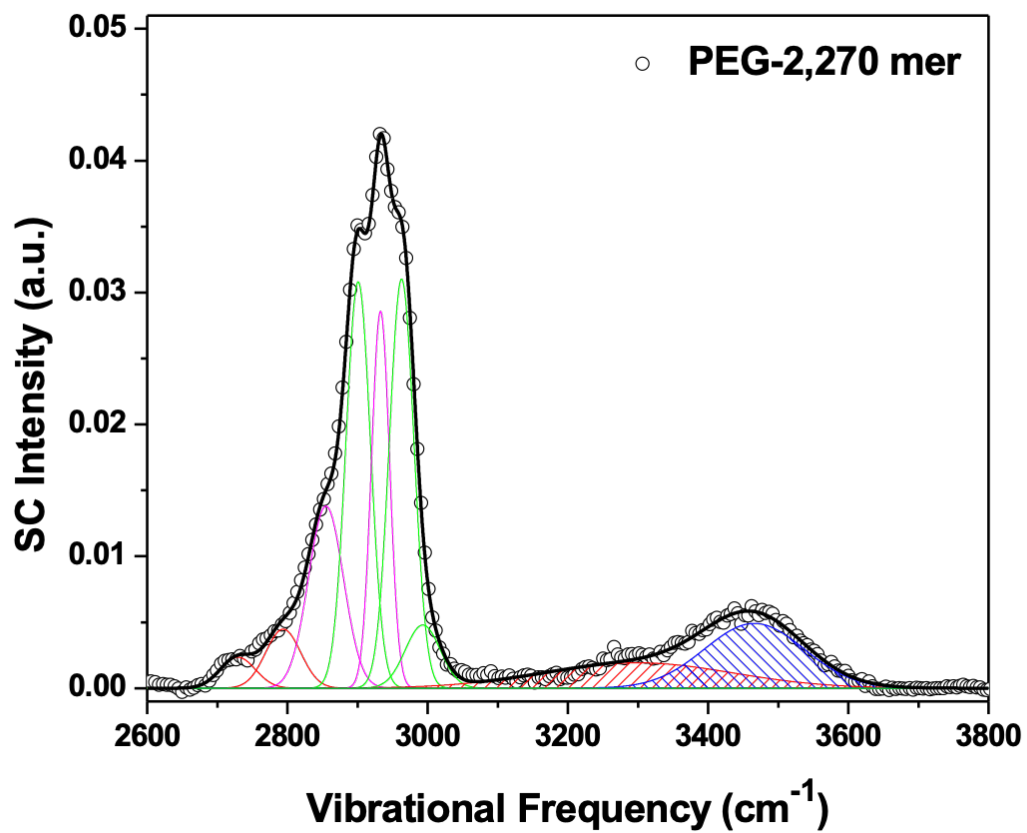


Figure A-11: Solute-correlated spectrum for PEG-2k. The spectrum is normalized to the area under the CH stretches from 2600 to 3050 cm⁻¹.

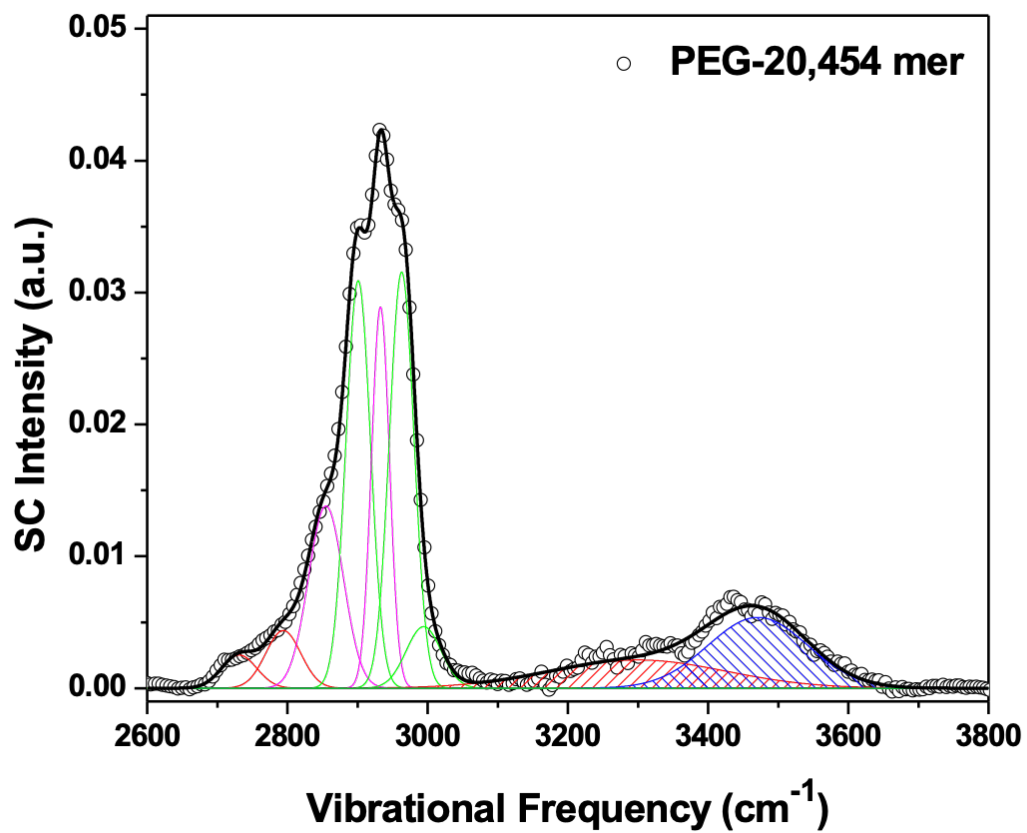


Figure A-12: Solute-correlated spectrum for PEG-20k. The spectrum is normalized to the area under the CH stretches from 2600 to 3050 cm⁻¹.

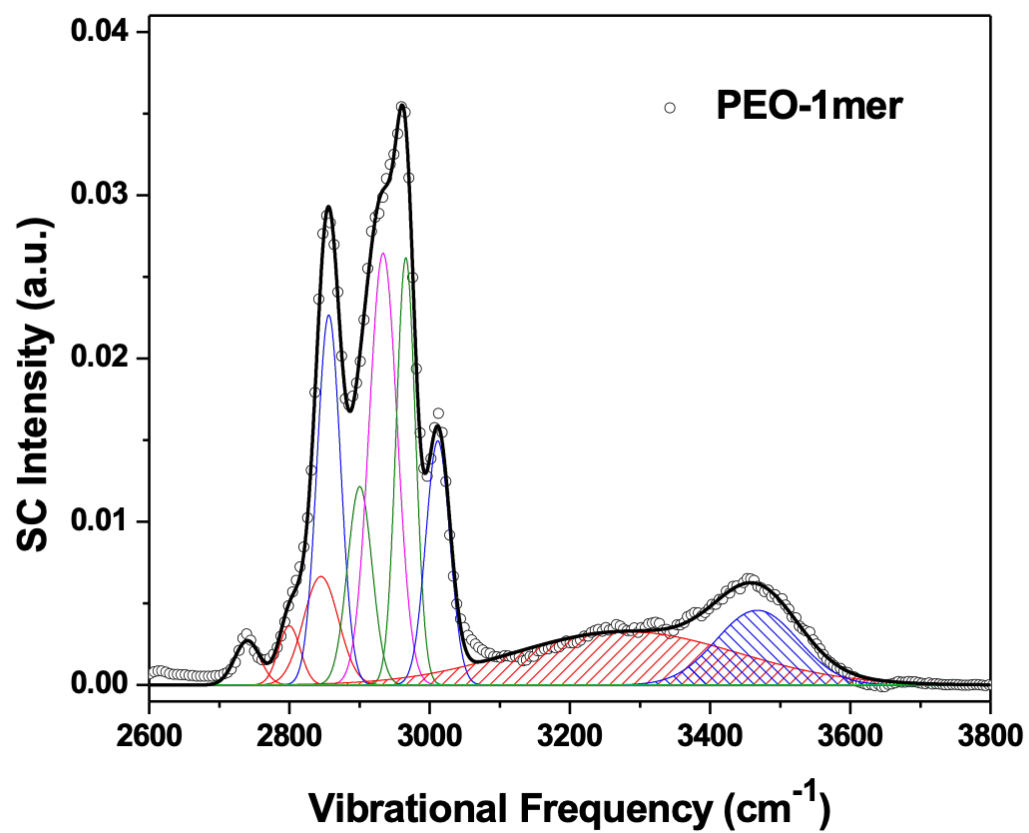


Figure A-13: Solute-correlated spectrum for PEO-1. The spectrum is normalized to the area under the CH stretches from 2600 to 3050 cm⁻¹.

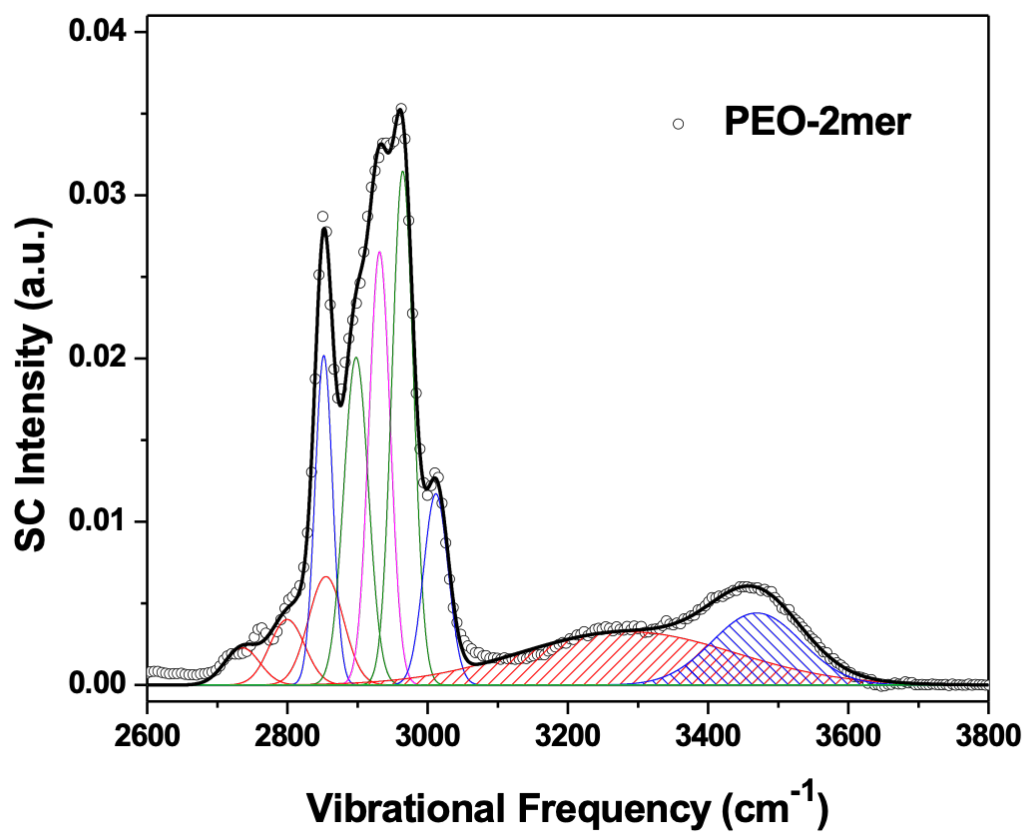


Figure A-14: Solute-correlated spectrum for PEO-2. The spectrum is normalized to the area under the CH stretches from 2600 to 3050 cm⁻¹.

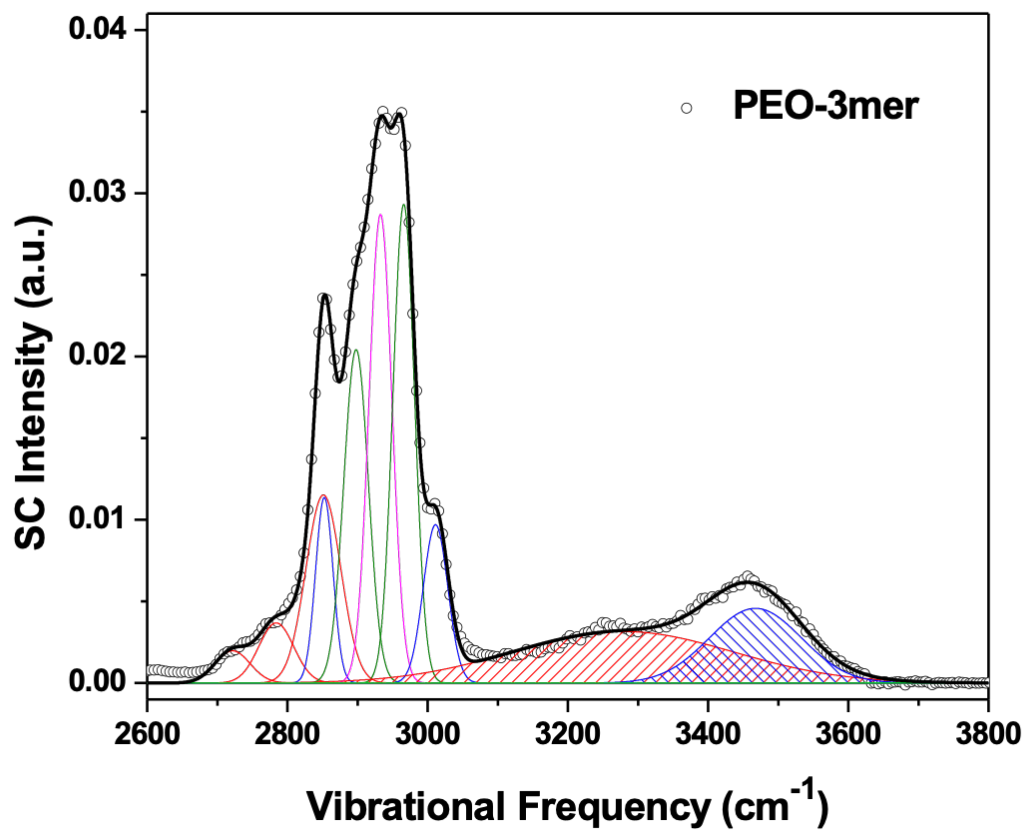


Figure A-15: Solute-correlated spectrum for PEO-3. The spectrum is normalized to the area under the CH stretches from 2600 to 3050 cm⁻¹.

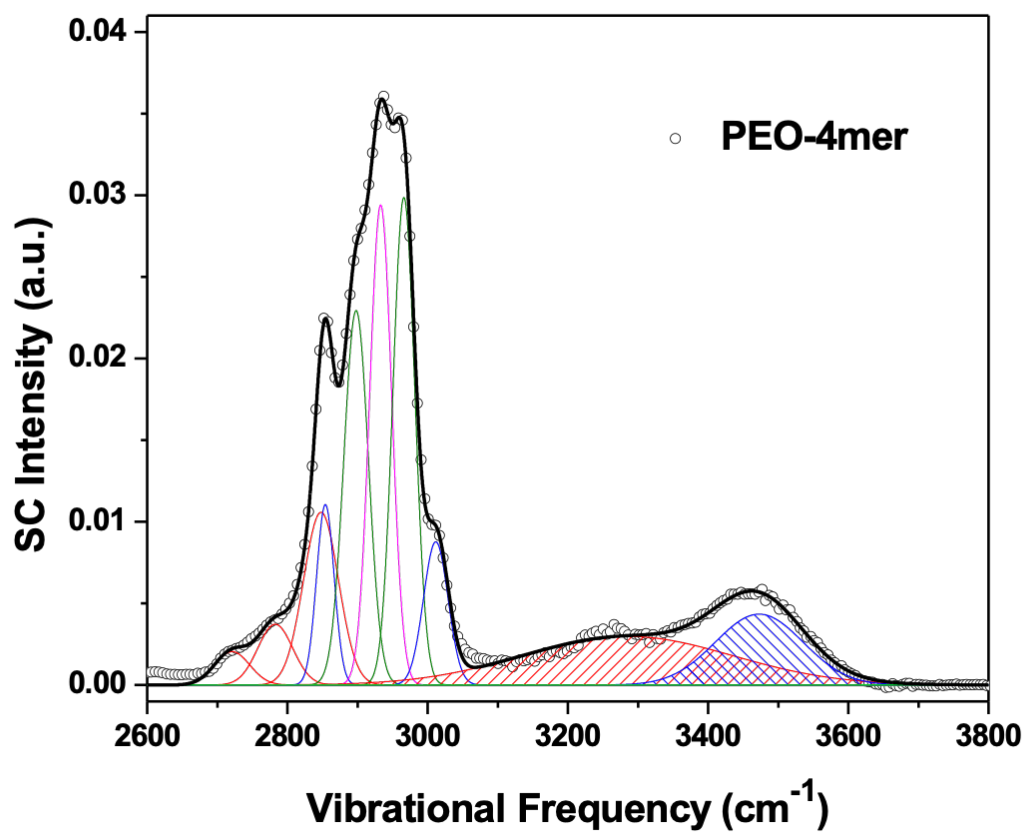


Figure A-16: Solute-correlated spectrum for PEO-4. The spectrum is normalized to the area under the CH stretches from 2600 to 3050 cm⁻¹.

The amplitude of the two OH peaks obtained by fitting the spectra to a sum of gaussian peaks are summarized in Figure A-17.

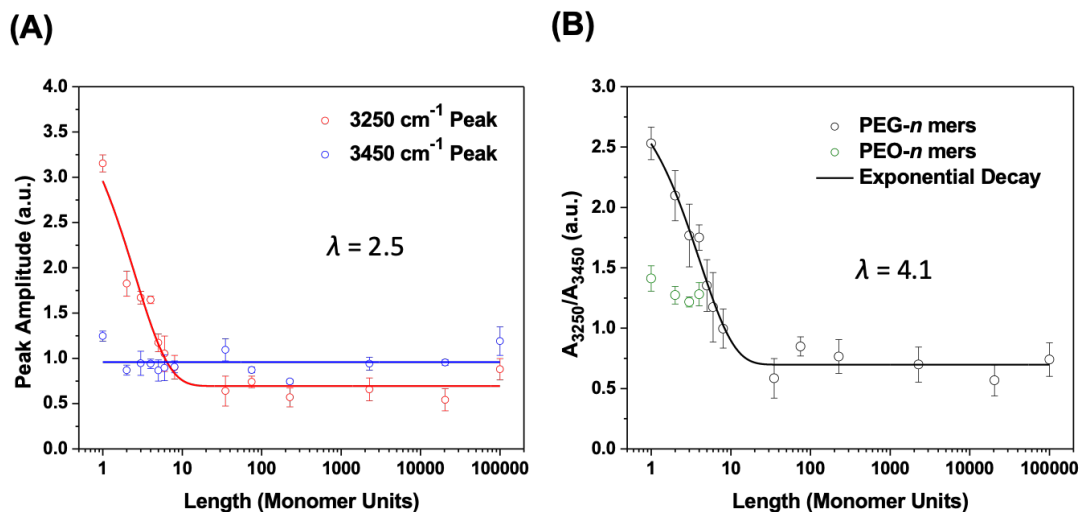


Figure A-17: OH stretch parameters obtained from the gaussian deconvolution plotted as a function of solute chain length. (A) Effect of chain length on the amplitude. (B) Effect of chain length on the ratio of the amplitudes.

The amplitude of the four dominant CH peaks obtained by fitting the PEG-*n* spectra to a sum of gaussian peaks are summarized in Figure A-18.

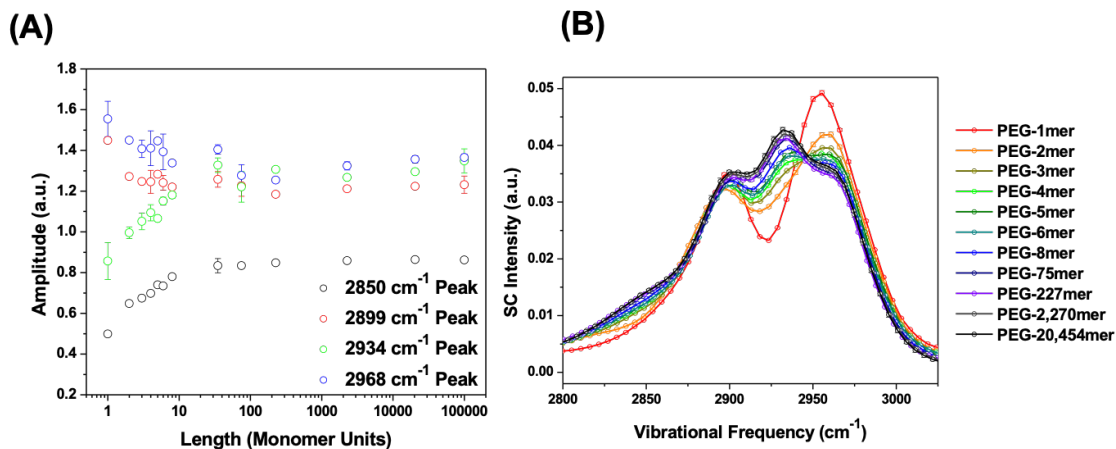


Figure A-18: OH stretch parameters obtained from the gaussian deconvolution plotted as a function of solute chain length. (A) Effect of chain length on the amplitude. (B) Overlay of the CH stretches of PEG-*n* solutes.

An overlay of the CH region of the PEO-*n* solutes is provided in Figure A-19.

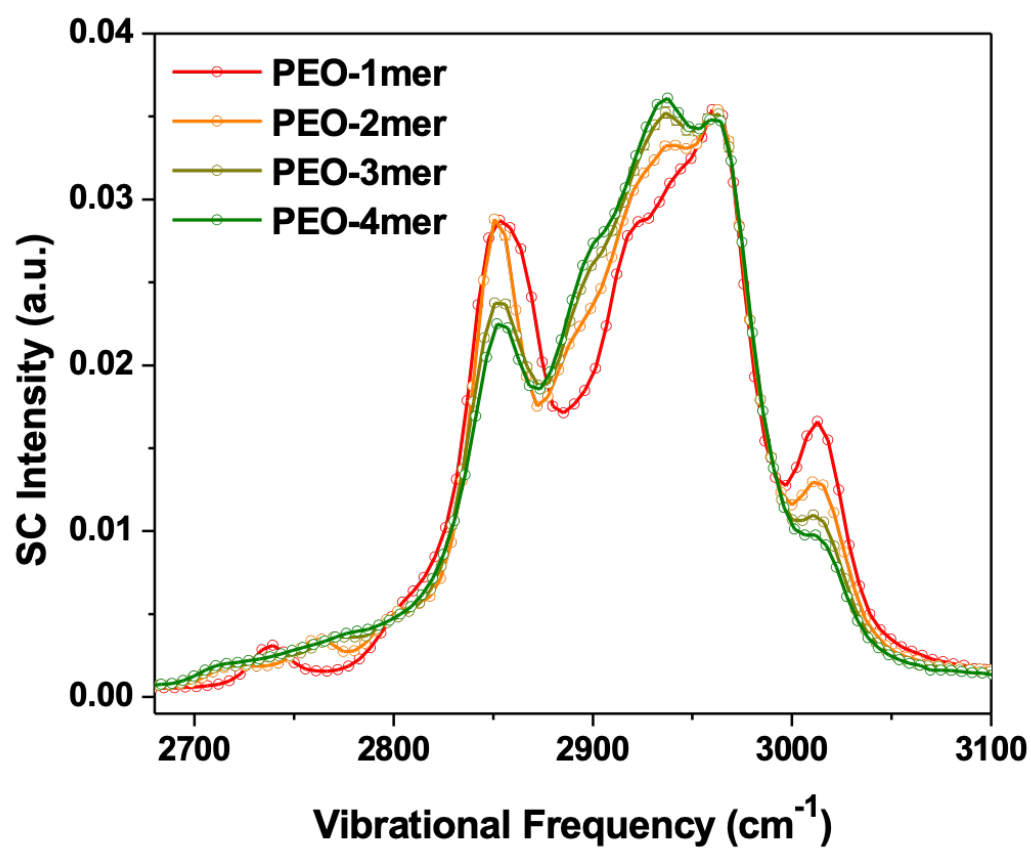


Figure A-19: Overlay of the CH stretches of PEG-*n* solutes.

The center frequency, width, and amplitude parameters of the gaussian peaks are summarized in Table A-1, A-2, and A-3, respectively.

Table A-1: Center frequencies, ν_c , of the Gaussian peaks obtained from fits to the solute-correlated spectra of polyether solutes. The data are arranged as a function of chain length and peak number.

Mode Assignment	Peak #	CH overtones					CH stretches					OH stretches		
		1		2		3	4	5	6	7	8	9	10	11
		ρ -CH ₂ ,1	ρ -CH ₂ ,2	ν -CH ₂ -s,1	ν -CH ₂ -s,1	ν -CH ₂ -s,2	ν -CH ₂ -as,1	ν -CH ₂ -as,2	ν -CH ₂ -comb	ν -CH ₂ -as,1	ν -OH,1	ν -OH,2		
Solute	Notation 1	δ^*2	δ^*2	d^*	r^*	d^*	d^*	d^*	d^*	r^*	-	-		
	Notation 2	δ^*2	δ^*2	d^*	r^*	d^*	d^*	d^*	d^*	r^*	-	-		
	Length	ν_c (cm ⁻¹)	ν_c (cm ⁻¹)	ν_c (cm ⁻¹)	ν_c (cm ⁻¹)	ν_c (cm ⁻¹)	ν_c (cm ⁻¹)							
PEG- <i>n</i>	PEG-1	2741.9	2799.9	2855.0	-	2900.1	2945.0	2963.9	2990.0	-	3277.7	3467.6		
	PEG-2	2726.4	2790.3	2855.0	-	2898.0	2933.8	2962.0	2990.7	-	3282.4	3468.4		
	PEG-3	2728.4	2793.5	2855.0	-	2898.2	2932.9	2962.3	2991.2	-	3285.0	3467.4		
	PEG-4	2730.1	2794.0	2855.0	-	2898.9	2933.1	2962.5	2990.6	-	3286.2	3469.8		
	PEG-5	2729.7	2793.8	2855.0	-	2899.9	2933.7	2963.5	2993.3	-	3288.0	3471.8		
	PEG-6	2729.2	2793.6	2855.0	-	2899.6	2933.2	2963.1	2995.9	-	3295.6	3472.5		
	PEG-8	2728.2	2793.5	2855.0	-	2900.0	2932.8	2962.8	2994.5	-	3281.3	3468.3		
	PEG-35	2731.7	2794.4	2855.0	-	2900.8	2932.6	2962.5	2991.7	-	3300.0	3475.4		
	PEG-75	2726.7	2792.3	2854.4	-	2900.3	2932.6	2963.2	2997.6	-	3296.4	3472.1		
	PEG-227	2727.3	2792.9	2854.3	-	2900.1	2932.1	2962.8	2998.4	-	3300.0	3468.8		
	PEG-2k	2730.2	2794.1	2855.0	-	2901.0	2933.0	2963.3	2994.1	-	3300.0	3466.8		
	PEG-20k	2731.8	2794.4	2855.0	-	2901.1	2932.8	2962.9	2991.5	-	3300.0	3469.9		
	PEO- <i>n</i>	PEO-1	2740.2	2800.0	2855.0	2854.8	2898.0	2929.1	2965.4	-	3011.9	3285.0	3468.8	
		PEO-2	2745.9	2800.0	2855.0	2851.4	2898.0	2930.4	2964.4	-	3012.0	3282.4	3472.0	
PEO-3		2724.9	2786.8	2852.4	2852.4	2898.0	2933.1	2966.3	-	3010.4	3282.5	3470.3		
PEO-4		2722.1	2783.7	2848.6	2854.0	2898.0	2933.8	2966.6	-	3009.3	3290.9	3476.6		

Table A-2: Width parameters, w , for the Gaussian peaks obtained from fits to the solute-correlated spectra of polyether solutes. The data are arranged as a function of chain length and peak number.

Mode Assignment	Peak #	CH overtones					CH stretches					OH stretches		
		1		2		3	4	5	6	7	8	9	10	11
		ρ -CH ₂ ,1	ρ -CH ₂ ,2	ν -CH ₂ -s,1	ν -CH ₂ -s,1	ν -CH ₂ -s,2	ν -CH ₂ -as,1	ν -CH ₂ -as,2	ν -CH ₂ -comb	ν -CH ₂ -as,1	ν -OH,1	ν -OH,2		
Solute	Notation 1	δ^*2	δ^*2	d^*	r^*	d^*	d^*	d^*	d^*	r^*	-	-		
	Notation 2	δ^*2	δ^*2	d^*	r^*	d^*	d^*	d^*	d^*	r^*	-	-		
	Length	w (cm ⁻¹)	w (cm ⁻¹)	w (cm ⁻¹)	w (cm ⁻¹)	w (cm ⁻¹)	w (cm ⁻¹)	w (cm ⁻¹)	w (cm ⁻¹)	w (cm ⁻¹)	w (cm ⁻¹)	w (cm ⁻¹)		
PEG- <i>n</i>	PEG-1	50.0	38.8	42.4	-	35.0	27.2	35.0	49.4	-	283.7	148.8		
	PEG-2	50.0	49.1	50.0	-	35.0	28.4	35.0	50.0	-	283.7	135.2		
	PEG-3	50.0	50.0	50.0	-	35.0	28.1	35.0	50.0	-	290.8	143.9		
	PEG-4	50.0	50.0	50.0	-	35.0	27.5	35.0	50.0	-	293.3	139.8		
	PEG-5	50.0	50.0	50.0	-	35.0	26.8	35.0	50.0	-	257.3	124.1		
	PEG-6	50.0	50.0	50.0	-	35.0	27.0	35.0	49.5	-	272.8	137.2		
	PEG-8	50.0	50.0	50.0	-	35.0	26.0	35.0	50.0	-	279.7	142.4		
	PEG-35	50.0	50.0	50.0	-	35.0	25.0	34.6	39.5	-	250.0	147.5		
	PEG-75	50.0	50.0	50.0	-	35.0	26.2	35.0	50.0	-	251.1	140.1		
	PEG-227	50.0	50.0	50.0	-	35.0	25.8	35.0	50.0	-	251.9	134.3		
	PEG-2k	50.0	50.0	50.0	-	35.0	26.0	35.0	50.0	-	264.0	145.1		
	PEG-20k	50.0	50.0	50.0	-	35.0	25.4	35.0	50.0	-	250.0	147.2		
	PEO- <i>n</i>	PEO-1	37.5	31.8	50.0	29.3	35.0	40.0	30.9	-	28.2	252.4	120.8	
		PEO-2	50.0	40.0	50.0	25.0	35.0	30.7	32.5	-	29.9	250.0	133.0	
PEO-3		50.0	50.0	50.0	25.0	35.0	33.0	30.2	-	33.4	250.0	133.6		
PEO-4		50.0	50.0	50.0	25.0	35.0	32.2	29.9	-	35.0	250.0	125.8		

Table A-3: Center frequencies for various Gaussian peaks obtained from fits to the solute-correlated spectra of PEO-*n* solutes. The data are arranged as a function of chain length and peak number.

Mode Assignment	Peak #	CH overtones					CH stretches					OH stretches		
		1		2		3	4	5	6	7	8	9	10	11
		ρ -CH ₂ ,1	ρ -CH ₂ ,2	ν -CH ₂ -s,1	ν -CH ₂ -s,1	ν -CH ₂ -s,2	ν -CH ₂ -as,1	ν -CH ₂ -as,2	ν -CH ₂ -comb	ν -CH ₂ -as,1	ν -OH,1	ν -OH,2		
Solute	Notation 1	δ^*2	δ^*2	d^*	r^*	d^*	d^*	d^*	d^*	r^*	-	-		
	Notation 2	δ^*2	δ^*2	d^*	r^*	d^*	d^*	d^*	d^*	r^*	-	-		
	Length	A (a.u.)	A (a.u.)	A (a.u.)	A (a.u.)	A (a.u.)	A (a.u.)	A (a.u.)	A (a.u.)	A (a.u.)	A (a.u.)	A (a.u.)		
PEG- <i>n</i>	PEG-1	0.221	0.163	0.508	-	1.457	0.765	1.391	0.445	-	3.153	1.246		
	PEG-2	0.187	0.273	0.670	-	1.298	0.680	1.499	0.445	-	1.824	0.870		
	PEG-3	0.187	0.278	0.687	-	1.280	0.778	1.436	0.412	-	1.670	0.945		
	PEG-4	0.172	0.265	0.720	-	1.294	0.818	1.411	0.409	-	1.646	0.940		
	PEG-5	0.175	0.273	0.756	-	1.323	0.848	1.431	0.364	-	1.172	0.866		
	PEG-6	0.175	0.277	0.756	-	1.302	0.870	1.435	0.348	-	1.052	0.896		
	PEG-8	0.183	0.287	0.800	-	1.306	0.857	1.400	0.315	-	0.903	0.906		
	PEG-35	0.123	0.234	0.833	-	1.419	0.923	1.471	0.234	-	0.639	1.093		
	PEG-75	0.174	0.301	0.851	-	1.311	0.936	1.342	0.274	-	0.740	0.872		
	PEG-227	0.177	0.299	0.861	-	1.321	0.927	1.357	0.264	-	0.569	0.744		
	PEG-2k	0.151	0.280	0.865	-	1.346	0.939	1.359	0.292	-	0.658	0.941		
	PEG-20k	0.153	0.271	0.866	-	1.371	0.926	1.379	0.303	-	0.542	0.955		

Peak #	1	2	3	4	5	6	7	8	9	10	11	
Mode	ρ -CH ₂ ,1	ρ -CH ₂ ,2	ν -CH ₂ -s,1	ν -CH ₂ -s,1	ν -CH ₂ -s,2	ν -CH ₂ -as,1	ν -CH ₂ -as,2	ν -CH ₂ -comb	ν -CH ₂ -as,1	ν -OH,1	ν -OH,2	
Assignment	Notation 1	Notation 2	δ^*2	δ^*2	d^*	r^*	d^*	d^*	d^*	r^*	-	-
Solute	Length	A (a.u.)	A (a.u.)	A (a.u.)	A (a.u.)	A (a.u.)	A (a.u.)	A (a.u.)	A (a.u.)	A (a.u.)	A (a.u.)	A (a.u.)
PEO- <i>n</i>	PEO-1	0.127	0.151	0.865	0.557	0.356	1.302	1.124	-	0.528	1.076	0.762
	PEO-2	0.202	0.168	0.538	0.550	0.850	0.985	1.314	-	0.432	1.065	0.836
	PEO-3	0.129	0.230	0.714	0.368	0.896	1.218	1.118	-	0.417	1.039	0.853
	PEO-4	0.131	0.233	0.671	0.341	1.000	1.229	1.094	-	0.396	0.983	0.767

Appendix B

Supporting Information for Chapters 4-5

The parameters of the mAb-1 phase diagram are summarized in Table B-1.

Table B-1: Summary of fitted parameters for the effects of mAb concentration on the phase transition temperatures using Equation 5-12.

Transition	T_{crit} (K)	C_{crit} (mg/mL)	A (a.u.)
T_{ph}	301	118	2.4
T_{meta}	296	121	2.1

The raw rate constants for ATPS formation at different temperatures and mAb-1 concentrations are summarized in Table B-2.

Table B-2: Fitted parameters of the KWW model for the 90, 60, and 40 mg/mL mAb solutions with 20 mg/mL PEG-3350.

90 mg/mL			60 mg/mL			40 mg/mL		
T (K)	k (s^{-1})	β (a.u.)	T (K)	k (s^{-1})	β (a.u.)	T (K)	k (s^{-1})	β (a.u.)
290.4	1.89E-08	0.206	289.9	2.584E-08	0.201	290.1	7.170E-08	0.264
290.6	7.95E-07	0.25	290.3	3.096E-07	0.213	290.4	3.177E-06	0.295
290.8	4.91E-06	0.253	290.6	3.789E-06	0.225	290.8	2.308E-05	0.331
290.9	1.75E-05	0.282	290.8	6.929E-05	0.341	291.1	1.597E-04	0.406
291.1	5.26E-05	0.334	291.0	1.115E-04	0.304	291.3	3.202E-04	0.431
291.2	1.55E-04	0.363	291.2	3.366E-04	0.422	291.5	8.770E-04	0.668
291.3	2.37E-04	0.359	291.4	7.695E-04	0.468	291.6	1.780E-03	1.161
291.4	5.97E-04	0.412	291.6	1.297E-03	0.572	291.8	2.629E-03	1.398
291.5	8.18E-04	0.482	291.7	2.118E-03	0.975	292.0	3.038E-03	1.631
291.6	1.41E-03	0.513	291.9	2.953E-03	1.229	292.1	3.369E-03	1.551
291.7	1.95E-03	0.532	292.1	3.431E-03	1.417	292.3	3.406E-03	1.563
291.8	2.15E-03	0.632	292.3	3.750E-03	1.530	292.5	3.424E-03	1.573
291.9	2.68E-03	0.752	292.5	3.904E-03	1.538	292.6	3.405E-03	1.593
292.0	3.26E-03	0.96	292.7	3.972E-03	1.547	292.8	3.311E-03	1.618
292.1	3.83E-03	1.085	292.8	4.063E-03	1.475	293.0	3.267E-03	1.626
292.2	4.11E-03	1.157	293.0	4.014E-03	1.473	293.2	3.212E-03	1.685
292.3	4.23E-03	1.264	293.2	3.979E-03	1.478	293.3	3.155E-03	1.761
292.4	4.81E-03	1.321	293.4	3.957E-03	1.468	293.5	3.155E-03	1.761
292.5	5.26E-03	1.4	293.6	3.928E-03	1.421	293.7	3.101E-03	1.890
292.6	5.39E-03	1.471	293.8	3.793E-03	1.465			
292.7	5.57E-03	1.487	293.9	3.733E-03	1.459			
292.8	5.82E-03	1.501	294.1	3.696E-03	1.433			
293.0	5.85E-03	1.649	294.3	3.696E-03	1.433			
293.2	6.33E-03	1.506	294.5	3.533E-03	1.406			
293.3	6.14E-03	1.647	294.7	3.417E-03	1.425			
293.5	6.29E-03	1.61	294.9	3.272E-03	1.452			
293.7	6.40E-03	1.574	295.0	3.231E-03	1.441			
293.9	6.30E-03	1.594	295.2	3.127E-03	1.433			
294.0	6.39E-03	1.535	295.4	3.004E-03	1.465			
294.2	6.40E-03	1.515	295.6	2.876E-03	1.471			
294.4	6.52E-03	1.466	295.8	2.751E-03	1.486			
294.5	6.71E-03	1.355	295.9	2.627E-03	1.512			
294.7	6.48E-03	1.42	296.1	2.472E-03	1.606			
294.9	6.23E-03	1.544	296.3	2.365E-03	1.684			
295.1	6.12E-03	1.514	296.5	2.238E-03	1.836			

295.2	6.09E-03	1.498							
295.4	6.11E-03	1.473							
295.6	6.02E-03	1.452							
295.7	6.12E-03	1.388							
295.9	5.83E-03	1.415							
296.1	5.81E-03	1.376							
296.3	5.51E-03	1.442							
296.4	5.65E-03	1.378							
296.6	5.31E-03	1.431							
296.8	5.15E-03	1.465							
297.0	5.10E-03	1.368							
297.1	4.88E-03	1.466							
297.3	4.89E-03	1.352							
297.5	4.51E-03	1.457							
297.6	4.44E-03	1.419							
297.8	4.39E-03	1.343							
298.0	4.05E-03	1.394							
298.2	3.81E-03	1.421							
298.3	3.67E-03	1.371							
298.5	3.40E-03	1.421							
298.7	3.23E-03	1.372							
298.8	2.97E-03	1.422							
299.0	2.66E-03	1.458							
299.2	2.44E-03	1.418							
299.4	2.09E-03	1.506							
299.5	1.75E-03	1.534							
299.7	1.33E-03	1.612							

The VFT parameters for various mAb-1 concentration are summarized in Table **B-3**.

Table **B-3**: The fitted parameters of the VFT model for various mAb concentrations.

mAb Conc. (mg/mL)	τ_0 (s)	T_0 (K)	D_{VFT} (a.u.)
90	0.57	289.6	0.05
60	0.24	288.7	0.08
40	0.28	288.9	0.07

VITA

Bradley A. Rogers

EDUCATION

- The Pennsylvania State University**, University Park, PA Dec 2019
Ph.D. in Chemistry
- James Madison University**, Harrisonburg, VA May 2014
B.S. in Chemistry

PROFESSIONAL AND RESEARCH EXPERIENCE

- The Pennsylvania State University**, University Park, PA Aug 2014 - Dec 2019
Ph.D. Dissertation in Prof. Paul S. Cremer's Lab:
Conformational and Colloidal Stability of Macromolecules in Aqueous Salt Solutions
- Teaching Assistant:*
- | | |
|---|---------------------|
| Quantum Chemistry (John B. Asbury) | SP 2018 and SP 2019 |
| Electroanalytical Chemistry (Thomas E. Mallouk) | SP 2017 |
| Physical Chemistry Lab (Bratoljub H. Milosavljevic) | SP 2015 - FA 2015 |
| General Chemistry (Mary Jo Bojan) | FA 2014 |
| General Chemistry Lab (Joe T. Keiser) | FA 2014 |
- James Madison University**, Harrisonburg, VA Aug 2010 - May 2014
B.S. Thesis in Prof. Yanjie Zhang's Lab:
Hofmeister Anion Effects on the Thermodynamics of Caffeine Partitioning between Aqueous and Cyclohexane Phases
- NSF Research Experience for Undergraduates*
Caffeine Solubility in Aqueous Salt Solutions SU 2013
- General and Organic Chemistry Tutor:*
Math and Science Learning Center (Amy Tam) FA 2012 - SP 2014

PUBLICATIONS

- (1) **Rogers, B. A.**; Rembert, K. B.; Poyton, M. F.; Okur, H. I.; Kale, A. R.; Yang, T.; Zhang, J.; Cremer, P. S. A Stepwise Mechanism for Aqueous Two-Phase System Formation in Concentrated Antibody Solutions *Proc. Nat. Acad. Sci. U.S.A.* **2019** 116 (32), 15784-15791.
- (2) Drexler, C. I.*; Miller, T. C.*; **Rogers, B. A.**; Li, Y. C.; Daly Jr, C.A.; Yang, T.; Corcelli, S. A.; Cremer, P. S. Counter Cations Affect Transport in Aqueous Hydroxide Solutions with Ion Specificity *J. Am. Chem. Soc.* **2019** 141 (17), 6930-6936.
- (3) Bruce, E. E.*; Bui, P. T.*; **Rogers, B. A.**; Cremer, P. S.; van der Vegt, N. F. A Nonadditive Ion Effects Drive Both Collapse and Swelling of Thermoresponsive Polymers in Water *J. Am. Chem. Soc.* **2019** 141 (16), 6609-6616.
- (4) **Rogers, B. A.**; Thompson, T. S.; Zhang, Y. Hofmeister Anion Effects on Thermodynamics of Caffeine Partitioning between Aqueous and Cyclohexane Phases *J. Phys. Chem. B* **2016**, 120(49), 12596-12603.

PATENTS

- (1) **Rogers, B. A.**; Yang, T.; Zhang, J.; Cremer, P. S. A TEC-based Design for Temperature Gradient Microfluidics *Patent Pending* filed on **3/12/2019**, PCT/US2019/021885.
- (2) **Rogers, B. A.**; Cremer, P. S. Method of Use for Temperature Gradient Microfluidics *Provisional Patent Pending* filed on **12/14/2018**, PSU/62/780,145.